Investigation of the Magnetic and Magneto-dielectric Properties of few Complex Spinels

A Thesis Submitted to
Indian Institute of Technology Guwahati
for the degree of

Doctor of Philosophy

By

Sanjib Nayak

Department of Physics
Indian Institute of Technology Guwahati
Guwahati-781039, Assam (India)

Dedicated to my father Late Mr. Swapan Kumar Nayak, Mother Smt. Iva Nayak, my Elder Brother and Bhabi

INDIAN INSTITUTE OF TECHNOLOGY GUWAHATI

Department of Physics

Guwahati – 781039

Declaration

"*Investigation of the magnetic and magneto-dielectric properties of few complex spinels*" is the result of my own doctoral research work. This work was carried out under the supervision of Dr. Subhash Thota at the Department of Physics, Indian Institute of Technology Guwahati. To the best of my knowledge, the work presented in this thesis has not been submitted to any other Institute/University for the award of any degree.

Sanjib Nayak
Research Scholar (Roll No: 136121018)
Department of Physics
Indian Institute of Technology Guwahati
Guwahati-781039, India

INDIAN INSTITUTE OF TECHNOLOGY GUWAHATI

Department of Physics

Guwahati – 781039

Certificate

It is certified that the work described in this thesis, entitled "*Investigation of the magnetic and magneto-dielectric properties of few complex spinels*", done by Mr. Sanjib Nayak, a Ph.D. student of Department of Physics, Indian Institute of Technology Guwahati, for the award of degree of Doctor of Philosophy has been carried out under my supervision. This work has not been submitted elsewhere for the award of any degree.

Dr. Subhash Thota
Associate Professor
Department of Physics
Indian Institute of Technology Guwahati
Guwahati-781039, India

Acknowledgements

More than four years of hard work and the innumerable help and support from the people around me made it possible in completion of the thesis work.

First I express my sincere gratitude to my thesis supervisor Dr. Subhash Thota for giving me the opportunity to work with him. During the course of my doctoral research I have not only learned the physics from him but also learn so many personal things. I must acknowledge him for providing the unconditional freedom to work, think and express on whatever I have done in my research work by keeping the faith on my capabilities.

I am highly thankful to my doctoral committee members, Prof. S. Ghosh (Chairman), Dr. D. Pal and Prof. M. Qureshi for their continuous academic guidance and checking my work progress and seminars during my Ph. D. Their advices, and valuable discussions helped me to understand the basics of the subject along with skills and also improve the quality of my thesis work. I would like to express my sincere gratitude to Prof. P. Poulose, Head of the Department of the Physics for giving me the opportunity to work in the department and to use all the departmental facilities.

I am also grateful to all the faculty members of the Physics department. I would also like to thank Dr. Sidananda Sarma for his technical assistance and friendly discussions. My special thanks to all scientific officers and staff members in our department.

My Sincere thanks to all the collaborators Prof. M. S. Seehra, Dr. T. Sarkar, Prof. R. Mathieu, Dr. A. Waske, Dr. M. Krautz, Prof. J. Eckert, Dr. Kiran Dasari, Dr. V. Sathe, Dr. A. Banerjee for providing me the instrumental facilities and rich data, without their help I would not be able complete my thesis work.

The financial support for this thesis is provided by Indian Institute of Technology Guwahati and Ministry of Human Resource and Development. I also acknowledge the facilities provided by Science and Engineering Research Board (SERB)/Department of Science and Technology (DST) under Young Scientist Scheme (YSS) (Ref. No. YSS/2014/000340) and Department of Atomic Energy (DAE)-Board of Research in Nuclear Sciences (BRNS) under Young Scientist Research Award (YSRA) (Grant No. 34/20/02/2015/BRNS).

The Central instrument Facility provided by Indian Institute of Technology Guwahati and the XRD facility provided by DST, New Delhi, through FIST program [SR/FST/PSII-020/2009] is also acknowledged.

I am also thankful to Dr. Debasish Das for helping me in one my paper work and also Anindya da who help me initially for sample preparation.

I am thankful to my lab mates, Deep, Prativa, Robin, Rohan, Tanveer Bhaiya, Sayandeep, Tere Nagendra babu, Ram Kumar for their help, suggestions and enjoyable company.

I am thankful to my seniors Dr. T. Santosh Kumar, Dr. P. Rajender, Dr. P. Mahesh, Ranganadha Gopal Rao, and Gone Rajender for their help and encouragements.

I am thankful to my friends Noor, Srikrishna, Eshita, Kamal, Rajkumar, Pankaj, Kajwal, Camelia, Priyadarshini, Sushmita, Arun, Pratap, Ujjal, Ganesh and all other batchmates also Ayan, Sobhit, Indranil, Moin, Arup, Roopam and also my graduation friends Dulal, Chiranjit, Somnath, Rajkamal, Swadesh and Mrinmoy, Atanu for their constant encouragement.

I am also thankful to my seniors Bappa da, Ramesh da, Biswajit da, Obaidullah da, Kartik da, Tapas da, Arnab da, Abhijit da, Rahul da, Ramiz da, Sudin da, Ashis da, Sahoo da, Kallol da, Vanki anna, Anil anna, Prahladh bhaiya, and other seniors, and also my juniors Purroshtom, Gobinda, Srinivas, Sasmita, Jagan, Ruma, Joydip, Makur, Susmita, Sumit, Karuna, Apurba …., for their constant encouragement and sharing enjoyful environment in the department.

Finally, I would like to express my deepest gratitude to my family, especially, my parents, my brother, bhabi and all other family members, who gave blessings, moral support and continuous encouragement.

by

Sanjib Nayak

Synopsis Report

Spinel oxides (AB_2O_4) and their composites have proven to be an abundant research field due to their fascinating magnetic, electronic, chemical and optical properties [1-6]. The atomic arrangement in spinel compounds is interpreted as a pseudo-close-packed arrangements of the oxygen anions with divalent cations occupying tetrahedral A-lattice sites (T( )) and trivalent cations residing at the octahedral B-sites (O[ ]) of the cubic unit-cell of space group $Fd\bar{3}m$ [7, 8]. A spinel with the configuration (A^{2+}) $[B_2^{3+}]$ O_4 is termed as 'normal-spinel' while the other possible configuration (B^{3+}) $[A^{2+}B^{3+}]$ O_4 is called 'inverse-spinel'. Magnetic-spinels are well-established systems because of their remarkable applications in microwave devices, isolators, circulators, super-capacitors and phase-shifters [3, 8, 9]. Ferrites (Fe_3O_4) and Mn and Co-based spinels are widely investigated systems owing to the possibility of forming extremely large variety of solid solutions allowing a precise tailoring of their physical properties, which is a major advantage for microwave technology and other industrial applications [3, 9 - 16]. In the magnetic spinels alone, materials such as tricobalt tetroxide (Co_3O_4 = Cobalt (II, III) oxide), cobalt-orthostannate (Co_2SnO_4), cobalt-orthotitanate (Co_2TiO_4), and Hausmannite (Mn_3O_4) exhibit rich phase diagrams involving charge, orbital, geometrical frustration, canted Yafet-Kittle type and spiral antiferro/ferromagnetic orderings. Besides such rich magnetic properties, the low-temperature reentrant spin-glass transitions and sign-reversal exchange bias phenomena often occur which are associated with the competing exchange interactions and strong coupling between charges, spin and lattice degrees of freedom. Moreover, the magnetic ground state of the doped spinels are very sensitive to the average radius ratio B/A of cations ($<r_A>$) and charge fluctuations on them.

The present research work was primarily motived by the desire to understand the magnetic structure and other physical properties of few complex inverse spinels; (*i*) Co_2SnO_4, (*ii*) Co_2TiO_4, and a tetragonally distorted normal spinel Mn_3O_4. The layout of the thesis is as follows:

Chapter 1 provides an introduction to the spinels and their applications, crystal structure of spinels, and basic concepts of magnetism. Various magnetic phenomena are discussed both from an experimental and theoretical point of view in which the underlying physical principles are first presented with a follow up macroscopic and microscopic theories appropriately. This chapter also reviews the physics of spin-glasses and other disordered magnetic phases together with the Néel two-sublattice model of ferrimagnetism. This chapter concludes with the identification of few spinels that exhibits complex magnetic ordering and some critical issues of low-temperature disordered state which are addressed in the subsequent chapters.

Chapter 2 presents a detailed overview of various experimental techniques employed in this research work including the synthesis procedure based on standard solid-state reaction method and oxalate based low-temperature sol-gel processing. The structural characterization using X-ray diffraction technique (performed by Panalytical Xpert Pro diffractometer) followed by the Rietveld refinement method using Fullprof software was discussed briefly for the verification of the phase purity of the prepared samples. Details of elemental analysis

performed in the present work using the X-ray photoelectron spectroscopy (XPS) and X-ray energy dispersive analysis (EDAX) was described thereafter. Material characterization techniques like field emission scanning electron microscopy (FESEM) and transmission electron microscopy (TEM) were discussed because these instruments are used to study the microstructure/morphology and stoichiometry. A commercial superconducting quantum interference device (SQUID) based magnetometer, which was used to measure the dc-magnetization and ac-susceptibility was introduced in the subsequent section. Basic principle of temperature dependent specific-heat ($C_P(T)$) measurement procedure performed by means of a physical property measurement system (PPMS) was described. This chapter also describes the details of dielectric measurements carried out at various frequencies (10 Hz - 32 MHz) using a Novocontrol Alpha AN impedance analyzer over a wide temperature interval ($80\ K \leq T \leq 600\ K$). Finally, some spectroscopic characterization techniques like Fourier transformed infrared (FTIR) spectroscopy, electron-spin resonance (ESR) and micro-Raman are illustrated.

Chapter 3 presents synthesis of cobalt-orthostannate (Co_2SnO_4) polycrystals at different sintering temperatures and provides its structural characterization, elemental analysis using XPS, morphological and magnetization studies. A systematic comparison of the magnetic properties of Co_2SnO_4 samples sintered at two different temperatures, 1200ºC (S1200) and 1350ºC (S1350) was reported. The role of few percent of unreacted non-magnetic SnO_2 clusters on the global magnetic behavior of Co_2SnO_4 samples was discussed in terms of both ac-magnetic susceptibility (χ' and χ'') and dc-magnetization (M) studies. The elemental analysis by XPS reveals the presence of divalent and tetravalent states of cobalt and tin, respectively in S1350 which confirmed the structure: $(Co^{2+})[Sn^{4+}Co^{2+}]O_4$. From the results of temperature dependence of χ_{dc} and χ_{ac} two magnetic transitions was evident: the first one is ferrimagnetic ordering with Néel temperature $T_N \sim 41$ K with a follow-up freezing of the spins at 39 K. Such co-existence of longitudinal ferrimagnetic order below $T_N = 41$ K and transverse spin-glass state below T_{SG} is suggested to result from the presence of non-magnetic Sn^{4+} ions on the octahedral 'B' sites. The ferrimagnetic ordering is suggested to result from different magnetic moments of Co^{2+} on the A- sites (3.87 μ_B) and B-sites (4.91 μ_B) with antiferromagnetic molecular field constants $N_{AA} = 21.56$, $N_{BB} = 10.68$ and $N_{AB} = 33.20$ (S1350). This chapter also deals with the origin of low-temperature exchange bias and temperature dependent vibration excitations in Co_2SnO_4 inverse spinel.

Chapter 4 deals with the complex magnetic ordering of cobalt-orthotitanate (Co_2TiO_4) inverse spinel. Initial part of this chapter contains the literature review, synthesis procedure and crystal structure analysis. The electronic structure obtained from XPS analysis reveals the presence of Ti^{3+} instead of Ti^{4+} in the B-sites ($(Co^{2+})_A[Ti^{3+}Co^{3+}]_BO_4$), which significantly contribute to the overall magnetic moment. The χ_{dc} versus T data shows the existence of ferrimagnetic long-range ordering with $T_N \sim 47.4$ K, and a crossover in sign for χ(ZFC) and χ(FC) at a compensation temperature ~ 32 K (T_{COMP}), where the magnetization of the two sublattice (M_A and M_B) balance each other. The weak anomalies noticed in specific heat versus temperature data at 47.4 K (T_N) and 31.7 K (T_{COMP}) supports the existence of ordering temperatures in the system estimated from the magnetization measurements. From the analysis of temperature dependence of inverse dc paramagnetic susceptibility, the magnetic moments

$\mu(A) = 3.87\ \mu_B$ and $\mu(B) = 5.19\ \mu_B$ on the A and B sites are determined with $\mu(B)$ in turn yielding $\mu(Ti^{3+}) = 1.73\ \mu_B$ and $\mu(Co^{3+}) = 4.89\ \mu_B$. This chapter also discusses the frequency (f) dispersion of the cusp observed in χ_{ac} versus T which was analyzed using two scaling laws: (*i*) the Vogel-Fulcher law, which is given by the expression $\tau = \tau_0 \exp\left(\frac{E_a}{k_B(T - T_0)}\right)$, where τ_0 is the relaxation time constant, T_0 is a measure of the interaction between magnetic clusters, k_B is the Boltzmann constant and E_a is an activation energy parameter; and (*ii*) the Power-law, which describes the critical slowing down in a spin glass phase transition at T_g, and is given by $\tau = \tau_0\left(\frac{T}{T_g} - 1\right)^{-z\nu}$, where T_g is the freezing temperature, τ_0 is related to the relaxation of the individual cluster magnetic moment and $z\nu$ is a critical exponent. Here $\tau = \frac{1}{\omega} = \frac{1}{2\pi f}$. The best fits of experimental data to the Vogel-Fulcher law, gives $T_0 = 45.8$ K and $\tau_0 = 3.2 \times 10^{-16}$ s. However, an attempt to fit the data using Power-law, yielded the fit parameters ($\tau_0 \sim 10^{-33}$ s and $z\nu > 16$), indicates deviation from a proper spin-glass transition. Moreover, the temperature dependence of M_{FC} and M_{ZFC} data in Co_2TiO_4 measured using different cooling fields was interpreted in terms of frozen spin clusters which are responsible for the large magnitudes of the coercivity $H_C \sim 20$ kOe and exchange bias $H_{EB} \sim -20$ kOe observed below 10 K.

Chapter 5 presents a systematic comparison of the magnetic properties of both the compounds Co_2SnO_4 and Co_2TiO_4 with a special emphasis on the compensation point T_{COMP} and low-temperature anomalous magnetic behavior. This chapter also summarizes the similarities and differences in the phonon spectra (for $T \leq T_N$) and other physical properties of these compounds. The role of 'Sn' substitution on the 'Ti' site of Co_2TiO_4 and the corresponding changes in the magnetic structure was discussed in detail. Issues like; (*i*) random anisotropy and random distribution of cations in the A and B-sites, (*ii*) different temperature dependence of magnetic moments $\mu(A)$ and $\mu(B)$, (*iii*) pseudo first-order transition below 15 K involving Arrot-plot analysis, (*iv*) giant bipolar exchange bias (H_{EB}) obtained under ZFC condition, and (*v*) dynamical spin-fluctuation of spin-liquid state exiting in both the compounds are also discussed.

Chapter 6 discusses the phonon spectra, electronic spin resonance, magnetization, dielectric studies of the two-phase composites comprising (1-x) Co_3O_4 + x Co_2TiO_4 ($0 \leq x \leq 1$). Major changes occurring in the bond-angles and bond-lengths due to higher ionic size of 'Ti' ions (1.34 Å) than 'Co^{3+}' ions (1.09 Å) are highlighted. Hipsochromic shift (~ 6.3 cm^{-1}) of A_{1g} phonon mode and a giant bathochromic red-shift (~ 25.3 cm^{-1}) of F_{2g} Raman modes were discussed as the crystal structure of the system transform from complete normal spinel (Co_3O_4) to inverse spinel (Co_2TiO_4). The temperature variation of peak positions of A_{1g} and F_{2g} vibrational modes of both Co_2TiO_4 and Co_3O_4 shifts towards high frequencies with clear anomalies across the ferrimagnetic ordering (~ 48 ± 5 K) and antiferromagnetic $T_N \sim 30 \pm 10$ K, respectively. A detailed compositional dependence of magnetic exchange interactions in these two-phase spinel composites was discussed in detailed. This chapter also deals with

the high frequency (500 Hz ≤ f ≤ 10 MHz) temperature variation (80 K ≤ T ≤ 573 K) of broadband dielectric-spectroscopic studies with a special emphasis on the; ac-conductivity $\sigma_{ac}(T)$, dielectric permittivity $\varepsilon_r(T)$ and loss-tangent (Tan δ). These studies reveal the dominance of Arrhenius like conductivity instead of variable range hopping of charge carriers. Whereas, the frequency variation of ac-conductivity $\sigma_{ac}(f)$ was found to increase progressively with increasing f which follows Power-law relation ($\sigma_{ac} = A\omega^s$). Possible origins of such anomalous changes occurring in the $\sigma_{ac}(T)$ and $\varepsilon_r(T)$ are discussed in this chapter in a very detailed manner.

Chapter 7 is devoted to the tetragonally distorted normal spinel Mn_3O_4 (Hausmannite). This chapter reports the magneto-dielectric ($\Delta\varepsilon_r/\varepsilon_r(H)$) and ac-magnetic ($\chi_{ac}(f,T)$) response of the sequential magnetic transitions occurring below the T_N = 42.5 K. The zero-field temperature dependence of relative dielectric permittivity ($\varepsilon_r(T)$) curves exhibits a large hysteresis of about ~ 5.15 K in consonance with the first-order nature of spiral incommensurate to commensurate planar transition taking place at 33 K (T_2). This chapter also deals with the Arrott plot (H/M versus M^2) criterion to distinguish the nature of all the sequential transitions occur below T_N. All the complex magnetic transitions occurring below T_N including the field-induced structural transition at 33 K and lock-in transition at 38 K was successfully probed by means of χ_{ac} (f_{ac}, H) and (ε_r versus T). The meta-magnetic like features in the M-H isotherms near to T_2 are discussed which are associated with first-order nature of the transition at T_2. This chapter also clearly demonstrates the evidence of magneto-electric coupling in Mn_3O_4 system in which the electric polarization ($P \sim 3 \times 10^{-6}$ C/m^2) takes maximum value below the spiral-incommensurate to commensurate transition at 33 K.

Chapter 8 presents a brief summary of the important findings of our experiments on all the three investigated systems. In this chapter we also identify some open issues which are potentially interesting for the future studies.

List of Publications:

(a) <u>In Peer Reviewed Journals:</u>

(1) S. Thota, K. Singh, **S. Nayak**, Ch. Simon, J. Kumar and W. Prellier, *"The ac-magnetic susceptibility and dielectric response of complex spin ordering processes in Mn_3O_4"*. J. Appl. Phys. **116**, 103906 (2014).

(2) S. Thota, V. Narang, **S. Nayak**, S. Sambasivam, B. C. Choi, T. Sarkar, M. S. Andersson, R. Mathieu and M. S. Seehra, "*On the nature of magnetic state in the spinel Co_2SnO_4*". J. Phys.: Condens Matter **27**, 166001 (2015).

(3) **S. Nayak**, S. Thota, D. C. Joshi, M. Krautz, A. Waske, A. Behler, J. Eckert, T. Sarkar, M. S. Andersson, R. Mathieu, V. Narang, M. S. Seehra, *"Magnetic compensation, field-dependent magnetization reversal, and complex magnetic ordering in Co_2TiO_4"*. Phys. Rev. B **92,** 214434 (2015).

(4) **S. Nayak**, D. C. Joshi, M. Krautz, A. Waske, J. Eckert, S. Thota, *"Reentrant spin-glass behavior and bipolar exchange-bias effect in 'Sn' substituted cobalt-orthotitanate"*. J. Appl. Phys. **119**, 043901 (2016).

(5) **S. Nayak**, K. Dasari, D. C. Joshi, P. Pramanik, R. Palai, A. Waske, R. N. Chauhan, N. Tiwari, T. Sarkar, S. Thota *"Low-temperature anomalous magnetic behavior of Co_2TiO_4 and Co_2SnO_4"*. J. Appl. Phys. **120**, 163905 (2016).

(6) **S. Nayak**, K. Dasari, D. C. Joshi, P. Pramanik, R. Palai, V. Sathe, R. N. Chauhan, N. Tiwari, S. Thota *"Spectroscopic studies of Co_2TiO_4 and Co_3O_4 two-phase composites"*. Phys. Stat. Sol. (b) **253**, 2270 (2016).

(7) **S. Nayak**, D. C. Joshi, P. Pramanik, A. Banerjee and S. Thota "*Tunable Exchange-Bias and Magnetic Compensation Temperature of Two-Phase Spinel Composites (1-x) (Co_3O_4) + x (Co_2TiO_4)*". [to be communicated].

(8) **S. Nayak**, J. Dhillon, S. K. Deshpande, and S. Thota *"Dielectric studies of Co_3O_4-Co_2TiO_4 two phase composites"* [to be communicated].

(9) **S. Nayak,** K. Dasari and S. Thota "Spectroscopic studies and dielectric properties of Co_2SnO_4" [to be communicated]

(b) <u>Conference Presentations:</u>

(1) **S. Nayak**, D. C. Joshi and S. Thota *"Micro-Raman and Electron Spin Resonance studies of $Co_{3-x}Ti_xO_4$",* 2nd International Conference on Nanotechnology ICNT-2015 & Indo-USA joint symposium, Haldia (W.B), India.

(2) **S. Nayak**, D. C. Joshi, M. Krautz, A. Waske, J. Eckert, S. Thota, *"Reentrant spin-glass behavior and bipolar exchange-bias effect in 'Sn' substituted cobalt-orthotitanate"* International Conference on Magnetic Materials and Applications (ICMAGMA – 2015), VIT University, Vellore, Tamil Nadu, India.

(3) **S. Nayak**, D. C. Joshi, P. Pramanik, M. Krautz, A. Waske and S. Thota, *"Structural and Magnetic properties of Cu doped Cobalt-Orthotitanate"* 2nd International Conference on Materials Science and Technology, (2016) St. Thomas College Pala Arunapuram, Kottayam, Kerala, India.

(4) S. Thota, K. Dasari, **S. Nayak**, D. C. Joshi, P. Pramanik, A. Waske, T. Sarkar, M. Andersson and R. Mathieu, *"Low-temperature anomalous magnetic behavior of Co_2TiO_4"* The IEEE International Conference on Microwave Magnetics 2016, University of Alabama in Tuscaloosa, USA.

(5) **S. Nayak**, K. Dasari, D. C. Joshi, V. Sathe, R. Palai, and S. Thota, "*Temperature dependence of micro-Raman spectroscopy of Co_2TiO_4, Co_3O_4 and their composites*" 2016 MRS Fall Meeting & Exhibit, Boston, Massachusetts.

(6) **S. Nayak**, D. C. Joshi, P. Pramanik, A. Banerjee and S. Thota "*Tunable Exchange-Bias and Magnetic Compensation Temperature of Two-Phase Spinel Composites (1-x) (Co_3O_4) + x (Co_2TiO_4)*" International Conference on Magnetic Materials and Applications (ICMAGMA – 2017), 1-3, February 2017 at Hyderabad, India.

(7) **S. Nayak**, J. Dhillon, S. K. Deshpande, D. C. Joshi, P. Pramanik, R. George, and S. Thota "*Dynamic ac-conductivity studies of Cobalt-Orthotitanate*", National conference on Advances on Materials Science, (2017) Gauhati University, Assam, India.

Table of Contents

		Page No.
List of Figures		*i - ix*
List of Tables		*x*
List of Symbols		*xi*
Chapter 1:	**Introduction to Spinels and their Complex Magnetic Structure**	**1 - 14**
	1.1 Background	1
	1.2 Applications of Spinels	3
	1.3 Magnetic Exchange Interactions using Molecular field Theory	4
	1.4 Dilution Effects and Reentrant Spin-glass State	8
	1.5 Negative Magnetization in Spinels	10
	1.6 Description of the Problem and the Approach	13
Chapter 2:	**Experimental Techniques**	**15 - 25**
	2.1 Synthesis of the Oxide Spinels	15
	2.1.1 Solid State Reaction	15
	2.1.2 Sol-gel Method	15
	2.2 Characterization Techniques	18
	2.2.1 Structural Characterization	18
	2.2.2 Surface Morphology and Microstructure	18
	2.2.3 X-ray Photoelectron Spectroscopy	18
	2.2.4 DC & AC-magnetization Measurements	20
	2.2.5 Physical Property Measurement System (PPMS)	22
	2.2.6 AC-resistivity and Dielectric Permittivity Measurements	23
	2.2.7 Vibrational Excitations and Raman Spectroscopy	23
	2.2.8 Fourier Transform Infrared Spectroscopy	25
Chapter 3:	**Nature of Magnetic Ordering in Co_2SnO_4**	**26 - 48**
	3.1 Introduction	26
	3.2 Experimental Details	26
	3.3 Results and Discussion	28
	3.3.1 Structural Characterization	28
	3.3.2 Morphology and Microstructure Analysis	30
	3.3.3 X-ray Photoelectron Spectroscopy (XPS)	30
	3.3.4 Magnetic Properties	31
	3.3.4(a)Temperature Dependence DC-magnetization and AC-susceptibility	31
	3.3.4(b)Temperature Dependence of the Hysteresis Loop Measurements	40
	3.3.4 (c) Temperature Dependence of the Paramagnetic Susceptibility	42

3.3.5 Temperature Dependence of Specific Heat 45
3.3.6 Summary 48

Chapter 4: Negative Magnetization and Compensation Effect in Co_2TiO_4 49 - 72

4.1 Literature Review 49
4.2 Experimental Details 50
4.3 Results and Discussion 50
4.3.1 Structural Characterization 50
4.3.2 X-ray Photoelectron Spectroscopy 52
4.3.3 Temperature Dependence of the DC-magnetic Susceptibility 54
4.3.4 Temperature Dependence of the AC-magnetic Susceptibilities 58
4.3.5 Temperature Dependence of the Hysteresis Loop Parameters 60
4.3.6 Temperature Dependence of Specific-heat 66
4.3.7 Summary 71

Chapter 5: Tuning the Compensation Point: Role of Sn Substitution in Co_2TiO_4 73 - 92

5.1 Introduction 73
5.2 Experimental Details 74
5.3 Characterizations 74
5.3.1 Crystal Structure Analysis 74
5.3.2 Coexistence of Ferrimagnetism and Spin-Glass Ordering 76
5.3.3 Observation of Giant-Coercivity and Exchange Bias 83
5.3.4 Temperature Dependence of the Paramagnetic Susceptibility 88
5.3.5 Compositional Dependence of Exchange-Interaction 89
5.3.6 Summary 91

Chapter 6: Crystal Structure, Vibrational Excitations, Dielectric and Magnetic Properties of Co_3O_4 and Co_2TiO_4 Two-Phase Composites 93 - 126

6.1 Background 93
6.2. Experimental Details 94
6.3 Characterizations 95
6.3.1 Structural Analysis 95
6.3.2 Morphology and Microstructure Analysis 98
6.3.3 Vibrational Excitations and Micro-Raman Spectroscopy 99
6.3.4 Fourier Transform Infrared (FTIR) Spectroscopy 103
6.3.5 Elemental Analysis using X-ray Photoelectron Spectroscopy 105
6.3.6 Tailoring the Compensation Point (T_{COMP}) and Néel Temperature (T_N) 111
6.3.7 Dielectric Permittivity and AC-Conductivity 116

6.3.8 Summary 124

Chapter 7: Lock-in Transition at 38 K in Tetragonally Distorted Frustrated Spinel Mn_3O_4 **127 - 144**

7.1 Literature Survey 127

7.2 Experimental Details and Growth of Hausmannite 128

7.3 Experimental Results and Analysis 129

7.3.1 Structural and Morphological Characterization 129

7.3.2 Magnetic Properties and Evidence for the Lock- in transition 131

7.3.3 Dielectric and Magneto-dielectric Properties 138

7.3.4 Isothermal Magnetization 141

7.3.5 Summary 144

Chapter 8: Conclusions and Scope for Future Research **145 - 147**

8.1 Conclusions 145

8.2 Future Scope 147

Bibliography **148 - 159**

List of Figures

Figure No.	Figure Description	Page No.
	Chapter 1	
1.1	Schematic representation of Type-I octant containing cations A in the tetrahedral co-ordinations [5].	2
1.2	Type-II octant containing 'B' cations in octahedral co-ordinations [5].	2
1.3	The cubic spinel structure of AB_2X_4 with Type I octant containing 'A' cations in tetrahedral and Type II octant having 'B' cations in octahedral voids of oxygen ions [5].	2
1.4	Various application of spinels.	3
1.5	Schematic diagram of triangular and spiral or canted spin-spiral arrangements.	4
1.6	Ion pair configuration of super-exchange interaction. Large spheres represents oxygen ions, cations in 'A' sites represent by small blue color sphere and small green color sphere are the cations in B sites [18].	6
1.7	Schematic representation of frozen spin glass with $J_1 > 0$ (ferromagnetic) and $J_2 < 0$ (antiferromagnetic). The zig-zag links indicate a broken bond [67].	9
1.8	Schematic diagram of frustrated triangular (hexagonal) lattice with all antiferromagnetic interactions ($J_1 < 0$) [67].	10
1.9	Temperature variation of magnetization M(T) for the N-type ferrimagnetism as per the Néel's theory. The net magnetization is represented as the dotted red color line [62].	12
	Chapter 2	
2.1	Schematic diagram of standard solid state reaction method employed in the present work.	16
2.2	Flow diagram of sol-gel method used to synthesize single phase ceramics.	17
2.3	Schematic diagram of Photoemission process.	19
2.4	(a) Schematic diagram of the superconducting quantum interference device (SQUID) flux to voltage converter and (b) pick-up coil.	21
2.5	Energy level diagram of the Rayleigh and Raman Scattering.	24
2.6	Schematic diagram of the Fourier transform infrared spectrometer.	24
	Chapter 3	
3.1	The X-ray diffraction pattern (dotted symbols) together with the Rietveld refined data (red line) of Co_2SnO_4 bulk samples sintered at 1200ºC (S1200) in air. The asterisk mark shows the position of the SnO_2 secondary peak. Vertical lines represent the Bragg positions and the bottom line represents the difference between the intensities of the observed (Yobs) and calculated (Ycalc) pattern.	27
3.2	The X-ray diffraction pattern (scattered circular symbols) together with the Rietveld refined data (red line) of Co_2SnO_4 bulk samples sintered at 1350°C (S1350) in air. Vertical lines represent the Bragg positions and the bottom line represents the difference between the intensities of the observed (Yobs) and calculated (Ycalc) pattern.	28

3.3	Field Emission Scanning Electron (FESEM) Micrograph of Co_2SnO_4 bulk samples sintered at (a) 1200ºC (S1200) and 1350°C (S1350) in air.	29
3.4	The X-ray-photoemission spectra of (a) Sn-3d, (b) Co-2p and (c) O-1s peaks in the S1200 sample.	30
3.5	Temperature dependence of dc-magnetization M(T) measured under ZFC and FC (H@100 Oe) conditions for both Co_2SnO_4 bulk samples (a) sintered at 1200ºC (S1200) and (b) 1350°C (S1350).	32
3.6	The differential susceptibility plots ($\partial(\chi_{dc}T)/\partial T$ versus T) of S1200 sample at various external fields H = 200 Oe, 1 kOe, and 2 kOe. The insets depict $\partial(\chi_{dc}T)/\partial T$ plotted with a logarithmic scale to show the variation in the peak clearly	33
3.7	Plots of $\partial(\chi_{dc}T)/\partial T$ versus T plots of S1350 sample at various external fields H = 100, 500, 1000 and 5000 Oe. The insets show the $\partial(\chi_{dc}T)/\partial T$ in logarithmic scale to show the variation in the peak clearly.	33
3.8	Temperature dependence of the (a) real-component $\chi'(T)$ and (b) imaginary-components $\chi''(T)$ of ac-magnetic susceptibility for S1200 recorded using different measuring frequencies under zero-dc bias field with the amplitude of dynamic magnetic-field h_{ac} = 4 Oe.	34
3.9	Temperature dependence of the (a) real-component $\chi'(T)$ and (b) imaginary-components $\chi''(T)$ of ac-magnetic susceptibility for S1350 recorded using different measuring frequencies under zero-dc bias field with the amplitude of dynamic magnetic-field h_{ac} = 4 Oe.	35
3.10	The best fit of the relaxation times to the Vogel–Fulcher law for (a) S1200 and (b) S1350 sample.	36
3.11	The best fit of the relaxation times to the Power–law for (a) S1200 and (b) S1350 sample.	36
3.12	Temperature dependence of ac-magnetic susceptibilities: *(i)* real part (χ') and (*ii*) imaginary part (χ'') component of S1200 recorded at various dc-bias fields H_{dc} = 20, 50, 100 and 150 Oe with constant frequency f = 2 Hz and amplitude h_{ac} = 1 Oe. The insets (a)-(c) depict the zoom view of the same curves at various temperature regimes to show the transition better.	37
3.13	Temperature variation of $\partial(\chi'_{ac}T)/\partial T$ plots at different bias fields 20 Oe $\leq H_{dc} \leq$ 150 Oe for S1200 sample.	38
3.14	Variation of ferrimagnetic Néel temperature T_N and spin-glass transition temperature T_{SG} with respect to $H^{2/3}$ for S1200 sample. The solid lines show the linear fit to the data (often called the de Almeida-Thouless AT line) whereas the dotted line for T_{SG} is for visual aid.	38
3.15	Temperature variation of $\partial(\chi'_{ac}T)/\partial T$ plots at different bias fields 0 Oe $\leq H_{dc} \leq$ 200 Oe for S1350 sample.	39
3.16	Variation of ferrimagnetic Néel temperature T_N and spin-glass transition temperature T_{SG} with respect to $H^{2/3}$ for S1350 sample. The solid lines show the linear fit to the data (often called the de Almeida-Thouless AT line) whereas the dotted line for T_{SG} is for visual guide.	39
3.17	Magnetization (M) versus magnetic field (H) hysteresis loops recorded at various temperatures in the range 5 K $\leq$ T $\leq$ 45 K under zero-field conditions for S1200 samples. Inset shows the zoomed view at selected temperature.	40

3.18 Magnetization (M) versus magnetic field (H) hysteresis loops recorded at various temperatures in the range 5 K ≤ T ≤ 41 K under zero-field conditions for S1350 samples. Inset shows the zoomed view at selected temperature. 41

3.19 Temperature dependent coercivity (H_C) for both S1200 and S1350 sample. 41

3.20 Temperature dependent remanence (M_R) for both S1200 and S1350 sample. 42

3.21 Temperature dependence of exchange-bias (H_{EB}) for both the S1200 and S1350 samples. 43

3.22 Temperature dependence of susceptibility (χ versus T) (R.H.S) and inverse susceptibility (L.H.S) (χ^{-1} versus T) for the samples (a) S1200 (b) S1350 are shown. The solid lines are fits to the Néel's expression for ferrimagnets as discussed in this chapter. 44

3.23 The temperature dependence of specific heat $C_P(T)$ for the samples; (a) S1200, and (b) S1350 measured under both zero magnetic field and in the presence of magnetic field of H = 1 kOe recorded under warming condition. The corresponding derivative plots $\partial C_P(T)/\partial T$ versus T is shown on the right-hand-side scale. 46

3.24 The temperature variation of the C_P/T and its first derivative $\partial(C_P T^{-1})/\partial T$ for the two samples (a) S1200 and (b) S1350 in H = 0 Oe and H = 1 kOe. There is no measurable field dependence of the C_P data. 47

Chapter 4

4.1 X-ray diffraction patterns of (a) Co_2TiO_4 and (b) Co_2SnO_4. The scattered symbols represent the experimental data whereas the red lines depict Rietveld refined data. The vertical lines represent the Bragg positions and the bottom blue line shows the difference between the experimental and calculated intensity. 51

4.2 The left hand side panel shows the X-ray photoelectron spectra (XPS) of Co-2*p* peaks of (a) Co_3O_4 (b) Co_2TiO_4, and (c) Co_2SnO_4. Whereas, right hand side panel shows the XPS spectra of (d) Ti-2p (e) Sn-3d, and (f) O-1s peaks of Co_2TiO_4, Co_2SnO_4, Co_3O_4 bulk systems. 53

4.3 Temperature variation of the inverse paramagnetic susceptibility $\chi^{-1}(T)$ of Co_2TiO_4 and Co_2SnO_4 systems. The solid lines are best-fits to the Néel's expression for ferrimagnets discussed in the section 4.3.3. 54

4.4 Temperature dependence of dc-magnetic susceptibility $\chi(T)$ (= M/H_{dc} (T)) for Co_2TiO_4 measured under both zero-field-cooled (ZFC) and field-cooled (FC) conditions recorded at various magnetic fields in the range 50 Oe ≤ H_{dc} ≤ 10 kOe. 55

4.5 High-field (5 kOe ≤ H_{dc} ≤ 40 kOe) magnetization (M) versus temperature (T) data for Co_2TiO_4 measured under both the ZFC and FC conditions. 56

4.6 Temperature dependence of dc-magnetic susceptibility $\chi(T)$ (= M/H_{dc} (T)) for Co_2SnO_4 measured under both zero-field-cooled (ZFC) and field-cooled (FC) conditions recorded at various magnetic fields. 57

4.7 Temperature variation of the ac-magnetic susceptibility (a) $\chi'(T)$, and (b) $\chi''(T)$ for Co_2TiO_4 measured at 2 Hz in h_{ac}= 4 Oe with superposed dc-bias fields H_{dc} = 0, 10, 20 and 30 Oe. 58

4.8 Temperature dependence of ac-magnetic susceptibilities (a) χ′(T) and (b) χ″(T) of Co_2TiO_4 measured at various frequencies between 0.17 Hz and 1202 Hz under 59

warming conditions using h_{ac} = 4 Oe and H_{dc} = 0 Oe. The inset shows the best fits of the relaxation times to the Vogel-Fulcher law in Co_2TiO_4.

4.9 The de Almeida-Thouless (AT) line T_P versus $H^{2/3}$ of Co_2TiO_4. The dotted lines show the linear fit to the experimental data. Inset shows the field dependence of T_{SG} raised to 2/3 power obtained from dc-susceptibility measurement. 60

4.10 Plots of hysteresis loops (M versus H) in Co_2TiO_4 are shown at selected temperatures of (a) 10 K, (b) 20 K, (c) 30 K and (d) 50 K recorded under ZFC condition. The insets show the zoomed view of M-H loops near origin showing the asymmetry in the loops. 61

4.11 Magnetization versus field (M-H) hysteresis loops measured at low-temperatures T = 5 K, 6 K, 7 K, 8 K and 9 K under zero-field-cooled (ZFC) condition. The insets show asymmetry in the M-H loops measured at T = 5 K under FC (20 kOe) condition. 62

4.12 The temperature variation of (a) coercive field H_C(T) and Remanence Magnetization M_R and (b) exchange bias H_{EB}(T) and high field (H ~ 90 kOe) magnetization M_{MAX} measured under both ZFC and FC(20 kOe) conditions in Co_2TiO_4. The lines connecting the data points are visual guides. 63

4.13 The magnetization versus field (M-H) isotherms of Co_2TiO_4 recorded at various temperatures 5 K ≤ T ≤ 55 K. 63

4.14 The magnetization versus field (M-H) isotherms of Co_2SnO_4 recorded at various temperatures 5 K ≤ T ≤ 40 K. 64

4.15 Arrott plots (H/M versus M^2) of Co_2TiO_4 computed from magnetization (M) field (H) isotherms recorded at different temperatures between 5 K and 55 K. 64

4.16 Arrott plots (H/M versus M^2) of Co_2SnO_4 computed from magnetization (M) field (H) isotherms recorded at different temperatures between 5 K and 40 K. 65

4.17 Temperature dependence of isothermal entropy change (ΔS(T)) computed from M-H isotherms using Maxwell equations for a field change ΔH = 50 kOe for (a) Co_2TiO_4 (b) Co_2SnO_4. 66

4.18 The temperature variation of specific-heat C_P(T) for Co_2TiO_4 sample recorded at various magnetic fields (H_{dc} = 0, 10, and 50 kOe). The insets show the zoomed view across the ferrimagnetic Nèel temperature (T_N) and compensation temperature (T_{COMP}). 67

4.19 Temperature variation of C_PT^{-1} measured in the presence of H = 0 Oe and 50 kOe for Co_2TiO_4 (LHS) and H=0 Oe and 1 kOe for Co_2SnO_4 (RHS). 68

4.20 Temperature variation of $\partial(C_PT^{-1})/\partial T$ versus T measured in the presence of H = 0 Oe and 50 kOe for Co_2TiO_4 (LHS) and H = 0 Oe and 1 kOe for Co_2SnO_4 (RHS). 68

4.21 Temperature dependence of experimentally obtained zero-field heat capacity data of (a) Co_2TiO_4 and (b) Co_2SnO_4 shown in green color open circles together with the red color solid line represents the specific heat calculated from numerical fits as described in the text and blue hollow square symbols represents the magnetic contribution to the specific heat. 69

4.22 The magnetic entropy (S_M) versus temperature (T) (L.H.S) and the differential entropy $\partial S_M/\partial T$ versus T (R.H.S) plots of Co_2TiO_4 for different magnetic fields. 70

4.23 Temperature variation of heat-capacity C_P(T) measured under both zero field and with field for (a) Co_2TiO_4, and (b) Co_2SnO_4. The solid lines correspond to the linear fit to AT^2. 71

Chapter 5

5.1 The X-ray diffraction pattern together with Reitveld refined data of $Co_2Ti_{1-x}Sn_xO_4$ (a) x = 1.0, (b) x = 0.4 (c) x = 0.2 (d) x = 0.0, samples sintered at 1350ºC for 18 h in air. 75

5.2 Temperature dependence of dc-magnetic susceptibility $\chi_{dc}(T)$ = M/H_{dc} (T) for (a) x = 0.0, (b) x = 0.2 (c) x = 0.4 (d) x = 1.0 measured under both zero-field-cooled (ZFC)and field-cooled (FC)conditions recorded at magnetic field H_{dc} = 50 Oe. 76

5.3 The plots of $\partial(\chi_{dc}T)/\partial T$ versus T of $Co_2Ti_{0.6}Sn_{0.4}O_4$ sample at various external fields H_{dc} = 50, 100, 1000, 2000, 10000, 50000 Oe. The inset (*i*) and (*ii*) of shows the peak variation clearly in logarithmic scale. 77

5.4 The variation of the transition temperatures T_{P1} (a) and T_{P2} (b) of $Co_2Ti_{0.6}Sn_{0.4}O_4$ sample as a function of the applied magnetic field H. The inset shows variation of the transition temperatures T_{P1} and T_{P2} as a function of $H_{dc}^{2/3}$ for $Co_2Ti_{0.6}Sn_{0.4}O_4$. 78

5.5 Temperature dependence of the ac-magnetic susceptibility of $Co_2Ti_{0.6}Sn_{0.4}O_4$ sample: (a) the real component $\chi'(T)$, (b) the imaginary component $\chi''(T)$ recorded at various frequencies (0.17 Hz $\leq f \leq$ 510 Hz) under warming condition using h_{ac}= 3 Oe and zero static magnetic field. The inset (*i*) of figure (a) and the inset (*i*) of figure (b) show the ln$f$ versus $[1/(T_f - T_o)]$ using the peak positions in $\chi'(T)$ and $\chi''(T)$ respectively. The solid line shows Vogel-Fulcher law fit of experimental data. The inset (*ii*) of figure (a) and inset (*ii*) of figure (b) shows the ln f versus ln($[T_P-T_F]/T_F$) using the peak positions in $\chi'(T)$ and $\chi''(T)$ respectively, the solid line shows are the linear fits to the experimental data. 79

5.6 Temperature dependence of ac-magnetic susceptibility (a) real part $\chi'(T)$, and (b) imaginary $\chi''(T)$ components of bulk $Co_2Ti_{0.6}Sn_{0.4}O_4$ recorded at various bias fields H_{dc} (10 Oe $\leq$ H_{dc} $\leq$ 200 Oe) with constant frequency 2 Hz and amplitude of 3 Oe. The insets of figure b depict the temperature variation of $\partial(\chi'_{ac}T)/\partial T$ plots at different bias fields H_{dc} = 10 and 200 Oe. 81

5.7 $H_{dc}^{2/3}$ dependence of ferrimagnetic Néel temperature T_N and freezing temperature T_F . The solid lines show the linear fit to the data (often called the de Almeida-Thouless AT line). The inset shows compositional variation of T_N and T_F. 82

5.8 The magnetization (M) versus field (H) hysteresis loops of $Co_2Ti_{0.6}Sn_{0.4}O_4$ samples recorded at select temperatures (a) 5 K, (b) 12 K, (c) 20 K (d) 30 K (e) 40 K and (f) 50 K under zero-field-cooled ZFC condition. The insets show the zoomed view of M-H loops near origin showing the asymmetry in the loops. 84

5.9 The magnetization (M) versus field (H) hysteresis loops of $Co_2Ti_{0.6}Sn_{0.4}O_4$ samples recorded at select temperatures (a) 5 K, (b) 12 K, (c) 20 K (d) 27 K (e) 40 K and (f) 50 K under @ 20 kOe field-cooled (FC) condition. The insets show the zoomed view of M-H loops near origin showing the asymmetry in the loops. 85

5.10 The temperature variation of (a) coercive field H_C(T) and (b) exchange bias H_{EB}(T) of $Co_2Ti_{0.6}Sn_{0.4}O_4$ recorded from the M-H curves measured under both ZFC and FC conditions. The inset of Figure (b) clearly shows the anomalous behavior of H_{EB} across the T_{COMP}. 86

5.11 Left-hand-side scale shows the remanence magnetization versus temperature (M_R versus T) of $Co_2Ti_{0.6}Sn_{0.4}O_4$ system measured under (a) zero-field-cooled (ZFC), and (b) field-cooled (FC) conditions. The right-hand-side scale shows the variation of the high field (H~ 68.3 kOe) magnetization versus temperature measured under both (a) 87

ZFC and (b) FC conditions. All these cures clearly show the sudden drop of magnetization value across the T_{COMP} (~ 27 K).

5.12 Temperature variation of the inverse-magnetic susceptibility $\chi^{-1}(T)$ *of* $Co_2Ti_{1-x}Sn_xO_4$ ($0 \leq x \leq 1$). The solid lines are best-fits to the Néel's expression for ferrimagnets as discussed in the text. 88

5.13 The compositional variation of the (a) molecular field constants, and (b) exchange constants of $Co_2Ti_{1-x}Sn_xO_4$. 90

Chapter 6

6.1 The X-ray diffraction pattern together with the Rietveld refined data of composite system (1-x) Co_3O_4 + x Co_2TiO_4 for (a) x = 0, (b) x = 0.23, (c) x = 0.463, (d) x = 0.706, (e) x = 0.882, and (f) x = 1. 96

6.2 (a) Intensity of the (311) reflection of both Co_3O_4 and Co_2TiO_4 phases of the composites ((1-x) Co_3O_4+ x Co_2TiO_4 [$0 \leq x \leq 1$ (100 wt%)]) (b) The composition variation of lattice parameter 'a' and unit-cell volume 'V' of Co_3O_4 /Co_2TiO_4 two phase composite. Note: The contribution of both the phases (Co_3O_4 and Co_2TiO_4) is plotted separately. 97

6.3 The composition variation of (a) bond-angles [(B-O-B) and (A-O-B)] (b) and bond-lengths [(A-O) and (B-O)]. 98

6.4 Scanning electron micrographs of two-phase composites recorded under secondary-electron (SE) mode for different compositions (a) x = 0, (b) x = 0.463, (c) x = 0.706, and (d) x = 1. 99

6.5 Room temperature Raman spectra (intensity versus wavenumber) of the two-phase composites (1-x) Co_3O_4 + x Co_2TiO_4 ($0 \leq x \leq 1$). The peaks represent various vibrational modes of the spectra. 100

6.6 Raman spectra of Co_3O_4 recorded at various temperatures in the range 300 K – 25 K. 101

6.7 Raman spectra of the inverted spinel Co_2TiO_4 at various temperatures between 300 K and 25 K. 102

6.8 Temperature variation of the location of Raman active phonon modes A_{1g} and F_{2g} of (a) normal spinel Co_3O_4, and (b) inverse spinel Co_2TiO_4. 103

6.9 Transmittance (T(%)) versus wavenumber (cm^{-1}) of Fourier-transform infrared spectroscopy (FTIR) spectra of (1 - x) Co_3O_4 + x Co_2TiO_4 two-phase composites recorded at room temperature for different compositions (a) x = 1, (b) x = 0.706, (c) x = 0.23, (d) x = 0. 104

6.10 The enlarge view of the Fourier-transform infrared spectroscopy (FTIR) spectra of Co_2TiO_4 sample between 450 to 750 cm^{-1}. 105

6.11 The core-level X-ray photoelectron spectra of (a) Co-2p peak of un-doped Co_3O_4 sample, (b) and (c) shows the enlarged views of Co-2$p_{3/2}$ and Co-2$p_{1/2}$ peaks, respectively. 106

6.12 The core-level X-ray photoelectron spectra of Co-2p peak of Co_2TiO_4 sample. 107

6.13 The core-level X-ray photoelectron spectra of (a) Ti-2p peak of Co_2TiO_4 sample, (b) and (c) are O-1s peak of Co_3O_4 and Co_2TiO_4 respectively. 108

6.14 Temperature dependence of dc-magnetic susceptibility $\chi_{dc}(T)$ = M/H_{dc} (T) for (a) x = 0.23, (b) x = 0.706 (c) x = 0.882 (d) x = 1.0 measured under both zero-field-cooled (ZFC) and field-cooled (FC) conditions recorded at magnetic field H_{dc} = 50 Oe. 110

6.15 The compositional variation of compensation temperature (T_{COMP}) and ferrimagnetic Néel temperature (T_N). 111

6.16 The plots of $\partial(\chi_{dc}T)/\partial T$ versus T of (1 - x) Co_3O_4 + x Co_2TiO_4 (x = 0.23, 0.706, 0.882 and 1.0) sample at external fields H_{dc} = 50 Oe. The inset shows the zoomed view of peak variation of various composites. 111

6.17 Temperature dependence of the ac-magnetic susceptibility of the composite system (1 - x) Co_3O_4 + x Co_2TiO_4 for x = 0.23 with (a) the real component $\chi'(T)$, and (b) the imaginary component $\chi''(T)$ recorded at various frequencies (1.3 Hz $\leq f \leq$ 1339.3 Hz) under warming condition using h_{ac}= 3 Oe and zero static magnetic field. The scattered symbols shown in the inset (*i*) of figure (a), and inset (*i*) of figure (b) represents the frequency dependence of peak position whereas the solid line shows the Vogel-Fulcher law fit of experimental data. The inset (*ii*) of figure (a) and inset (*ii*) of figure (b) shows the frequency dependence of peak positions in $\chi'(T)$ and $\chi''(T)$, respectively. The solid line shows the theoretical fit to the experimental data. 112

6.18 Temperature dependence of the ac-magnetic susceptibility of the composite system (1 - x) Co_3O_4 + x Co_2TiO_4 for x = 0.706 with (a) the real component $\chi'(T)$, and (b) the imaginary component $\chi''(T)$ recorded at various frequencies (1.3 Hz $\leq f \leq$ 1339.3 Hz) under warming condition using h_{ac}= 3 Oe and zero static magnetic field. The scattered symbols shown in the inset (*i*) of figure (a), and inset (*i*) of figure (b) represents the frequency dependence of peak position whereas the solid line shows the Vogel-Fulcher law fit of experimental data. The inset (*ii*) of figure (a) and inset (*ii*) of figure (b) shows the frequency dependence of peak positions in $\chi'(T)$ and $\chi''(T)$, respectively. The solid line shows the theoretical fit to the experimental data. 113

6.19 Temperature dependence of the ac-magnetic susceptibility of the composite system (1 - x) Co_3O_4 + x Co_2TiO_4 for x = 0.882 with (a) the real component $\chi'(T)$, and (b) the imaginary component $\chi''(T)$ recorded at various frequencies (1.3 Hz $\leq f \leq$ 1339.3 Hz) under warming condition using h_{ac}= 3 Oe and zero static magnetic field. The scattered symbols shown in the inset (*i*) of figure (a), and inset (*i*) of figure (b) represents the frequency dependence of peak position whereas the solid line shows the Vogel-Fulcher law fit of experimental data. The inset (*ii*) of figure (a) and inset (*ii*) of figure (b) shows the frequency dependence of peak positions in $\chi'(T)$ and $\chi''(T)$, respectively. The solid line shows the theoretical fit to the experimental data. 114

6.20 Magnetization versus field (M vs. H) hysteresis loops recorded under field-cooled (FC) conditions at constant temperature T = 10 K for (1 - x) Co_3O_4 + x Co_2TiO_4 (a) x = 0.23 (b) x = 0.706 (c) x = 0.882. 114

6.21 (a) The composition variation of the coercive field $H_C(x)$ [LHS]and exchange bias $H_{EB}(x)$ [RHS] estimated from the M-H curves measured at 10 K under 20 kOe field cooled (FC) condition (b) The composition variation of the remanence magnetization $M_R(x)$ [LHS] and maximum magnetic moment @ 50 kOe ($M_{MAX}(x)$ [RHS] obtained from the M-H curves measured at 10 K under 20 kOe field cooled (FC) condition. 115

6.22 Composition variation of high field susceptibility $\chi_{hf}(x)$ calculated from the 50 kOe M-H loops measured at 10 K under field-cooled (FC) condition. 115

6.23 The frequency dependence of real component of complex permittivity (ε') for different compositions (*i*) x = 0 (*ii*) x = 0.23 (*iii*) x = 0.46 of two-phase composites ((1-x) Co_3O_4 + x Co_2TiO_4) measured between the temperatures 123 K and 293 K; and (*iv*) x = 0 (*v*) x = 0.23 (*vi*) x = 0.46 of two-phase composites ((1-x) Co_3O_4 + x Co_2TiO_4) 117

measured between the temperatures 303 K and 573 K. Insets shows the corresponding frequency dependence of imaginary component of complex permittivity (ε″).

6.24 Cole-Cole plots (ε″ vs. ε′) recorded at different temperatures between 123 K and 273 K for different compositions (*i*) $x = 0$, (*ii*) $x = 0.23$, (*iii*) $x = 0.46$, (*iv*) $x = 0.706$, (*v*) $x = 0.882$, and (*vi*) $x = 1.0$. Insets show the zoomed view of the selected region. 118

6.25 Cole-Cole plots (ε″ vs. ε′) recorded at different temperatures between 303 K and 573 K for different compositions (*i*) $x = 0$, (*ii*) $x = 0.23$, (*iii*) $x = 0.46$, (*iv*) $x = 0.706$, (*v*) $x = 0.882$, and (*vi*) $x = 1.0$). Insets show the zoomed view of the selected region. 119

6.26 Frequency dependence of ac-electrical conductivity of (1-x) Co_3O_4 + x Co_2TiO_4 for different compositions (*i*) $x = 0$, (*ii*) $x = 0.23$, (*iii*) $x = 0.46$, and (*iv*) $x = 0.706$ measured at various temperatures between 123 K and 293 K. 120

6.27 Frequency dependence of ac-conductivity of (1-x) Co_3O_4 + x Co_2TiO_4 (*i*) $x = 0.23$, (*ii*) $x = 0.46$ (*iii*) $x = 0.706$, and (*iv*) $x = 1.0$ measured at various temperatures between 303 K and 573 K. 121

6.28 Frequency exponent (s) plotted as a function of composition (x) measured at selected temperatures. 122

6.29 Logarithmic variation of σ_{ac} versus 1000/T for the compositions (*i*) $x = 0.0$, (*ii*) $x = 0.23$, (*iii*) $x = 0.46$, and (*iv*) $x = 0.882$ calculated at different frequencies. 122

6.30 $\ln\sigma_{ac}$ versus 1000/T for (*i*) $x = 0.0$, (*ii*) $x = 0.23$, (*iii*) $x = 0.46$, and (*iv*) $x = 0.882$ composites; measured at different frequencies. 123

6.31 Frequency dependence activation energies (E_1 and E_2) of various compositions (*a*) $x = 0.23$, [for $123K \leq T \leq 293K$] (*b*) $x = 0.23$ [for $303K \leq T \leq 573K$], (*c*) $x = 0.46$ [for $123K \leq T \leq 293K$], (*d*) $x = 0.46$ [for $303K \leq T \leq 573K$], (*e*) $x = 0.882$ [for $123K \leq T \leq 293K$], (*f*) $x = 0.882$ [for $303K \leq T \leq 573K$]. 124

6.32 Activation energies (E_1 and E_2) plotted as a function of compositions measured at two different frequencies (16.7 kHz and 125 kHz). 125

Chapter 7

7.1 The schematic representation of magnetic and structural transitions observed in polycrystalline Mn_3O_4 below the Néel temperature T_N. The abbreviations FOT and SOT correspond to first- and second-order transitions, respectively [312,313]. 128

7.2 XRD pattern and the corresponding Rietveld refined data of Mn_3O_4 polycrystals prepared from the thermal decompositions of the oven dried precursors followed by (a) sintering at 1100°C without quenching and (b) after quenching from 1100°C to liquid nitrogen temperature (77 K). The inset of (a) shows zoomed view of the reflection pattern between $2\theta = 31.5°$ and 34° depicting the reflection of (222) peak of Mn_2O_3 which is presented as minor phase and inset of (b) shows the Williamson hall plot. 130

7.3 Field Emission Scanning Electron Microscope image of Mn_3O_4 131

7.4 Temperature dependence of dc magnetization M(T) recorded under zero-field cooled ZFC and field cooled FC conditions at an external magnetic field 200 Oe. 132

7.5 The temperature variation of the first derivative plots of dc-magnetic susceptibility $\partial(\chi_{dc}T)/\partial T$ for the magnetic fields H = 50 Oe, 100 Oe and 200 Oe. Inset shows the zoomed view of magnetically ordered regime which clearly depicts all the magnetic transitions. 133

7.6	Temperature dependence of real component ac-magnetic susceptibility $\chi'(T)$ recorded at various frequencies under warming condition. The inset shows the zoomed view of the susceptibility cusps within the regime 39 K to 43 K and 38.5 K to 40 K.	134
7.7	Temperature dependence of imaginary component ac-magnetic susceptibility $\chi''(T)$ recorded at various frequencies under warming condition. The inset shows the zoomed view of the susceptibility cusps within the regime 37 K to 41 K.	135
7.8	Derivative plots of $\chi'T$ (i.e. $\partial(\chi'T)/\partial T$) plotted as a function of temperature for various frequencies. Inset represent the zoomed view of the derivative plots where all the transitions are clearly able to trace (vertical arrows indicates the magnetic transitions).	136
7.9	The temperature dependence of the (a) real component $\chi'(T)$ (b) imaginary component $\chi''(T)$ of the ac-magnetic susceptibility recorded under the superposition of different weak static bias magnetic fields for constant frequency 2 Hz and constant ac-field amplitude h_{ac} = 1Oe.	137
7.10	The temperature dependence of the $\partial(\chi'T)/\partial T$ plots for various static magnetic fields (H_{dc}). The in inset shows zoomed view of the graph depicting the magnetic transitions at T_2, T_1 and T^*.	137
7.11	The temperature dependence of the relative dielectric permittivity $\varepsilon_r(T)$ measured under zero-magnetic field. The inset (*i*) shows the dielectric anomaly corresponding to the transition T^*. The inset (*ii*) shows the hysteresis lag in $\varepsilon_r(T)$ measured during cooling and heating cycles as represented by the red color arrow marks.	138
7.12	The positive and negative branches of the Polarization (P) versus temperature (T) curves measured in the temperature range 7 K - 100 K after poling with the static-electric field of strength ± 800 kV/m.	139
7.13	The relative dielectric permittivity $\Delta\varepsilon_r/\varepsilon_r$ (%) scanned as a function of static magnetic field H_{dc} under decreasing and increasing cycles (±15 kOe) of magnetic field at various temperatures. Here $\Delta\varepsilon_r/\varepsilon_r = ([\varepsilon_r (H=0)- \varepsilon_r(H)]/\varepsilon_r(H=0))$. The inset shows the square of the magnetization value M^2 in red colored data points plotted on the left hand side scale as a function of magnetic field and a zoomed view of the low field hysteresis response of $\Delta\varepsilon'/\varepsilon'_{H=0}$ (%) versus magnetic field H_{dc}.	140
7.14	The ratio of magnetic field 'H' and its corresponding magnetization 'M' values (H/M) plotted as a function of the square of magnetization (M^2) for different temperature $T<T_N$ (Arrott plots). Note: Only selected M-H curves and H/M-M^2 plots are shown at characteristic temperature intervals.	142
7.15	The magnetization versus field (M-H) isotherms recorded at various temperatures $T<T_N$. Note: Only selected M-H curves are shown at characteristic temperature intervals.	142
7.16	Temperature dependence of remanence magnetization $M_r(T)$ shown on the left-hand-side scale and the right-hand-side scale depicts the magnetization values recorded at H=1 kOe and 90 kOe during the hysteresis loop measurements at various temperatures. The inset shows zoomed view of the low-temperature regime of $M_r(T)$ depicting the down turn of the M_r values below 15 K.	143

List of Tables

Table No.	Table Description	Page No.
	Chapter 3	
3.1	The list of lattice parameters (a = b = c), bond lengths and bond angles of S1200 and S1350 samples. (The interaxial angles $\alpha = \beta = \gamma = 90°$).	29
3.2	The list of various parameters obtained from the Néel fits of χ^{-1} versus T curve recorded under zero-field condition.	45
	Chapter 4	
4.1	The list of lattice parameters (a = b = c), bond lengths and bond angles in Co_2SnO_4 and Co_2TiO_4. (The interaxial angles $\alpha = \beta = \gamma = 90°$).	51
4.2	The list of various parameters obtained from the Néel fits of χ^{-1} versus T curve recorded under zero-field-cooled condition.	55
	Chapter 5	
5.1	List of various crystal structure parameters (*i*) lattice parameter, (*ii*) bond Length and (*iii*) bond angles of various compositions of bulk samples $Co_2Ti_{1-x}Sn_xO_4$ ($0 \leq x \leq 1$). [*Co_2TiO_4 sample sintered at 1100°C, results of previous chapter].	75
5.2	The list of various parameters obtained from the Néel's fits of χ^{-1} versus T curve with the experimental data points of various compositions of $Co_2Ti_{1-x}Sn_xO_4$ ($0 \leq x \leq 1$) recorded under zero-field-cooled condition. [*Co_2TiO_4 sample sintered at 1100°C, results of previous chapter].	89
5.3	The list of molecular -field constants, exchange constants and Landé g-splitting factors obtained from the Néel's fits of paramagnetic susceptibility χ^{-1} versus T for various compositions of $Co_2Ti_{1-x}Sn_xO_4$ ($0 \leq x \leq 1$) recorded under zero-field-cooled condition. *Co_2TiO_4 sample sintered at 1100°C.	91
	Chapter 6	
6.1	Line positions and widths (FWHM) of the Raman-active modes of (1-*x*) Co_3O_4 + *x* Co_2TiO_4 (*x* = 0, 0.46(46.3) and 1(100 wt%) sintered at 1200ºC in air recorded at Room temperature.	102
6.2	Atomic quantification of the normal-spinel Co_3O_4 and the inverse-spinel Co_2TiO_4 using the XPS data.	109
6.3	The fitting parameters obtained from Vogel-Fulcher law and Power law of (1-*x*) Co_3O_4 + *x* Co_2TiO_4 (*x* = 0, 0.706(70.6) and 0.882(88.2 wt%) sintered at 1200ºC.	113
	Chapter 7	
7.1	List of various crystal structure parameters (*i*) lattice parameter, (*ii*) bond Length and (*iii*) bond angles of both quenched and without quenched Mn_3O_4 samples obtained from the refinement process.	130

List of Symbols

XRD — X-ray diffraction
XPS — X-ray Photoelectron spectroscopy
BE — Binding Energy
T_N — Néel temperature
h — hours
ZFC — Zero-Field Cooled
FC — Field Cooled
A, B sites — Tetrahedral, Octahedral sites
M_R — Remanance
H_C — Coercievity
H_{EB} — Exchange bias
T_{COMP} — Compensation temperature
ASD — Antisite disorder
FWHM — Full width at half maxima
SOT — Second order transition
FOT — First order transition
Å — Angstrom
ε_r — Relative dielectric permitivitty
pm — Picometer
nm — Nanometer
mm — Millimeter
cm — Centimeter
μm — Micro-meter
K — Kelvin
μ_B — Bohr magnetron

Chapter 1

Introduction to Spinels and their Complex Magnetic Structure

1.1 Background:

Spinels are a special class of materials with general formula $A^{2+}B^{3+}{}_2X^{2-}{}_4$ in which the anions (X = O, S, Se) are arranged in cubic close-packed lattice and the cations A and B occupies partially or all of the octahedral and tetrahedral sites in the lattice. Although the oxidation states of A and B in the archetypal spinel structure are +2 and +3, respectively, other combinations integrating divalent, trivalent, or tetravalent cations are also possible [1, 2]. The unit cell of a spinel contains eight units of AB_2X_4 in which the atoms are located in the following positions:
Equivalent positions (0, 0, 0; 0, ½, ½; ½, 0, ½; ½, ½, 0) + 8 A cations at 0, 0, 0; ¼, ¼, ¼;
16 B cations at 5/8, 5/8, 5/8; 5/8, 7/8, 7/8; 7/8, 5/8, 7/8; 7/8, 7/8, 5/8
and 32 anions 'X' at x, x, x; ¼ - x, ¼ - x, ¼ - x

x, x, x; ¼ - x, ¼ - x, ¼ - x

x, x, x; ¼ - x, ¼ - x, ¼ - x

In ideal spinel structure the anion parameter is 0.375 with ideal position <111>. But most of the cases the anions are displaced from their ideal positions away from the tetrahedron positions. The crystal structure of spinel is quite complex. The large unit cell can be divided into eight small (octants), half of which contain tetrahedral arrangement of anions around the A cations. The anions located in half of the corners at the top and bottom of the small unit cell known as type-I structure (figure 1.1). In the other unit cell, type-II the anions are located at sites similar to those occupied by the anions in type-I cells (figure 1.2). When the cell type-I and type-II are brought together the connection between the anion tetrahedra and octahedra can be clearly seen (figure 1.3). It is interesting to note that this kind of arrangement is, quite similar to that of lattice sites in Cu_2Mg structure in which the magnesium atoms sit at the corners, at the center of the faces and in two diagonally opposite upper and two diagonally opposite lower octants of the cubic unit cell. On the other hand, the copper atoms are arranged in the tetrahedral sites of the cubic unit cell with similar atomic positions as that of spinel lattice. In the spinel structure, there are one A and three B cations around each anion. The B-X-B bond angle is about 90° and A-X-B is about 125°. The distance between A and X is a $(x - ¼)\sqrt{3}$ and the distance between B and X is $a(5/8 - x)$. These bond-angles and the bond-lengths play a crucial role in determining the magnetic properties of the spinels. The cations in the sublattice of the spinel interact among each other antiferromagnetically via non-magnetic anions known as super-exchange interactions (J_{ij}) (will discuss in the later section). In general, the interaction between the 'A' cations in the tetrahedral sites and the 'B' cations in the octahedral sites is stronger than others (i.e, $J_{AB} > J_{BB}$ and J_{AA}). Thus the cation distribution in each site plays a decisive role in various physical properties, especially magnetic and magneto-dielectric properties.

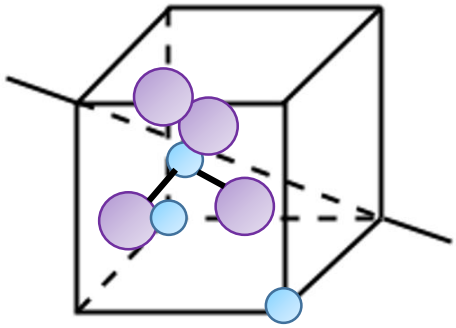

Figure 1.1: Schematic representation of Type-I octant containing cations A in the tetrahedral co-ordinations [5].

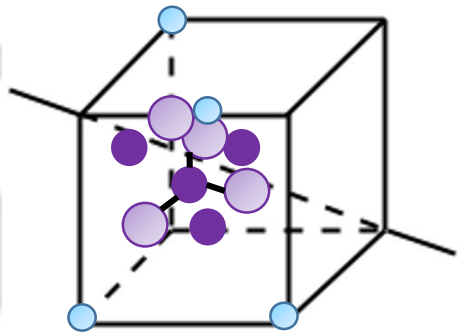

Figure 1.2: Type-II octant containing 'B' cations in octahedral co-ordinations [5].

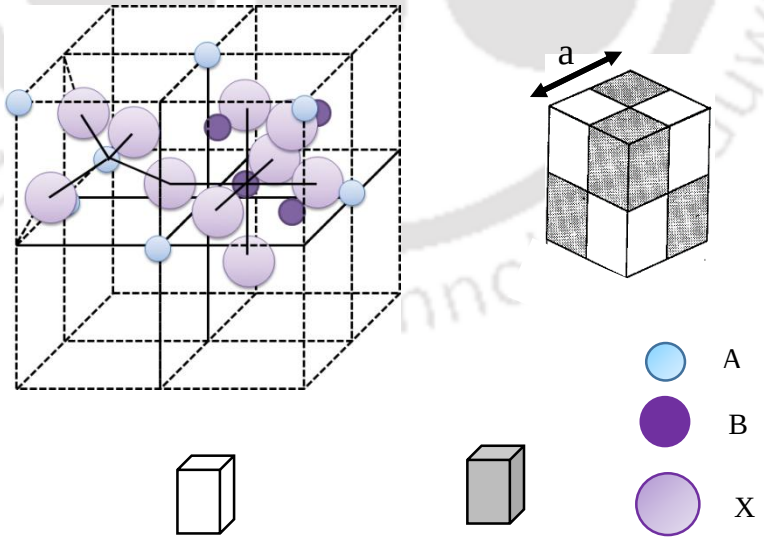

Figure 1.3: The cubic spinel structure of AB_2X_4 with Type I octant containing 'A' cations in tetrahedral and Type II octant having 'B' cations in octahedral voids of oxygen ions [5].

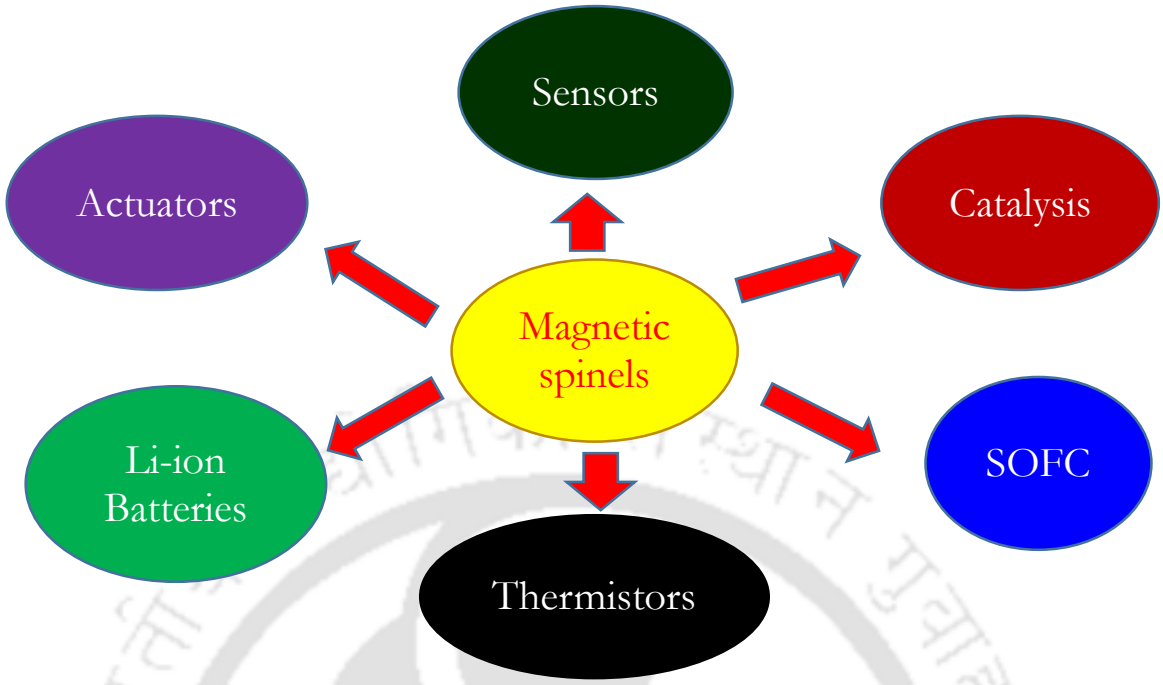

Figure 1.4: Various application of spinels

Generally, spinel can be classified into two categories (*i*) Normal spinels: $(A^{2+})_{tetra}[B^{3+}{}_2]_{oct}X^{2-}{}_4$, in this configuration all 'A' cations occupy the tetrahedral voids and all 'B' cations occupy the octahedral voids. Example: $MgAl_2O_4$, $CoCr_2O_4$, Co_3O_4, Mn_3O_4, etc., (*ii*) Inverse spinels: $(B^{3+})_{tetra}[A^{2+}B^{3+}]_{oct}X^{2-}{}_4$, in this configuration half of the B cations occupy tetrahedral voids and rest of the 'B' cations along with 'A' sit in the octahedral voids. Examples of Inverse are Fe_3O_4, Co_2TiO_4, Co_2SnO_4, Co_2MnO_4, etc. Including these two types another class of spinels is also possible that is the Mixed spinel structure where both 'A' and 'B' cations occupy the tetrahedral as well as octahedral sites, for example $Mn_{0.8}Fe_{0.2}[Mn_{0.2}Fe_{1.8}]O_4$, $Mg_{0.1}Fe_{0.9}[Mg_{0.9}Fe_{1.1}]O_4$.

1.2 Applications of Spinels:

Since 1960's magnetic spinels are widely studied because of their potential applications in various research areas, including magnetic-recording and microwave devices [3-6]. Among a wide variety of spinel compounds, manganese and cobalt based oxide-spinels drawn immense attention in recent years due to their strong catalytic activity towards the oxygen reduction reaction in alkaline solutions [3-8]. The oxygen reduction reaction has been one of the most important issues of electrochemistry owing to its importance in a variety of energy applications including fuel-cells and batteries [9-12]. Due to its catalytic activity, low cost, simple fabrication and ability to accommodate wide range of dopants, these spinel oxides have been investigated extensively as electro-catalysts and electrode in solid oxide fuel cell technology [13]. Magneto-dielectric can be described as materials in which

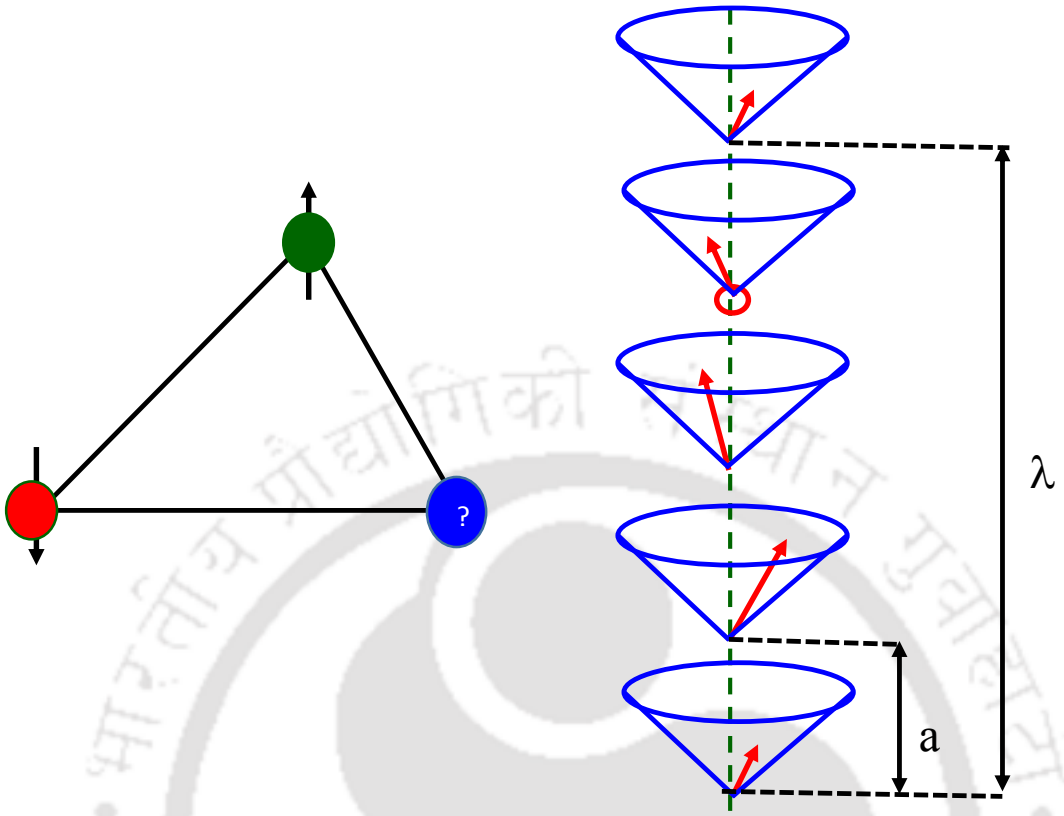

Figure 1.5: Schematic diagram of triangular and spiral or canted spin-spiral arrangements.

magnetic ordering produces dielectric anomalies or alternately, materials in which the low frequency dielectric constant is sensitive to an external magnetic field [14]. Spinels which show such magneto-electric coupling also find a large number of potential applications like magnetic read-write heads, magnetically tunable capacitor, magnetic field sensors, non-volatile multi bit data storage devices and transducers (figure 1.4) [13, 15-17].

1.3 Magnetic Exchange Interactions using Molecular Field Theory:

It is well known that the fundamental aspect of magnetism is linked with the orbital and spin degrees of freedom of electrons and their interaction with one another. The magnetic behavior of materials can be classified into the following five main categories: (*i*) Diamagnetism (*ii*) Paramagnetism (*iii*) Ferromagnetism (*iv*) Ferrimagnetism (*v*) Antiferromagnetism. Materials in the first two groups are those that exhibit no collective magnetic interactions and are not magnetically ordered. Whereas, materials in the last three groups exhibit long-range magnetic order below a certain critical temperature, known as Curie temperature (T_C) or Néel (T_N) temperature. In the ferromagnetic systems, the moments are aligned parallel to each other and exhibits spontaneous magnetization below T_C even in the absence of external magnetic field. In antiferromagnetic compounds, the adjacent moments align antiparallel to each other in such a way that the net magnetic moment is

zero below the characteristic temperature T_N. Ferrimagnetic materials also contain antiparallel alignment of the unequal magnetic moment with the partial cancellation of the two magnetic sub-lattices with different magnetic moments and they undergo parallel alignment of intra sub-lattice moments and antiparallel alignment of inter sub-lattice moments with partial cancellation of the moment. In 1970, Louis Eugène Félix Néel proposed that antiferromagnetic and ferrimagnetic substances contain two sublattices, one of those spins tends to be antiparallel to those of each other. In case of antiferromagnetic compounds Néel assumed that the magnetic moment of the two sublattices to be equal, so that the net moment of the materials was zero. Since Néel's original hypothesis the term antiferromagnetism has been extended to include materials with more than two sublattices and those with triangular, spiral, or canted spin arrangements; the latter may have a non-zero magnetic moment (figure 1.5) [18-26].

The superexchange interaction between two cations via an intermediate oxygen ion is greatest if the three ions are collinear and if their separations are not too great. The ion arrangements in the spinels are likely to be most important are shown in figure 1.6. The first configuration is depicted in figure 1.6a; in this figure both the angle and the distance between the ions are favorable for superexchange. In all other cases, either the angle (figure 1.6c), or the distance (figure 1.6b, 1.6d), or both are unfavorable (figure 1.6e). Thus, the interaction between the sublattices is stronger than those within the sublattices and further that the interaction between ions in 'A' sites is weakest of all. This result thus supports the assumption that sublattice magnetizations are antiparallel to each other; substantial evidence for such configuration comes from neutron diffraction experiments. The molecular field theory first developed to understand the interactions in two sublattice systems ('A' and 'B') [27-30]. For simplicity, consider a body-centered-cubic lattice, in which the 'A' cations occupy the corner positions, and the 'B' cations occupy body center positions of the lattice. An atom situated on tetrahedral (A) site then has nearest neighbors that all lie on octahedral (B) sites and next nearest neighbors that all lie on 'A' sites. An equivalent picture holds for an atom positioned at 'B' site. According to the phenomenological theory of ferromagnetism the molecular field acting on an atom 'A' site

$$H_{mA} = -N_{AA}M_A - N_{AB}M_B \quad \ldots \quad (1.1)$$

where M_A and M_B are the magnetizations corresponding to the 'A' and 'B' sublattices, respectively, whereas N_{AB} and N_{AA} are the molecular field constant for the nearest neighbor and next nearest neighbor interaction, respectively. Similarly, for the atom sitting on the 'B' site the molecular field (H_{mB}) can be written as

$$H_{mB} = -N_{BA}M_A - N_{BB}M_B \quad \ldots \quad (1.2)$$

Since, similar kind of atoms occupies the 'A' and 'B' sublattices, we can conclude that $N_{AA} = N_{BB} = N_{ii}$ and $N_{AB} = N_{BA}$. Then, if an external magnetic field H is also applied, the field associated to the 'A' and 'B' sublattices, can be written as

$$H_A = H - N_{ii}M_A - N_{AB}M_B \ldots 1.3(a)$$

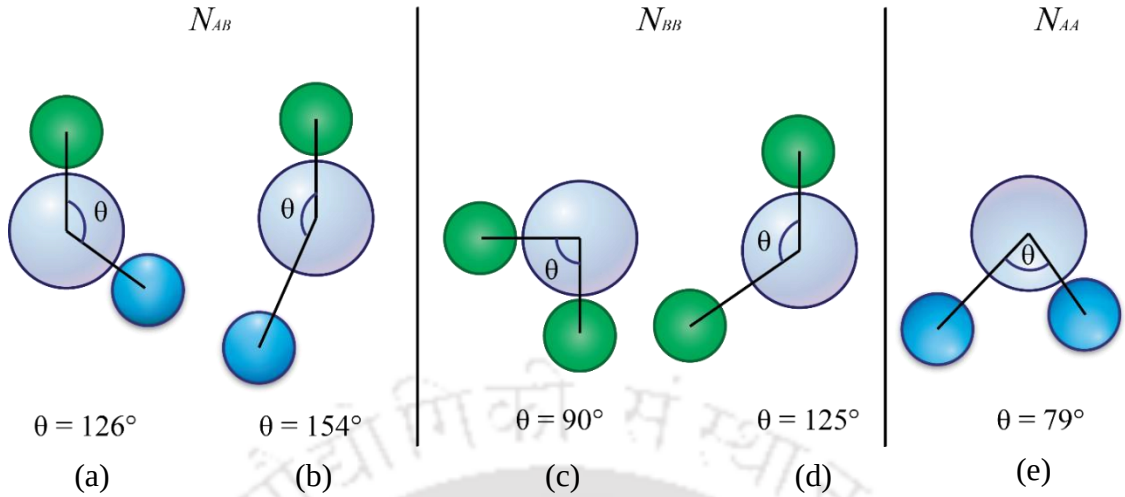

Figure 1.6: Ion pair configuration of super-exchange interaction. Large spheres represents oxygen ions, cations in 'A' sites represent by small blue color sphere and small green color sphere are the cations in B sites [18].

and

$$H_B = H - N_{AB}M_A - N_{ii}M_B \quad \ldots 1.3(b)$$

The molecular field constant N_{AB} must be positive as the nearest neighbor interaction between the atoms in the A and B sublattices is antiferromagnetic. On the other hand, the next nearest neighbor interactions may be positive, negative or zero depending on the particular material.

At thermal equilibrium the magnetizations of the sublattices can be written as

$$M_A = \frac{1}{2} N g \mu_B S B_S(x_A) \quad \ldots \ (1.4)$$

where

$$x_A = \left(\frac{Sg\mu_B}{kT}\right) H_A \quad \ldots \ (1.5)$$

and the Brillouin function

$$B_S(x_A) = \left[\frac{2S+1}{2S}\right] \coth\left[\frac{2S+1}{2S}\right] x_A - \left(\frac{1}{2S}\right) \coth\left(\frac{x_A}{2S}\right)$$

and

$$M_B = \frac{1}{2} N g \mu_B S B_S(x_A) \quad \ldots \ (1.6)$$

where

$$x_B = \left(\frac{Sg\mu_B}{kT}\right) H_B$$

and

$$B_S(x_B) = \left[\frac{2S+1}{2S}\right] coth \left[\frac{2S+1}{2S}\right] x_B - \left(\frac{1}{2S}\right)\left(\frac{x_B}{2S}\right)$$

In the above equations 'N' represents the total number of atoms or ions per unit volume having a permanent dipole moment, and 'J' has been set equal to 'S'.

Although there is no antiferromagnetic ordering above the T_N, a small magnetization is induced in the system in the presence of applied magnetic field. For the minimal applied fields, saturation effects are negligible and the Brillouin function can be substituted by the first term in the above equations, after the expansion of the series with respect to *x*, namely, $B_S(x) = [(S+1)/3S]x$. The revised equations become

$$M_A = \frac{Ng^2\mu_B^2 S(S+1)}{6kT} H_A \ldots (1.7)$$

and

$$M_B = \frac{Ng^2\mu_B^2 S(S+1)}{6kT} H_B \ldots (1.8)$$

now

$$H_A = |H - N_{ii}M_A - N_{AB}M_B|$$

$$= H - N_{ii}M_A - N_{AB}M_B$$

Since H, M_A, and M_B are parallel in the paramagnetic region. Similarly,

$$H_B = H - N_{AB}M_A - N_{ii}M_B$$

Substitution of these values of H_A and H_B into the foregoing equations for M_A and M_B gives,

$$M_A = \frac{Ng^2\mu_B^2 S(S+1)}{6kT} (H - N_{ii}M_A - N_{AB}M_B) \ldots (1.9)$$

and

$$M_B = \frac{Ng^2\mu_B^2 S(S+1)}{6kT} (H - N_{AB}M_A - N_{ii}M_B) \ldots (1.10)$$

Adding of the equations (1.9) and (1.10) results,

$$M = M_A + M_B = \frac{Ng^2\mu_B^2 S(S+1)}{6kT} [2H - (N_{ii} + N_{AB})M] \ldots (1.11)$$

Hence the susceptibility $\chi = M/H$ is given by

$$\chi = \frac{C}{T+\theta} \ldots (1.12)$$

where,

$$C = \frac{Ng^2\mu_B^2 S(S+1)}{3k}$$

and

$$\theta = \frac{1}{2} C(N_{ii} + N_{AB})$$

Since, generally, $N_{AB} > N_{ii}$, θ is positive. It is interesting to compare the equation $\chi = C/(T+\theta)$ With equation $\chi = C/(T - \theta)$, the Curie-Weiss law so that one can easily evaluate the molecular field constant discussed above [18].

1.4 Dilution Effects and Reentrant Spin-glass State:

Magnetic frustration resulting from either the competing exchange interactions or dilution of magnetic elements can disrupt the long-range magnetic ordering of any magnetic-material and may lead to spin-glass (SG) state [31-36]. Such disorder driven SG state preceded by a long-range magnetic ordering at higher temperatures are often termed as re-entrant SG systems, which is the subject of this paper [33-36]. Among many such diverse disordered magnetic materials which show re-entrant SG state, cobalt (Co) based inverse-spinel oxides (e.g. Co_2SnO_4 and Co_2TiO_4) are considered as unique systems mainly because of their interesting magnetic properties resulting from octahedrally coordinated divalent 'Co' ions [37, 38]. Usually, frozen-spin behavior can be seen in dilute metallic alloys and nonmetallic systems [39]. At the point of transition the alignment of the canting-spin freeze due to a high degree of randomness and strong competing interaction among the crystal sub-lattice of the systems without developing long-range order [40]. Recently, spin-glass behavior has also been observed in magnetic-spinel due to the presence nonmagnetic cations in the two sub-lattices lead to geometric frustration [31-36]. The following sections describe the origin of disorderness in standard spin-glass systems.

Figure 1.7 represents the square lattice whose sites are denoted by the dots. A certain fraction '*x*' is occupied by the magnetic moment or spin which are distributed randomly all over the lattice sites and are indicated by the arrows. In order to avoid too many nearest-neighbor occupancies we keep the '*x*' small (~ ¼). Now the magnetic moments interacts ferromagnetically (parallel) between the nearest neighbor and antiferromagnetically (antiparallel) between the next nearest neighbors. Such a situation is illustrated in figure 1.7 where we have removed any thermal disorder by reducing the temperature to a negligible value. In the figure we choose arbitrarily the alignment of the top right moment to upwards. Though there are spins or arrows are completely decoupled from the large clusters, but almost all of them connected in the lattice environment strongly and also able to propagate from top to bottom. A perfect balancing of the up and down spins (exhibits zero net moment) also observed. However, a certain number of spins or moments still unable to satisfy their second neighbor bond due to the creation of frustrations. The frustration comes when first neighbor ferromagnetic coupling strength ($J_1 > 0$) exhibits equal values of two second neighbor's antiferromagnetic coupling strength ($J_2 < 0$) i.e, $|J_1| = |2J_2|$, then the spin will not know which way to point and disconnects to the two spins below itself.

The most salient example of an entirely frustrated spin-lattice is triangular one, where all the interactions are antiferromagnetic and the surroundings spins are in a totally confused state once the direction of the center spin is chosen (as shown in figure 1.8). In terms of energy consideration, the frustrated spins unable to make any difference as they are not capable to change the rotation of the magnetization vector. Such situation is popularly known as 'frozen state', an identical state in 3D lattice at T = 0 K. The basic ingredients of the frozen state of a spin-glass are (*i*) randomness (*ii*) mixed interaction and (*iii*) frustration, such conditions lead to many possible ground state configurations. Now in order to know much about the SG state, we have to understand the formation of the random mixing of the spins at high temperature. The randomness in SG systems and compounds with mixed

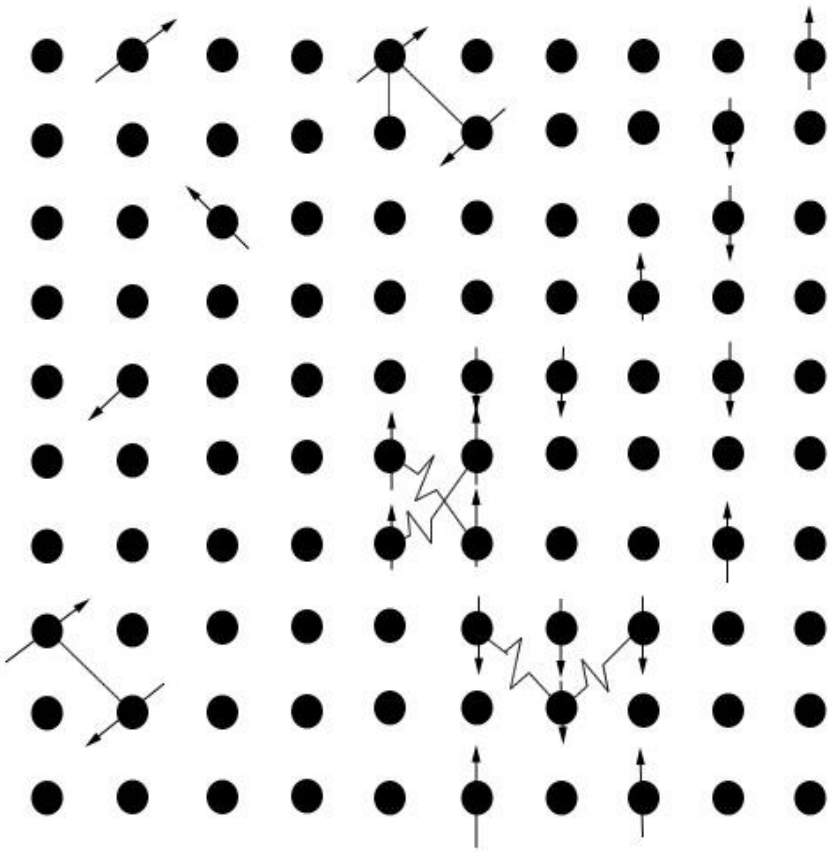

Figure 1.7: Schematic representation of frozen spin glass with $J_1 > 0$ (ferromagnetic) and $J_2 < 0$ (antiferromagnetic). The zig-zag links indicate a broken bond [67].

interacting spin configuration follows a co-operative freezing of spins at a definite temperature often called as "Freezing temperature (T_f)". Below T_f, a highly irreversible, metastable frozen state occurs which is short range spatial magnetic order in nature [33-36]. In a single word spin-glass represents the 'frozen state' of the compound.

The two most key requirements of spin-glass are the randomness in positions of the spins, or the signs of the neighboring couplings: ferro (↑↑) or antiferromagnetic (↑↓) or in both. There must be disorder, as the site or bond disorder creates spin-glass state, otherwise the magnetic transition will be normal long range ordering transitions (ferromagnetic or antiferromagnetic) [41, 42]. The combine effects of the randomness and the competing or mixed interactions is the source of frustration, as illustrated in figure 1.7. This second requirement of frustration is the sole characteristic of the spin-glass ground state, which is disordered, but still exhibits many exciting properties associated to its co-operative nature. For example, a macroscopic anisotropy is created and peculiar metastabilities (time and aging dependence) occur especially in reaction to an applied magnetic field. Observation of exchange-bias phenomena below T_f is one of the recent observations noticed in re-entrant SG system which will be discussed in more detailed way in the coming chapters. It is sufficient to say that, there must be disorder in the constitution

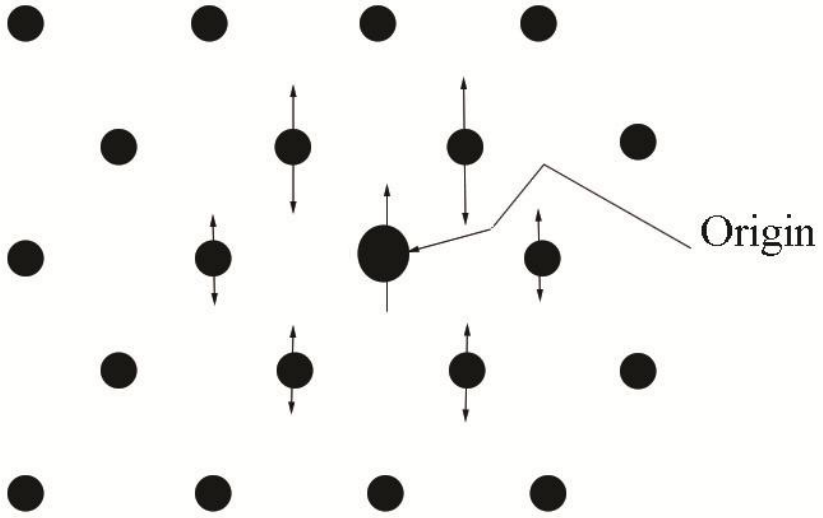

Figure 1.8: Schematic diagram of frustrated triangular (hexagonal) lattice with all antiferromagnetic interactions ($J_1 < 0$) [67].

of a spin glass: either site randomness with various distances between the magnetic spins, or bond randomness where the nearest neighbor interaction varies between parallel and antiparallel coupling + J and - J.

The spin-glass problem is the interactions between the spins and these exchange interactions creates a randomness through which a unique type of ground state is formed. According to quantum mechanics magnetic exchange interaction in the form of spin Hamiltonian can be written as $H_{ij} = - J_{ij} S_i.S_j$, which couples the spins at lattice sites '*i*' and '*j*'. The energy difference between the parallel and antiparallel configurations should be equivalent to the magnitude of exchange energy. In 1979, theoretical studies by Villian (Scholl and Binder) predicted that increasing of dilution in mixed ferrimagnetic spinels (like $Mg_{1-t}Fe_{2-2t}Ti_tO_4$ with $J_{AB} >> J_{BB} > J_{AA}$) may increase the unsatisfied bonds causes competition between percolation and frustration finally results to a new mixed state called (reentrant) spin-glass-like state [40]. Thus J_{AB} renders the undiluted spinel ferrimagnet, with all A-site moments oriented antiparallel to all B-site moments, but with BB and AA bonds remaining unsatisfied. However, frustration of certain moments occurs due to the dilution of any of the two sublattices and the collinearity of ferrimagnetic phase will collapse well below the percolation threshold for AB bonds [43].

1.5 Negative Magnetization in Spinels:

Negative magnetization or magnetization reversal is an exciting phenomenon of the magnetically ordered system, where the dc magnetization verge from a positive value to a negative value as a function of temperature. Such an interesting behaviour is observed in magnetic spinels below their T_C or T_N including some perovskite systems, molecular magnets, garnets, intermetallic alloys, and multilayers [44 - 51]. In 1948, Néel gave the first phenomenological theory for the explanation of negative magnetization under the framework of molecular field

theory **[**52**]**. Later in 1950, this magnetic reversal phenomenon first observed experimentally in ferrites [53 - 55]. In ferrites, the magnetic moment at the tetrahedral 'A' and 'B' sublattices are coupled antiferromagnetically with each other. According to the Néel theory, the local molecular fields at the 'A' and 'B' sublattices can be expressed as

$$H_A = \gamma(\alpha M_A - M_B) \ldots (1.13)$$

$$H_B = \gamma(M_A - \beta M_B) \ldots (1.14)$$

where, M_i is the i^{th} sublattice magnetization and γ represents molecular field coefficients corresponding to the A-B magnetic exchange interaction. In this equation 'α' and 'β' are the molecular field coefficient for intra-sublattices interactions (A-A, and B-B) normalized by 'γ'. The sublattices Brillouin function $B_J(x)$ can be given by,

$$B_J(x) = \left[\frac{2J+1}{2J}\right]\coth\left[\frac{(2J+1)x}{2J}\right] - \left(\frac{1}{2J}\right)\coth\left[\left(\frac{1}{2J}\right)x\right] \ldots (1.15)$$

and $x = gJ\mu_B H/k_B T$

In the above equation 'J' is the total angular momentum, 'g' is the Lande g-factor, μ_B is the Bohr magneton, k_B is the Boltzmann constant, and 'N' is the total number of magnetic atoms/ions per unit volume. The Brillouin function dependence of the 'A' and 'B' site magnetizations with respect to temperature (T) and external magnetic field (H) are given by

$$M_A = \lambda N g\mu_B S_A B_{S(A)}\left[\frac{g\mu_B S_A(H+H_A)}{k_B T}\right] \ldots (1.16)$$

and

$$M_B = \lambda N g\mu_B S_B B_{S(B)}\left[\frac{g\mu_B S_B(H+H_B)}{k_B T}\right] \ldots (1.17)$$

where 'N' is the total number magnetic ion per unit volume and S_A and S_B are the spin angular momenta for the 'A' and 'B' sites, respectively. The parameters 'λ' and 'δ' are the molar fractions of the magnetic ions at the A and B sites so that λ + δ = 1. Equations 1.13 to 1.17 can be solved numerically to obtain the temperature as well as external field variations of the 'A' and 'B' sublattice magnetizations (M_A and M_B) and also the net magnetization (ΔM). In his theory, Néel's pointed out all prospects of ferrimagnetism i.e, Q-type, P-type, R-type, and N-type ferrimagnetism based on the values of α, β, λ, δ, S_A and S_B [52, 53]. Out of the above mentioned ferrimagnetism, N-type is the most interesting ferrimagnetism with the compensation temperature (T_{COMP}) $0 < T < T_N$. This situation arises when $\alpha > \beta$, and $0 > \beta > -1$. Under this condition, M_A and M_B exactly balancing each other and for $\lambda S_A < \lambda S_B$ and the net magnetization is parallel to B sublattice magnetization with a possibility of a negative magnetization below T_N. Figure 1.9 shows temperature dependence of M_A and M_B along with the net magnetization. According to molecular field theory, it is evident that the sublattice magnetization respond

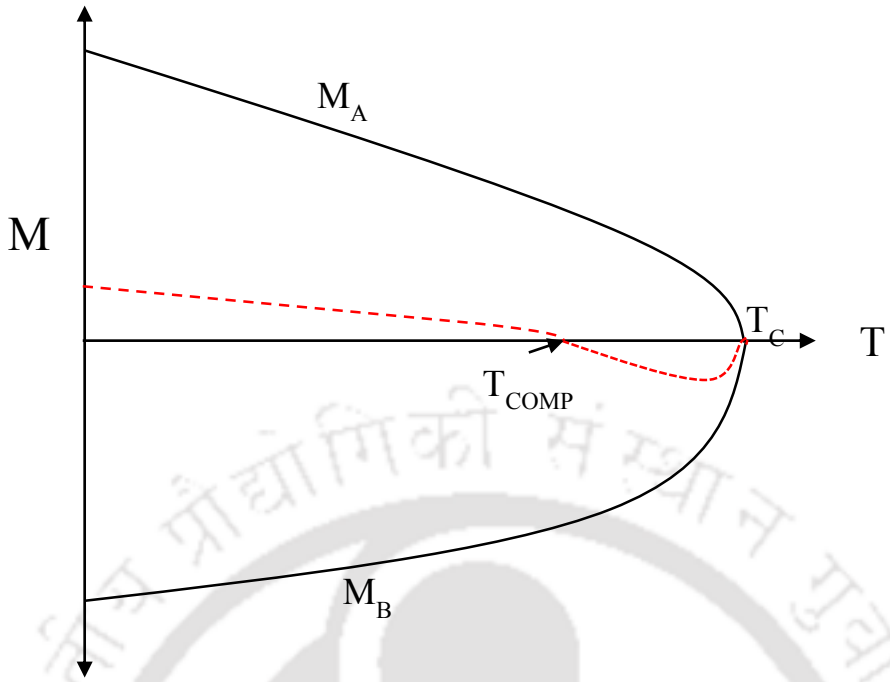

Figure 1.9: Temperature variation of magnetization M(T) for the N-type ferrimagnetism as per the Néel's theory. The net magnetization is represented as the dotted red color line [62].

differently with temperature resulting the magnetization reversal. Néel's theory (by considering two/three magnetic sublattices) successfully explained the observed magnetization reversal in a large varieties of spinel compounds, e.g, $NiFe_{2-x}V_xO_4$ [56], Fe_2MoO_4 [57], $CoCr_{2-x}Fe_xO_4$ [58, 59], $Li_{0.5}Fe_{1.7}Al_{0.8}O_4$ [60]. However, Néel's theory, unable to predict the nature of net-magnetization once it becomes negative and opposite to the field direction. If the system exhibits finite value of anisotropy, then in presence of low magnetic field the Zeeman energy is suppressed by the anisotropy energy as a result, the net magnetization reversed to the applied field direction and hence negative magnetization appears. Later Belov *et al.* explained the negative magnetization in some other ferrites and garnets using the concept of weak magnetic sublattice [61]. According to this theory, the ferrimagnetic systems contain (*i*) a weak magnetic sublattice having anomalous temperature dependence of magnetization, and (*ii*) strong magnetic sublattice with normal 'Weiss-type' temperature dependence of magnetization. At $T < T_{COMP}$, magnetization of the weak magnetic sublattices behaves like that of a strong magnetic sublattice, whereas above T_{COMP} it behaves like an 'exchanged-enhanced' paramagnetic sublattice [61]. Belov *et al*. further predicted that weak magnetic sublattice exits due to the presence of the unidirectional magnetic anisotropy in ferrites [61]. This anisotropy arises because of the presence of the effective exchange field of the 'strong' sublattices, ordered at a high temperature. Ferrimagnetic systems like $Zn_xMg_{0.75-x}Cu_{0.25}Fe_2O_4$, $Zn_xCu_{1-x}FeCrO_4$, $Zn_xNi_{1-x}FeCrO_4$, and $Zn_{0.4}Co_{0.6}Al_xFe_{2-x}O_4$ shows sign reversal of a net magnetization as a consequence of either different ordering temperatures of 'A' and 'B' sublattices or a non-Weiss type ordering of A or B sublattice moment, which support Belov hypothesis [62-66].

1.6. Description of the Problem and the Approach:

Besides their potential technological applications, number of exciting magnetic properties exhibited by the spinel oxides poses many challenges to researchers in understanding their exact origin. In particular, phenomena like the low temperature spin-liquid state, exchange-bias under zero-field-cooled condition and reentrant spin-glass ordering in spinel oxides drawn immense attention recently [67-76]. In the present thesis, we first attempt to study the role of dilution on the low-temperature magnetic ordering of ferrimagnetic spinel cobalt orthostannate (Co_2SnO_4) and cobalt orthotitanate (Co_2TiO_4). Although few reports are available in the literature dealing with the dc-magnetization of both these oxides with ordering temperature 41 K and 55 K for Co_2SnO_4 and Co_2TiO_4, respectively, but a clear understanding of the low-temperature ac-magnetization studies at different frequencies was lacking in the literature when we endeavored this problem. It was believed that non-magnetic Sn^{4+} or Ti^{4+} randomize the cationic distribution in the octahedral site, which may break the symmetry of octahedral crystal field [77 - 83]. As a result, the system possess frustration in the magnetic ordering, and may result spin-glass-like ordering, negative magnetization and compensation effect below T_N, which are the main objectives of the current thesis [62-65, 77, 82, 83]. Our approach to understand the role of dilution is two-fold: first to perform a detailed temperature, frequency and dc-magnetic field dependence of ac-magnetic susceptibility, and secondly to perform the heat-capacity measurements under various dc-fields, and probe the nature of magnetic transitions in both the systems. Though there are few reports available in the literature showing the signatures of (*i*) asymmetry in hysteresis loops, (*ii*) two-peak behavior in the temperature dependence of magnetization, and (*iii*) random-anisotropy in both Co_2SnO_4 and Co_2TiO_4. However, a detailed work involving the low-temperature Raman active modes, Arrott plots (H/M versus M^2) analysis, dynamic-scaling studies (e.g. Vogel-Fulcher law and Power-law of critical slowing down), and magnetic field dependence of specific heat was missing in the literature. Such issues are addressed in this thesis. We have also made attempts to understand the high-temperature ac-electrical resistivity, vibrational excitations using Raman spectroscopy and other characteristics of both Co_2SnO_4, Co_2TiO_4 and the two-phase composites of Co_3O_4 and Co_2TiO_4.

Field induced magneto-structural quantum phases reported in tetragonally distorted ferrimagnetic normal-spinel Hausmannite (Mn_3O_4= (Mn^{2+}) $[Mn^{3+}]_2O_4$) is another topic motivated us to reinvestigate [84 - 90]. In 2010, Kim *et al.* reported the complex magnetic structure of Mn_3O_4 below T_N (= 43 K) using the temperature and magnetic field dependent X-ray diffraction and vibrational spectra of single-crystal Mn_3O_4 [91]. These authors observed a significant shift in the Raman active T_{2g} mode frequency between 33 K and 39 K, where, the system exhibits incommensurate magnetic phase regime. Below 33 K, the T_{2g} mode abruptly splits into two modes near 290 cm^{-1} and 300 cm^{-1}. Such splitting was consistent with the tetragonal to monoclinic structural phase transitions taking place below 33 K, which lift the degeneracy of T_{2g} mode by expanding the Mn^{2+}-O^{2-} bond length along the easy axis direction and contracting the Mn^{2+}-O^{2-} bond length along the hard axis direction (such stretching is linked with the giant atomic displacement of ~ 0.25 Å without breaking inversion symmetry and colossal magnetic anisotropy below T_N). Nonetheless, the magnetization dynamics below the long-range ordering at varying ac-

magnetic field frequencies was lacking in the literature. Hence, an attempt has been made to understand the ac-magnetic response of all the phase transitions occurring below T_N under the superimposition of various dc-bias fields. We also studied the magnetic-field dependence of dielectric permittivity $\{\varepsilon_r(H,T)\}$ under both cooling and heating cycles with special emphasis to probe the newly observed lock-in transition at 38 K below the Yafet-Kittle type and spiral incommensurate transitions.

Chapter 2

Experimental Techniques

2.1 Synthesis of the Oxide Spinels:

This chapter describes the synthesis procedure of the investigated compounds and the characterization techniques implemented for studying the structural, magnetic, morphological and optical properties. All the high quality precursors were procured from Alfa Aesar GmbH and Sigma-Aldrich Chemicals. Several methods are available to synthesize polycrystalline samples in bulk grain forms, such as, solid-state-reaction, sol-gel processing, co-precipitation method, vapor phase transport etc. In this thesis, we employed both solid-state-reaction technique and sol-gel process for the preparation of Co_2SnO_4, Co_2TiO_4 and Mn_3O_4 polycrystals.

2.1.1 Solid State Reaction:

Solid-state-reaction method is the most versatile technique, thermodynamically stable and environment friendly process for the synthesis of polycrystalline bulk cobalt and manganese oxides. The main advantage of the solid state reaction method is that it provides a wide range of selection of precursors like oxides, carbonates etc. As the starting materials do not react with each other at room temperature, prominent temperature with proper heating and cooling rates are needed for the appropriate reaction. Thus, the thermodynamic as well as the kinetic factors are important for the solid state reaction method in which raw materials react in the absence of any solvent at very high temperature. Therefore, after the heat-treatment process the final product obtained from this method is in form of solid with big grain sizes. Figure 2.1 shows the flowchart of the synthesis procedure. High purity binary transition metal oxides of fine grain size were taken in stoichiometric amounts and grind them together in an agate mortar using a pestle for 4 h so that the mixed powders attain a high degree of homogeneity and better contact is achieved between surfaces of the reactants. This product was calcined in air for 4 h between 500-600°C to remove the volatile substances present in the mixture. This mixture was regrind for 1 h and pelletized using a 13 mm KBr die and hydraulic press (5 tons/cm^2) to form compact cylindrical pellets. These pellets are sintered at high temperature 1200°C-1350°C for 8 - 12 h in air with cooling and heating rates 4°C/minute to form dense ceramic compound of desired composition. The final sintering temperature and pre-sintering conditions are varied depending on the nature of the sample for required properties. For the preparation of polycrystalline Co_2SnO_4, Co_2TiO_4 and the Co_3O_4 - Co_2TiO_4 two-phase composites we followed the above mentioned procedure. However, Mn_3O_4 was synthesized using the sol-gel process described below.

2.1.2 Sol-gel Method:

Sol-gel process involves conversion of monomers into a colloidal solution (commonly known as sol) that acts as the precursor for an integrated network (or gel) of either discrete particles or polymer networks. In this method wide variety of precursors can be selected as starting materials to prepare magnetic and non-magnetic ceramic

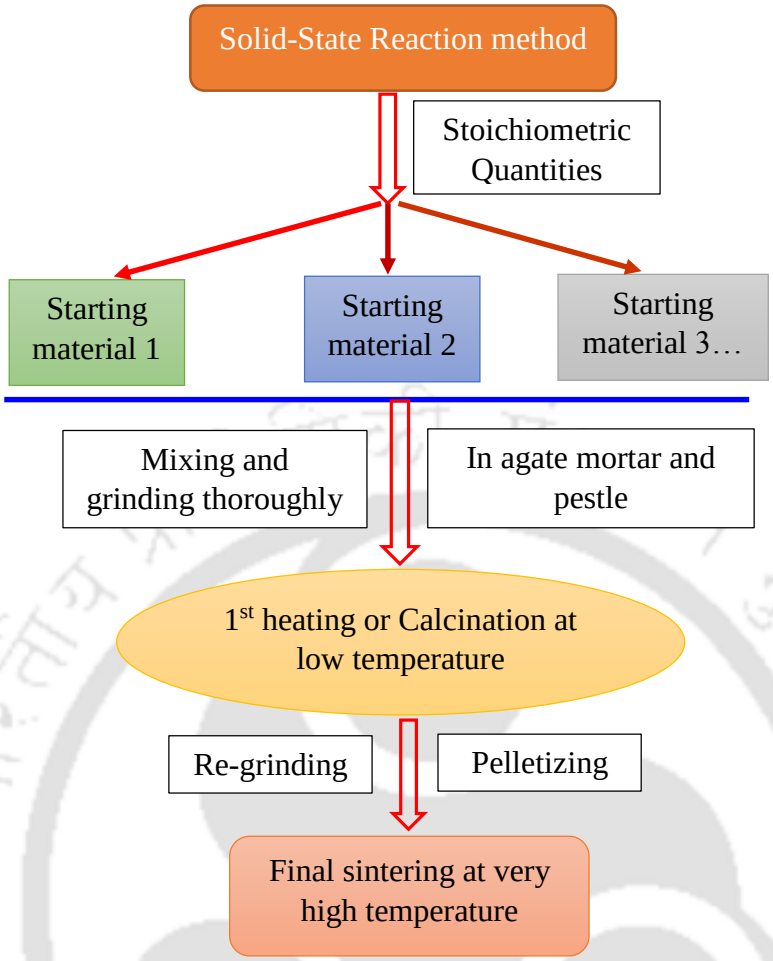

Figure 2.1: Schematic diagram of standard solid state reaction method employed in the present work.

oxides. Sol-gel process has many advantages like simple, cost effective, requires low temperature for processing, allows high degree of solubility, provides homogenous dispersion of dopants, and controls the composition accurately [92]. The precise size control of the particle is the main strength of the sol-gel process. Due to this oxides nanoparticles obtained from alkoxide are preferred to prepare by sol-gel technique. It also provides better control of the microstructure and density.

Figure 2.2 depicts various steps of sol-gel method involves in the synthesis of crystalline oxides. Initially, the starting materials were dissolved in the solvent (distilled water, ethanol or acid) and then mixed together thoroughly. The resultant mixture was kept under stirring for 1-2 h at 50°C to ensure the homogeneity of the solution. Proper amount of citric acid or oxalic acid solution added to the mixture. Here citric acid/oxalic acid act as a gilating agent and carboxylate group in it act as ligands to form linked-complex network with the cations. The obtained gel kept at 80-100°C in a hot air oven for several hours till the water/ethanol/acids evaporate. The oven dried product obtained after this process is called metal xerogel. This xerogel was calcined at temperatures between 500-800°C to remove the volatile substances such as crystallizing water, CO and CO_2 to form the final

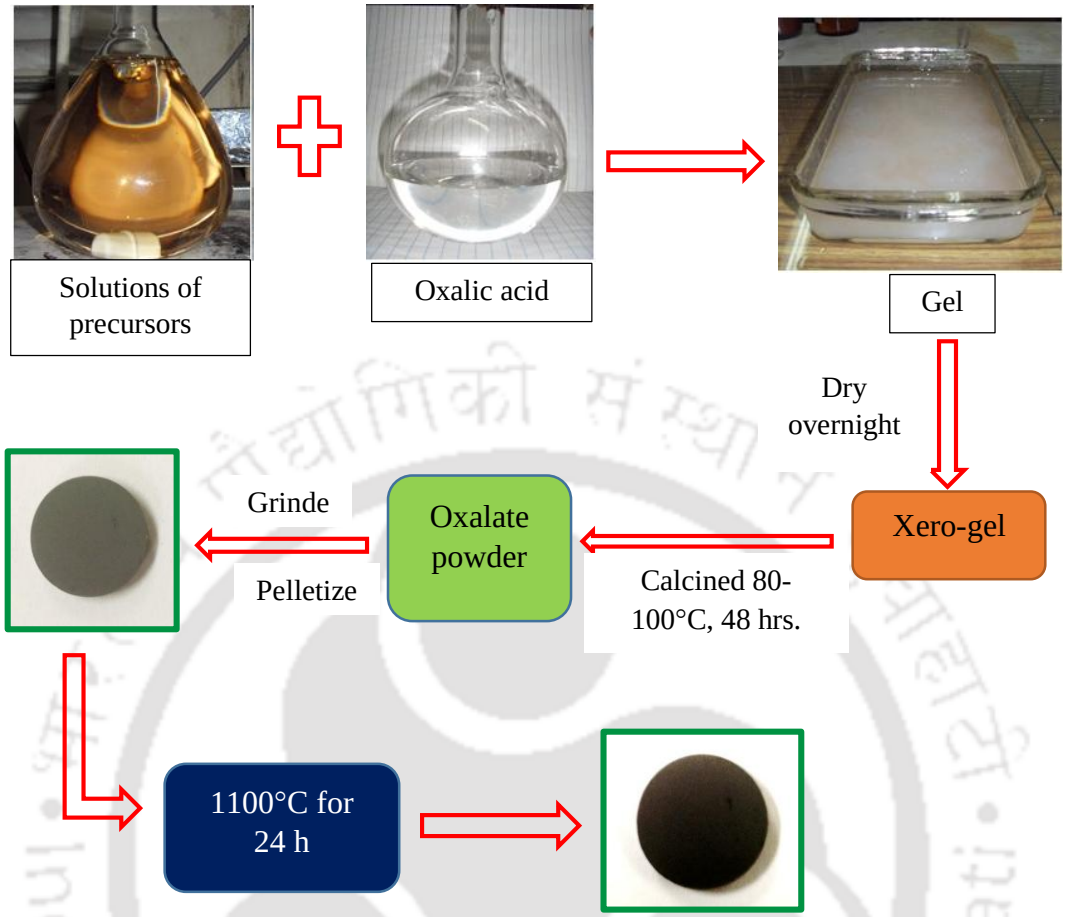

Figure 2.2: Various stages of the sol-gel method used to synthesize single phase ceramics.

product. In the present case polycrystalline Mn_3O_4 sample was synthesized by sol-gel process using manganese acetate tetrahydrate [$Mn(CH_3COO)_2.4H_2O$] and oxalic acid [$C_2H_2O_4.2H_2O$] as precursors and ethanol as solvent. Initially, manganese acetate tetrahydrate was dissolved in ethanol under constant stirring and moderate heating to obtain transparent wine color solution (called sol) [93]. The oxalic acid solution was added drop-wise to the transparent sol yielding a thick wet-gel network called aerogel. This aerogel was then dried in a hot air oven at 80-100°C for 48 h to obtain the manganese oxalate dihydrate [$MnC_2O_4.2H_2O$], which further heated at 500°C for 2 h in air to obtain mainly Mn_2O_3 as major product which was further heat treated at 1100°C for 4 h [93]. This product was ground in an agate mortar, then pressed into pellets and finally sintered at 1200°C for 48 h and quenched from 1200°C to liquid nitrogen temperature. Such quenching is necessary to avoid the formation of other stable manganese oxides e.g. MnO_2, Mn_2O_3, and Mn_5O_8.

2.2 Characterization Techniques:

2.2.1 Structural Characterization:

We employed X-ray diffraction technique to determine the crystal structure of the synthesized spinel oxides because this technique is a powerful and non-destructive structural characterization tool. In the present work we used two different X-ray sources; the first one is Co-K_α radiation of wavelength λ = 1.7889 Å and the second source is Cu- K_α radiation with λ = 1.5406 Å from PHILIPS (Model: PW-1050) X-ray powder diffractometer and from Rigaku (Model: TTRAX-III) X-ray diffractometer in θ - 2θ geometry. These diffractometers consist of scintillation detectors on the circumference of the vertical circle. Few micron thick Ni foil is placed in the form of the source window to filter out the K_β lines from K_α radiation. The sample stage is fixed and positioned at the center of the circle while the goniometer assembly provides uniform rotation of both the source and detector. We also used the software called FullProf programme to perform the Rietveld refinement of the experimentally extracted X-ray diffraction pattern.

2.2.2 Surface Morphology and Microstructure:

To probe the surface morphology and microstructure of the samples investigated in the present work we employed a scanning electron microscope (SEM, M/s LEO, 1430vp) and a field-emission-scanning electron microscope (FESEM, from m/s Zeiss, Sigma). Both these electron microscopes were used under secondary-electron (SE) mode to probe the microstructure of the bulk samples studied in this work. SEM is also equipped with energy dispersive X-ray spectrometer (EDS/EDAX) which is used to trace the elements present in the samples.

2.2.3 X-ray Photoelectron Spectroscopy:

In this thesis, we extensively used the X-ray photoelectron spectroscopy (XPS) for the determination of the electronic structure of the samples. It is well known that the XPS is a surface-sensitive quantitative spectroscopic technique involving photon and electrons that mainly use for the quantification of the elemental composition. XPS spectra are obtained by exposing a material from the top-surface to few nanometers depth (typically from 0 to 10 nm) with a beam of X-rays while simultaneously measuring the kinetic energy and number of electrons (similar to Photoelectric effect). It requires high vacuum ($P \sim 10^{-8}$ millibar) or ultra-high vacuum (UHV; $P < 10^{-9}$ millibar) to analyze the samples at pressures of a few tens of millibar. XPS mainly involves the interaction of X-ray photons with electrons in the energy range 1-5 keV (for soft X-rays), and 5 - 8 keV (for hard X-rays) and is widely used to study the chemical composition and/or speciation of the outer 1-2 nm of solid surface. XPS is also a sensitive probe of the chemical environment and/or oxidation state of surface species. Core level XPS is highly sensitive to the chemical environment (the binding energy may be strongly dependent on the oxidation state of the investigated ion, as well as on the neighboring atoms). Photoelectric effect can be understood by means of the following three

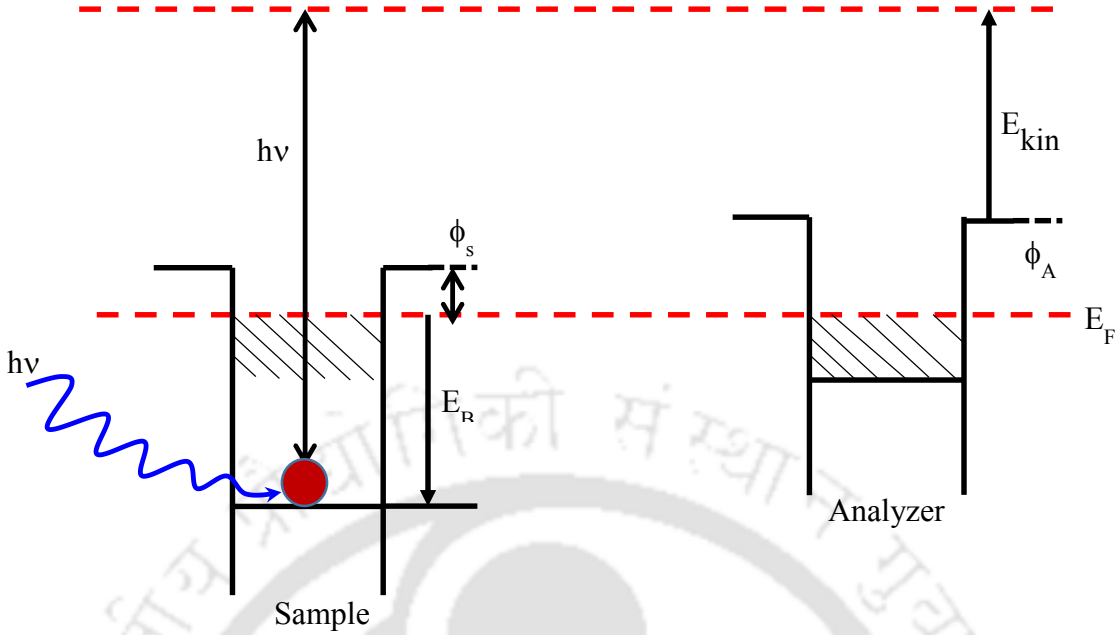

Figure 2.3: Schematic diagram of Photoemission process.

steps: (*a*) Probability of creation of photoelectron by photo-excitation of the solid, (*b*) Transport of photoelectron to sample surface, and (*c*) Emission of photoemission into vacuum and then to the energy analyzer. Photoelectrons generated by the incident photon energy *hv* are transported to the continuum where they are detected by electron energy analyzer. This is possible only if the incident photon energy is greater than or equal to the sum of binding energy (E_B or BE) of the electron with respect to energy of Fermi level (E_F), and the work function (Φ_s) of the sample. So that, one can write

$$h\nu = E_B + \Phi_s + E_{kin} \ldots (2.1)$$

Where E_{kin} in the kinetic energy of the photoelectron. Since the electron has to overcome work function in order to be detected by the analyzer. Thus, the modified equation becomes

$$h\nu = E_B + \Phi_s + (\Phi_A - \Phi_s) + E_{kin} \ldots (2.2)$$

From the above equation we can obtained the binding energy of the emitted electron

$$BE = E_B = h\nu - \Phi_A - E_{kin} \ldots (2.3)$$

The intensity of XPS spectra is recorded as a function of binding energy and it has contributed from a background signal. The resonance peaks above the background are the characteristic of the bound states of the electrons in the surface atoms. Since Φ_s cancels in the equation (2.2), the photoelectron energy is known and the Φ_A is constant, the E_{kin} determines the E_B and vice versa. For calculating Φ_A the energy scale is set to zero at the Fermi edge of the reference samples like Ag, or Ni or Au [94, 95]. This calibration results in Φ_A equal to zero, and relate E_B and E_{kin} directly by the equation: $E_{kin} = h\nu - E_B$. Note that the above analysis is only valid for conducting samples where the energy of the Fermi level of the sample and analyzer is almost equal as depicted in

figure 2.3. In the case of insulators, the Fermi-level is not well defined due to charging effect and consequently a shift in the binding energy observed. In general, the following six features are observed in any XPS spectra [94].

(a) *Sharp peaks*: due to photoelectrons created within the first few atomic layers (elastically scattered). These peaks constitute the main spectral feature which correspond to the particular element of interest.

(b) *Multiplet splitting*: occurs when unfilled shells in atoms contain unpaired electrons.

(c) *Satellites*: (shake-off and shake-up) are due to a sudden change in Coulombic potential as the photo-ejected electron passes through the valence band.

(d) *Plasmons*: which are created by collective excitations of the valence band.

(e) *Auger peaks*: produced by X-rays (transitions from L to K shell).

(f) *Background*: A broad structure due to electrons from deeper in the solid which are ineslastically scattered (reduced KE) forms the background.

In the present thesis, all the spectra were recorded by a dual source X-ray photoelectron spectroscope (Al-K_α @ 1486.8 eV, Mg-K_α @ 1253.6 eV) from VG-Microtech equipped with an ultrahigh vacuum (8×10^{-8} Torr) chamber with pass energy of 100 eV was employed. The data were recorded from 0 to 1100 eV of binding and calibrated against the C-1s peak 284.5 eV.

2.2.4 DC & AC-Magnetization Measurements:

All the temperature (2 - 320 K) and magnetic field (± 7-9 Tesla) dependence of DC and AC magnetization measurements are performed using the superconducting quantum interference device (SQUID) based magnetometer from Quantum design. In particular, Magneto property Measurement system (MPMS) (7XL SQUID) was used [96]. The device may be configured as a magnetometer to detect extremely small magnetic fields small enough to measure the magnetic fields in living organisms using the Josephson junctions. The basic phenomena governing the operation of SQUID devices are flux quantization in superconducting loops and the Josephson- effect [97]. In 1962, B. D. Josephson showed that the electrical current density through a weak electric contact between two superconductors depends on the phase difference $\Delta\varphi$ of the two superconducting wave functions [98, 99]. Moreover, the voltage across the weak contact is interrelated with the time derivative of $\Delta\varphi$. In a typical superconducting ring with one (known as RF-SQUID) or two (DC-SQUID figure 2.4) weak contacts, $\Delta\varphi$ is additionally influenced by the magnetic flux Φ through this ring. Hence, such a structure can be used to convert magnetic flux into an electrical voltage which is the basic working principle of a SQUID magnetometer. When a sample moves up and down it produces an alternating magnetic flux in the pick-up coils. These coils together with a SQUID antenna transferring the magnetic flux from the sample to an RF-SQUID with high degree of accuracy of measuring the magnetic moment ~ 10^{-8} emu. The RF-SQUID act as a magnetic-flux to voltage converter. The variation in the voltage is proportional to the change in magnetic flux of the sample. The voltage is then magnified and read out by the magnetometer's electronics (figure 2.4). The principal components of this measurement system comprise the following aspects:

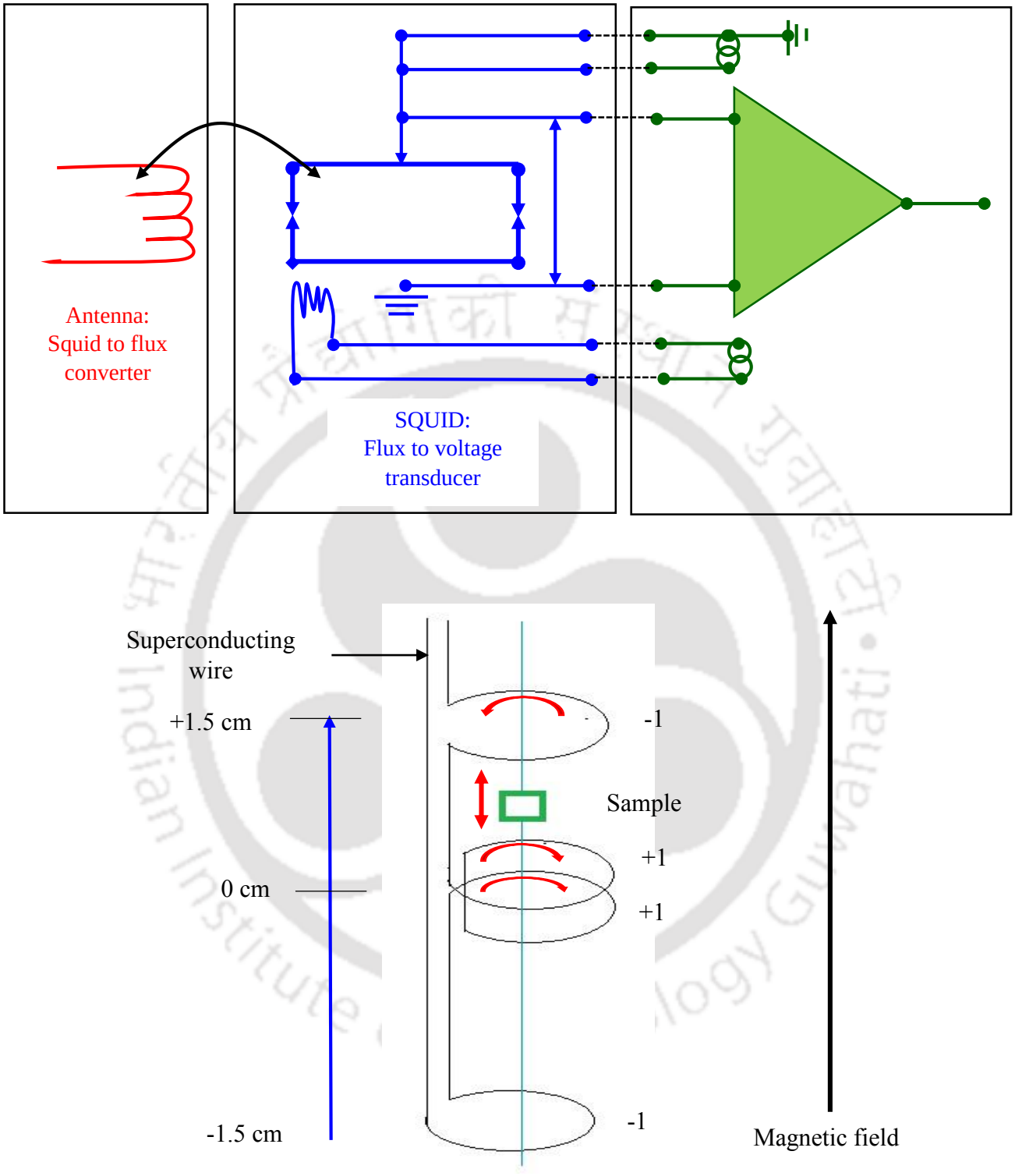

Figure 2.4: (a) Schematic diagram of the superconducting quantum interference device (SQUID) flux to voltage converter and (b) pick-up coil.

(i) Temperature control system: Precision control of the temperature in the range 2 K to 400 K.

(ii) Magnet control system: Current from a power supply is set to provide magnetic fields from zero to ±7 Tesla.

(iii) Superconducting SQUID amplifier system: The RF-SQUID detector is the heart of the magnetic moment detection system. It provides reset circuitry, auto-ranging capability, a highly balanced second-derivative sample coil array.

(iv) Sample handling system: The ability to step and rotate the sample through the detection coils without transmitting undue mechanical vibration to the SQUID is of primary importance.

(v) Computer operating system: All operating features of the MPMS are automated, computer control. The user interface at the PC console provides the option of working under standard sequence control, or diagnostic control which will invoke individual functions.

2.2.5 Physical Property Measurement System (PPMS):

The temperature and magnetic field dependence of specific-heat ($C_P(T,H)$) of the bulk samples Co_2SnO_4 and Co_2TiO_4 were performed by means of a physical property measurement system (PPMS) from Quantum Design (Model 6000 PPMS). Furthermore, temperature dependence of pyroelectric current measurements and the high-filed (±14 Tesla) magneto-dielectric measurements of Mn_3O_4 system are also performed by the PPMS. Heat capacity is a very useful quantity and play a major role in many fields of physics and chemistry. From the heat capacity measurement of solid sample, one can get substantial information about the lattice properties, phase transitions, electronic, and even magnetic properties of the materials. Generally, the heat capacity measurements of any compound can be performed well below the Debye temperature, because it directly probes the electronic and magnetic energy levels of that material and hence allow comparison between theory and experiment. A very small piece of sample (usually ≤ 10 mg) is mounted on this platform for precise and fast measurements using a standard cryogenic grease or adhesive such as Apiezon N or H Grease (addenda). The heat capacity of the sample is determined by subtracting the addenda from the total heat capacity. Typically, heat capacity measurement involves some separate stages: first, the sample platform and puck (PPMS 12 pin format electronic connection) temperatures are stabilized at some initial temperature, after this the sample platform is elevated to a certain temperature. Next the temperature of the sample platform relaxes towards the puck temperature. The sample platform temperature is monitored during both heating and cooling cycles, providing the raw data of the heat capacity calculation. The sophisticated two-tau model is used to analyze the heat capacity of the sample [100, 101]. The two-tau model simulates the effect of heat flowing between the sample platform and sample, and also between the sample platform and puck. By optimizing the agreement between the experimental data and the two-tau model the heat capacity values along with other physical parameters are determined. In the two-tau model, the first time constant (τ_1) represents the relaxation time between the sample platform and the puck, and the second time constant (τ_2) represents the relaxation time between the sample platform and the sample itself. On the other

hand, magneto-dielectric measurements were performed using the impedance and gain phase analyzer from Agilent technologies (Model No- 4284 A) which was assembled with the low-temperature accessory of the PPMS.

2.2.6 AC-resistivity and Dielectric Permittivity Measurements:

High frequency ($100\ \text{Hz} \leq f \leq 20\ \text{MHz}$) ac-electrical resistivity and dielectric permittivity studies of Co_2SnO_4 and Co_2TiO_4 were performed between the temperatures 120 K and 570 K using the impedance and gain-phase analyzer from Novocontrol Alpha AN impedance analyzer with Quatro cryosystem. A pour-fill liquid nitrogen cryostat was assembled with the impedance analyzer to achieve the low-temperatures (-160°C), where as a home-made heater was designed to realize high temperatures. Sample holder from Novocontrol BDS 1200 based passive parallel plate ZG4 4-wire was used. The dielectric properties of the insulating spinels Co_2SnO_4 and Co_2TiO_4 are unknown in the literature until now, this aspect motivated us to study the ac-conductivity and dielectric behavior of these samples. Magnetic ceramic materials are of usual interest for practical applications such as thermistors, memristor and magneto-dielectric devices [102, 103].

2.2.7 Vibrational Excitations and Raman spectroscopy:

Raman spectroscopy probes molecular vibration of the sample and is a versatile technique for analysis of a wide range of samples. Qualitative analysis can be performed by measuring the frequency and intensity of scattered radiations [104, 105]. Raman spectroscopy is sensitive to the crystal structure, bonding, and chemical composition of the material and does not require any sample preparation [106]. In Raman spectroscopy, the monochromatic laser beam falls and interact with the molecule of the sample and scattered light is generated. Due to the inelastic scattering of monochromatic incident light with the atoms/molecules of the compound a shift in the frequency of output spectrum (scattered light) can be observed, based on such difference in the frequency Raman spectra can be classified either Stokes or Anti-stokes (figure 2.5). In case of Stokes*:* the frequency of incident radiation is higher than the frequency of the scattered radiation. If the frequency of incident radiation is lower than the frequency of the scattered radiation then such spectrum is known as Anti-stokes. However, if the scattered radiation frequency is equal to the frequency of incident radiation then such scattering is known as Rayleigh scattering (shown in figure 2.5). Stokes lines are more intense than anti-stokes lines. Hence stokes are used to measure the conventional Raman spectroscopy while anti-stokes bands are measured with fluorescing samples because fluorescence causes interference with Stokes bands. The magnitude of the Raman shift is independent of the wavelength of the incident radiation. Since Raman scattering due to water is low, water is used as an ideal solvent for dissolving liquid samples. Solid samples can directly mount on a glass substrate and perform the measurements by mean of the optical components (mirror, lens, sample cell) in Raman spectrophotometer [104, 105, 107]. In the present thesis, two different Raman spectrophotometers are used. The room temperature measurements are performed using LABRAM HR800 Raman spectrometric analyzer with an excitation wavelength of 488 nm of an Ar-ion laser. For low temperature Raman measurements (down to 25 K) a different

Raman spectrophotometer (Jobin Yvon T64000) with wavelength 514 nm was used. This instrument is equipped with a dedicated heating/cooling sample stage (Linkam, THMS600). All the spectra were recorded in a backscattered geometry furnished with a 50× objective, an appropriate edge filter, and a Peltier-cooled charge-coupled device detector. An Ar^+ ion excitation laser source in a high-resolution dispersive geometry was used for these low-temperature micro-Raman measurements with λ = 514 nm and an 1800 mm^{-1} grating. The spectral resolution of the system is 1 cm^{-1}. For high degree of positional accuracy, the grating was fixed during the entire temperature scan.

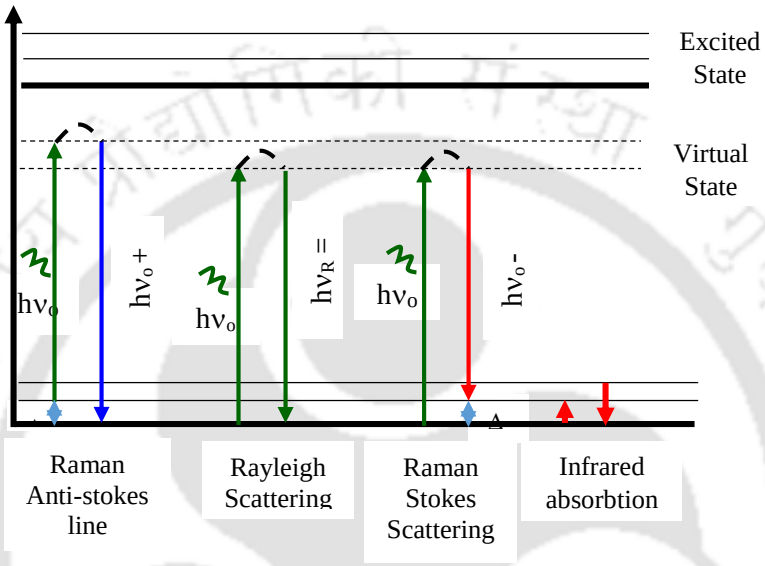

Figure 2.5: Energy level diagram of the Rayleigh and Raman Scattering.

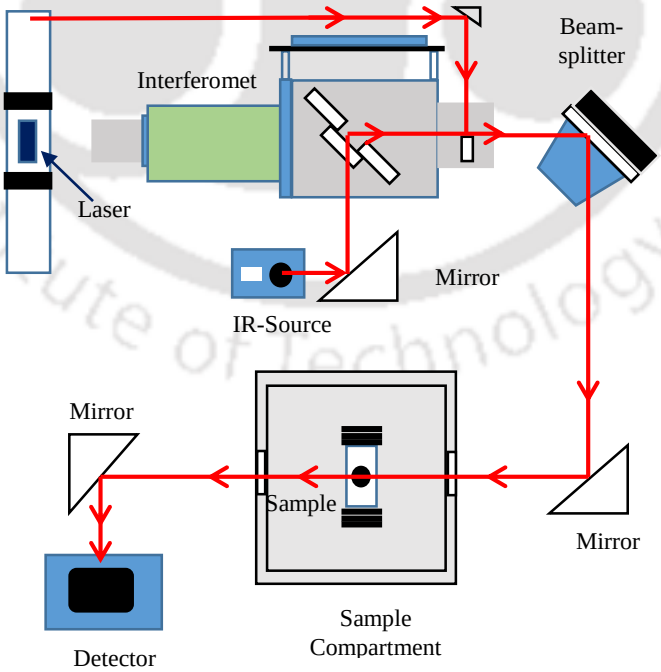

Figure 2.6: Schematic diagram of the Fourier transform infrared spectrometer.

2.2.8 Fourier Transform Infrared Spectroscopy:

In past few years Fourier transform infrared spectroscopy (FTIR) is used as an important technique for material analysis. The term Fourier-transform infrared spectroscopy originates from the fact that a Fourier transform (a mathematical process) is required to convert the raw data into the actual spectrum. Basically, FTIR is the study of interaction of infrared radiation with matter as a function of photon frequency. It provides many valuable scientific information about the vibration and rotation of the chemical bonds and molecular structures, which are useful for analyzing and also identifying the materials. An infrared spectrum represents a finger-print of a compound with absorption peaks of certain vibrational frequencies of chemical bonds. In addition, the size of the peaks in the spectrum is a direct measure of the quantity of the material. With the invention of modern software algorithms, this infrared characterization technique becomes an excellent tool for quantitative analysis of the chemicals. Infrared spectroscopy generally measured in the wavenumber range 4000-400 cm^{-1}. When a material is exposed to the infrared radiation, atoms/molecules absorbed the radiation at frequencies equivalent to their vibrational modes. The corresponding radiation absorbed by the atoms is recorded as a function of frequency of the electromagnetic radiation which further analyze to identify the functional group and/or stretching of the chemical bonds of the investigated compounds. Figure 2.6 represents the schematic diagram of a FTIR spectrometer. The basic ingredients of the instruments are:

(a) *Source:* Infrared energy is emitted from a glowing black-body source. The beam allowed to pass through an aperture to control the amounted of energy falling on the sample.

(b) *Interferometer:* After passing through the aperture the beam enters into the interferometer. The interferometer guides the beam via a beam-splitter and mirror to incident exactly on the sample.

(c) *Sample:* A small amount of sample was first diluted with 150 mg of vacuum-dried IR-grade potassium bromide (KBr) powder and subjected to a pressure of 39.2 bar. After that the sample placed in the sample-holder and it is exposed by the incident beam. In this process, specific frequencies of energy are absorbed which are characteristic of the sample.

(d) *Detector:* The beams scattered from the sample finally passes to the detector for final measurement. These detectors are specially designed to measure the special interferogram signal.

(e) *Computer:* The measured signal is digitized and sent to the computer where the Fourier transformation takes place. The final infrared spectrum is then presented to the user for further interpretation.

In the present thesis work, FTIR spectra of all the compounds were recorded using a Perkin-Elmer 180 Spectrometer in the wavenumber range 4000 cm^{-1} (far-IR) - 400 cm^{-1} (IR) with the spectral resolution of ± 2 cm^{-1}.

Chapter 3

Nature of Magnetic Ordering in Co_2SnO_4

3.1 Introduction:

This chapter deals with the synthesis and characterization of the Cobalt-Orthostannate, (Co_2SnO_4) polycrystalline system with special emphasis on the role of magnetic dilution on the long-range ordering. Co_2SnO_4 possess inverted cubic spinel crystal structure ($[Co^{2+}]_A[Co^{2+}Sn^{4+}]_BO_4$) with two divalent cobalt ions [$Co^{2+}(3d^7)$] occupied in two-different sublattice (tetrahedral A and octahedral B sites) [81, 108, 109]. Earlier studies reveal that Co_2SnO_4 exhibits ferrimagnetic properties due to the unequal magnetic moments of Co^{2+} ions in A- and B-sublattices [$\uparrow M_A \neq M_B\downarrow$] [57]. In 1976, Hermon *et al.* first reported that, Co_2SnO_4 undergoes a long-range ferrimagnetic to paramagnetic transitions at Néel temperature $T_N \sim 44 \pm 2$ K [81]. These authors also reported that in the limit $T \rightarrow 0$ K, the nearest neighbor molecular field constant N_{AB} is antiferromagnetic, whereas, the next-nearest neighbor molecular field constant N_{AA} and N_{BB} is ferrimagnetic in nature [81]. On the other hand, later studies by Strooper *et al*. reported that all the three exchange constant are antiferromagnetic in nature with different magnitude of magnetic moments of Co^{2+} in the A and B-sublattices [82]. In single crystal Co_2SnO_4, Sagerdo *et al*. observed a strong irreversibility below T_N in both zero-field cooled (ZFC) and field-cooled (FC) magnetization curves [83]. The non-magnetic Sn^{4+} ions essentially randomize the cationic distribution in the B-site which may break the octahedral crystal field symmetry. As a result, the system possesses frustrated magnetic behavior along with short range spin-glass ordering and magnetic training effect [83]. Srivastava *et al.* observed two peak behavior in the ac- susceptibility measurements (χ_{ac} versus T) of Co_2SnO_4 polycrystals [108]. It was believed that the second peak in χ_{ac} versus T curve indicated a separate freezing of spins located at A and B-sites [108]. As discussed earlier in the introduction chapter, such kind of peak-splitting in χ_{ac}-T is associated with the semi-spin-glass behavior predicted by Villian [40]. Such interesting behavior along with enthralling physics, originated from the different magnetic moments at A and B sites ($\mu_A \neq \mu_B$) motivated us to work on this compound. Not only from the fundamental physics perspective, but from the applications point-of-view Co_2SnO_4 has attracted immense attention recently due to its excellent catalytical properties and its positive temperature coefficient of resistance which make it a useful material for thermistor devices [81, 108, 109]. Therefore, we extensively investigated its physical properties like crystal structure, magnetic, electrical, specific heat which gives insights into its local atomic environment. Such properties are discussed extensively in this chapter along with a detailed synthesis procedure.

3.2 Experimental Details:

The polycrystalline bulk-grain size Co_2SnO_4 was prepared by standard solid-state reaction method using stoichiometric amounts of Co_3O_4 (Alfa Aesar, purity 99.99%) and SnO_2 (Alfa Aesar, purity 99.99%) as the starting

materials. Appropriate amount of these two oxides was grounded in an agate mortar for 4 h with the help of a pestle. This mixed powder was first calcined at 800°C for 24 h in air and then pressed into 13 mm pellets using a hydraulic press with maximum load of 5 tons per cm^2. These pellets were then heat-treated at high temperatures (1200°C) for long time duration 48 h in air (sintering) with precise heating and cooling rate (3°C/min). Inter-diffusion of the chemical species occurs at these higher temperatures which creates an environment for grain growth and finally leads to the formation of strong solid material. This sample sintered at 1200°C is given a code: S1200. A second method was also implemented to prepare the Co_2SnO_4 by ball-milling method. In this case the precursors Co_3O_4 and SnO_2 were first ball-milled using Retsch (PM-100 from FRITSCH GmbH) at 100 revolutions per minute for 2 h using zirconia jar and balls with ethanol as the milling media. After drying the resulting powder at 120°C for 24 h in air, this sample, was hydraulically pressed at pressure of 110 MPa in a stainless-steel die to form of cylindrical pellet of size 13 mm followed by sintering at 1350°C for 8 h in air using slower heating and cooling rates. This sample was named as S1350.

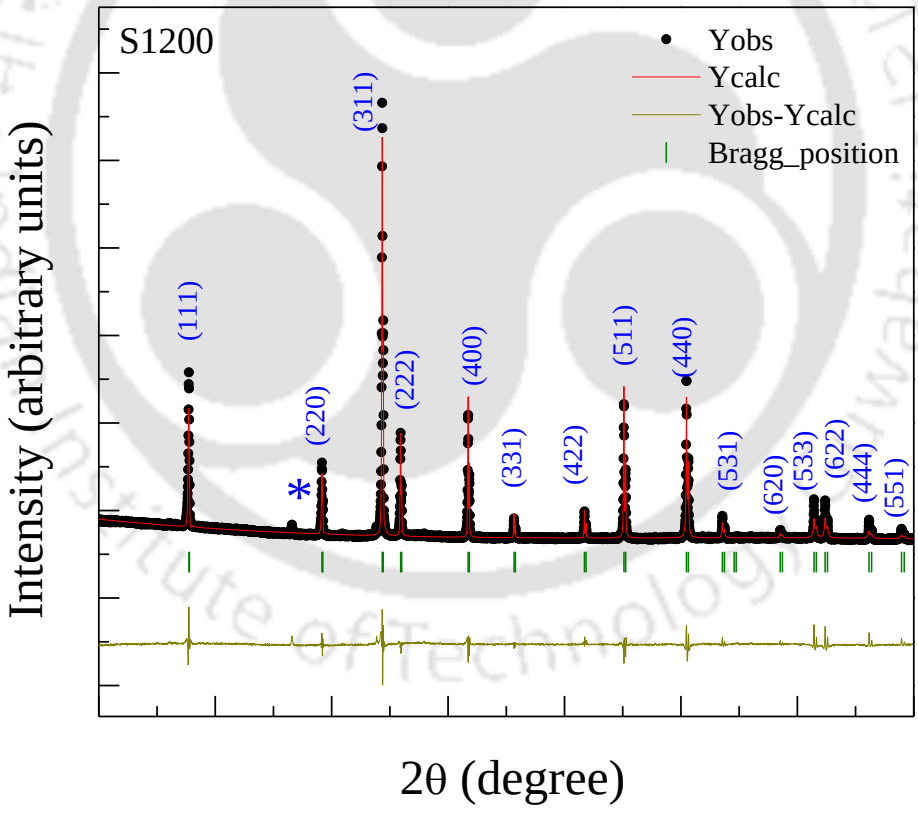

Figure 3.1: The X-ray diffraction pattern (dotted symbols) together with the Rietveld refined data (red line) of Co_2SnO_4 bulk samples sintered at 1200°C (S1200) in air. The asterisk mark shows the position of the SnO_2 secondary peak. Vertical lines represent the Bragg positions and the bottom line represents the difference between the intensities of the observed (Yobs) and calculated (Ycalc) pattern.

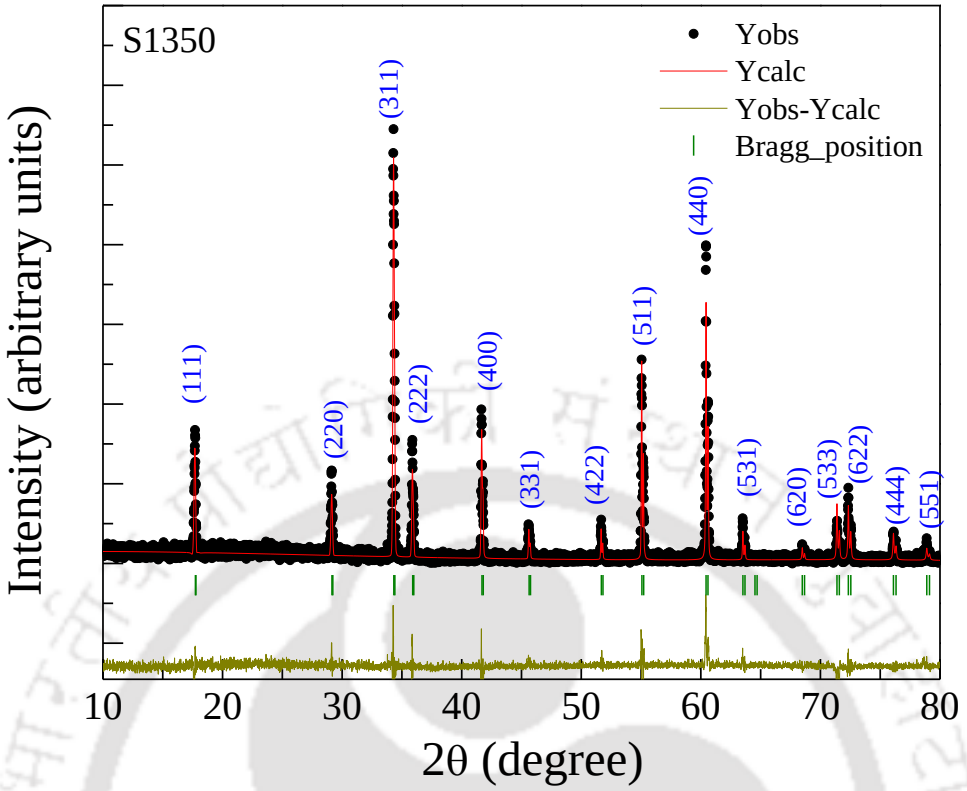

Figure 3.2: The X-ray diffraction pattern (scattered circular symbols) together with the Rietveld refined data (red line) of Co_2SnO_4 bulk samples sintered at 1350°C (S1350) in air. Vertical lines represent the Bragg positions and the bottom line represents the difference between the intensities of the observed (Yobs) and calculated (Ycalc) pattern.

3.3 Results and Discussion:

3.3.1 Structural Characterization:

The X-ray diffractogram recorded at room temperature using Cu-K_α (λ = 1.5406 Å) along with the Rietveld refinement data (performed by FullProf program) of both S1200 and S1350 samples are shown in figures 3.1 and 3.2. The Miller-Indices of planes of these patterns belongs to the cubic spinel family with and space group *Fd-3m* (227) and lattice parameter a = 8.637(3) Å for S1200. The asterisk mark shown in the figure 3.1 is corresponding to the peak due to unreacted non-magnetic SnO_2. The weight % of this secondary phase present in the major phase of Co_2SnO_4 was quantified using the following expression [110].

$$W_{SnO_2} = \left[\frac{1}{\left\{1 + 1.265\left(\frac{I_{Co_2SnO_4}}{I_{SnO_2}}\right)\right\}}\right] \times 100 \quad \ldots (3.1)$$

where W_{SnO2} indicates the weight fraction of the SnO_2 phase, and I_{SnO2} and $I_{Co2SnO4}$ represents the strongest X-ray diffraction line intensities of the SnO_2 and Co_2SnO_4, respectively. The intensity ratio $I_{Co2SnO4}/I_{SnO2}$ is independent of variations in diffractometer. In the present case, intensities of (311) peak for Co_2SnO_4 phase and (110) peak for

Table 3.1: The list of lattice parameters (a = b = c), bond lengths and bond angles of S1200 and S1350 samples. (The interaxial angles $\alpha = \beta = \gamma = 90°$).

System (Co_2SnO_4)	Lattice Parameter	Bond Length		Bond Angle	
		A-O	B-O	A-O-B	B-O-B
S1200	8.45±0.01 Å	1.92 ± 0.011 Å	2.09 ± 0.017 Å	123.68º ± 0.62°	91.95º ± 0.48°
S1350	8.66±0.02 Å	1.88 ± 0.02 Å	2.16 ± 0.021 Å	125.01º ± 0.65°	90.37º ± 0.45°

SnO_2 were the maximum intense peaks. Using the above equation, we found that ~ 1.47 wt% of SnO_2 present in the 98.53% of Co_2SnO_4 matrix.

In order to avoid the formation of SnO_2 phase we sintered the sample at higher temperature ~ 1350°C. The diffraction pattern shown in figure 3.2 is also consistent with the standard cubic spinel phase with space group F*d-3m* (227) without any signature of SnO_2. However, the lattice parameter obtained for S1350 is a = 8.657(3) Å which is slightly higher than that of S1200. Such variation in the lattice parameter is generally associated with the variation in the bond lengths and angles caused by the higher sintering temperature. Table-3.1 clearly summarizes the bond lengths and bond angles of both S1200 and S1350 obtained from the refinement process. It is evident that the average bond length (B-O) between the oxygen ion and elements present in the octahedral sites (B-O) of S1350 is higher than that in S1200 while the reverse is true for the tetrahedral sites (A-O). Whereas an opposite trend was observed in the case of bond-angles (A-O-B and B-O-B).

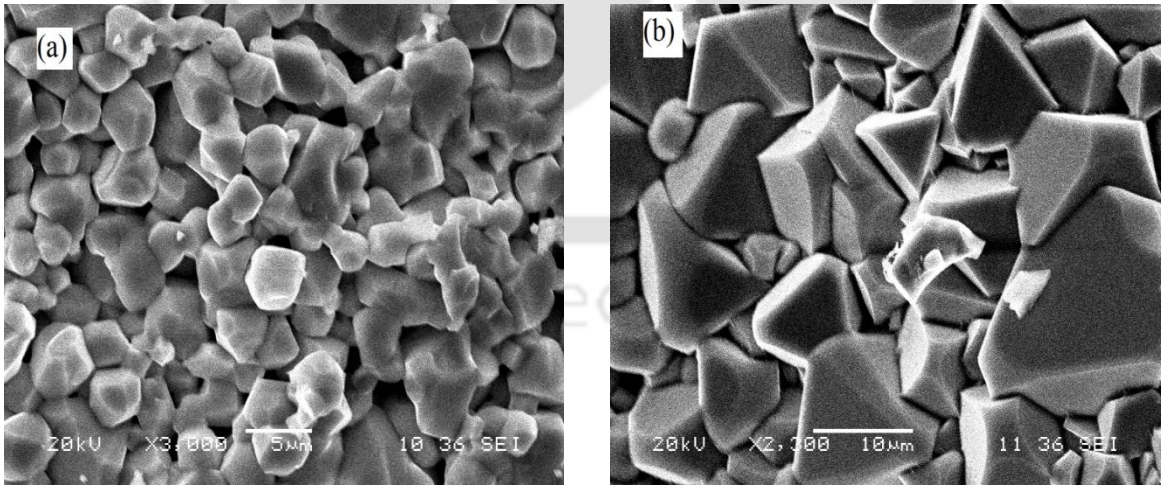

Figure 3.3: Field Emission Scanning Electron (FESEM) Micrograph of Co_2SnO_4 bulk samples sintered at (a) 1200ºC (S1200) and 1350°C (S1350) in air.

3.3.2 Morphology and Microstructure Analysis:

Figure 3.3 shows the micrographs of both S1200 (*a*) and S1350 (*b*) recorded using a field emission scanning electron microscope (FESEM) under secondary electron mode. These FESEM images show the formation of polygonal shape of micro-grains. The average grain sizes for S1200 and S1350 samples are coming out to be ~ 3.73 μm and ~ 6.47 μm, respectively.

3.3.3 X-ray Photoelectron Spectroscopy (XPS):

For a detailed understanding of the electronic state of the elements present in Co_2SnO_4, XPS measurements were performed using Al-K_α X-rays as source. Figure 3.4 shows the photoelectron intensity versus binding energy of the Sn-3*d*, Co-2*p* and O-1*s* spectra. The sharp peaks at 485.65 and 494.8 eV and a weak shoulder at 496.75 eV

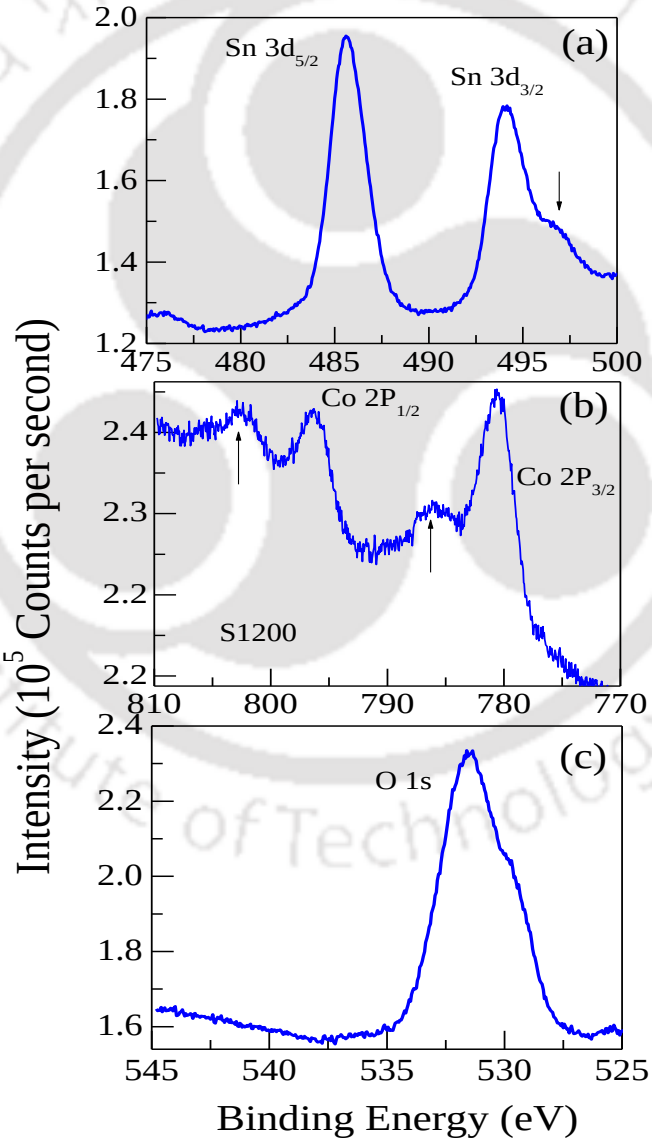

Figure 3.4: The X-ray-photoemission spectra of (a) Sn-3d, (b) Co-2p and (c) O-1s peaks in the S1200 sample.

in figure 3.4(a) are characteristics of the Sn^{4+} state [111, 112]. The XPS spectra of 'Co' shows two major peaks centered at 780.6 and 796.3 eV with satellite peaks at 786.15 and 802.4 eV. It is known that both divalent and trivalent cobalt cations (Co^{2+} and Co^{3+}) exhibit similar binding energy peaks in XPS with the peak near 780 eV identified with the $2p_{3/2}$ level and peak near 796 eV identified with the $2p_{1/2}$ level. However, the energy splitting ΔE of the two levels due to spin–orbit coupling is different for the Co^{2+} and Co^{3+} configurations with ΔE = 15.0 eV for Co^{3+} and ΔE = 15.7 eV for Co^{2+} [112 - 114]. From the data in figure 3.4(b), we get ΔE = 15.7 eV, characteristic of Co^{2+}. In addition, the two weaker satellite peaks observed here are usually absent in systems with a Co^{3+} electronic state. Therefore, the above XPS studies confirmed the presence of Co^{2+} and Sn^{4+} states in Co_2SnO_4. Finally, figure 3.4(c) shows an intense peak at 531.5 eV due to bonded lattice oxygen with the weak shoulder at 529.35 eV due to the surface oxygen [112 - 116].

3.3.4 Magnetization Studies:

(a) Temperature Dependence DC-Magnetization and AC-Susceptibility:

Figure 3.5 depicted the temperature dependence of the magnetization M(T) of both S1200 and S1350 sample measured under zero-field cooled (ZFC) and field-cooled (FC) conditions at an external magnetic field H_{dc} of 100 Oe for T < 80 K. In ZFC mode, first the sample was cooled to 2 K in absence of magnetic field from a temperature (T) much above its ferrimagnetic Néel temperature T_N and the magnetic-field is applied at 2 K and then the data is measured during warming. In FC condition, the sample was cooled to 2 K in presence of a static magnetic-field from a temperature much above its T_N and the magnetization is measured again while warming the sample by keeping the same magnetic-field. Both the magnetization curves M_{ZFC} and M_{FC} display a characteristic cusp across 38.1 K with strong irreversibility below this cusp. In order to probe the exact magnetic ordering temperatures, we calculated the derivative of the product of T and magnetic susceptibility (χ_{dc}=M/H_{dc}), i.e ($\partial(\chi_{dc}T)/\partial T$) and plotted as a function of T. Figure 3.6 depicts temperature variation of $\partial(\chi_{dc}T)/\partial T$ for S1200 sample. It is well known that, the temperature variation of $\partial(\chi_{dc}T)/\partial T$ is analogous to the temperature variation of the specific-heat $C_P(T)$ in the systems which shows antiferromagnetic variations [117, 118]. From the Curie-Weiss law one can write $\partial(\chi T)/\partial T = -C\theta/(T-\theta)^2$, which will give a negative minimum at T = θ and for negative values of 'θ' the equation $\partial(\chi T)/\partial T$ gives a positive maximum as observed in figure 3.6 [77]. This exercise leads to the determination of the $T_N \sim 41$ K and the second transitions $T_P \sim 35.4$ K. Similar type of analysis provide the existence of two transitions for S1350 sample i.e, T_N = 41 K and T_P = 37.1 K (as depicted in figure 3.7). In general, the second transition T_P signify the presence of either blocking phenomenon or spin-glass state in the Co_2SnO_4 system. Since the average grain sizes observed from the FESEM micrograph are in the μm range, T_P cannot be attributed to the blocking phenomena as the grain size in this case should be of the order of nm (< 30 nm). The data in the inset of figure 3.6 shows that with increase in H_{dc} from 200 Oe to 2 kOe, T_N shifts towards the higher value whereas T_P shifts towards the lower value, which is a typical signature of spin-glass transitions. Similar behavior observed in S1350 also (as shown in the inset figure 3.7). The decrease of magnetization with decrease in temperature as seen in

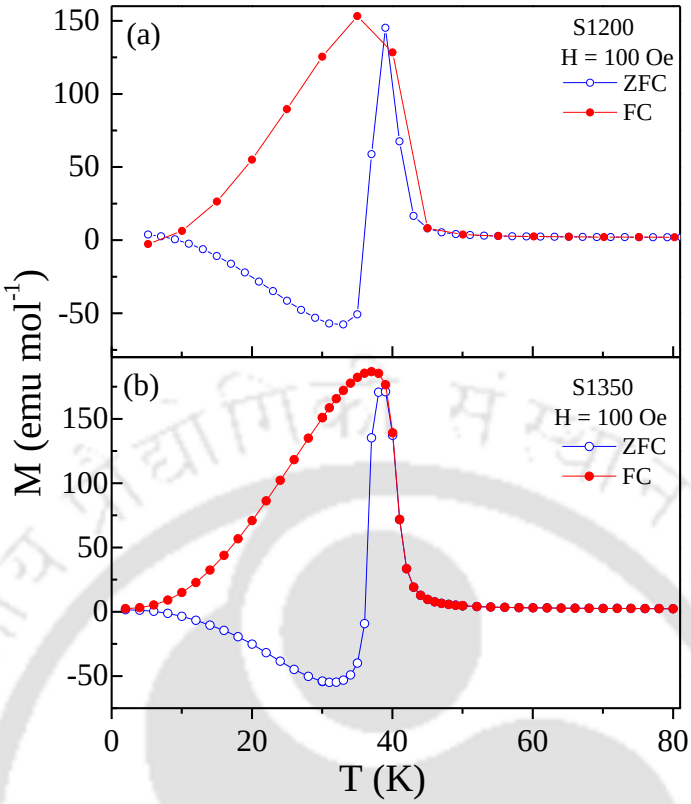

Figure 3.5: Temperature dependence of dc-magnetization M(T) measured under ZFC and FC (H@100 Oe) conditions for both Co_2SnO_4 bulk samples (a) sintered at 1200ºC (S1200) and (b) 1350°C (S1350).

figure 3.5 suggests that the temperature dependence of A-sublattice magnetization M(A) is different from that of B-sublattice magnetization M(B) since the measured magnetization for a collinear ferrimagnet is proportional to the magnitude of the difference between M(A) and M(B). The observed variation of M versus T below T_N in figure 3.5 is quite consistent with the expected variations in ferrimagnets with different temperature dependences of M(A) and M(B).

Figures 3.8 and 3.9 show the temperature dependence of the real-component χ'(T) and imaginary component χ''(T) of ac-magnetic susceptibility $\chi_{ac}(T)$ recorded using different measuring frequencies (*f*) ranging from 0.17 to 1202 Hz and under zero dc-bias field for the samples S1200 and S1350, respectively. It is well known that the dynamic susceptibility is an important phenomenon to understand the nature of magnetism in diluted systems such as Co_2SnO_4 below T_N where the short-range ordering arises again due to the competing interactions. In both the samples S1200 and S1350 the data was recorded from 30 K to 50 K with very close interval ΔT = 0.1 K in presence of dynamic ac-magnetic field amplitude h_{ac} ~ 4 Oe. One can clearly notice the frequency dispersion of cusp in both χ'(T) and χ''(T) for both S1200 and S1350. Such shift of peak position towards higher temperatures in both χ'(T) and χ''(T) clearly signify the existence of the glassy behavior in the investigated systems [42, 67, 119]. In

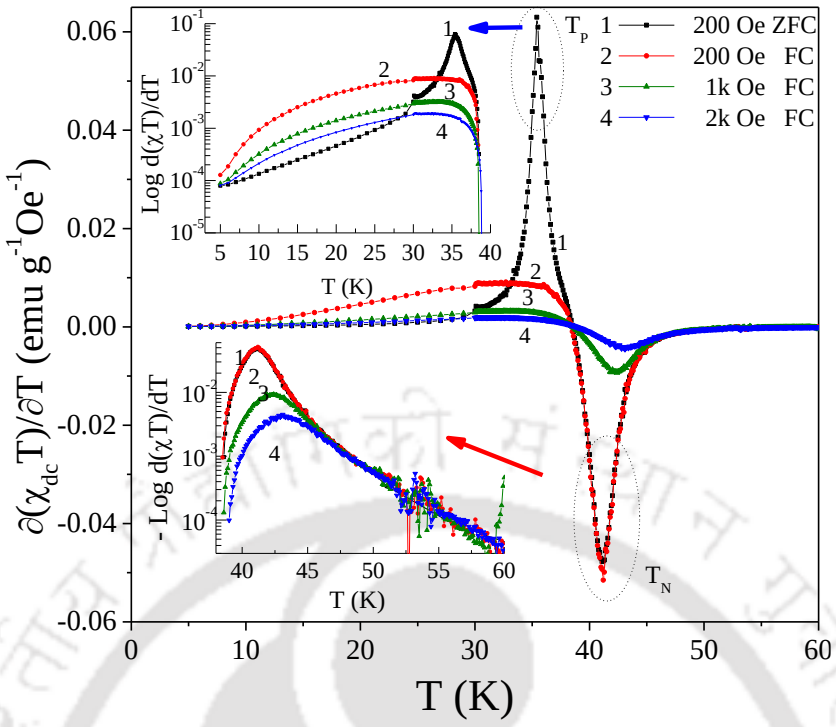

Figure 3.6: The differential susceptibility plots ($\partial(\chi_{dc}T)/\partial T$ versus T) of S1200 sample at various external fields H = 200 Oe, 1 kOe, and 2 kOe. The insets depict $\partial(\chi_{dc}T)/\partial T$ plotted with a logarithmic scale to show the variation in the peak clearly.

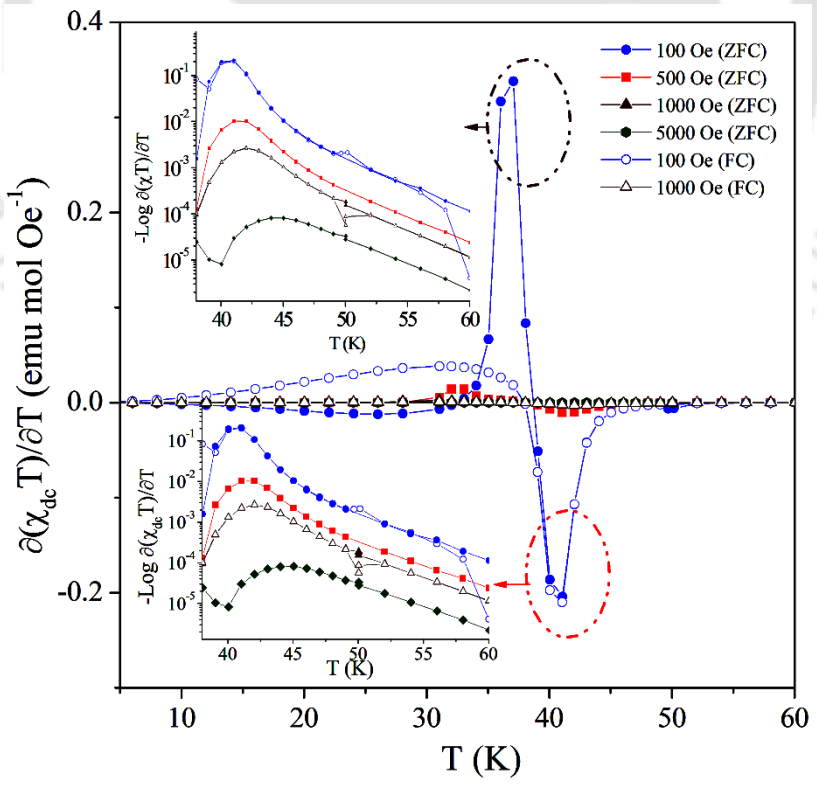

Figure 3.7: Plots of $\partial(\chi_{dc}T)/\partial T$ versus T plots of S1350 sample at various external fields H = 100, 500, 1000 and 5000 Oe. The insets show the $\partial(\chi_{dc}T)/\partial T$ in logarithmic scale to show the variation in the peak clearly.

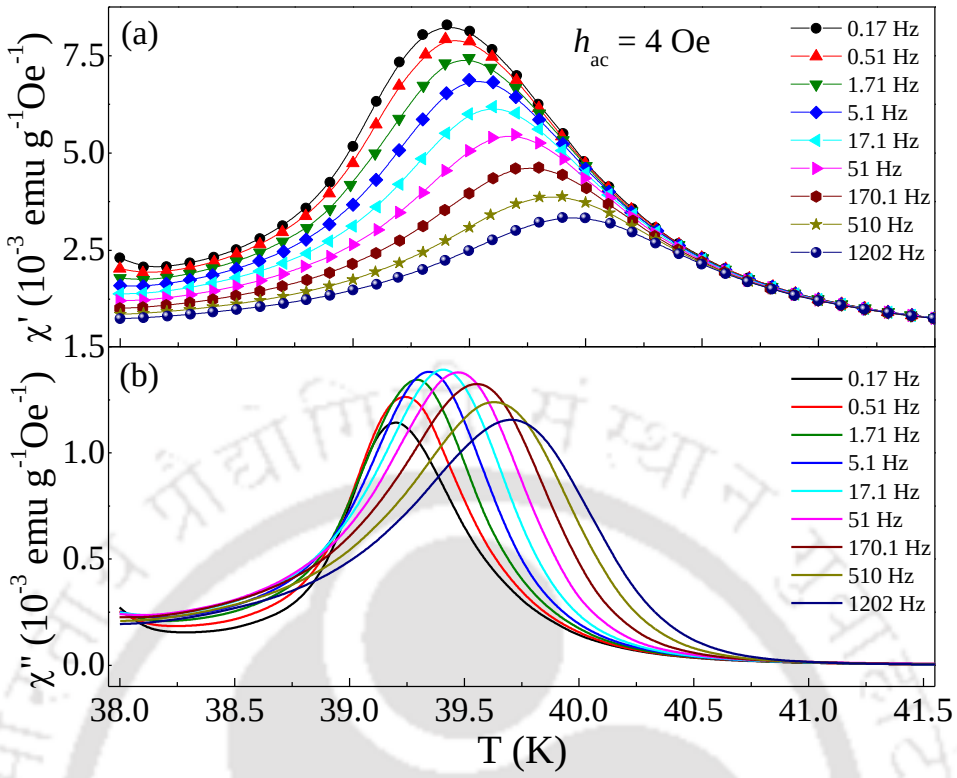

Figure 3.8: Temperature dependence of the (a) real-component χ'(T) and (b) imaginary-components χ''(T) of ac-magnetic susceptibility for S1200 recorded using different measuring frequencies under zero-dc bias field with the amplitude of dynamic magnetic-field h_{ac} = 4 Oe.

order to examine such spin-glass behavior in detail, we analyzed the data using two dynamic scaling laws – (*i*) Vogel-Fulcher law for interacting particle system and *(ii)* Power law describing the critical slowing down in phase transition [67]. Vogel-Fulcher law can be expressed as: $\tau = \tau_o \exp(E_a/k_B(T - T_o))$, where $\tau = 1/2\pi f$, τ_o is the relaxation time constant, T_o is a measure of the interparticle interaction strength, k_B is the Boltzmann constant, and E_a is an activation energy parameter. The best fits using the Vogel-Fulcher law (shown in figure 3.10) yields the value $\tau_o = 6.3 \times 10^{-14}$ s (7.3×10^{-8} s) and T_o = 38 K (39.3 K) for S1200 (S1350) samples, respectively. In the above fitting analysis we obtained a very large value of τ_o for S1350 sample. Such large value of τ_o has been observed in other system as well, such as CuMn, $Y_{0.7}Ca_{0.3}MnO_3$ which indicates the presence of interacting magnetic spin clusters of significant sizes in the system [120, 121]. We, believe that the spin clusters arise from a short range order which occurs due to the competition between ferrimagnetism and magnetic frustration in the system. On the other hand, the Power-law can be represented as: $\tau = \tau_o ((T/T_g) - 1)^{-zv}$, where T_g is the freezing temperature, τ_o is related to the relaxation of the individual cluster magnetic moment and *zv* is a critical exponent. Figure 3.11 shows the least square fit of the data using Power-law relation. An equally good fit as the Vogel–Fulcher law was obtained with T_g = 39.1 K (39.6 K), $\tau_o = 1.7 \times 10^{-22}$ s (1.4×10^{-15} s) and zv = 12. 6 (6.4) for

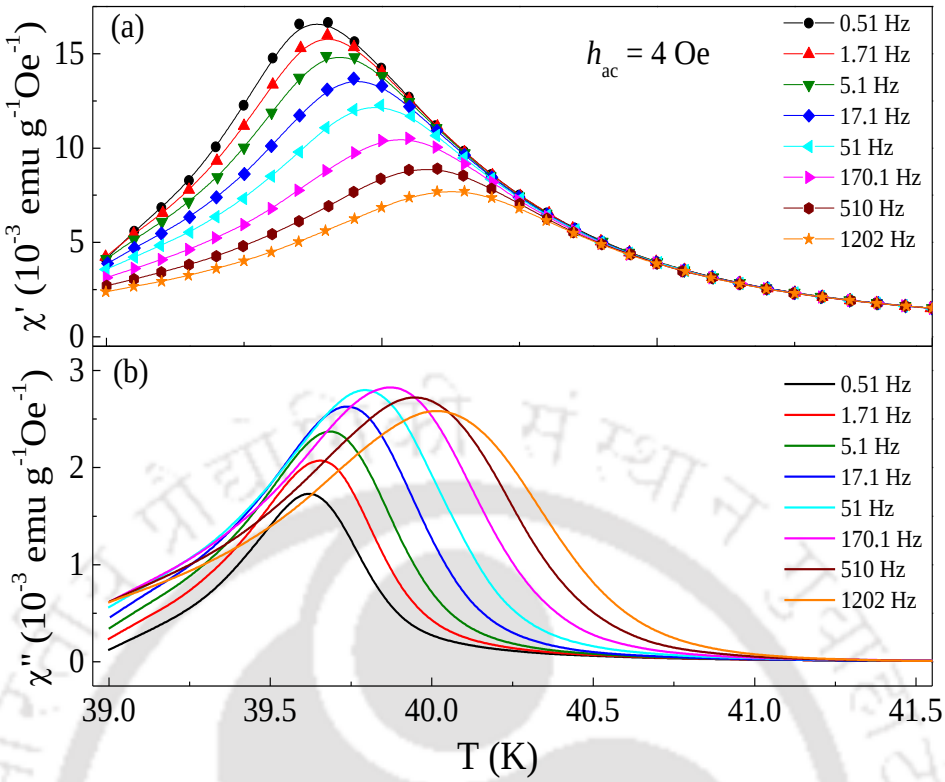

Figure 3.9: Temperature dependence of the (a) real-component χ'(T) and (b) imaginary-components χ''(T) of ac-magnetic susceptibility for S1350 recorded using different measuring frequencies under zero-dc bias field with the amplitude of dynamic magnetic-field h_{ac} = 4 Oe.

S1200 (S1350) samples, respectively. For an ideal spin-glass system the *zv* value should lie between 4 and 12 [67]. However, we obtained a little high value for S1200 system which is quite unphysical for spin-glass system, but very small difference between T_o and T_g suggest the system is close to a spin-glass transition. It is important to mention that while fitting the data for the sample S1200 to the power law, we could obtain more than one set of parameters giving almost equally good fits (the value of goodness of fit R^2 changing after the 5^{th} decimal place). However, for the pure sample (S1350 without any SnO_2 impurity), the data could be fitted using a set of parameters which gave an unambiguous best fit.

For further understanding the nature of magnetism below T_N, we measured the ac-magnetic susceptibility superimposed with various dc-bias fields (H_{dc}). Figure 3.12(*a*) and 3.12(*b*) represent the temperature dependence of χ' and χ'' measured at a constant driving frequency (f = 2 Hz) and the ac-field-amplitude h_{ac} = 1 Oe superimposed with external dc-bias field (0 Oe ≤ H_{dc} ≤ 200 Oe) for S1200 system. The in-phase ac-susceptibility (χ') shows two-peak behavior with their splitting increases with increasing H_{dc}. On the other hand, χ'' versus T curves show a single peak with decreasing intensity and shift towards lower temperatures with increase in H_{dc}. Since, the out of phase susceptibility is related to the transverse spin component. These observations reveal the co-existence of ferrimagnetism of longitudinal spin component along with the freezing of transverse spin

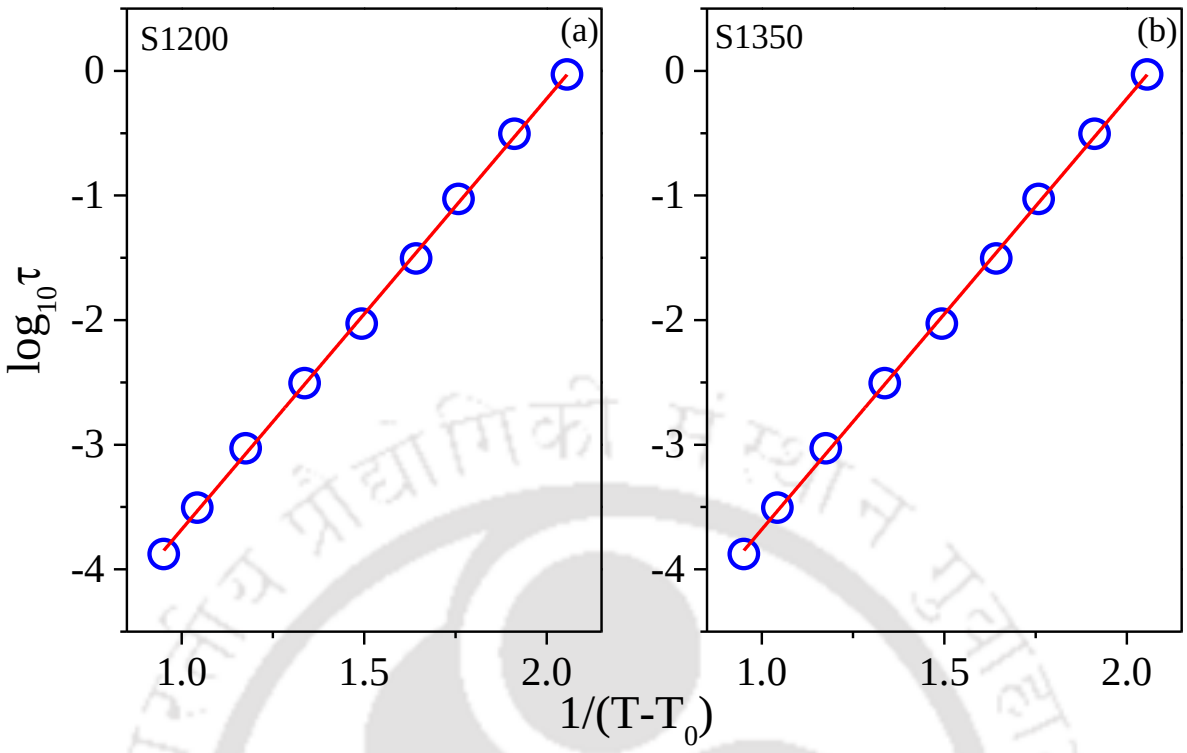

Figure 3.10: The best fit of the relaxation times to the Vogel–Fulcher law for (a) S1200 and (b) S1350 sample.

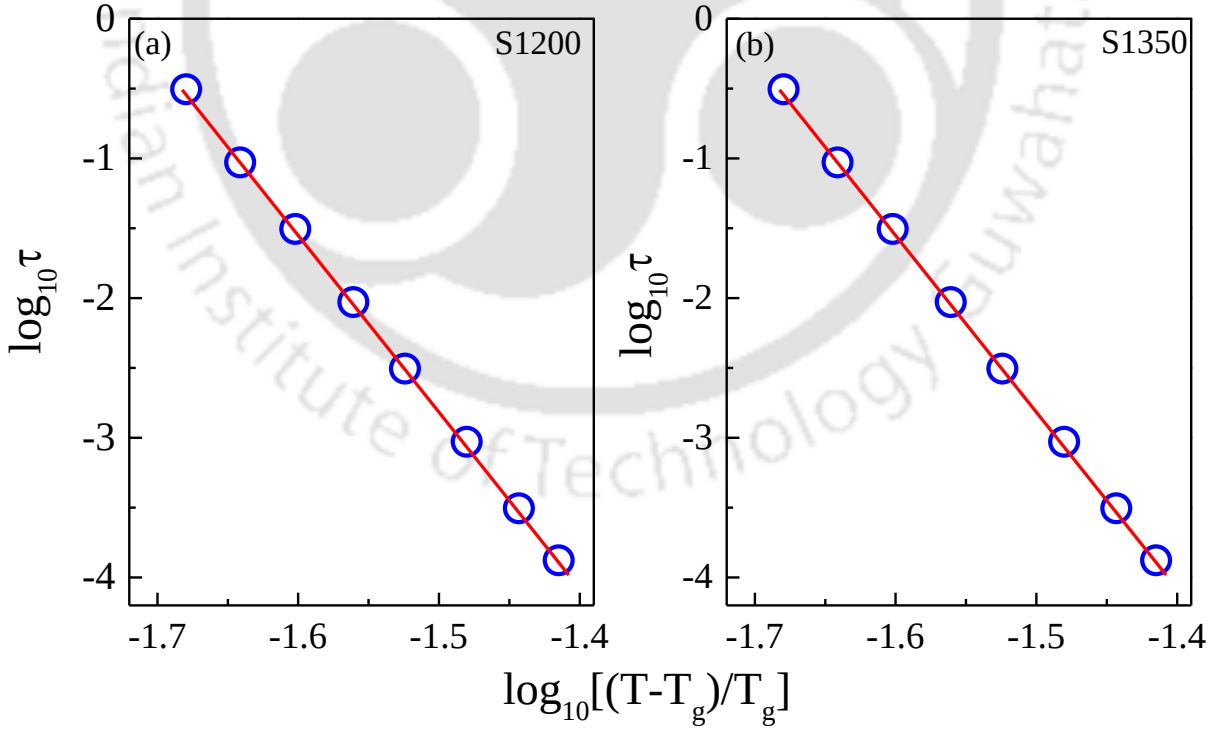

Figure 3.11: The best fit of the relaxation times to the Power–law for (a) S1200 and (b) S1350 sample.

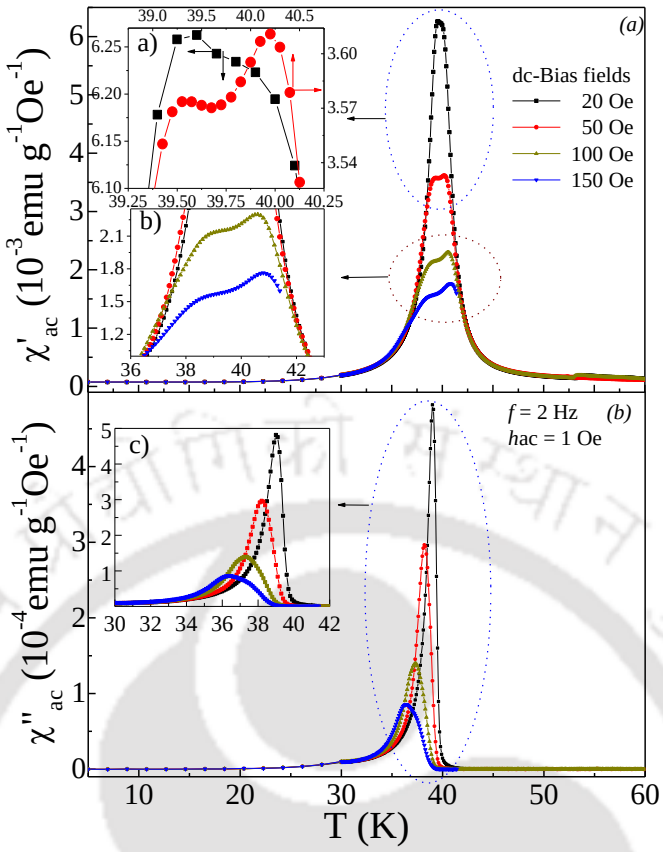

Figure 3.12: Temperature dependence of ac-magnetic susceptibilities: (*a*) real part (χ') and (*b*) imaginary part (χ'') component of S1200 recorded at various dc-bias fields H_{dc} = 20, 50, 100 and 150 Oe with constant frequency f = 2 Hz and amplitude h_{ac} = 1 Oe. The insets (a)-(c) depict the zoom view of the same curves at various temperature regimes to show the transition better.

component in Co_2SnO_4 system. Such type of semi-spin-glass state was first predicted by Villian in magnetically diluted systems and later established theoretically by Gabay and Thoulouse [40, 122]. Figure 3.13 shows temperature dependence of $\partial(\chi'T)/\partial T$ for S1200 sample. Since, the temperature dependence of $\partial(\chi'T)/\partial T$ and χ'' versus T are found to be comparable in many systems and has a strong theoretical basis [123 - 125], similar type of peaks should be observed in $\partial(\chi'T)/\partial T$ (T) and $\chi''(T)$. In S1200, the peaks in the $\partial(\chi'T)/\partial T$ versus T curve and in χ'' versus T curve occur at different temperatures. Besides that, we observe that there is a single peak in χ'' versus T but two peaks in $\partial(\chi'T)/\partial T$ versus T (associated with T_N and T_{SG}) which suggest a more complicated magnetic ordering of bulk Co_2SnO_4 system. The position of two peaks in $\partial(\chi'T)/\partial T(T)$ and the location of single peak in $\chi''(T)$ are plotted as function of $H_{dc}^{2/3}$ (figure 3.14). It is clear from the figure that the peak associated with the T_N shifts towards higher temperature with increase in the magnetic-field. Such type of behavior justifies the ferrimagnetic character of Co_2SnO_4 in which the direct coupling occurs between the order parameter and the applied field. Conversely, the linear behavior of the second peak in $\partial(\chi'T)/\partial T(T)$ and the single peak in $\chi''(T)$

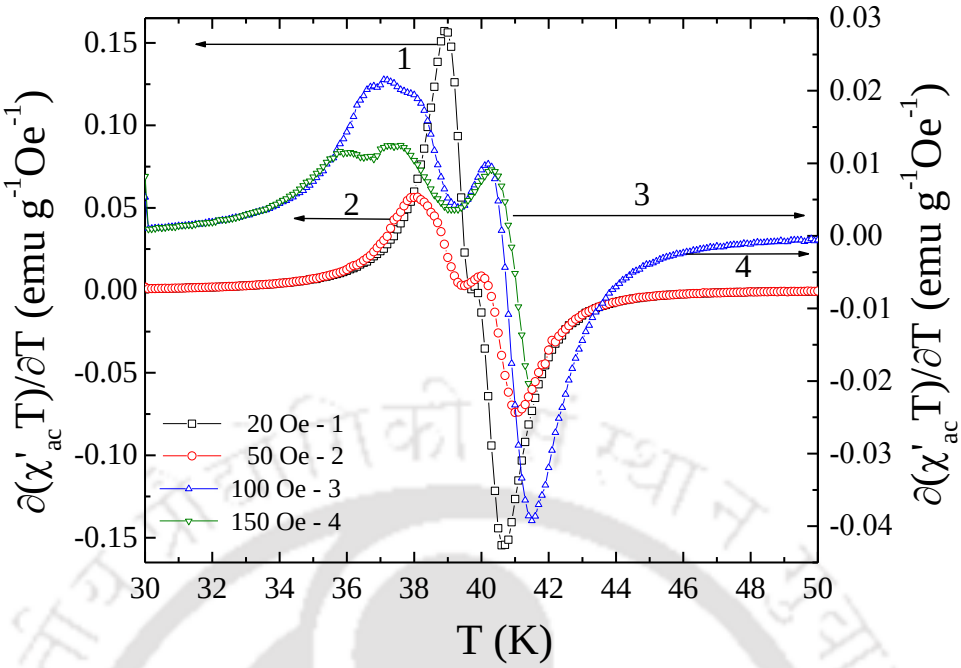

Figure 3.13: Temperature variation of $\partial(\chi'_{ac}T)/\partial T$ plots at different bias fields 20 Oe $\leq H_{dc} \leq$ 150 Oe for S1200 sample.

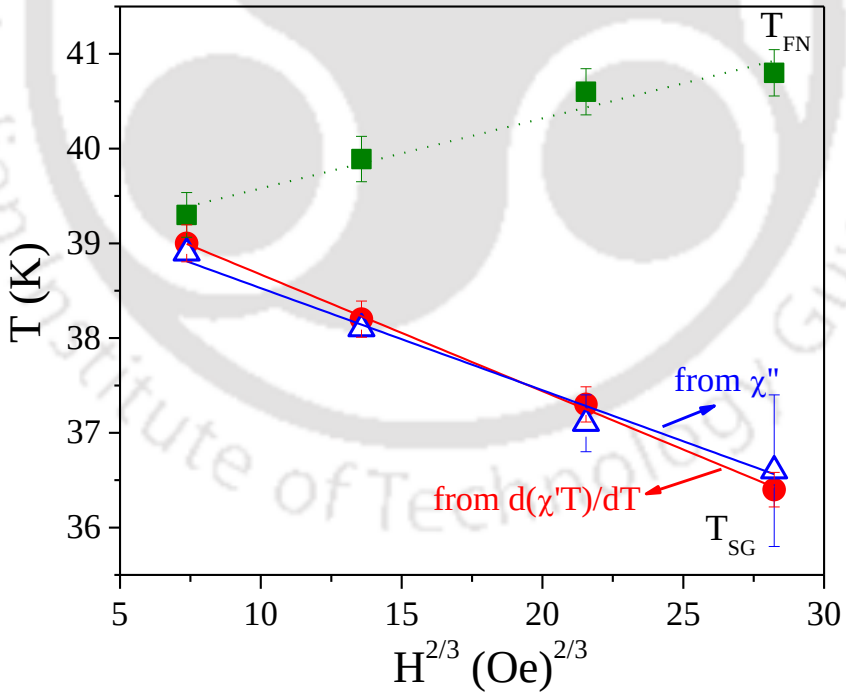

Figure 3.14: Variation of ferrimagnetic Néel temperature T_N and spin-glass transition temperature T_{SG} with respect to $H^{2/3}$ for S1200 sample. The solid lines show the linear fit to the data (often called the de Almeida-Thouless AT line) whereas the dotted line for T_{SG} is for visual aid.

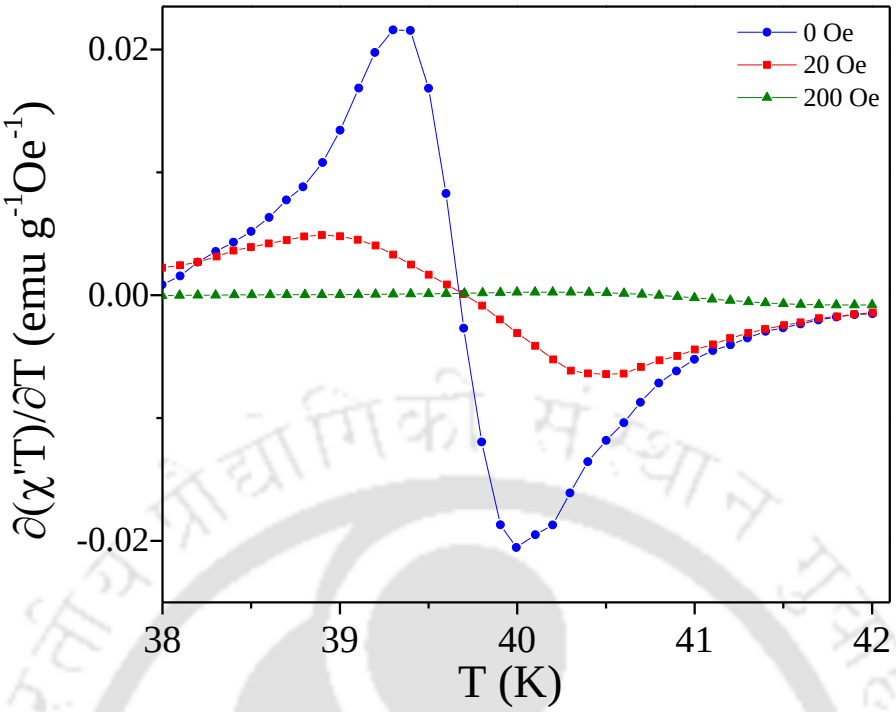

Figure 3.15: Temperature variation of $\partial(\chi'_{ac}T)/\partial T$ plots at different bias fields 0 Oe ≤ H_{dc} ≤ 200 Oe for S1350 sample.

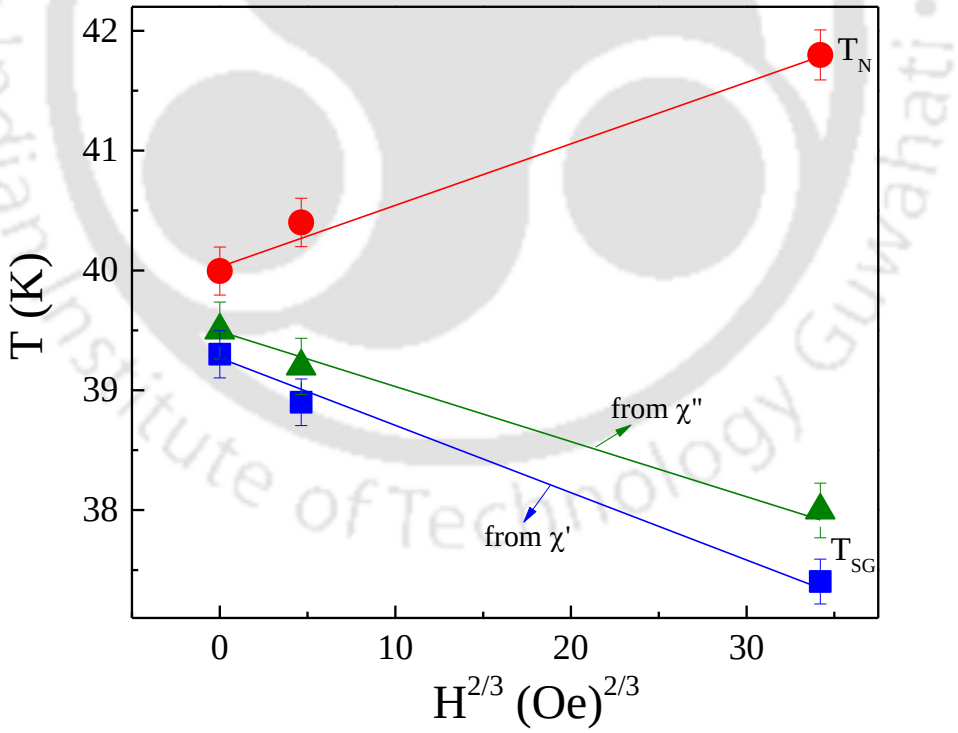

Figure 3.16: Variation of ferrimagnetic Néel temperature T_N and spin-glass transition temperature T_{SG} with respect to $H^{2/3}$ for S1350 sample. The solid lines show the linear fit to the data (often called the *de Almeida-Thouless* AT line) whereas the dotted line for T_{SG} is for visual guide.

shift identically with $H_{dc}^{2/3}$. Such $H_{dc}^{2/3}$ variation of the peak is characteristic of the de Almeida-Thouless line (popularly known as AT-line) for a spin-glass state and such variation is often used as one of the tests for the presence of spin-glass like short range ordering in a variety of disordered systems [126 - 129]. In Co_2SnO_4, the semi-spin-glass state arises due to magnetic frustration and dilution (i.e. non-magnetic Sn^{4+} substituted at octahedral B-sites). The indiscriminate distribution of Sn^{4+} on the B-sites weaken the A-B exchange interaction, which randomize the canting of Co^{2+} below T_N. Application of the external dc-magnetic field reduces this random canting and shifts T_{SG} towards a lower temperature value. Figure 3.15 shows the ac-susceptibility of S1350 for f = 51 Hz, and h_{ac} = 4 Oe with different dc bias fields. No field induced transition to long range order seems to be observed. The magnitude of ac-susceptibility is strongly suppressed in the presence of dc-magnetic field suggests the existence of glassy behavior. The AT-line analysis of S1350 sample (shown in figure 3.16) supports the above spin-glass behavior similar to that of S1200 sample discussed above.

(b) Temperature Dependence of the Hysteresis Loop Measurements:

The hysteresis loops measured at various temperatures in the magnetic field range -60 kOe to +60 kOe are shown in the figure 3.17 and 3.18 for S1200 and S1350, respectively. The inset shows a zoomed view of magnetization versus field i.e, M-H curves at selected temperatures 10 K, 20 K, 29 K and 41 K to avoid overcrowding for both the samples. These measurements were done for samples cooled in 'zero-field' from room

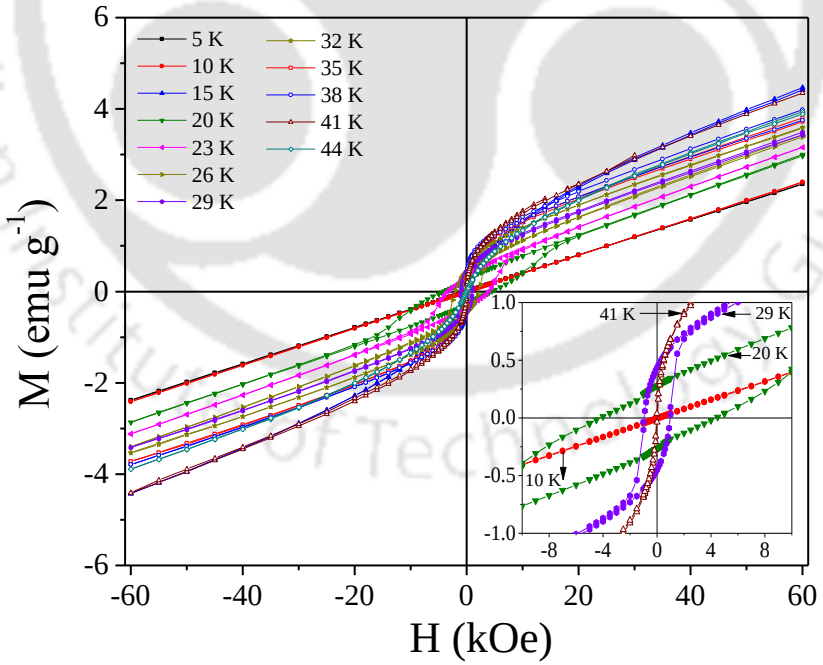

Figure 3.17: Magnetization (M) versus magnetic field (H) hysteresis loops recorded at various temperatures in the range 5 K ≤ T ≤ 45 K under zero-field conditions for S1200 samples. Inset shows the zoomed view at selected temperature

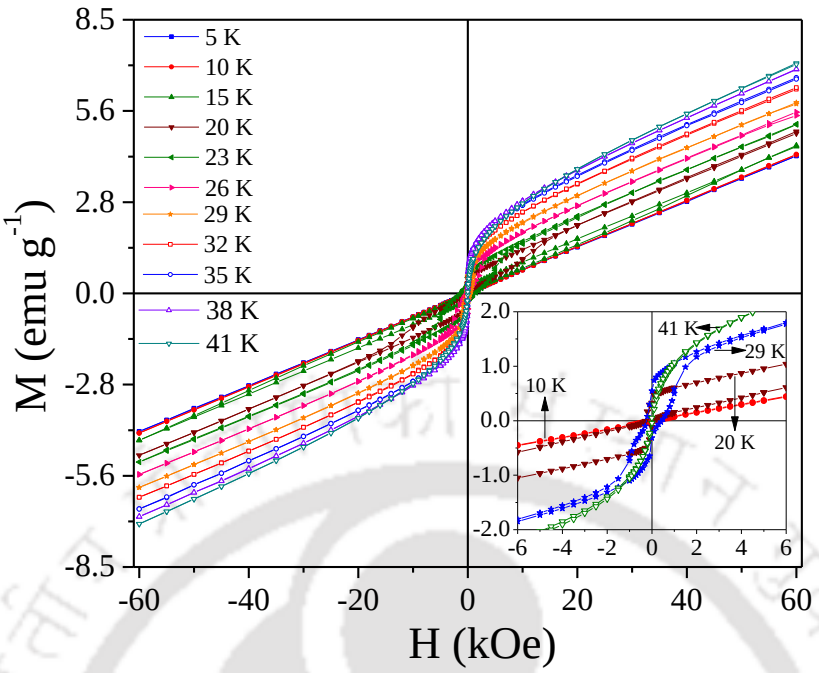

Figure 3.18: Magnetization (M) versus magnetic field (H) hysteresis loops recorded at various temperatures in the range 5 K ≤ T ≤ 41 K under zero-field conditions for S1350 samples. Inset shows the zoomed view at selected temperature.

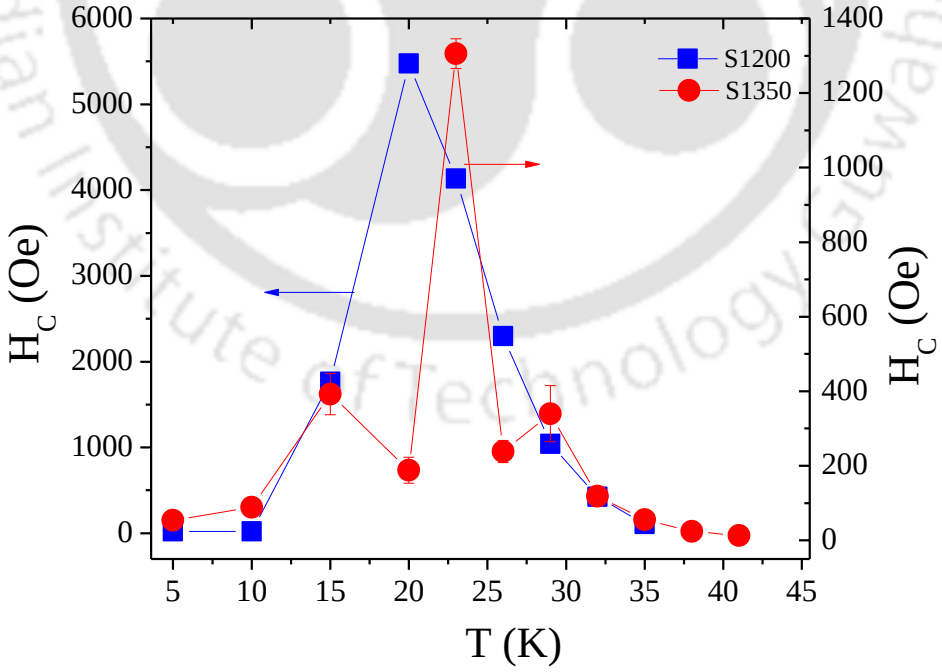

Figure 3.19: Temperature dependent coercivity (H_C) for both S1200 and S1350 sample.

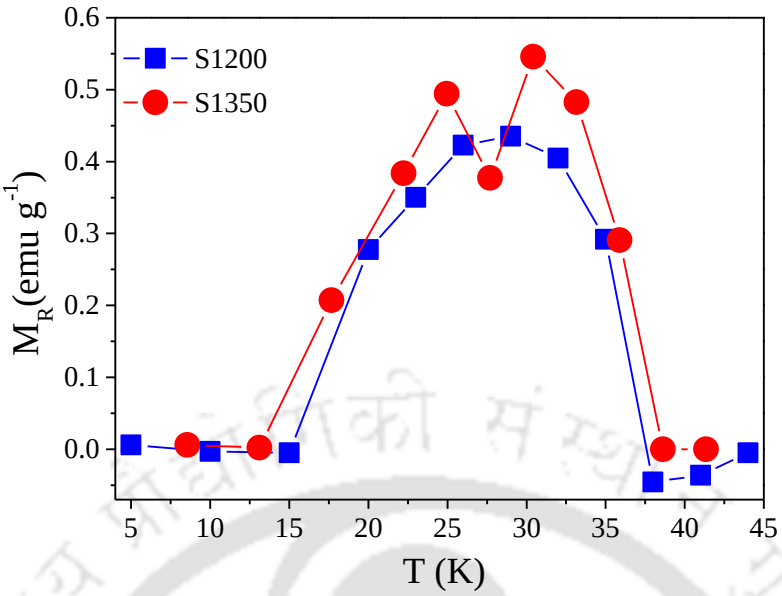

Figure 3.20: Temperature dependent remanence (M_R) for both S1200 and S1350 sample.

temperature to the measuring temperature. The coercive field H_C, remanence M_R and the loops asymmetry H_{EB} (EB = exchange-bias) were measured from the above loops. The temperature variation of H_C and M_R are plotted in figure 3.19 and 3.20. One can clearly notice that H_C and M_R are practically zero outside the temperature range of 15 K < T < 39 K with their peak magnitudes occurring near 25 K. Also the magnitudes of M_R (~ 0.45 emu-g^{-1}) and their temperature dependences in the two samples (S1200 and S1350) are nearly identical. The magnitudes of the loop asymmetry parameter H_{EB} for the ZFC samples were also determined from the measured hysteresis loops (figure 3.21). However, their magnitudes at different temperatures were found to be quite small (zero to 100 Oe) as compared to the magnitudes of H_C, and, their temperature dependence did not show any systematic pattern. Such small values of H_{EB} might be due to the residual field present in the zero-field cooling process as mentioned above, it is inappropriate at present to attach a great deal of significance to this small asymmetry observed in the hysteresis loops. Generally, H_{EB} has been observed only in samples cooled in presence of a magnetic field containing ferromagnetic (FM)–antiferromagnetic (AFM) [130], FM-spin glass (SG) [131], FM-ferrimagnetic [132], AFM-ferrimagnetic [133] and AFM-SG [134, 135] interfaces from above the Néel temperature or spin-glass temperature. Recently, few papers have reported significant H_{EB} in ZFC samples in bulk Ni–Mn–In alloys [136] and in bulk Mn_2PtGa [137]. They predicted that the source of this unusual H_{EB} in the ZFC sample can be attributed to the presence of complex magnetic ordering containing ferrimagnetic, spin–glass and AFM phases [136, 137].

(c) Temperature Dependence of the Paramagnetic Susceptibility:

Figure 3.22(a) and 3.22(b) shows the temperature dependence of dc-magnetic susceptibility $\chi(T)$ and its inverse $\chi^{-1}(T)$ of both the samples S1200 and S1350 above the Néel temperature. One can clearly notice higher values of

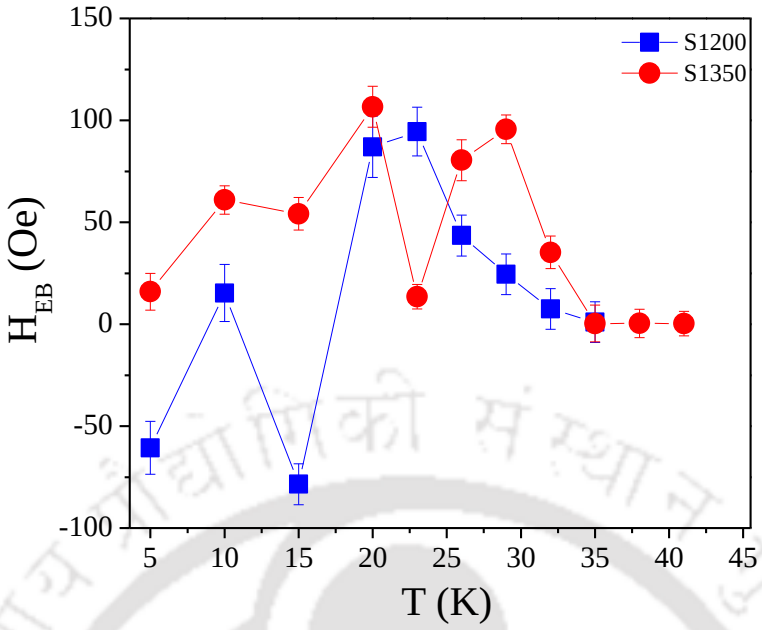

Figure 3.21: Temperature dependence of exchange-bias (H_{EB}) for both the S1200 and S1350 samples.

susceptibility in S1350 sample as compared to S1200 which contains few percent of unreacted SnO_2. The solid lines shows least square fits to the Néel expression for ferrimagnets [18]. $(1/\chi) = (T/C) + (1/\chi_0) - [\sigma_0/(T- \theta)]$. The ratio $C/\chi_0 = T_a = 130.99$ K (112.13 K) for S1200 (S1350) represents the strength of the antiferromagnetic exchange coupling between the spins on the 'A' and 'B' sites and is often termed as asymptotic Curie temperature 'T_a'. Using the Curie constant 'C' value ($=N\mu^2_{eff}/3k_B$) we have evaluated the total effective magnetic moment μ_{eff} = 6.31 μ_B (6.25 μ_B) for S1200 (S1350) which is equivalent to $\mu_{eff} = [\mu(A)^2 + \mu(B)^2]^{0.5}$. Assuming spin only moment of Co^{2+} ion in A –sites i.e, $\mu(A) = 3.87\ \mu_B$ (3.87 μ_B) for S1200 (S1350) with S = 3/2 and g =2, we obtained the 'B' site magnetic moment $\mu(B) = 4.98\ \mu_B$ (4.91 μ_B) for S1200 (S1350) samples respectively. Table 3.2 summarizes the magnetic moments of A and B-sites along with the other parameters obtained from the fitting analysis. Using the fitted parameters of the Néel's expression we have evaluated the molecular field constants (N_{AA}, N_{BB} and N_{AB}) between nearest neighbor and next nearest neighbors, and the corresponding exchange constants (J_{AA}, J_{BB} and J_{AB}) for both S1200 and S1350 systems. Among all the theoretical and experimental techniques, temperature dependent paramagnetic susceptibility is the most constructive and useful method to determine the magnitude of such exchange parameters. The obtained molecular field constants and the exchange constants are listed in table 3.2. From the table one can clearly observe that molecular field constants follows the trend $N_{AB} > N_{AA} > N_{BB}$. However, the antiferromagnetic exchange coupling constants $J_{BB} = 6.14\ k_B$ (4.28 k_B) and $J_{AB} = 5.97\ k_B$ (5.26 k_B) are greater than $J_{AA} = 4.07\ k_B$ (4.05 k_B) for S1200 and S1350 systems, respectively. Such trend of exchange constants was observed earlier in other spinels also [138-140]. From the above analysis, we can conclude that the difference in μ_{eff} for Co^{2+} on A and B-sites along with the antiferromagnetic coupling constants is responsible for the ferrimagnetism in Co_2SnO_4.

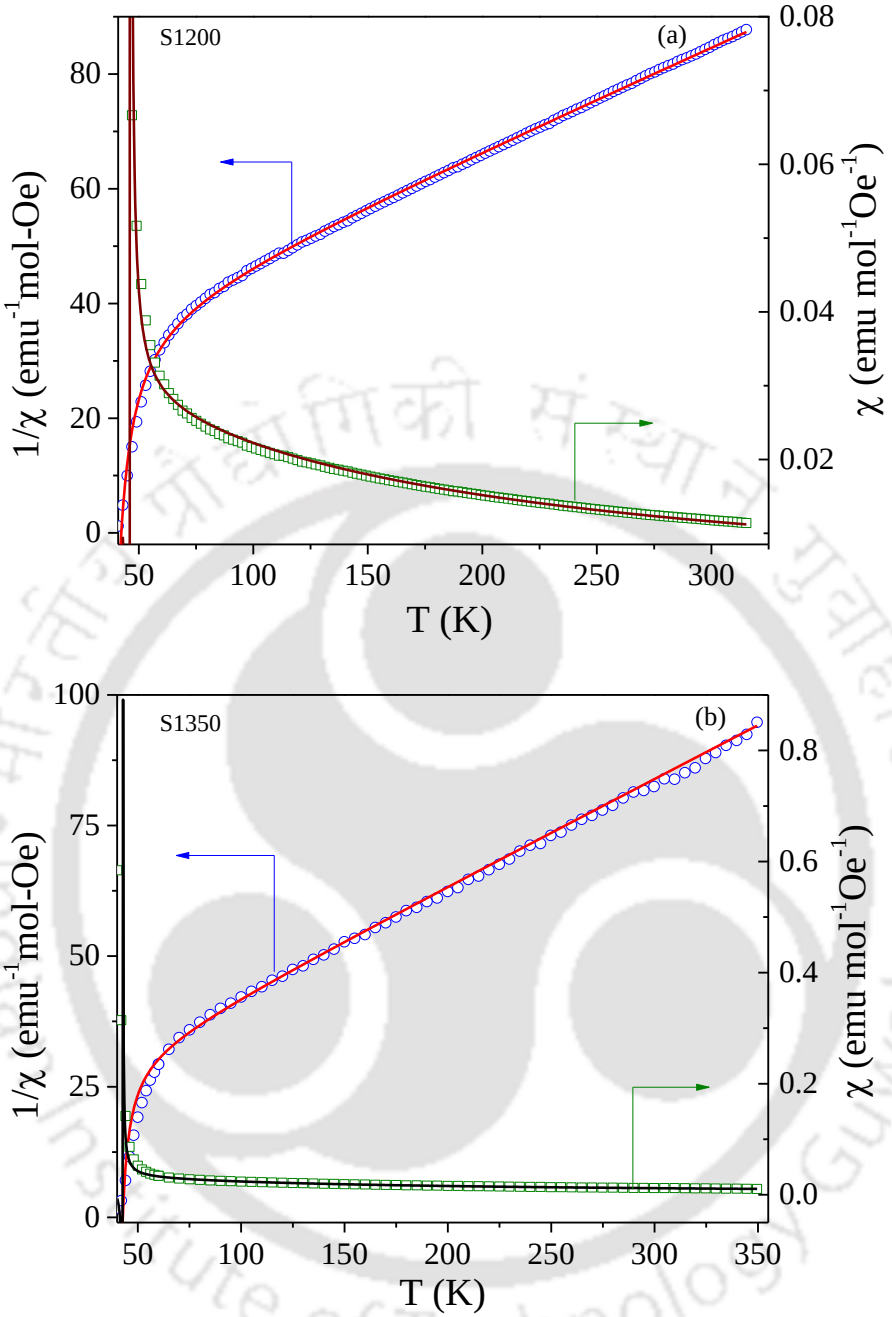

Figure 3.22: Temperature dependence of susceptibility (χ versus T) (R.H.S) and inverse susceptibility (L.H.S) (χ^{-1} versus T) for the samples (a) S1200 (b) S1350 are shown. The solid lines are fits to the Néel's expression for ferrimagnets as discussed in this chapter.

We now compare the magnetic properties of Co_2SnO_4 with those reported in literature for some other relevant spinels. In 1956, Anderson predicted that in normal spinels such as $ZnFe_2O_4$ in which the magnetic ions Fe^{3+} all occupy the B-sites and the geometrical frustration will lead to lack of long range magnetic order [141]. This has been confirmed recently in $ZnFe_2O_4$ in that although the system orders antiferromagnetically at $T_N \sim 10.5$ K, short

Table 3.2: The list of various parameters obtained from the Néel fits of χ^{-1} versus T curve recorded under zero-field condition.

System	C (emu K $mol^{-1}Oe^{-1}$)	χ_o (emu $mol^{-1}Oe^{-1}$)	σ_o ($emu^{-1}Oe$ mol K)	θ (K)	μ_{eff} (μ_B)	μ (A) (μ_B)	μ (B) (μ_B)
	4.987	0.03807	77.001	44.1228	6.313	3.872	4.985
Co_2SnO_4	$g_A = 2$	N_{AA}	N_{BB}	N_{AB}	J_{AA}	J_{BB}	J_{AB}
(S1200)	$g_B = 2.53$	21.73	14.82	37.12	4.07 k_B	6.14 k_B	5.97 k_B
	4.889	0.0436	102.400	39.5	6.2508	3.8729	4.9064
Co_2SnO_4	$g_A = 2$	N_{AA}	N_{BB}	N_{AB}	J_{AA}	J_{BB}	J_{AB}
(S1350)	$g_B = 2.57$	21.564	10.678	33.201	4.05 k_B	4.28 k_B	5.26 k_B

range order is observed at temperatures as high as 10 T_N and well below T_N [8]. In the inverse spinel $CoFe_2O_4$ with ionic distribution of $[Fe^{3+}][Co^{2+}Fe^{3+}]O_4$, ferrimagnetism is observed with T_N ~ 793 K [18]. In this case, Fe^{3+} moments on the A- and B-sites are antiparallel with Co^{2+} provides the ferrimagnetic component. Recently, Bhowmik *et al*. reported the nature of magnetism in magnetically diluted $Co_{0.2}Zn_{0.8}Fe_2O_4$ system [142]. The 20% concentration of Co^{2+} obtained by 80% dilution of the Co^{2+} with Zn^{2+} is well below the percolation threshold pc = 33% of Co^{2+} needed for long-range magnetic ordering. Interestingly, the reported magnetic studies indicate T_N ~ 110 K and for 110 K ≤ T ≤ 260 K, it is inferred that short range ferrimagnetic phase coexists with cluster spin-glass phase [142]. In the $Co_{0.2}Zn_{0.8}Fe_{1.95}Ho_{0.05}O_4$ system, ferrimagnetism with T_N ~ 225 K followed by cluster spin-glass state below 120 K is reported. [143] Since it is well established that for magnetic concentration p < pc, the system consists of unconnected magnetic clusters often with spin-glass like ordering, [104, 105] it is highly likely that cluster spin-glass states reported in these systems is due to the magnetic dilution of Co^{2+} site well below its pc. The $Co_2SnO_4 = [Co^{2+}][Co^{2+}Sn^{4+}]O_4$ system investigated here differs substantially from the $Co_{0.2}Zn_{0.8}Fe_2O_4$ system noted above in that the magnetic dilution of Co^{2+} B-site by Sn^{4+} is only 50%, well above pc = 33%. Consequently, this system is expected to exhibit long-range magnetic ordering of the longitudinal component followed by the predicted spin-glass freezing of the transverse component in a diluted spinel. The $H^{2/3}$ dependence of the spin-glass freezing temperature T_{SG} provides the confirmatory evidence. These results suggest paramagnetism in Co_2SnO_4 for T >> T_N, but normal spin correlations develop as T approaches T_N from above.

3.3.5 Temperature Dependence of Specific Heat:

The temperature dependence of the specific-heat $C_P(T)$ for the S1200 and S1350 samples in H = 0 Oe and H = 1 kOe, measured from 5 K to 60 K in 1 K steps, is shown in figure 3.23 (a) and (b). For both samples, no measurable difference is observed for the data recorded in H = 0 and H = 1 kOe, and, there is no indication of any

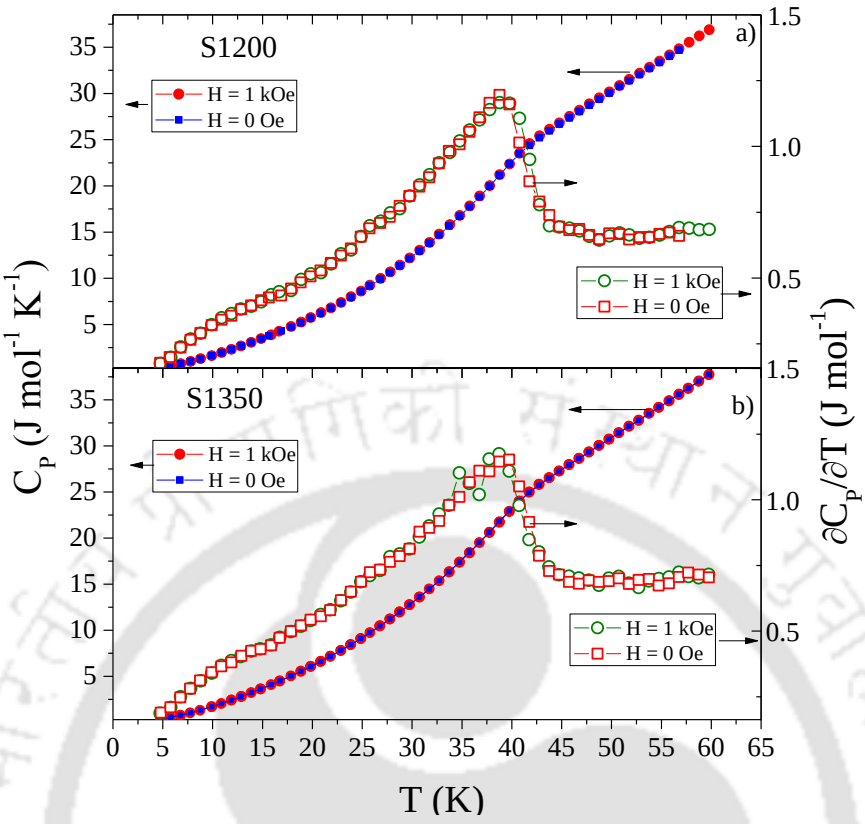

Figure 3.23: The temperature dependence of specific heat $C_P(T)$ for the samples; (a) S1200, and (b) S1350 measured under both zero magnetic field and in the presence of magnetic field of H = 1 kOe recorded under warming condition. The corresponding derivative plots $\partial C_P(T)/\partial T$ versus T is shown on the right-hand-side scale.

peak in $C_P(T)$ near 41 K or 39 K expected for a conventional first or second order magnetic phase transition [146, 147]. Instead, there is only an inflection point near 39 K which yields a peak in $\partial(C_P)/\partial T$ near 39 K as shown in figure 3.23 (right hand scale). Furthermore, there is an indication of another weak anomaly in $\partial(C_P)/\partial T$ near 15 K below which $\partial(C_P)/\partial T$ continues to increase. The absence of peak in C_P is a well-known characteristic of spin-glass ordering near T_{SG} [146, 147]. Thus the new measurements of C_P versus T reported here for both the S1200 and S1350 samples of Co_2SnO_4 indicate the presence of a spin-glass transition near 39 K and suggest some changes in magnetic ordering taking place below 15 K. A detailed study related to this low-temperature anomalous magnetic ordering will be discussed in the coming chapter where we compare the low-temperature magnetic properties of Co_2SnO_4 with its sister compound Co_2TiO_4.

Furthermore, we have plotted the C_P/T and its temperature derivative $\partial(C_PT^{-1})/\partial T$ versus T in figure 3.24 to look for any anomalous changes. There is a clear change in C_P/T versus T data at 39 K suggesting the entropy loss due to spin-glass ordering beginning near 39 K. There is another rapid decease in C_P/T with decreasing T beginning near 15 K, indicating further changes in the magnetic ordering of the system. These anomalies are clearly evident in the computed plots of $\partial(C_PT^{-1})/\partial T$ versus T in figure 3.24. Further support for these results comes from the temperature dependence of the magnetic hysteresis loop parameters discussed in section (*b*).

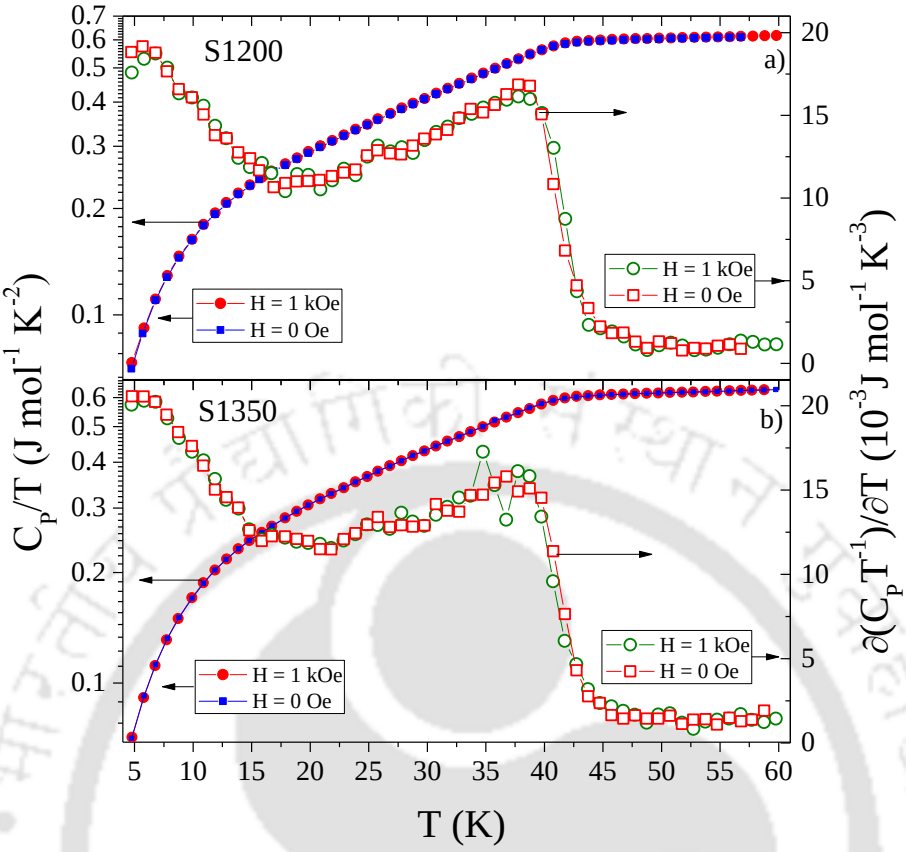

Figure 3.24: The temperature variation of the C_P/T and its first derivative $\partial(C_PT^{-1})/\partial T$ for the two samples (a) S1200 and (b) S1350 in H = 0 Oe and H = 1 kOe.

Comparison of the experimental results of Co_2SnO_4 with its sister compound Co_2TiO_4 should particularly illuminating because of the similarity of the two systems since non-magnetic Ti^{4+} on the B-sites in the former is replaced by non-magnetic Sn^{4+} in the later. In Co_2TiO_4, T_N at 55 K was followed by T_{SG} at 46 K [77] compared to T_N = 41 K and T_{SG} = 39 K in Co_2SnO_4 reported here. The temperature dependence of coercivity H_C in Co_2TiO_4 showed a compensation point near 28 K followed by a peak in H_C near 20 K and then dropping to very low values at 1.5 K, the lowest temperature attained in these experiments [77]. The results reported here for Co_2SnO_4 do not show a compensation point in either H_C or M_R but do show their peak values near 25 K as in Co_2TiO_4 followed by rapid drops to negligible magnitudes as the temperature is lowered below 15 K.

A quantitative explanation of the temperature dependence of H_C, and M_R in Co_2SnO_4 shown in figure 3.19 and 3.20 is not yet possible. However, following the observation of a compensation point in the sister compound Co_2TiO_4 [77], it is likely that the different magnitudes and different temperature dependences of the moments on the Co^{2+} ions on the 'A' and 'B' sites in Co_2SnO_4 are responsible for the peaks in H_C and M_R observed near 25 K. Below about 15 K, the data suggest that there is near complete effective balance of the antiferromagnetically coupled Co^{2+} moments at the 'A' and 'B' sites leading to negligible values of H_C and M_R. Earlier results from neutron diffraction in Co_2TiO_4 suggested the presence of canted-spins, likely resulting from magnetic frustration

caused by the presence of non-magnetic Ti^{4+} ions on the 'B'-sites. A similar canting of the spins might be present in Co_2SnO_4 although neutron diffraction studies are needed to verify this suggestion. There are a few subtle differences between the properties of S1200 which contains a few percent of unreacted SnO_2 and S1350 which does not. Structurally, S1350 was found to be relatively denser material and its lattice constant was slightly larger than that of S1200. Both of these effects were considered to be originated from the high sintering temperature (1350°C) of S1350. In magnetic properties, the major noticeable difference between the two samples is in the magnitudes of the coercivity H_C. Although the magnitudes of H_C in both samples peak near 25 K, H_C in S1200 is nearly 4 times larger than that in S1350. This suggests that in the two samples, the domain structures are somewhat different perhaps due to their different method of preparation although the positions and characteristics of the transitions near 41 and 39 K with peak magnitudes of H_C and M_R occurring 25 K and becoming negligible below 15 K are identical in S1200 and S1350. The ac-magnetic susceptibility data and its analysis suggest that the system consists of interacting magnetic clusters close to a spin glass state. These results are reminiscent of those shown in [148], [149] and [150]. In [148], the onset of the cusps in χ' (i.e. just above the cusp temperature) were found to be frequency independent, suggesting quasi-long-ranged ferri or antiferromagnetically ordered systems affected by the magnetic frustration. However, in [149] and [150], spin glass phase transitions were observed. In [150], $La_{1.1}Sr_{0.9}MnO_4$ was found to first order antiferromagnetically, yet the low temperature ac-magnetic susceptibility data indicated that spin glass correlations developed below T_N.

3.3.6 Summary:

Interpretation of the detailed temperature dependence of the ac- and dc-magnetic susceptibilities of the ferrimagnetic spinel Co_2SnO_4, presented in this chapter, has established the presence of two magnetic transitions in this system visualizing: T_N = 41 K and T_{SG} = 39.1 K. Also, all the molecular field exchange constants N_{AA} = 21.73 (21.56), N_{BB} = 14.82 (10.68) and N_{AB} = 37.12 (33.20) between the magnetic ions on the 'A' and 'B' sites with magnetic moments $\mu(A) = 3.87\ \mu_B$ (3.87 μ_B) and $\mu(B) = 4.98\ \mu_B$ (4.98 μ_B) for S1200 (S1350) respectively, were determined and found to be antiferromagnetic in nature. The ferrimagnetic transition at T_N is associated with ordering of the longitudinal spin component, whereas, T_{SG} was attributed to freezing of the transverse spin component. These observations confirm the prediction of Villian [40] in magnetic insulators with non-magnetic impurities, which have been found to be responsible the magnetic frustration and spin-glass like ordering of the transverse spin component.

Chapter 4

Negative Magnetization and Compensation Effect in Co_2TiO_4

4.1 Literature Review:

In the previous chapter we discussed the detailed magnetic structure of Co_2SnO_4; in this chapter we extend these studies for its sister compound cobalt-orthotitanate (Co_2TiO_4). Magnetization reversal and negative magnetization has been widely discussed in recent years because of their technological applications in spintronic devices [57, 60, 151 -154]. The magnetization reversal is defined as a crossover of dc magnetization value from a positive to a negative value as the temperature decreases below its long-range ordering. This phenomenon has been debated in literature in a variety of magnetic materials such as spinel ferrites, perovskites, molecular magnets, garnets, intermetallic alloys and multilayers [58]. Several intrinsic properties, e.g. size of the magnetic ions and their exchange interactions, global crystal structure of the compound, magnetic anisotropy, and different temperature dependence of the magnetization of individual cations sitting in the sublattice play a very important role on the magnetization reversal of a compound. Moreover, magnetization reversal and negative magnetization have gained technological importance because of their applications in the field of magneto-electronic switching devices with positive and negative stable states of magnetization under moderate applied fields. During 1950's Néel first observed the phenomenon of magnetization reversal in spinel ferrites. Nevertheless, the theoretical research related to such phenomena was reported a little earlier (in 1948's) than the experimental findings [52]. However, such a fundamental issue in magnetism, has not been paid enough attention in the literature until recent years [155-157]. Therefore, in this chapter, we focus on the magnetization reversal and negative magnetization in Co_2TiO_4 whose crystal structure is identical to Co_2SnO_4. In the previous chapter we discussed the nature of magnetic ordering in the spinel Co_2SnO_4, for which, the distributions of the cations on the A- and the B-sites were established to be $[Co^{2+}]_A[Co^{2+}Sn^{4+}]_BO_4$. Analysis of the temperature dependence of both the ac and dc magnetic susceptibilities, and specific heat measurements showed that Co_2SnO_4 is a ferrimagnet due to different magnetic moments of Co^{2+} sitting at the A- and the B-sites below its ordering temperature ~ 41 K.

Co_2TiO_4 is isostructural to Co_2SnO_4, in which, non-magnetic 'Sn' plays a similar role of 'Ti'. Although a few are available in the literature dealing with the nature of magnetism in Co_2TiO_4, the results have been controversial. Magnetization studies by Hubsch *et al.* reported ferrimagnetic ordering in Co_2TiO_4 with T_N ~ 55 K followed by spin glass transition at T_{SG} ~ 46 K with a magnetic compensation effect near 30 K [77 - 78]. However, later ac-susceptibility studies by Srivastava *et al.* [79] showed no indication of T_N ~ 55 K, rather only a single peak in χ_{ac} near 48 K when $H_{dc} = 0$. The temperature dependence of specific heat $C_P(T)$ of Co_2TiO_4 by Ogawa and Waki [80] reported only a weak transition near 49 K, which was associated with ferrimagnetic ordering. This indicates the absence of a proper transition near 55 K [80]. In all these reports, it has been assumed that the electronic state of 'Ti' in Co_2TiO_4 is Ti^{4+}, similar to Sn^{4+} in Co_2SnO_4 [77, 155 - 157].

In this chapter, we investigated the magnetic properties of Co_2TiO_4 in a very detailed way, aiming to address the unsettled issues listed above. We also examined the similarities and differences in the magnetic properties of the isostructural compounds Co_2TiO_4 and Co_2SnO_4. Differences such as why the compensation effect observed in Co_2TiO_4 near 30 K was not visible in Co_2SnO_4 despite of the identical electronic states of Co in both the systems. In these studies, we employed various characterization techniques, such as, X-ray diffraction (XRD), X-ray photoelectron spectroscopy (XPS), temperature and magnetic field dependence of the ac and dc magnetic susceptibilities, and specific-heat measurements to unravel the nature of magnetic ordering in Co_2TiO_4. In the following section we present a comprehensive experimental details including the synthesis procedure.

4.2 Experimental Details:

The polycrystalline Co_2TiO_4 samples were synthesized by standard solid state reaction method starting with stoichiometric amounts of Co_3O_4 (Alfa Aesar, purity 99.99%), and TiO_2 (Alfa Aesar, purity 99.99%) as precursors. Appropriate amounts of these materials were first ground in an agate mortar and sieved through 240 mesh. The mixed powders were pressed into cylindrical pellets of diameter ~ 13 mm using a hydraulic press with a maximum load of 5 ton per cm^2. The pellets of Co_2TiO_4 were finally sintered at 1120 - 1200ºC for 18 h in air to yield the desired compound without any impurities or unreacted TiO_2 precursor. The structural characterization was performed using PHILIPS PW 1050 X-ray powder diffractometer with Co-K_α radiation of wavelength 1.7889 Å, and a Rigaku X-ray diffractometer (model: TTRAX III) with Cu-K_α radiation (λ = 1.54056 Å). We also performed the Rietveld refinement of the diffraction patterns using FullProf program which confirmed the phase purity of the samples (Figure 4.1). Both dc-magnetization and frequency dependence (0.17 Hz - 1.2 kHz) of ac-magnetic susceptibility measurements were performed using a superconducting quantum interference device (SQUID) based magnetometer from Quantum Design with temperature capabilities of 2 K – 320 K and magnetic field (H) up to ± 90 kOe. The low temperature heat capacity data ($C_P(T)$) were recorded by means of a physical property measurement system (PPMS), from Quantum Design. The surface chemical composition of both the bulk samples were analyzed by means of XPS measurements performed with a dual source VG Microtech XPS microprobe system using Al-K_α radiation (1486.8 eV) source at a base pressure of 8×10^{-10} Torr. The XPS data was collected from 0 to 1100 eV of binding energy (B.E.) which is acquired with constant pass energy of 100 eV. All the spectra were analyzed using Gaussian-Lorentzian curve fitting.

4.3 Results and Discussion:

4.3.1 Structural Characterization

Figure 4.1(a) shows the XRD pattern of the Co_2TiO_4 polycrystalline sample along with the Rietveld refined data performed using FullProf program, the XRD pattern of Co_2SnO_4 also shown in this figure 4.1(b) for the sake of comparison. These patterns are consistent with the standard cubic spinel phase with space group *Fd-3m* (227). However, the lattice parameters obtained for Co_2TiO_4 (a = 8.45 Å) are slightly less than that of Co_2SnO_4 (a = 8.66 Å). Such variation in the lattice parameters is generally associated with the different ionic radii of the constituent

Table 4.1: The list of lattice parameters (a = b = c), bond lengths and bond angles in Co_2SnO_4 and Co_2TiO_4. (The interaxial angles $\alpha = \beta = \gamma = 90°$)

System	Lattice Parameter	Bond Length		Bond Angle	
		A-O	B-O	A-O-B	B-O-B
Co_2TiO_4	8.45±0.01Å	1.98±0.011Å	2.03±0.017Å	121.68°±0.612°	94.95°±0.478°
Co_2SnO_4	8.66±0.02Å	1.88±0.02Å	2.16±0.021Å	125.01°±0.625°	90.37°±0.452°

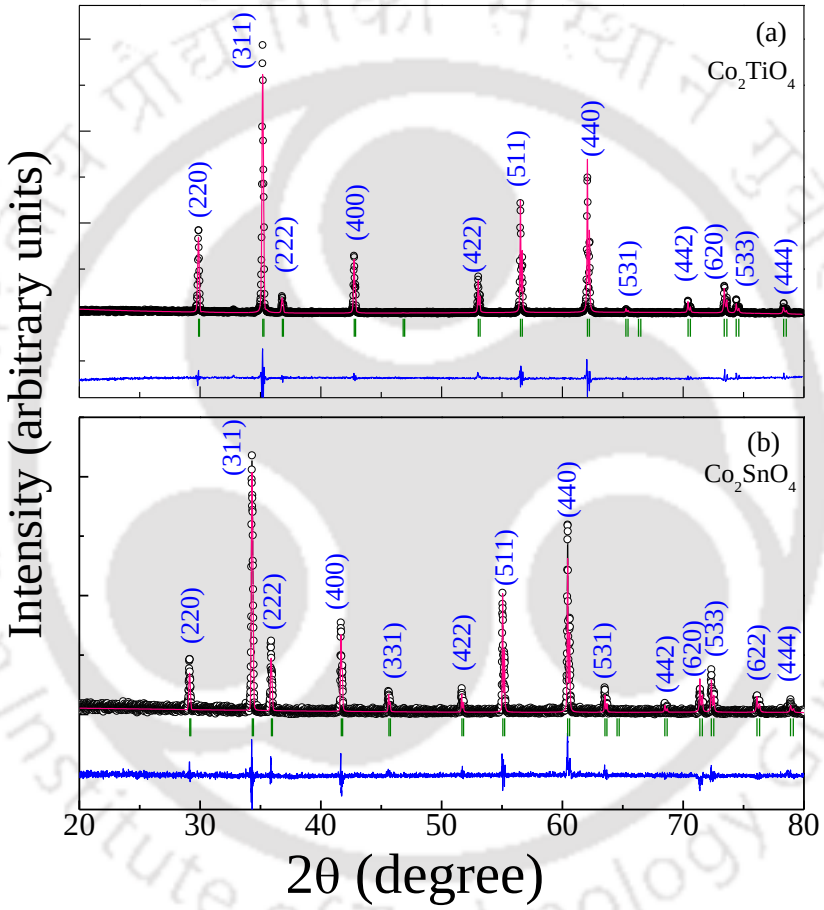

Figure 4.1: X-ray diffraction patterns of (a) Co_2TiO_4 and (b) Co_2SnO_4. The scattered symbols represent the experimental data whereas the red lines depict Rietveld refined data. The vertical lines represent the Bragg positions and the bottom blue line shows the difference between the experimental and calculated intensity.

elements. Since the ionic radius of tetravalent stannous ion (Sn^{4+} = 0.69 Å) is slightly greater than that of the titanium ion (either Ti^{4+} = 0.605 Å or Ti^{3+} = 0.67 Å), larger unit cell dimensions of Co_2SnO_4 as compared to that of Co_2TiO_4 is expected. On the other hand, the ionic radius of Co^{2+} ions in tetrahedral sites with coordination number four is smaller ($Co_{Tetra\text{-}A}^{2+}$ = 0.58 Å) than that in high spin octahedral sites with six coordination ($Co_{Octa\text{-}}$

$_B{}^{2+}$ = 0.745 Å). Table-4.1 summarizes the bond lengths and bond angles in both Co_2TiO_4 and Co_2SnO_4 estimated from the refinement process. It is evident that the average bond length (B-O) between the oxygen ion and elements present in the octahedral sites of Co_2SnO_4 are higher than that in Co_2TiO_4 while the reverse is true for the tetrahedral sites. Such differences in bond lengths in the octahedral and tetrahedral sites in the two systems result from the difference in the ionic sizes. Since the 'Sn' ion is larger than the 'Ti' ions, the B-O bond length in Co_2SnO_4 is greater than that in Co_2TiO_4, resulting in larger lattice parameter of Co_2SnO_4 than that of Co_2TiO_4 as observed experimentally.

4.3.2 X-ray Photoelectron Spectroscopy:

Figure 4.2 (a), (b) and (c) shows the intensity of XPS spectra versus binding energy of the Co-2p core levels for pure Co_3O_4, Co_2TiO_4 and Co_2SnO_4 systems, respectively. All these spectra exhibit two sharp peaks characteristic of Co-$2p_{3/2}$ and Co-$2p_{1/2}$ together with the weak intensity satellite peaks shown by arrows at 786.7 eV (S_1) and 802.91 eV (S_2). It is well known that both Co^{2+} and Co^{3+} exhibit similar binding energy peaks in XPS data with a sharp transition near 780 eV identified with $2p_{3/2}$ level and second peak near 796 eV identified with $2p_{1/2}$ level. However, the energy splitting (ΔE) between the two levels due to spin-orbit coupling should be different for the Co^{2+} and Co^{3+} configurations with ΔE = 15.0 eV for Co^{3+} and ΔE = 15.7 eV for Co^{2+} [112 - 114]. The XPS data in figure 4.2(a) for the spinel Co_3O_4 which contains both Co^{2+} and Co^{3+} ions distributed on the A and the B-sites as $[Co^{2+}]_A[2Co^{3+}]_BO_4$ clearly shows the presence of doublet at D_1 = 779.84 eV and D_2 = 780.34 eV for the Co-$2p_{3/2}$ level and a doublet for Co-$2p_{1/2}$ level centered at D_3 = 794.84 eV and D_4 = 796.09 eV. The separations between the doublet peaks are $\Delta E_{D1\text{-}D3}$ = 15 eV and $\Delta E_{D2\text{-}D4}$ = 15.75 eV which are close to the above mentioned values for Co^{3+} and Co^{2+} respectively, thus confirming the presence of Co^{3+} and Co^{2+} in Co_3O_4. These results are in good agreement with the previously reported data by Chuang *et al.* [158].

Figure 4.2(b) shows the core level XPS spectra of Co-$2p_{3/2}$ and Co-$2p_{1/2}$ for the spinel Co_2TiO_4. If the distribution of ions in Co_2TiO_4 is $[Co^{2+}][Co^{2+}Ti^{4+}]O_4$, as has been assumed in previous studies, then this system should not exhibit any Co^{3+} character. However, our XPS studies in Co_2TiO_4 (figure 4.2b) show clear signatures of Co^{3+} state in addition to the Co^{2+} state in terms of doublets discussed above for Co_3O_4. For the XPS spectra of Co-$2p_{3/2}$ and Co-$2p_{1/2}$ levels, the simulated Gaussian-Lorentzian fitting yields two different intensity peaks with narrow separation labeled by P_1 and P_2 for $2p_{3/2}$ and P_3 and P_4 for $2p_{1/2}$ as shown in figure 4.2b. The observed difference between the doublets $\Delta E_{P1\text{-}P3}$ = 14.98 eV and $\Delta E_{P2\text{-}P4}$ = 15.43 eV provides the signatures of the Co^{3+} and Co^{2+} respectively, as compared to the expected values of ΔE = 15.0 eV for Co^{3+} and ΔE = 15.7 eV for Co^{2+}. On the other hand, for Co_2SnO_4 case the data shown in figure 4.2c gives ΔE = 15.7 eV characteristic of Co^{2+} only and no additional signatures for the Co^{3+} state are noticed in Co_2SnO_4 as discussed in the previous chapter.

Next, we discuss the electronic states of 'Ti', 'Sn' and 'O'. For TiO_2 with 'Ti^{4+}' as the electronic state of titanium, binding energy for the Ti-$2p_{3/2}$ state is observed at 459.5 eV [127]. However, in the case of Co_2TiO_4 the maximum intensity peak for Ti-$2p_{3/2}$ appears at 457.65 eV (figure 4.2d), while the second maximum intensity

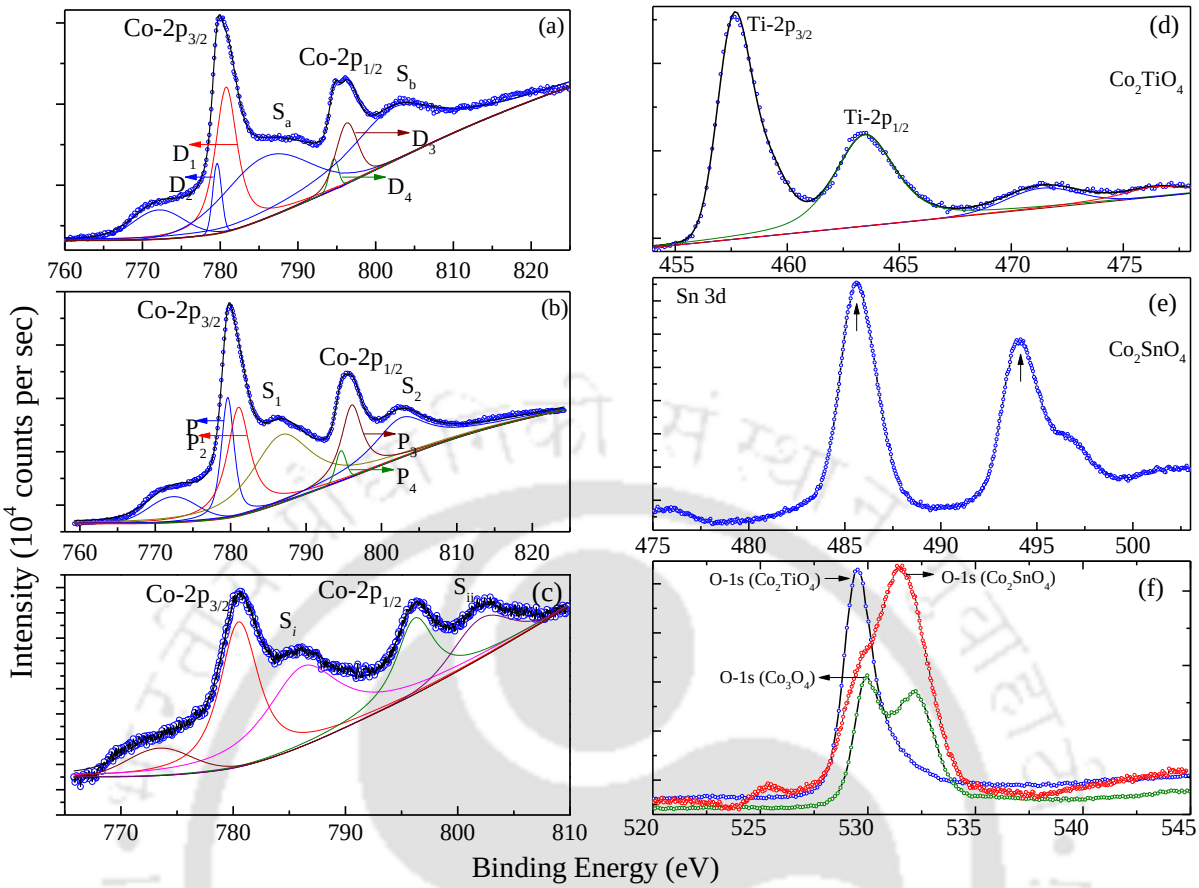

Figure 4.2: The left hand side panel shows the X-ray photoelectron spectra (XPS) of Co-2*p* peaks of (a) Co_3O_4 (b) Co_2TiO_4, and (c) Co_2SnO_4. Whereas, right hand side panel shows the XPS spectra of (d) Ti-2p (e) Sn-3d, and (f) O-1s peaks of Co_2TiO_4, Co_2SnO_4, Co_3O_4 bulk systems.

peak corresponding to Ti-$2p_{1/2}$ is centered at 463.53 eV. This result rules out the presence of Ti^{4+} state in Co_2TiO_4. Instead the observed position of the peak at 457.65 eV agrees with the previously reported data of Ti^{3+} surface defects at 457.7 eV in TiO_2 system [159]. In addition, these results also rule out the presence of any metallic 'Ti' ions in Co_2TiO_4 matrix which usually show their signatures in XPS spectra at 454 eV. For Co_2SnO_4, the sharp peaks observed at 485.65 eV and 494.8 eV and a weak shoulder at 496.75 eV in figure 4.2(e) are the characteristic signatures of Sn^{4+} state [111, 112]. Finally, figure 4.2(f) shows O-1s core level spectra for all the three systems with some signature of weakly bound surface oxygen at binding energy close to 533 eV [112 - 114, 158, 160, 161]. The major conclusions from these comparative XPS studies in Co_3O_4, Co_2TiO_4 and Co_2SnO_4 are that electronically, Co_2TiO_4 = $[Co^{2+}][Co^{3+}Ti^{3+}]O_4$ whereas Co_2SnO_4 = $[Co^{2+}][Co^{2+}Sn^{4+}]O_4$. This difference in the electronic state of 'Co' ions on the B-sites of these two systems has never been reported before, and, as we will show, it leads to major differences in the observed magnetic properties of Co_2TiO_4 from those of Co_2SnO_4.

4.3.3 Temperature Dependence of the DC-Magnetic Susceptibility:

The temperature dependence of inverse paramagnetic susceptibility ($\chi^{-1}(T)$) of both Co_2TiO_4 and Co_2SnO_4 for T > 45 K recorded under zero field cooled (ZFC) conditions is shown in figure 4.3. The blue circles and olive squares represents experimental points and red and brown solid lines as fits to the Néel expression for ferrimagnets viz. $(1/\chi) = (T/C) + (1/\chi_o) - [\sigma_o/(T- \theta)]$. The fit for Co_2TiO_4 yields the following parameters: $\chi_o = 41.92\times10^{-3}$ emu/mol-Oe, $\sigma_o = 31.55$ mol-Oe-K/emu, C = 5.245 emu-K/mol-Oe, $\theta = 49.85$ K. The ratio $C/\chi_o = T_a = 125.1$ K represents the strength of the antiferromagnetic exchange coupling between the spins on the A and B sites, and is often termed as the asymptotic Curie Temperature T_a. In Table 4.2, various fitting parameters obtained from the Néel expression for ferrimagnetism of both Co_2TiO_4 and Co_2SnO_4 are summarized. The effective magnetic moment $\mu_{eff} = 6.5\ \mu_B$ per formula unit (f.u.) of Co_2TiO_4 is determined using $C = N\mu^2_{eff}/3k_B$. A similar calculation yielded $\mu_{eff} = 6.25\ \mu_B$ per f.u. of $Co_2SnO_4 = [Co^{2+}][Co^{2+}Sn^{4+}]O_4$. Using $\mu^2_{eff} = [\mu(A)]^2 + [\mu(B)]^2$ with $\mu(A) = 3.87\ \mu_B$ for Co^{2+} ions on the A-sites with spin S = 3/2 and g = 2 since its tetrahedral co-ordination does not allow orbital contribution, yields $\mu(B) = 4.91\ \mu_B$ for Co_2SnO_4. This argument for Co_2SnO_4 yields ferrimagnetism below 'T_N' with net small moment of $1.04\ \mu_B$ per f.u. For Co_2TiO_4 with the electronic configuration of $[Co^{2+}][Co^{3+}Ti^{3+}]O_4$ determined using XPS, the above analysis yields $\mu_{eff} = 6.5\ \mu_B$ per f.u. Again using $\mu(A) = 3.87\ \mu_B$ for Co^{2+} ions on the A-site as in Co_2SnO_4, yields $\mu(B) = 5.19\ \mu_B$ for ions on the B-site. The trivalent titanium ions Ti^{3+} with its $3d^1$ electronic configuration has magnetic moment $\mu = 1.73\ \mu_B$ yielding $\mu(Co^{3+}) = 4.89\ \mu_B$ as the moment for the Co^{3+} ion on the B-site. In the high spin state, Co^{3+} ions should have spin only $\mu = 4.9\ \mu_B$ which agrees with the above estimate.

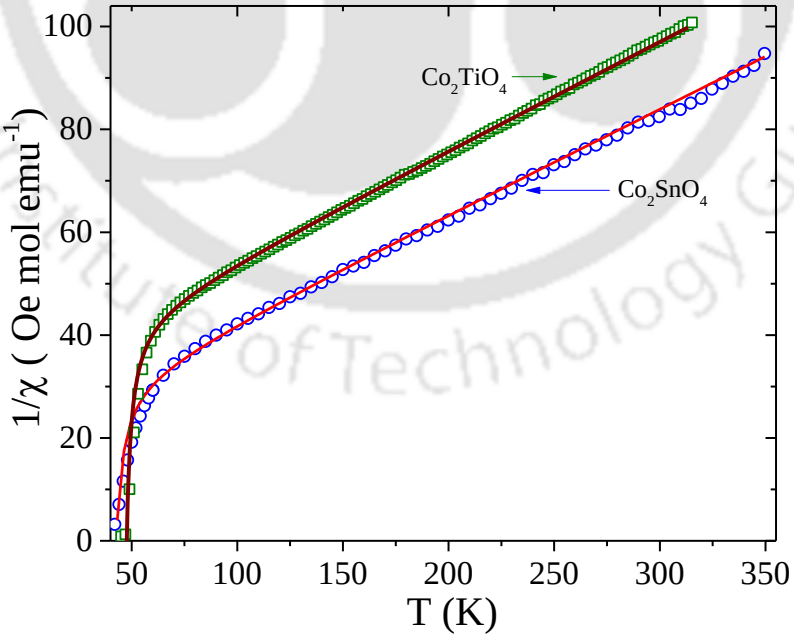

Figure 4.3. Temperature variation of the inverse paramagnetic susceptibility $\chi^{-1}(T)$ *of* Co_2TiO_4 and Co_2SnO_4 systems. The solid lines are best-fits to the Néel's expression for ferrimagnets discussed in the section 4.3.3.

Table 4.2: The list of various parameters obtained from the Néel fits of χ^{-1} versus T curve recorded under zero-field-cooled condition.

System	C (emu K $mol^{-1}Oe^{-1}$)	χ_o (emu $mol^{-1}Oe^{-1}$)	σ_o ($emu^{-1}Oe$ mol K)	θ (K)	μ_{eff} (μ_B)	μ (A) (μ_B)	μ (B) (μ_B)
Co_2TiO_4	5.245	0.0419	31.55	49.85	6.5	3.87	5.19
		N_{AA}	N_{AB}	N_{BB}	J_{AA}	J_{AB}	J_{BB}
		17.319	35.700	12.720	3.25 k_B	4.47 k_B	3.18 k_B
Co_2SnO_4	4.889	0.0436	102.370	39.5	6.25	3.87	4.91
		N_{AA}	N_{AB}	N_{BB}	J_{AA}	J_{AB}	J_{BB}
		21.564	33.201	10.678	4.05 k_B	5.26 k_B	4.28 k_B

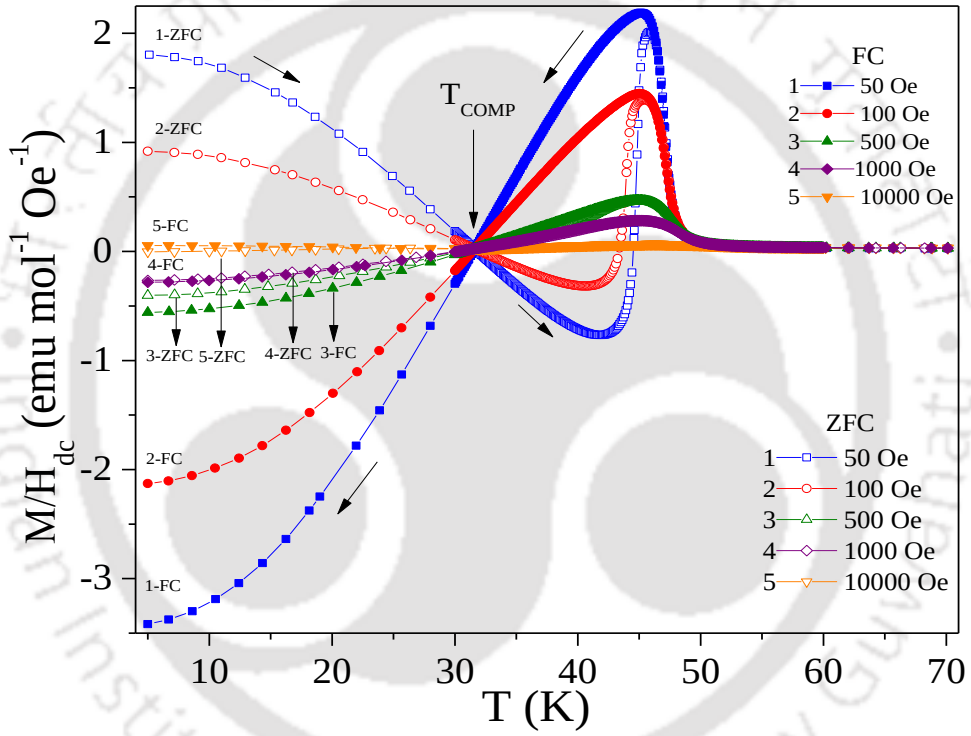

Figure 4.4: Temperature dependence of dc-magnetic susceptibility $\chi(T)$ (= M/H_{dc} (T)) for Co_2TiO_4 measured under both zero-field-cooled (ZFC)and field-cooled (FC)conditions recorded at various magnetic fields in the range 50 Oe ≤ H_{dc} ≤ 10 kOe.

So an important conclusion from this comparative analysis of the paramagnetic susceptibilities is that μ_{eff} = 6.5 μ_B per f.u. of Co_2TiO_4 is higher than that in Co_2SnO_4. This leads to the calculated net ferrimagnetic moment of μ = 1.32 μ_B per f.u. below T_N which is higher than μ = 1.04 μ_B per f.u. of Co_2SnO_4 below its T_N. This information below is used to explain the observed differences in the measured magnetic properties of Co_2TiO_4 against Co_2SnO_4 below T_N. Another important difference between the two systems is that in Co_2TiO_4, the B-site is occupied by Co^{3+} and Ti^{3+} both of which have magnetic moments unlike the case of Co_2SnO_4 in which the Sn^{4+} ion on the B-

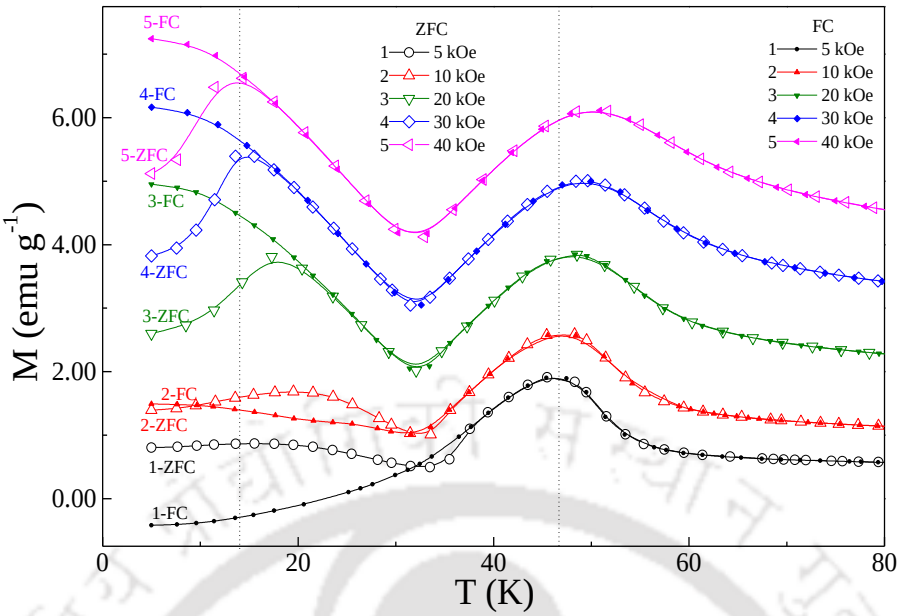

Figure 4.5: High-field (5 kOe ≤ H_{dc} ≤ 40 kOe) magnetization (M) versus temperature (T) data for Co_2TiO_4 measured under both the ZFC and FC conditions.

site does not have a magnetic moment. Therefore, the effects of magnetic dilution should be less prominent in Co_2TiO_4. Figure 4.4 shows the temperature dependence of χ_{dc} (= M/H_{dc}) for H_{dc} = 50, 100, 500, 1000 and 10,000 Oe of polycrystalline Co_2TiO_4 sample. The data are shown for both the traditional ZFC and FC cases. The significant features of the data are: (*a*) χ peaking at a temperature near 46 K suggesting ferrimagnetic ordering, and (*b*) a crossover in sign for χ(ZFC) and χ(FC) at a compensation temperature near 32 K where the magnetization of the two sublattices balance each other. These observations are similar to those reported by Hubsch *et al.* in Co_2TiO_4 and are discussed in more detail later [77]. The temperature dependence of the magnetization (M) for the ZFC and FC cases under applied H_{dc} = 5, 10, 20, 30 and 40 kOe is shown in figure 4.5.

Several features of the data are noteworthy: (*i*) the compensation temperature $T_{COMP} \simeq 32$ K is independent of applied H_{dc} and compensation is not complete, in that M at T_{COMP} is not zero but increases with increase in H_{dc}, (*ii*) the position of the peak temperature near 46 K shifts slightly to higher temperatures with increase in H_{dc}, and (*iii*) the temperature for which M(FC) bifurcates from M(ZFC) shifts to lower temperature with increase in H_{dc}. Very similar features have been recently observed in another spinel Ni-Fe-Sb-O spinel [161]. In order to compare the above observations in Co_2TiO_4 with similar measurements in Co_2SnO_4, new M/H_{dc} data on Co_2SnO_4 is shown in figure 4.6 for the ZFC and FC cases in H_{dc} = 100, 500, 1000 and 5000 Oe. Although there are some similarities with the data for Co_2TiO_4 in figure 4.4, the behavior near the compensation temperature of 32 K in Co_2TiO_4 is not observed in Co_2SnO_4. Instead, there is a bifurcation of the FC and ZFC data beginning near 7 K which is field-independent, and a second bifurcation at higher temperatures, the location of which is field-dependent. More information on these differences between the two systems become evident from the behavior of the hysteresis loop parameters in consonance with ac-magnetic susceptibility data which will be discussed in subsequent sections

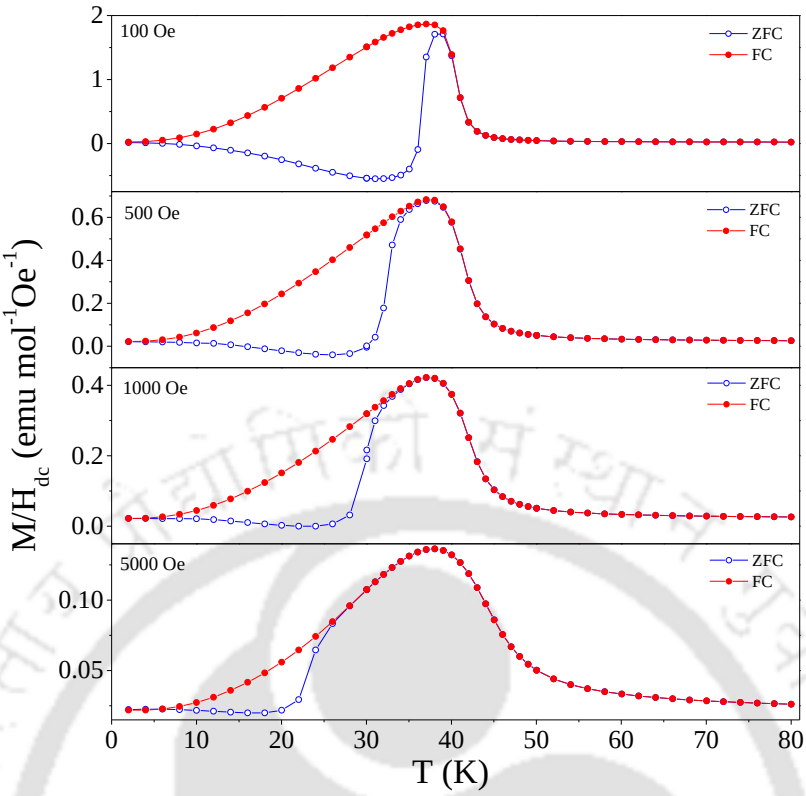

Figure 4.6. Temperature dependence of dc-magnetic susceptibility $\chi(T)$ (= M/H_{dc} (T)) for Co_2SnO_4 measured under both zero-field-cooled (ZFC) and field-cooled (FC) conditions recorded at various magnetic fields.

The paper by Hubsch *et al.* [77] on the nature of magnetic ordering in Co_2TiO_4 reported T_N = 55 K followed by a spin-glass ordering at T_{SG} = 46 K. However, between 55 K and 46 K, the remanence magnetization M_R was extremely small reaching a peak value of only about 0.05 emu/g at 50 K, and then becoming zero again at 46 K. Below 46 K, the M_R increased rapidly, peaking at M_R = 0.7 emu/g at 40 K before compensation sets in. In the specific-heat C_P versus T measurements of Ogawa *et al.* [80] a peak in C_P is observed only near 48 K, although under non-zero applied H_{dc}, this feature becomes more diffused and shifts to higher temperatures. The phenomenon of compensation observed near 32 K, in figure 4.4 and figure 4.5, confirms the earlier observation of Hubsch *et al.* [77] However, the compensation in Co_2TiO_4 is not complete because the magnetization measured at the minimum is not quite zero, and, it increases with magnetic field. In ferrimagnets with different magnetic moments on the A- and the B-sites, and having different temperature dependence, a complete compensation or at least a minimum in the observed moment $\mu(T) = \mu(A) - \mu(B)$ could occur at a certain temperature below T_N. The estimated magnetic moments on the A- and the B-sites of Co_2TiO_4 are sufficiently different with $\mu(A) = 3.87\ \mu_B$ and $\mu(B) = 5.19\ \mu_B$ as discussed earlier in Section 4.3.3. For comparison, in Co_2SnO_4 with smaller difference in $\mu(A) = 3.87\ \mu_B$ and $\mu(B) = 4.91\ \mu_B$, compensation is not as evident and clear-cut but below about 7 K, there is effectively no remanence or coercivity implying compensation. Another evidence for the difference in the two systems in this regard is the difference in the measured remanence M_R. For Co_2SnO_4, maximum in M_R = 0.45

emu/g was observed near 30 K whereas, in Co_2TiO_4, maximum in M_R = 3 emu/g observed near 10 K, which was larger by a factor of about six (will be discussed in section 4.3.5). The ratio of the observed M_R in Co_2TiO_4 and Co_2SnO_4 scales well with the difference in their μ(A) and μ(B) values when normalized with their molecular weights.

4.3.4 Temperature Dependence of the AC-Magnetic Susceptibilities:

The temperature dependence of the ac-magnetic susceptibilities, χ′(T) and χ″(T), were measured using ac-magnetic field frequency (f_m) of 2 Hz with amplitude h_{ac} = 4 Oe superimposed with various 'dc' fields H_{dc} between 10 Oe and 30 Oe. These results are shown in figure 4.7 in which one can clearly see the splitting of a single peak near 46.5 K into two peaks when H_{dc} is increased. In the χ′ versus T data, the higher temperature peak shifts toward higher temperature side with increase in H_{dc}, whereas, the reverse is true for the lower temperature peak. The transition at 46.5 K was probed further by measuring temperature dependence of χ′ and χ″ at nine different frequencies f_m between 0.17 Hz and 1202 Hz using h_{ac} = 4 Oe and H_{dc} = 0 (figure 4.8). For χ′, the peak at 46.8 K measured at the lowest frequency (0.17 Hz) shifts to higher temperatures with increase in frequency, approaching near 47.11 K at f_m = 1202 Hz. This kind of frequency dependence of the peak-shift in the ac susceptibility curves are qualitatively similar to what we discussed in previous chapter for Co_2SnO_4 system. However, a detailed quantitative analysis of the data revealed a marked difference between the two systems. As in the case of Co_2SnO_4 (section 3.3.4), we tried to analyze the frequency dependence seen of χ′(T) and χ″(T) in Co_2TiO_4 using both the

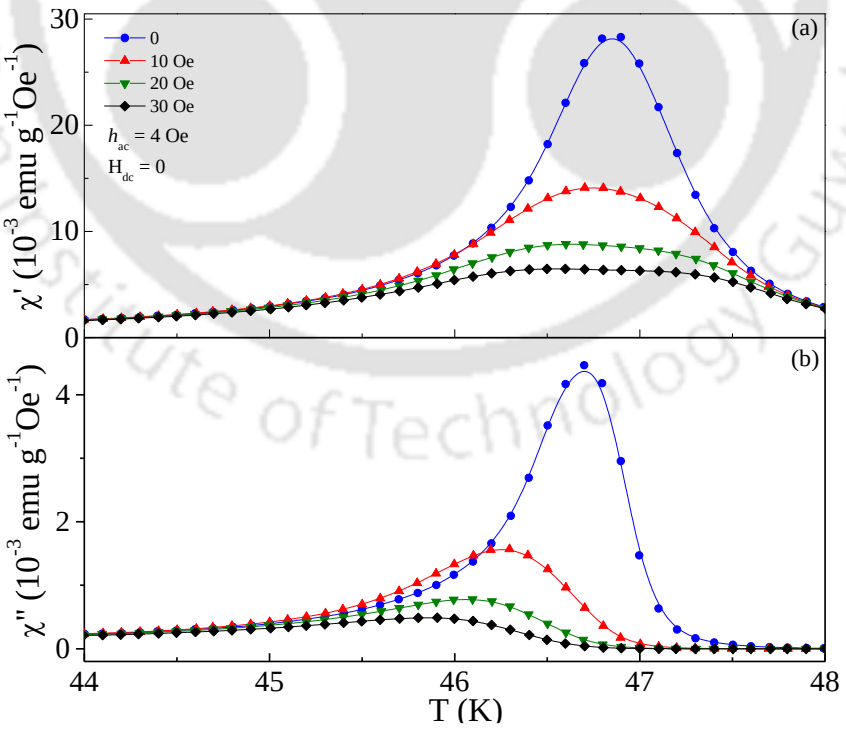

Figure 4.7: Temperature variation of the ac-magnetic susceptibility (a) $\chi'(T)$, and (b) $\chi''(T)$ for Co_2TiO_4 measured at 2 Hz in h_{ac}= 4 Oe with superposed dc-bias fields H_{dc} = 0, 10, 20 and 30 Oe.

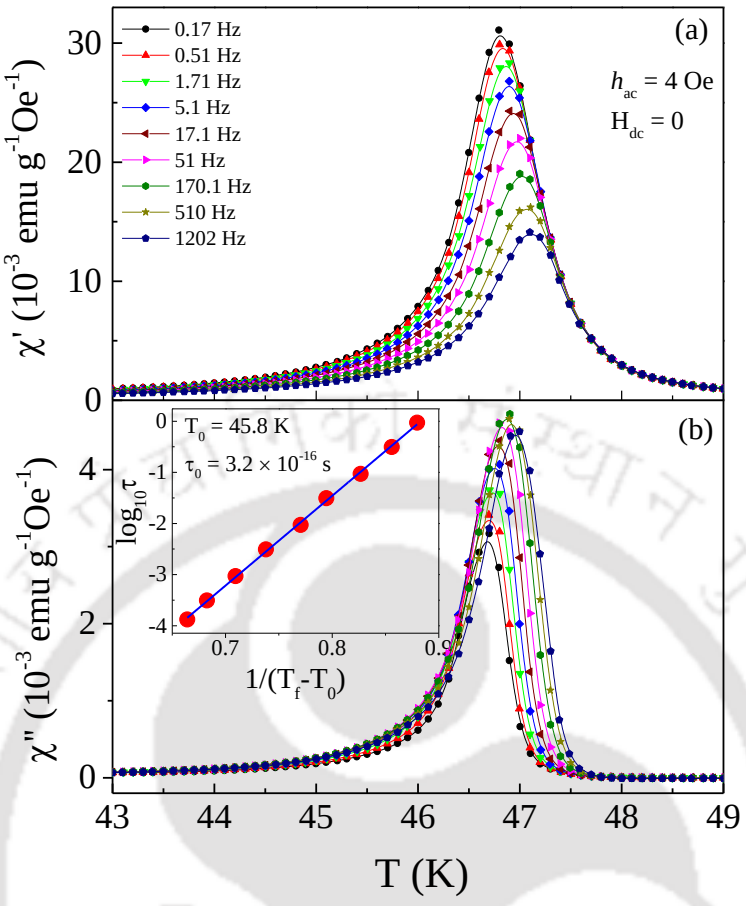

Figure 4.8: Temperature dependence of ac-magnetic susceptibilities (a) $\chi'(T)$ and (b) $\chi''(T)$ of Co_2TiO_4 measured at various frequencies between 0.17 Hz and 1202 Hz under warming conditions using h_{ac} = 4 Oe and H_{dc} = 0 Oe. The inset shows the best fits of the relaxation times to the Vogel-Fulcher law in Co_2TiO_4.

scaling laws: (*i*) the Vogel-Fulcher law (VFL; $\tau = \tau_o \exp(E_a/k_B(T - T_o))$, where τ_o is the relaxation time constant, T_o is a measure of the interaction between magnetic clusters, k_B is the Boltzmann constant and E_a is an activation energy parameter), and (*ii*) Power-law (PL) which describes the critical slowing down in a spin-glass phase transition at T_g, and is given by: $\tau = \tau_o ((T/T_g) - 1)^{-z\nu}$, where T_g is the freezing temperature, τ_o is related to the relaxation of the individual cluster magnetic moment and $z\nu$ is a critical exponent. Here $\tau = 1/\omega = 1/2\pi f$. While for Co_2SnO_4 case, (as discussed in section 3.3.4) we could obtain physically reasonable fit parameters using both the scaling laws albeit using a very limited temperature range, for Co_2TiO_4 the situation is different. In inset of figure 4.8 (b), we show the best representation of the data that was obtained using the Vogel-Fulcher law, with T_o = 45.8 K and $\tau_o = 3.2 \times 10^{-16}$ s. However, an attempt to fit the data using the power-law, yielded quite unphysical values of the fit parameters (viz. $\tau_o \sim 10^{-33}$ s and $z\nu > 16$), indicating the lack of proper spin-glass phase transition. Nonetheless, the main problem is the difficulty in deciding which law (either VFL or PL) is the best to decide the glassy nature. Soulietie and Tholence in 1985 tried to resolve such exasperating aspect and found that the Power-law gives better accountability of the experimental evidence of glassy behavior [162]. As we obtained physically reasonable fit parameters for Co_2TiO_4 using the VFL, however, PL gives quite unphysical values of the relaxation

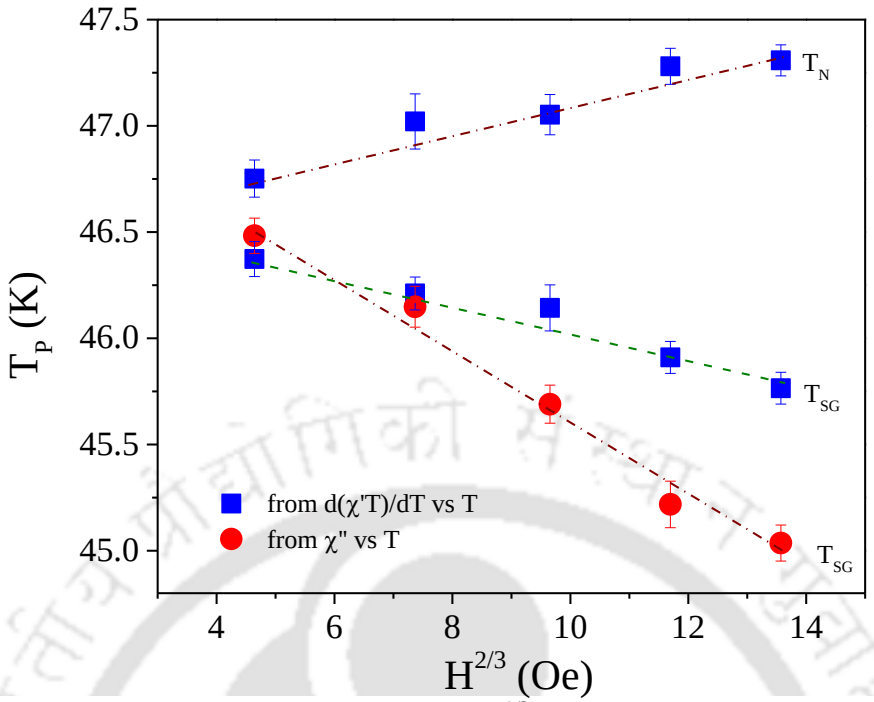

Figure 4.9: The de Almeida-Thouless (AT) line T_P versus $H^{2/3}$ of Co_2TiO_4. The dotted lines show the linear fit to the experimental data. Inset shows the field dependence of T_{SG} raised to 2/3 power obtained from dc-susceptibility measurement.

time constant ($\tau_o = 10^{-33}$ s) and critical exponent ($z\nu \sim 16$), indicating the lack of proper spin–glass transition. Although we saw systematic frequency dispersion of the peaks in $\chi'(T)$ and $\chi''(T)$ data and linear behavior in $H^{2/3}$ versus T_P (A-T line) (figure 4.9), but, using the PL fitting we concluded that the Co_2TiO_4 system exhibits pseudo-spin-glass properties rather than a proper real spin-glass ordering.

4.3.5 Temperature Dependence of the Hysteresis Loop Parameters:

The five cycle M versus H hysteresis loop measurements were performed on Co_2TiO_4 polycrystalline sample at selected temperatures between T = 5 K and 60 K in the magnetic field from -90 kOe to +90 kOe. The measurements were done in the ZFC (FC) protocol in which the sample is cooled in H_{dc} = 0 Oe (H_{dc} = 20 kOe) from the paramagnetic state to the measuring temperature followed by measurements of M versus H. For the data at the next temperature, the sample was again warmed to the paramagnetic state and cooled back to the next measurement temperature. Hysteresis loops, at four selected temperatures, shown in figure 4.10, exhibits that a weak ferromagnetic component M_{WF} is superimposed on a linear component with M_{WF} strongly temperature dependent. The inset of the figure 4.11 shows asymmetry in the M-H loops measured at 5 K under ZFC and FC (± 20 kOe) protocol. We used the standard definition of the coercivity $H_C = (H^+ - H^-)/2$, loop-shift or Exchange-Bias $H_{EB} = (H^+ + H^-)/2$ where $H^+(H^-)$ are magnetic field values for which M = 0, and the remanence M_R for the magnetization at H = 0 are used along with M_{MAX}, the measured magnetization at 90 kOe (shown in figure 4.12 a,b).

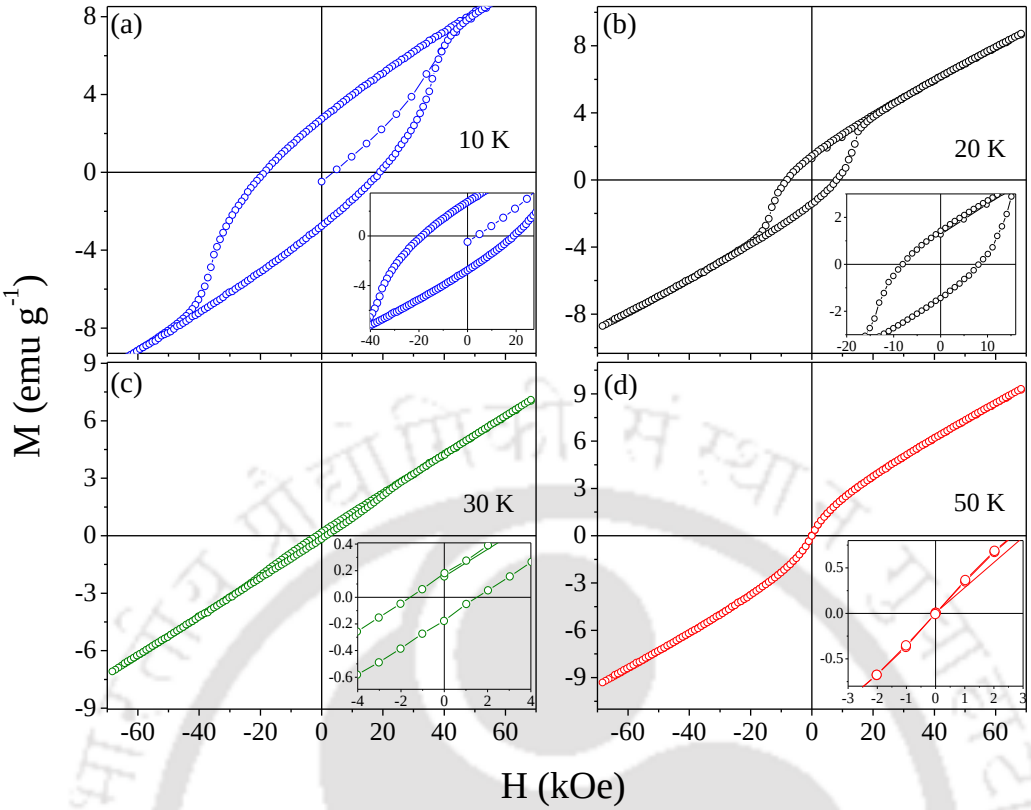

Figure 4.10: Magnetization versus field (M-H hysteresis loops) of Co_2TiO_4 are shown at selected temperatures of (a) 10 K, (b) 20 K, (c) 30 K and (d) 50 K recorded under zero-field-cooled (ZFC) condition. Insets show the zoomed view of M-H loops near origin displaying the asymmetry in the loops.

Note that below 10 K, all the M-H data appear like minor loops, thus, extracted magnitudes of H_C, H_{EB}, and M_R are underestimated significantly. Due to this reason we have not shown the data for T < 10 K. The noteworthy feature is the large magnitude of H_C ~ 20 kOe at low-temperatures. In addition, there is a minimum in M_R and M_{MAX} at 30 K, the temperature for which partial compensation of the two-sublattices was indicated in figure 4.4 and figure 4.5. Observation of non-zero M_R is the evidence for the presence of M_{WF}.

In the Stoner-Wohlfarth (SW) model of coercivity in single-domain particle, $H_C = K_A/M_S$, where K_A is the magneto-crystalline anisotropy constant and M_S is the saturation magnetization [124, 163]. Below T_N, $K_A \sim (M_S)^n$ where n is system dependent and can be as large as 10 [124, 163]. Therefore, in the SW model, H_C should continue to increase with decrease in temperature below T_N. In the plot of H_C versus T in figure 4.12a for Co_2TiO_4, an increase in H_C with a decrease in T is observed, reaching a peak at about 10 K below which H_C decreases and it is accompanied by the appearance of a very significant H_{EB}. In real systems, H_C is affected by impurities and grain boundaries which pin down the domain walls and prevent their rotation as the magnetic field is varied. The M versus T plot of figure 4.5 shows that below T_{COMP}, the FC and ZFC curves bifurcate at a certain temperature T_b, which decreases as H_{dc} increases. This is similar to the observation reported in Ni-hydroxide layered systems, [18, 164] where, this phenomenon was associated with the blocking temperature of nanocrystallites. In both Co_2TiO_4

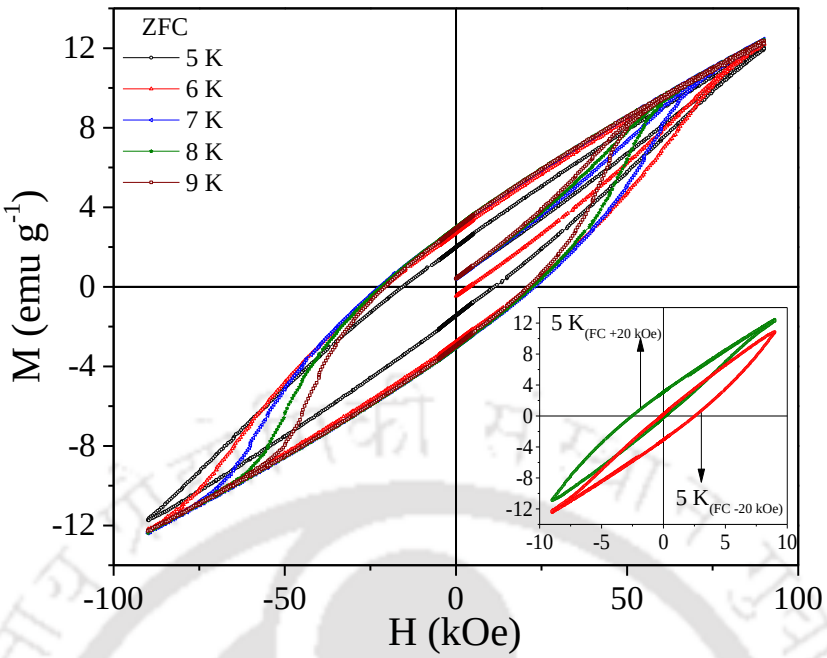

Figure 4.11: Magnetization versus field (M-H) hysteresis loops measured at low-temperatures T = 5 K, 6 K, 7 K, 8 K and 9 K under zero-field-cooled (ZFC) condition. The insets show asymmetry in the M-H loops measured at T = 5 K under FC (20 kOe) condition.

and Co_2SnO_4, the crystallite size is in the μm range. However, because of the substitution of the different magnetic ions with different magnetic moments on the B-sites, the formation of magnetic clusters is very likely. The bifurcation of the M(FC) and M(ZFC) curves in figure 4.5 and 4.6, at a specific temperature T_b, which decreases with increase in H_{dc}, which could be due to freezing of these magnetic clusters. The observations of very large H_C and H_{EB} –like behavior at 10 K, in Co_2TiO_4, could be a result from the inability of the spins to follow magnetic field in the frozen clusters.

Another noteworthy result in Co_2TiO_4 is the lack of saturation of the magnetization in H up to 90 kOe (figure 4.10 and 4.11). In the results reported by Hubsch *et al.* [77], lack of saturation was evident even up to 150 kOe. These results suggest a non-collinear ordering of spins in Co_2TiO_4. Preliminary neutron diffraction measurements by Hubsch *et al.* [77] reported an evidence for the canting of the spins, which is consistent with non-saturation of the magnetization. Qualitatively, this situation may be akin to that in the spinel Mn_3O_4, for which, the two sublattices were found to be inadequate to describe the magnetic structure below T_N [138]. In Co_2TiO_4, the B-sites are occupied by two different magnetic ions, Co^{3+} and Ti^{3+}, as reported here; therefore, at least a three-sublattice model is necessary to describe its magnetic structure. Srivastava *et al*. discussed a three-sublattice model in which magnitudes of the saturation magnetization and temperature dependence of paramagnetic susceptibility were used to solve for the exchange constants [165]. Since in Co_2TiO_4, magnetization does not saturate even up to 150 kOe as noted above, this model cannot be applied to Co_2TiO_4. Thus determining the nature of magnetic ordering of the spins below T_N in Co_2TiO_4 remains an outstanding challenge, both experimentally and theoretically.

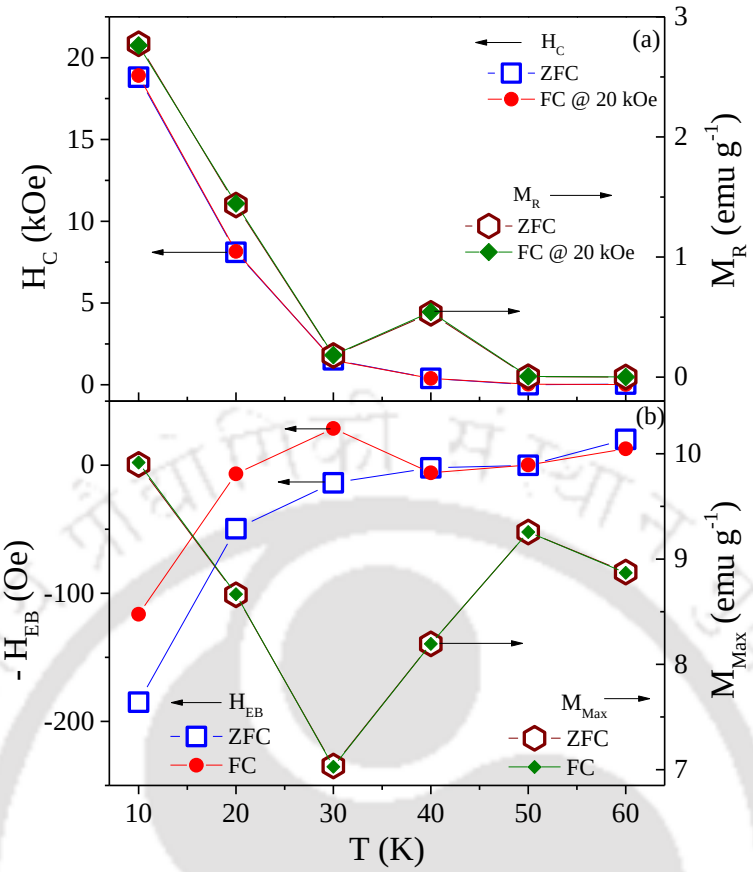

Figure 4.12: The temperature variation of (a) coercive field $H_C(T)$ and Remanence Magnetization M_R and (b) exchange bias $H_{EB}(T)$ and high field (H ~ 90 kOe) magnetization M_{MAX} measured under both ZFC and FC(20 kOe) conditions in Co_2TiO_4. The lines connecting the data points are visual guides.

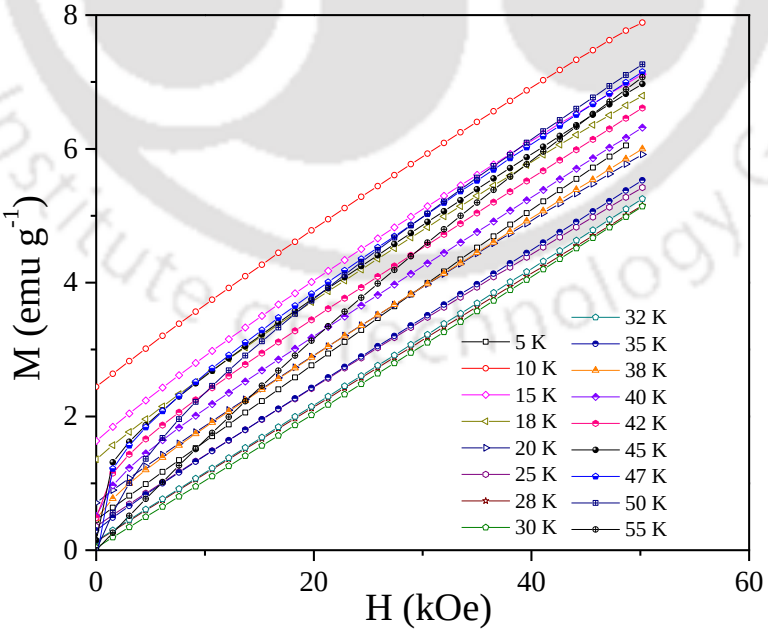

Figure 4.13: The magnetization versus field (M-H) isotherms of Co_2TiO_4 recorded at various temperatures 5 K ≤ T ≤ 55 K.

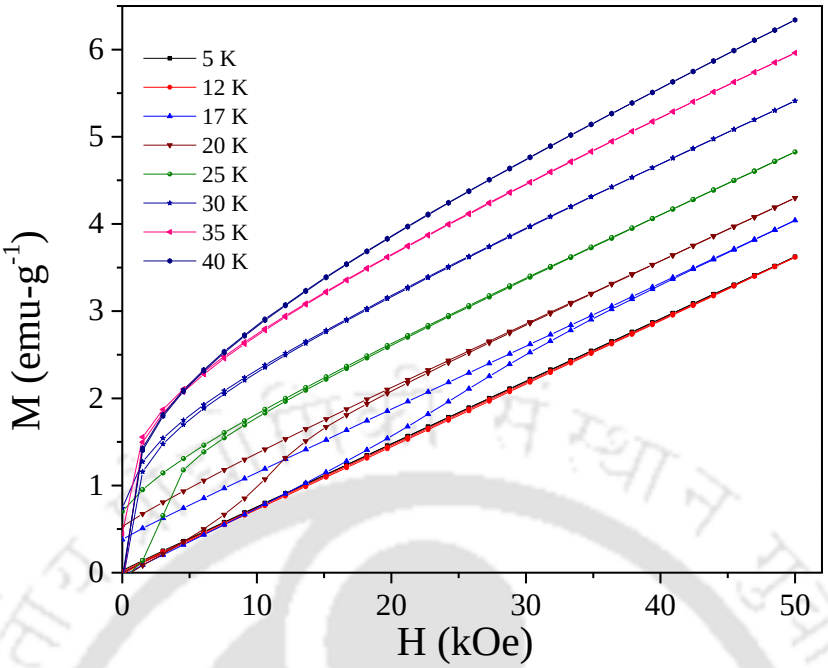

Figure 4.14: The magnetization versus field (M-H) isotherms of Co_2SnO_4 recorded at various temperatures 5 K ≤ T ≤ 40 K.

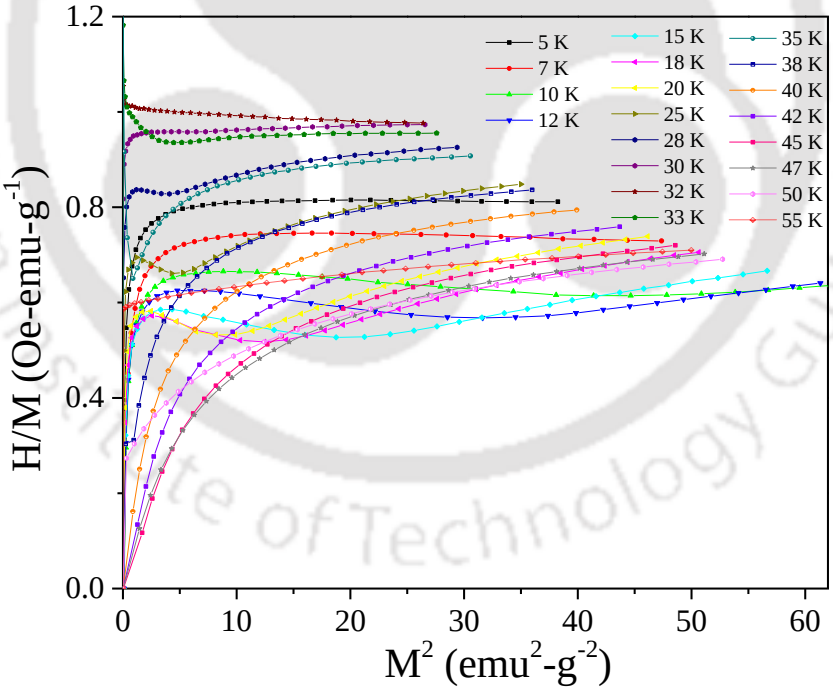

Figure 4.15: Arrott plots (H/M versus M^2) of Co_2TiO_4 computed from magnetization (M) field (H) isotherms recorded at different temperatures between 5 K and 55 K.

In order to understand the nature of magnetic transitions we plotted the ratio of magnetic field (H) to the value of magnetization (M) versus square of the magnetization (H/M versus M^2) curves. These curves are commonly

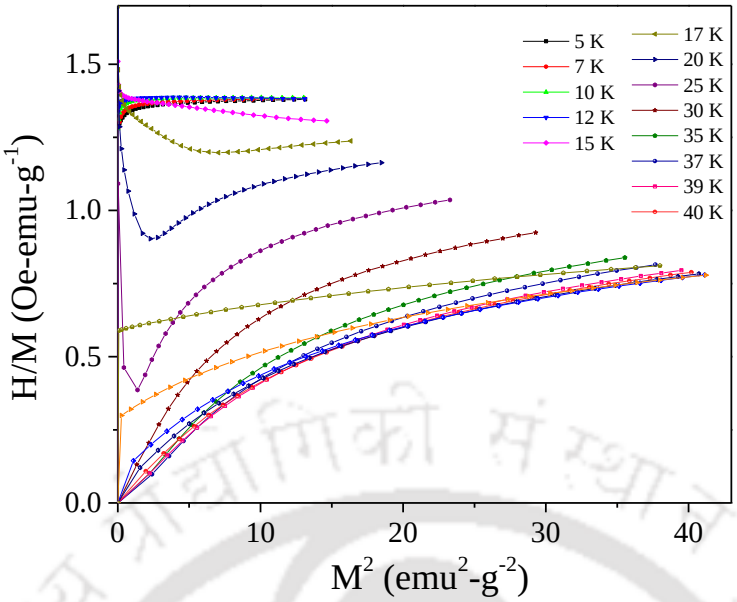

Figure 4.16: Arrott plots (H/M versus M^2) of Co_2SnO_4 computed from magnetization (M) field (H) isotherms recorded at different temperatures between 5 K and 40 K.

known as Arrott plots. These parameters were extracted from the isothermal magnetization (1^{st} quadrant M-H) curves recorded at various temperatures in the range of 5 – 48 K (figure 4.13 and 4.14) for both Co_2TiO_4 and Co_2SnO_4 (as depicted in figure 4.15 and 4.16). During the measurement of each M-H isotherms, the temperature was brought to 300 K to ensure that the measurement should begin from a virgin magnetic state without any magneto-thermal history, followed by a zero-field cooling. Also, the temperature difference (δT) between the two successive isotherms was set low in the region of the transition, whereas, δT was kept high for $T > T_{COMP}$. The magnetization values were recorded by increasing the magnetic field from zero to 50 kOe. A significant deviation from positive slope of the Arrott plots can be clearly seen in the region $T \leq T_{COMP} \leq T_N$ (figure 4.15). In particular, the isotherms recorded between 5 K and 32 K show negative slopes in the H/M versus M^2 plots confirming the magnetic field induced first-order discontinuous transition across 5-32 K consistent with the behavior of low-field $\chi_{dc}(T)$ plots discussed above.

The Arrott plots criterion successfully explains the nature of transitions in both isolated and mixed phase systems with sequential phase changes [166, 167]. Its applicability for the first-order phase transition replicates the fact that the magnetization value remains almost constant at low fields, and an abrupt jump in the magnetization value (metamagnetic-like character) occurs at a critical field called transition field (H_T), which corresponds to the point of maximum slope in the magnetization isotherm [166 - 170]. In the case of structurally coupled transitions, which are sensitive to the applied magnetic field, H_T gradually decreases with increasing temperature, and approaches to zero-near T_N [171]. Deviation from negative slopes are clearly noticeable on approaching the magnetically ordered regime 32 K ≤ T ≤ 48 K, indicating the second-order nature of the transition across Néel temperature (T_N) (figure 4.16).

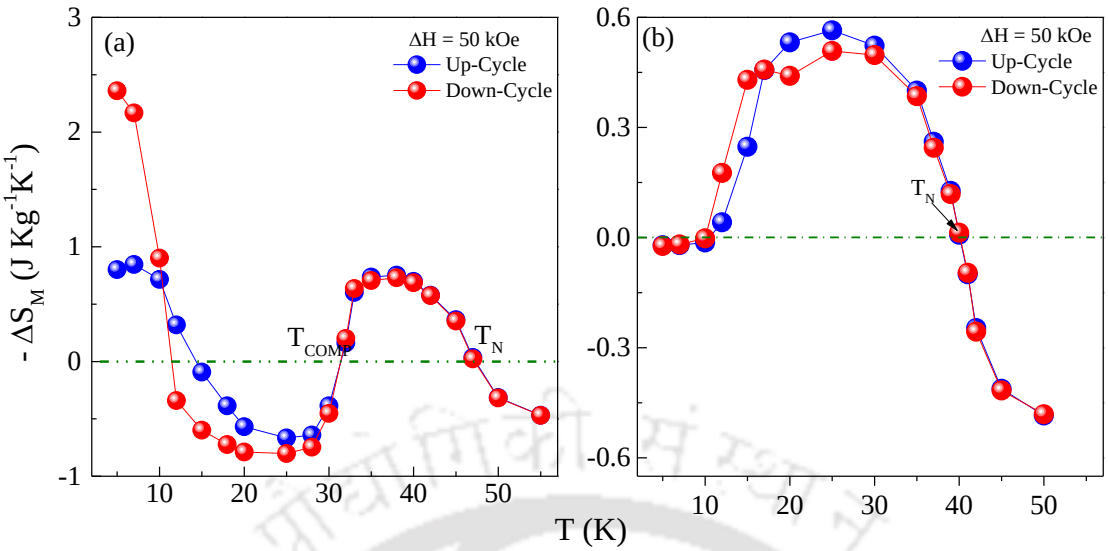

Figure 4.17: Temperature dependence of isothermal entropy change (ΔS(T)) computed from M-H isotherms using Maxwell equations for a field change ΔH = 50 kOe for (a) Co_2TiO_4 (b) Co_2SnO_4.

Using the M-H isotherms, magnetic field-induced isothermal entropy changes (ΔS) were derived from the Maxwell equation: $(\partial S/\partial H)_T = (\partial M/\partial T)_H$. The temperature dependence of ΔS associated to a magnetic field change ΔH from 0 to 50 kOe was derived from the following formula: $\Delta S\ (T, H) = \partial/\partial T \int M\ (T, H')\ dH'$.

Figures 4.17 (a) and (b) show the temperature variation of isothermal magnetic-entropy changes $\Delta S_M(T)$. From the figure 4.17(a) one can clearly noticed the zero-crossover of $\Delta S_M(T)$ across the T_N and T_{COMP}. Interestingly, the sign change of $\Delta S_M(T)$ below 10 K is consistent with the first-order-like behaviour noticed from Arrott plots analysis. Such a polarity reversal of $\Delta S_M(T)$, sudden drop in the remanent-magnetization values M_R (figure 4.12a), and sign-reversal exchange-bias H_{EB} (figure 4.12b) below the compensation point, is believed to have a common origin associated with the pseudo first-order-like transition observed in both Co_2TiO_4 and Co_2SnO_4 (figure 4.17 (a) and (b)). However, $\Delta S_M(T)$ for Co_2SnO_4 shows a zero-crossover only across T_N similar trend as that of Co_2TiO_4 except no zero-crossover (sign-change) below T_N, because, the compensation behaviour appears in Co_2SnO_4 only in the range 5-10 K.

4.3.6 Temperature Dependence of Specific-heat:

The plots of the temperature dependence of the specific heat $C_P(T)$ of Co_2TiO_4 measured in H_{dc} = 0, 10 kOe and 50 kOe are shown in figure 4.18. From 5 K to 28 K, the data were taken at temperature intervals of 2 K and from 28 K to 60 K in steps of 1 K. In H_{dc} = 0 Oe, a single shoulder in C_P versus T is observed at T_N = 47.8 K, very similar to the earlier studies by Ogawa and Waki [80]. In applied field of 10 kOe and 50 kOe, this peak becomes diffused and shifts by a few degrees to higher temperatures (as seen in the inset of figure 4.18). Interestingly, another peak is observed at 31.7 K when H_{dc} = 50 kOe suggesting some relationship of this peak with the compensation temperature noted above from M versus T data in figure 4.4 and 4.5.

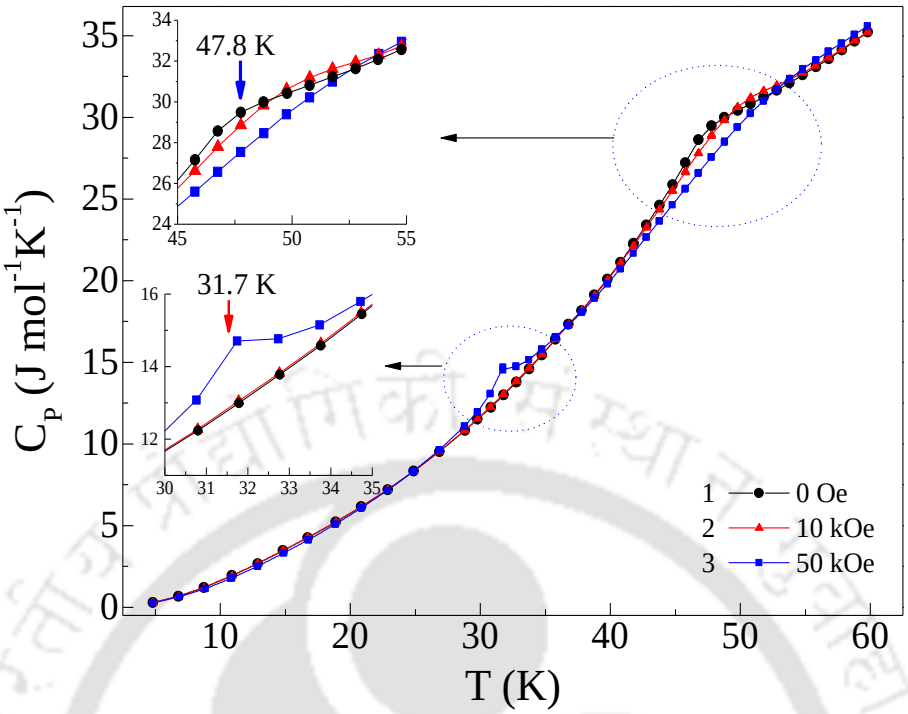

Figure 4.18: The temperature variation of specific-heat $C_P(T)$ for Co_2TiO_4 sample recorded at various magnetic fields (H_{dc} = 0, 10, and 50 kOe). The insets show the zoomed view across the ferrimagnetic Nèel temperature (T_N) and compensation temperature (T_{COMP}).

Figure 4.19 depicts the C_PT^{-1} versus T in the presence of H = 0 Oe and 50 kOe for Co_2TiO_4 and H = 0 Oe and 1 kOe for Co_2SnO_4 (S1350), respectively. We noticed clear changes in C_PT^{-1} versus T data for T < 50 K for both Co_2TiO_4 and Co_2SnO_4 suggesting the entropy loss due to spin-glass-like ordering starting near to T_{SG}. The zero-field C_PT^{-1} data shows a weak hump across the T_N, and without any signatures of T_{COMP}. However, after applying the field, a sharp transition across T_{COMP} emerged with complete suppression of the hump observed across T_N. There is a one-to-one concurrence between the location of these anomalies, and, the sharp transitions noticed in $\chi_{dc}(T)$ data at 45 K and 31.7 K. Nevertheless, no significant me.asurable difference was observed in the C_PT^{-1} values measured at H = 0 and 50 kOe except the emergence of T_{COMP}, and disappearance of weak anomaly across T_N. The fact that peak in 'C_PT^{-1}' at 'T_N' in H = 0 is quite weak compared to peaks observed in typical second order transitions in 3D systems, is due to unconventional ordering in Co_2TiO_4 (lack of proper long-range order and presence of spin-glass-like features). Therefore, the absence of sharp peak in the C_PT^{-1} (T) is a well-known characteristic feature of the existence of disordered spin configuration, and proof to the existence of spin-glass nature [150]. Nonetheless, a rapid decrease in C_PT^{-1} with decreasing T beginning near 15 K, indicating further changes in the magnetic ordering of the system as noticed from the Arrott plot analysis. These anomalies are clearly evident in the computed plots of $\partial(C_PT^{-1})/\partial T$ versus T (figure 4.20).

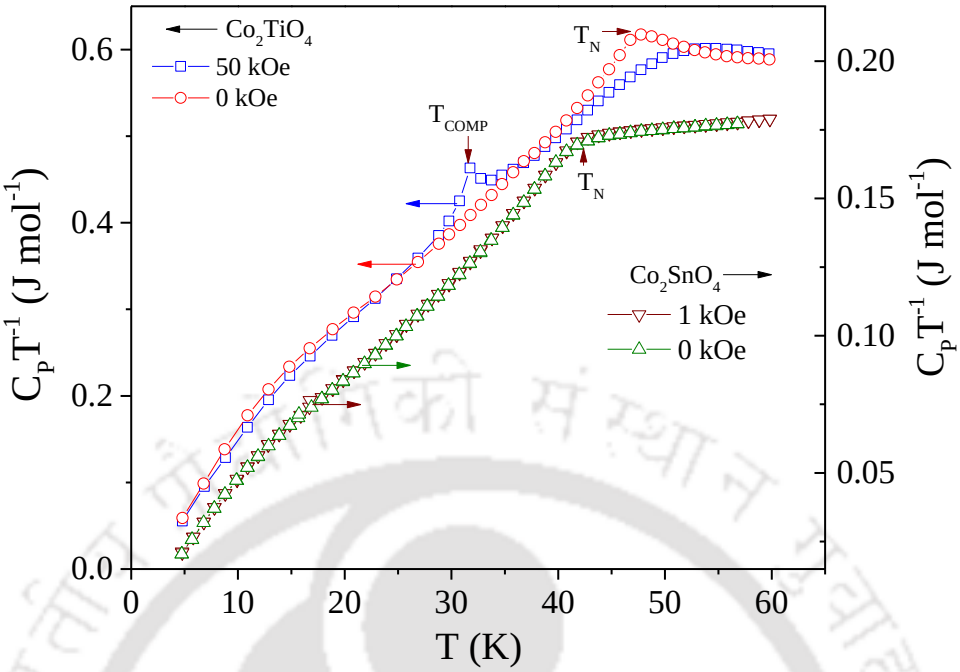

Figure 4.19: Temperature variation of C_PT^{-1} measured in the presence of H = 0 Oe and 50 kOe for Co_2TiO_4 (LHS) and H=0 Oe and 1 kOe for Co_2SnO_4 (RHS).

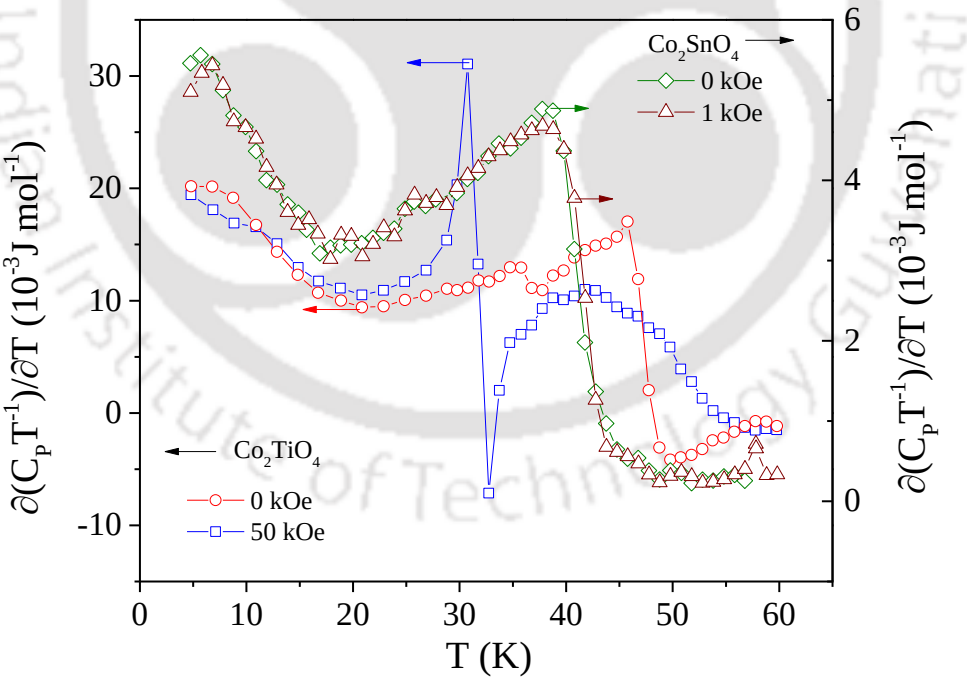

Figure 4.20: Temperature variation of $\partial(C_PT^{-1})/\partial T$ versus T measured in the presence of H = 0 Oe and 50 kOe for Co_2TiO_4 (LHS) and H = 0 Oe and 1 kOe for Co_2SnO_4 (RHS).

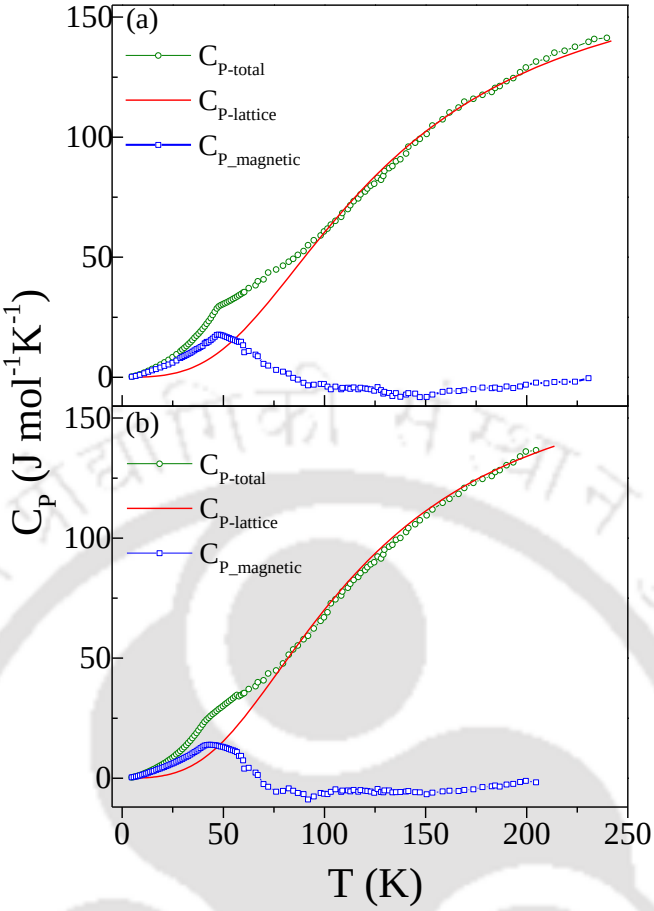

Figure 4.21: Temperature dependence of experimentally obtained zero-field heat capacity data of (a) Co_2TiO_4 and (b) Co_2SnO_4 shown in green color open circles together with the red color solid line represents the specific heat calculated from numerical fits as described in the text and blue hollow square symbols represents the magnetic contribution to the specific heat.

It is well known that the total specific heat $C_P(T)$ consists of mainly two parts *(i)* lattice specific heat (C_P^{latt}) *(ii)* magnetic contribution (C_P^{mag}) . The lattice contribution consists of the electronic part C_P^{el} and the phonon part C_P^{ph} (=N $f_D(\Theta_D/T)$ = 9 $N\,R\,(T/\Theta_D)^3\int_0^{\frac{\theta_D}{T}}\frac{x^4e^x}{(e^x-1)^2}dx$) where $f_D(\Theta_D/T)$ (=9R $(T/\Theta_D)^3\int_0^{\frac{\theta_D}{T}}\frac{x^4e^x}{(e^x-1)^2}dx$) is the single Debye function, N is the number of atoms per formula unit, R is the universal gas constant (8.314 J/mol-K), and Θ_D is the Debye temperature. Since the electronic contribution is significant only at very low temperatures, the phonon contribution has been extracted from the total specific heat. For this we have fitted the experimentally obtained specific heat data using Debye function ($f_D(\Theta_D/T)$) at temperatures much higher than the ordering temperature where the magnetic contribution vanishes [172]. Extrapolate data for both the systems are shown in figure 4.21 together with the individual contribution of the phonon and magnetic components obtained from the above relation [172, 173]. Consequently, we obtained Θ_D = 557 K and 473 K for Co_2TiO_4 and Co_2SnO_4, respectively. These values are close to the magnitude (Θ_D = 560 K) reported by Ogawa and Waki [80] for Co_2TiO_4 but less than the Θ_D = 525 K pure Co_3O_4 reported by Roth [174].

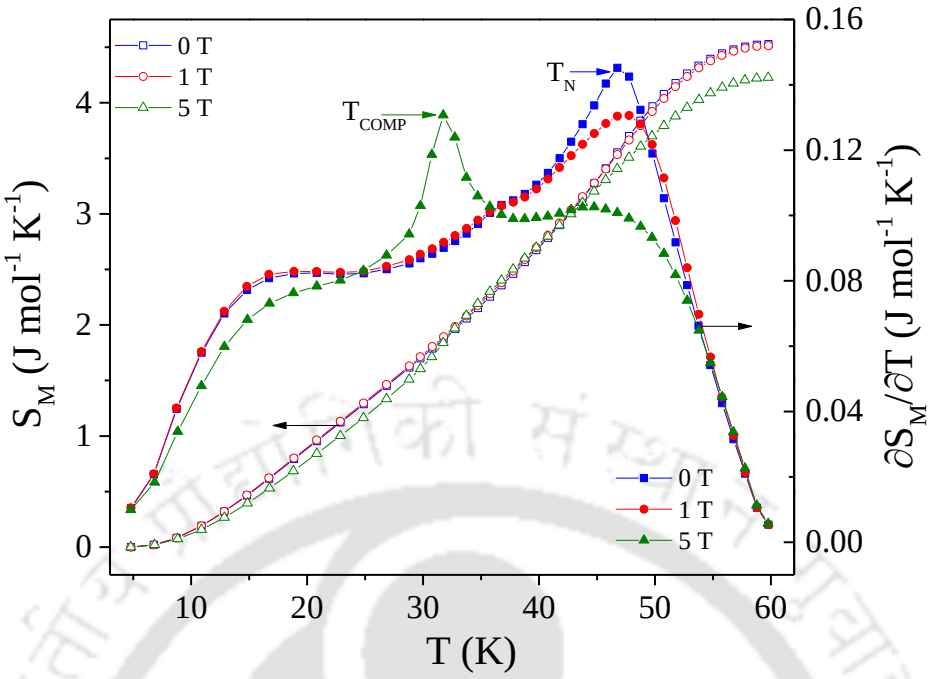

Figure 4.22: The magnetic entropy (S_M) versus temperature (T) (L.H.S) and the differential entropy $\partial S_M/\partial T$ versus T (R.H.S) plots of Co_2TiO_4 for different magnetic fields.

Moreover, temperature variation of the differential magnetic entropy $\partial S_M/\partial T$ (= C_{MP}/T) shows a sharp peak across the T_{COMP} of Co_2TiO_4 at high fields ($\geq$ 50 kOe) typical to a first-order-like transition, however, this field-dependent anomaly is not sharp at low fields (figure 4.22). Previous studies from Ogawa and Waki revealed that the $C_P(T)$ data of Co_2TiO_4 follows the simple $T^{3/2}$ dependence in a narrow range of temperatures whereas, the modified $T^{3/2}$ dependence (according to the equation $C_M = (k_B/8)(k_BT/\pi\hbar a)^{3/2} F(x)$) was noticed over a wide range of temperature (5 K - 30 K). The effective anisotropy constant K_a (~1.2×10^5 erg/cc) estimated by them was less than $K_a = 9.3 \times 10^5$ erg/cc as compared to the present case (at T = 10 K) [80]. In the low-temperature regime the logarithmic plot of C_P versus T shows a linear variation with slope ~ 1.91 (figure 4.23). This implies that the heat capacity follows T^2 dependence (for $T < T_N$) following the equation $C_P = AT^2$ with the coefficient 'A' = 18.96×10^{-2} J/mol K. For T < 15 K, the slope of $ln(C_P)$ versus $ln(T)$ turns out to be 2.14 with A = 14.78×10^{-2} J/mol-K. Such T^2 dependence is not natural to a typical canonical spin-glass phase, instead a T-dependence below the freezing temperature is universally observed [73, 175]. The T^2 dependence of C_P values at low temperatures has been shown by several compounds such as Kagome spin-glass, frustrate antiferromagnets, diluted 2D antiferromagnets (re-entrant systems). In these compounds the long- range order is set by geometrical frustration and the collective excitations of the spin-liquid; as a result the magnetic-heat capacity shows T^2 dependence [175, 176]. This behavior was found to be robust against the atomic substitution (dilution) for increasing the bond disorder. Therefore, in the present study anomalous T^2-dependence in heat-capacity data clearly suggests that the spin-liquid like excitations exists in both Co_2TiO_4 and Co_2SnO_4 with non-Heisenberg magnetic interactions at low temperatures [176 - 178].

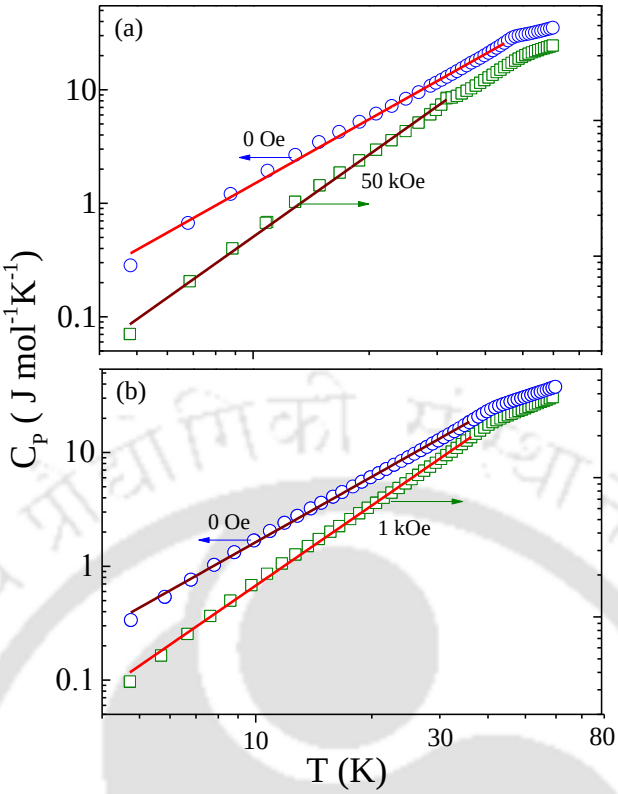

Figure 4.23: Temperature variation of heat-capacity $C_P(T)$ measured under both zero field and with field for (a) Co_2TiO_4, and (b) Co_2SnO_4. The solid lines correspond to the linear fit to AT^2.

Similar temperature dependence was found in $CuCr_{1-x}V_xS_2$ for $x \sim 0.30$, in which, the long-range non-collinear order was blocked by the lattice defects [175]. Moreover, the neutron diffraction data of polycrystalline Co_2TiO_4 reported by Hubsch *et al*. suggested the presence of canted-spins, likely resulting from magnetic frustration caused by the presence of non-magnetic 'Ti' ions on the 'B'-sites [77]. In addition, the contribution of nuclear specific heat of Co^{59} nuclei to the total magnetic specific heat of Co_2TiO_4 system cannot be ruled out [80].

4.3.7 Summary:

In this chapter a systematic comparative analysis of the structural and magnetic properties of both Co_2TiO_4 and Co_2SnO_4 was presented. The major results are as follows: (*i*) Analysis of the temperature dependence of the dc susceptibilities above T_N using the Néel expression for ferrimagnets yields magnetic moments $\mu(A) = 3.87\ \mu_B$ and $\mu(B) = 5.19\ \mu_B$ (4.91 μ_B) for Co_2TiO_4 (Co_2SnO_4), $\mu(B)$ being significantly different for the two cases. This difference in $\mu(B)$ was considered the major reason for differences in their magnetic properties. (*ii*) Analysis of the XPS data exhibited the electronic structure of Co_2TiO_4 to be $[Co^{2+}]\ [Co^{3+}Ti^{3+}]O_4$ as compared to $[Co^{2+}][Co^{2+}Sn^{4+}]O_4$ for Co_2SnO_4. This difference in the electronic structures of the ions on the B-sites was used to explain the difference in the observed $\mu(B)$ values and the lack of definite evidence for the presence of spin-glass transition in Co_2TiO_4 in contrast to the observation in Co_2SnO_4; (*iii*) A compensation temperature of T_{COMP}

$\simeq$ 32 K was observed for Co_2TiO_4 below which the system retained its ferrimagnetic character. In contrast, similar compensation point was not observed in Co_2SnO_4 although below 7 K, there was no coercivity or remanence, which are signatures of a compensated state. (*iv*) The large magnitudes of the coercivity H_C observed, in Co_2TiO_4, in the uncompensated state, most likely considered to be resulted from spin clusters. (*v*) The low-temperature complex magnetic ordering of Co_2TiO_4 and Co_2SnO_4 were studied using temperature dependence magnetization (M), Arrott-plot analysis and specific- heat (C_P). Our experimental results demonstrated the signatures of pseudo first-order-discontinuous transitions below the ferrimagnetic Néel temperature in both the systems. In the same temperature regime ($5\ K \leq T \leq 33\ K$), C_P followed T^2 dependence instead of the linear variation in both the systems suggesting the dynamical spin-fluctuation at low temperatures. The random distribution of the cations on the A and B-sites and the different temperature dependence of magnetic moments ($\mu[A](T)$ and $\mu[B](T)$) were the likely source of such anomalous low-temperature magnetic ordering in Co_2TiO_4 and Co_2SnO_4.

Chapter 5

Tuning the Compensation Point: Role of Sn Substitution in Co_2TiO_4

5.1 Introduction:

Tuning the magnetic properties such as: (*i*) exchange bias, (*ii*) anisotropy, and (*iii*) Curie or Néel temperature by the substitution of non-magnetic cations inside the ferro/ferrimagnets has been a subject of intense research, because, of the potential application of such properties in the field of magneto-electronic devices [179, 180]. For Co_2TiO_4 ($[Co^{2+}]_A[Co^{2+}Ti^{4+}]_BO_4$), tailoring the magnetic compensation point (~ 30 K), spin-glass ordering temperature (below T_N), and polarity of exchange bias, are the key ingredients to examine, which is the subject of the current chapter. To investigate the changes occurring in the above properties systematically by varying the 'Sn' doping at the octahedral 'B' sites of Co_2TiO_4 is the main objective of this chapter. This chapter also deals with the re-entrant spin-glass behaviour and the role of the competing exchange interactions or dilution of magnetic elements [31-36]. It is magnetic frustration resulting from either important to distinguish the role of different non-magnetic elements ('Ti' or 'Sn') or the alteration of the physical properties of antiferromagnetic Co_3O_4 spinel because of its applications viewpoint, which is the main motivation to substitute 'Sn' at 'Ti' sites in Co_2TiO_4 [181]. Moreover, inverse spinels such as Co_2VO_4 and Co_2TiO_4 continues to receive large attention recently because of their potential applications in Li-ion batteries, thermistors, solid-oxide fuel-cells, magnetic recording, microwave and RF devices [3, 9, 10, 182 - 190].

The cationic distribution and role of non-magnetic doping elements like germanium (Ge) and zinc (Zn) at the 'Ti' and Co-sites in the Co_2TiO_4 system were first studied by Strooper *et al*. [82, 191] For un-doped case, they obtained the magnitudes of two-sublattice magnetizations as $M_A(0)$ = 20450 (G/cm^3)/mol and $M_B(0)$ = 19750 (G/cm^3)/mol, T_N ~ 53 ± 2 K, Curie constant C = 5.4 ± 0.1 K cm^3/mol and exchange constants J_{AB} ~ - 6.3 ± 0.3 K, J_{AA} ~ - 4.6 ± 0.3 K and J_{BB} ~ - 5.5 ± 0.3 K [82, 191]. Although Strooper *et al.* reported the magnetic properties of various compositions of $Co_2Ti_{1-x}Ge_xO_4$ and $Co_{2-x}Mg_xTiO_4$, but a detailed analysis of the frequency dependence of $\chi_{ac}(T)$ in such systems is still lacking in the literature [82, 191]. Antic *et al.* reported spin-glass state at 17 K in $Li_{0.333}Co_{1.5}Ti_{1.167}O_4$ polycrystalline sample whose cationic distribution is $(Li_{0.09}Co_{0.01})_{8a}[Li_{0.24}Co_{0.59}Ti_{0.17}]_{16d}$ [13]. Except these reports, no other studies are available in the literature dealing with the physical properties of doped cobalt-orthotitanate. At first glance both the compounds Co_2TiO_4 and Co_2SnO_4 appear almost similar (despite slight differences in their ionic radii), but, they exhibit quite different magnetic structure; in-particular the compensation point, giant-exchange bias, and negative magnetization below the ferrimagnetic ordering of Co_2TiO_4 were not shown by its sister compound Co_2SnO_4 (as discussed in our previous chapter). These issues motivated us to study the magnetic interactions in the polycrystalline $Co_2Ti_{1-x}Sn_xO_4$ system. Our experiments were mainly focused to the temperature and frequency dependence of ac-magnetic measurements including the temperature dependence of remanence and coercivity measurements under various magnetic fields. Such measurements are important because they can provide a vital information related to the spin-glass ordering. For

example, estimation of (*i*) spin-glass freezing temperature 'T_F' , (*ii*) characteristic frequency of the cluster 'f_o', critical exponent of correlation length 'ν', and relative shift 'Ω' of the peak temperature per decade frequency etc. Our experimental results and analysis reveals the following fascinating features in $Co_2Ti_{1-x}Sn_xO_4$ system like for example (*i*) shift in the magnetic compensation point from 31.74 K to 27.1 K, (*ii*) large zero-field-cooled (ZFC) and field-cooled (FC) bipolar exchange bias effect (H_{EB} = 13.6 kOe (ZFC) and ~ 958 Oe (FC) at 7 K), and (*iii*) existence of spin-glass ordering at $T_F \simeq 44.05$ K, details of these results, and their discussion are presented in this chapter.

5.2 Experimental Details:

The bulk polycrystalline samples of $Co_2Ti_{1-x}Sn_xO_4$ ($0 \leq x \leq 1$) were synthesized by standard solid-state-reaction method. For this stoichiometric amount of Co_3O_4 (Alfa Aesar, purity 99.99%), TiO_2 (Alfa Aesar, purity 99.99%) and SnO_2 (Alfa Aesar, purity 99.99%) were chosen as precursors. Appropriate amount of these materials was first ground in agate mortar. These mixed powders were pressed into cylindrical pellets of diameter ~ 13 mm using a hydraulic press with a maximum load of 5 ton per cm^2. All the pellets were finally sintered at 1350ºC for 18 h in air. To check the phase purity and crystal structure information X-ray diffraction measurements were performed using a Rigaku X-ray diffractometer (model: TTRAX-III) with Cu-K_α radiation (λ = 1.54056 Å), and the diffraction data was analyzed using Rietveld refinement of the patterns by means of FullProf programme. The ac-susceptibility and dc-magnetization measurements were performed using a superconducting quantum interference device (SQUID) based magnetometer from Quantum design with temperature (T) and magnetic field (H) capable of reaching 5 K from 320 K and H_{dc} = ± 70 kOe, respectively.

5.3. Characterizations:

5.3.1 Crystal Structure Analysis:

Figure 5.1 shows the X-ray diffraction pattern of the $Co_2Ti_{1-x}Sn_xO_4$ polycrystalline for different compositions. All these diffraction patterns correspond to the inverse spinel crystal structure with space group F*d-3m* (227) similar to Co_2TiO_4. However, the lattice parameter a_o = 8.45 ± 0.01 Å (for x = 0 i.e. pure Co_2TiO_4) increases progressively with increasing the 'Sn' content, e.g. a_o = 8.512 ± 0.01 Å for x = 0.4 and a_o = 8.66 ± 0.012 Å for x = 1 (i.e. Co_2SnO_4). Approximately 7.5% increase in the unit-cell volume was noticed by incorporating the stannous within the Co_2TiO_4 matrix at 'Ti' sites. This value is close to the standard calculated value of ~ 7.38%. Table-5.1 summarizes the variation of lattice parameters, bond lengths and bond angles for different compositions of $Co_2Ti_{1-x}Sn_xO_4$ samples obtained from the Rietveld refinement process. It is clear from the table that the average bond length (B-O) between the oxygen ion and the Ti^{4+}-cations present in the octahedral sites increases progressively with the increase of Sn^{4+} substitution, while the reverse is true for the tetrahedral sites (A-O). Such deviation in the bond lengths of the octahedral and tetrahedral sites originates from the higher ionic radius of Sn^{4+} (0.69 Å) than Ti^{4+} (0.605 Å). Similarly, the bond angle A-O-B increases from 120˚ with increasing the Sn-content, while a

significant deviation from the orthogonality (90°) was noticed in B-O-B. Such canted behavior plays a major role in the magnetic ordering of the samples which is discussed below.

Table 5.1: List of various crystal structure parameters (*i*) lattice parameter, (*ii*) bond Length and (*iii*) bond angles of various compositions of bulk samples $Co_2Ti_{1-x}Sn_xO_4$ ($0 \leq x \leq 1$). [*Co_2TiO_4 sample sintered at 1100°C, results of previous chapter].

System	Lattice Parameter ($a = b = c$)	Interaxial angles $\alpha = \beta = \gamma$	Bond Length		Bond Angle	
			A-O	B-O	A-O-B	B-O-B
Co_2TiO_4	8.45±0.01Å	90º	1.98±0.01Å	2.02±0.02Å	121.68º±0.61°	94.93º±0.48°
$Co_2Ti_{0.8}Sn_{0.2}O_4$	8.49±0.01Å	90º	1.95±0.02Å	2.06±0.02Å	122.90º±0.62°	93.30º±0.47°
$Co_2Ti_{0.6}Sn_{0.4}O_4$	8.51±0.01Å	90º	1.89±0.02Å	2.09±0.02Å	124.30º±0.62°	91.40º±0.46°
Co_2SnO_4	8.66±0.01Å	90º	1.88±0.02Å	2.16±0.02Å	125.01º±0.63°	90.37º±0.45°
*Co_2TiO_4	8.45±0.01Å	90º	1.98±0.01Å	2.03±0.02Å	121.68º±0.61°	94.95º±0.48°

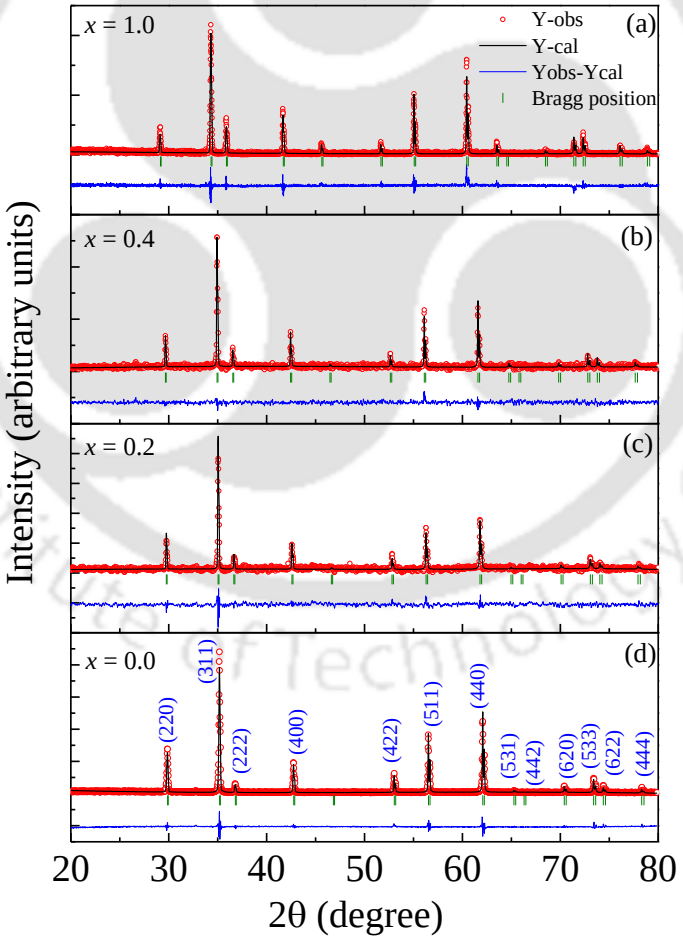

Figure 5.1: The X-ray diffraction pattern together with Reitveld refined data of $Co_2Ti_{1-x}Sn_xO_4$ (a) $x = 1.0$, (b) $x = 0.4$ (c) $x = 0.2$ (d) $x = 0.0$, samples sintered at 1350ºC for 18 h in air.

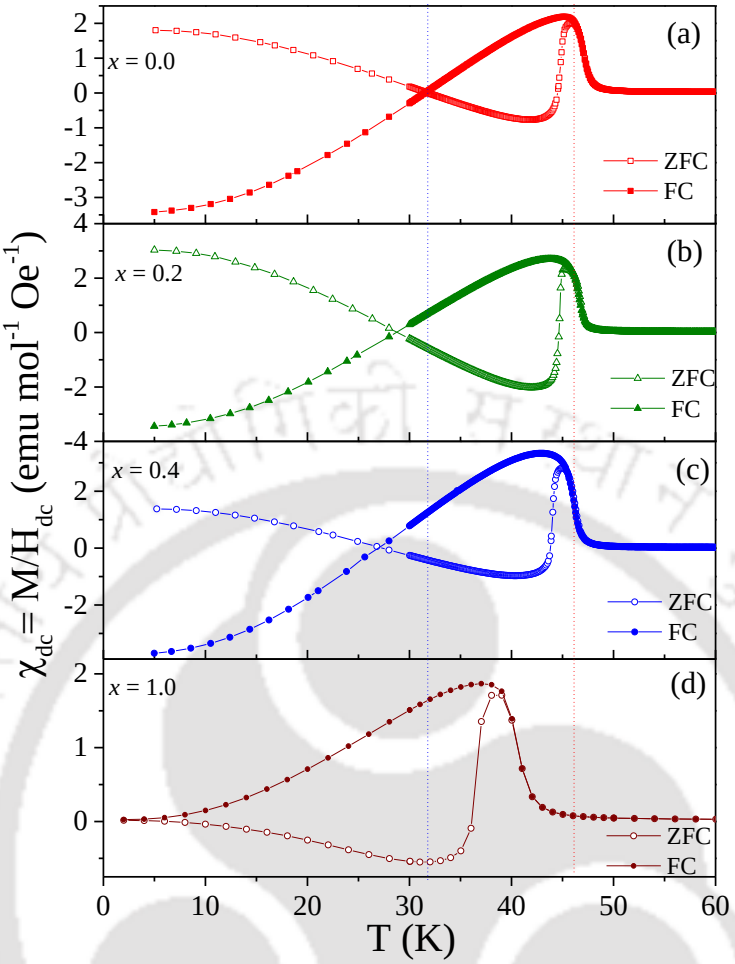

Figure 5.2: Temperature dependence of dc-magnetic susceptibility $\chi_{dc}(T)$ = M/H_{dc}(T) for (a) x = 0.0, (b) x = 0.2 (c) x = 0.4 (d) x = 1.0 measured under both zero-field-cooled (ZFC)and field-cooled (FC)conditions recorded at magnetic field H_{dc} = 50 Oe.

5.3.2 Coexistence of Ferrimagnetism and Spin-glass Ordering:

Figure 5.2 shows the temperature variation of dc-magnetic susceptibility χ_{dc} (=M/H_{dc}) plots for various compositions of $Co_2Ti_{1-x}Sn_xO_4$ recorded under both zero-field-cooled (ZFC) and field-cooled (FC, H @ 50 Oe) conditions. For all the compositions both the curves χ_{ZFC}(T) and χ_{FC}(T) exhibits a characteristic peak T_P (~ 45.9 K(ZFC) and 45.17 K(FC) for x = 0) corresponding to the ferrimagnetic Néel temperature T_N which decreases continuously with increasing the Sn-content (T_P ~ 45.01 K (ZFC) and 44.98 K (FC) for x = 0.4 and 39.06 K (ZFC) and 37.04 K (FC) for x = 1). Also both the curves χ_{ZFC}(T) and χ_{FC}(T) exhibits strong irreversibility below this peak temperature; while a slight variation in the peak position was noticed with increasing the H_{dc} values. It is interesting to note that both the susceptibility curves χ_{ZFC}(T) and χ_{FC}(T) exhibits a crossover in sign across the compensation temperature T_{COMP} ~ 31.74 K (χ_{ZFC}(T) = 0 = χ_{FC}(T)) where the bulk magnetizations of both sublattices balance each other (figure 5.2). Substitution of 'Sn' ions within the octahedral positions of 'Ti' in Co_2TiO_4 have pronounced effect on the compensation temperature; for example T_{COMP} decreases exponentially to

27.1 K for x = 0.4. By extrapolating the experimental data points with the exponential variation T_{COMP} = 24.58 + 7.04 exp (-2.603x), one can obtain T_{COMP} = 25.103 K for 100% substitution of 'Sn' inside the Co_2TiO_4 matrix i.e. for x = 1. However, this estimated value is quite large as compared to the experimentally obtained values of 6 K from the figure 5.2(d). Although both 'Sn' and 'Ti' are less-magnetic and their contribution to the global magnetic behavior is negligible as compared to Co^{2+}, but, we expect that the magnetic-dilution effect is more prominent in Sn^{4+}, due to which, the magnitude of T_{COMP} decreases drastically in Co-orthostannate than in Co- orthotitanate. Needless to say that the difference in the ionic sizes of both the ions ($2r_{Sn}$ = 1.38 Å > $2r_{Ti}$ = 1.21 Å) is responsible for the magnetic dilution. The temperature dependence of the coercive field $H_C(T)$ and remanence magnetization $M_R(T)$ (shown in figure 5.10 and 5.11 which will be discussed in section 5.3.3) both starts decreasing across 25 K and gradually approaches to zero at 6 K. A detailed analysis of such features will be discussed in the later section in terms of temperature dependence of exchange-bias $H_{EB}(T)$, $H_C(T)$ and remanence $M_R(T)$.

In order to probe the exact magnetic ordering temperatures, we calculated the $\partial(\chi_{dc}T)/\partial T$ from the χ-T data recorded under the ZFC case, and plotted the differentiated curve against the temperature in figure 5.3. It is well known that for antiferromagnets, the T_N does not exactly match with the peak temperature T_P in $\chi(T)$, instead it is given by the peak in $\partial(\chi_{dc}T)/\partial T$. Because theoretically the temperature variation of $\partial(\chi_{dc}T)/\partial T$ is analogous to the temperature variation of the heat capacity $C_P(T)$ in the systems which shows antiferromagnetic interactions [6, 18]. Figure 5.3 clearly shows a negative minimum and a positive maximum typical for the ferrimagnetic systems

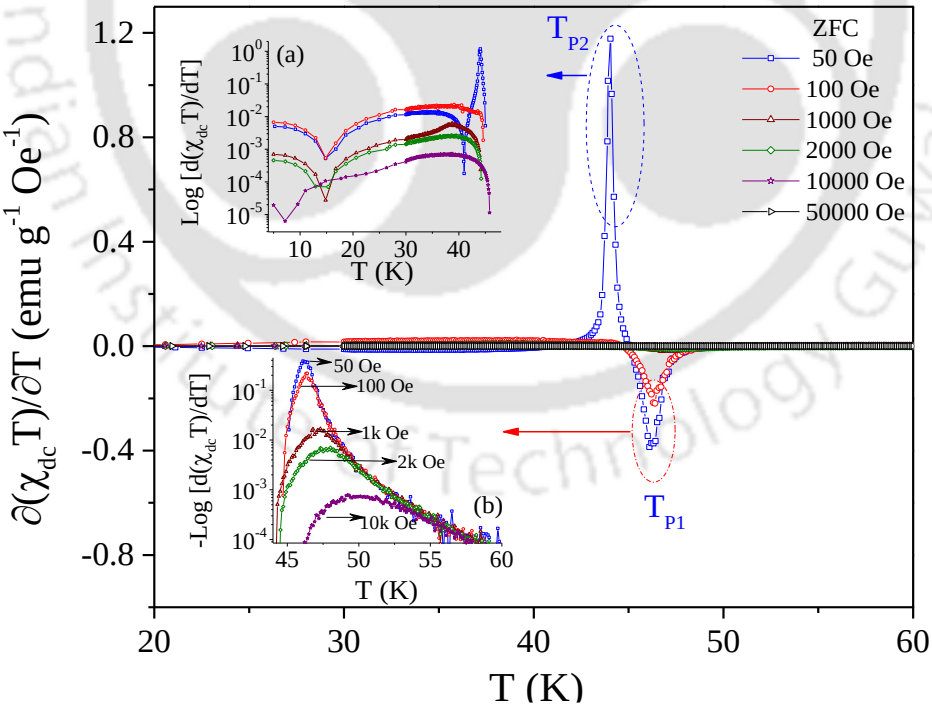

Figure 5.3: The plots of $\partial(\chi_{dc}T)/\partial T$ versus T of $Co_2Ti_{0.6}Sn_{0.4}O_4$ sample at various external fields H_{dc} = 50, 100, 1000, 2000, 10000, 50000 Oe. The inset (a) and (b) of shows the peak variation clearly in logarithmic scale.

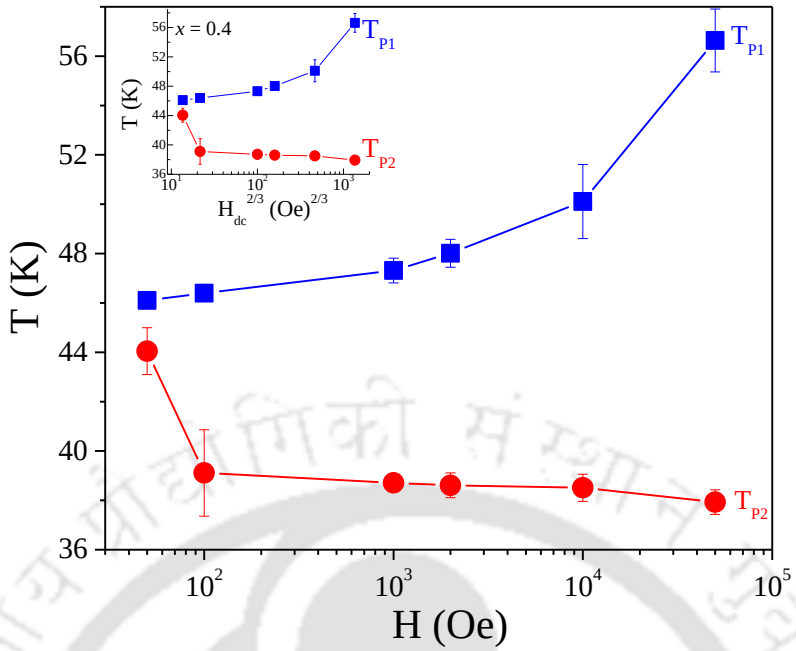

Figure 5.4: The variation of the transition temperatures T_{P1} (a) and T_{P2} (b) of $Co_2Ti_{0.6}Sn_{0.4}O_4$ sample as a function of the applied magnetic field H. The inset shows variation of the transition temperatures T_{P1} and T_{P2} as a function of $H_{dc}^{2/3}$ for $Co_2Ti_{0.6}Sn_{0.4}O_4$.

unlike in perfect antiferromagnetic systems, where, only a positive maximum is reported at T = T_N [77]. An upfront calculation from the Curie-Weiss variation yields $\partial(\chi T)/\partial T = - C\theta/(T-\theta)^2$, which will give a negative minimum at T = θ, and for negative θ (typical of most antiferromagnetic substances with dominant antiferromagnetic interaction) the equation $\partial(\chi T)/\partial T$ gives a positive maximum, as observed in figure 5.3. For the composition x = 0.4 the data recorded under ZFC protocol depicts a minimum value of $\partial(\chi T)/\partial T$ at 46.10 K, whereas, the maximum of $\partial(\chi T)/\partial T$ occurs at 44.05 K for H_{dc} = 50 Oe. This exercise leads to the determination of the Néel temperature 'T_N' = 46.10 K (designated as T_{P1} shown in the figure 5.3) and the second transition 'T_{P2}' = 44.05 K. Inset (*a*) and (*b*) depicts the small change in the peak position of T_{P1} and T_{P2} for various values of H_{dc}. The high-field (150 kOe) susceptibility data reported by Hubsch and Gavoille in Co_2TiO_4 did not show such two peak behaviour, instead they observed such two peak behaviour in the temperature dependence of remanence $M_R(T)$ and coercivity $H_C(T)$ with different ordering temperatures 46 K and 55 K [77]. The existence of second transition at T_{P2} gives the signatures of spin-glass behaviour just below the T_N. As the applied magnetic field increases from 50 Oe to 50 kOe the peak at T_{P1} corresponding to the T_N becomes broad, and shifts towards higher temperature side (T_{P1} ~ 56.64 K for H = 50 kOe expected for a typical ferrimagnetic transition (inset (*b*) of figure 5.3). On the contrary, the magnetic field variation of T_{P2} shows a decreasing trend typical to blocking/freezing of the local spins (figure 5.4). Since all the samples are having bulk grain sizes in the μm range so blocking effects are ruled out and glassy signatures prevail in the system below T_N. Such a variation of $T_{P2}(H_{dc})$ usually shows a straight line behaviour when plotted against $H_{dc}^{2/3}$ (de Almeida-Thouless (A-T) line) [192]. But, in the present

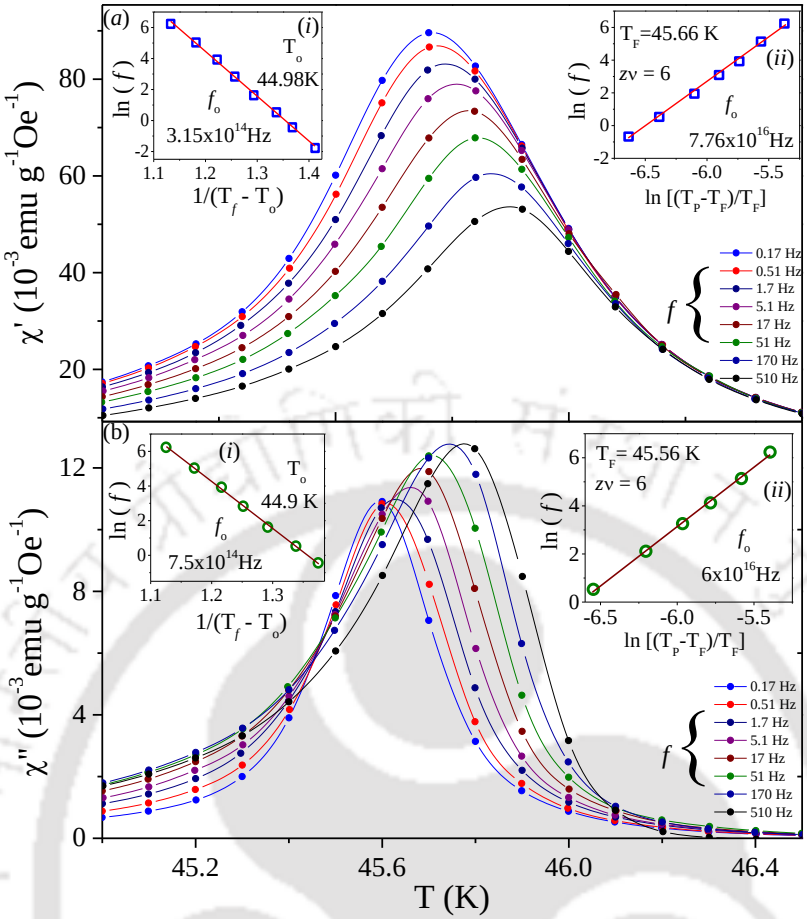

Figure 5.5: Temperature dependence of the ac-magnetic susceptibility of $Co_2Ti_{0.6}Sn_{0.4}O_4$ sample: (a) the real component $\chi'(T)$, (b) the imaginary component $\chi''(T)$ recorded at various frequencies (0.17 Hz $\leq f \leq$ 510 Hz) under warming condition using h_{ac}= 3 Oe and zero static magnetic field. The inset (*i*) of figure (a) and the inset (*i*) of figure (b) show the ln*f* versus $[1/(T_f - T_o)]$ using the peak positions in $\chi'(T)$ and $\chi''(T)$ respectively. The solid line shows Vogel-Fulcher law fit of experimental data. The inset (*ii*) of figure (a) and inset (*ii*) of figure (b) shows the ln *f* versus $\ln([T_P-T_F]/T_F)$ using the peak positions in $\chi'(T)$ and $\chi''(T)$ respectively, the solid line shows are the linear fits to the experimental data.

case analysis shown in the inset of figure 5.4 shows a linear behaviour above a threshold value H^*_{dc} = 100 Oe. For a clear understanding of glassy behaviour, we have investigated the temperature variation of the dynamic magnetic susceptibility at various ac-magnetic field frequencies (*f*). Since the experimental time window of the measurement is determined by '*f*' of the ac field, a wide-range of time span can be effortlessly set by changing the '*f*' itself.

Figure 5.5 shows the temperature dependence of in-phase (real component $\chi'(T)$) and out-of-phase (imaginary component $\chi''(T)$) of the ac-magnetic susceptibilities $\chi_{ac}(T)$ measured at various frequencies between the temperature window T_{P2} and T_{P1}. The parameters obtained from the $\chi_{ac}(T)$ analysis were very sensitive to thermodynamic phase changes and often been employed to probe the spin-glass phase-transition temperature. During the measurement process the amplitude of the peak-to-peak ac-magnetic field h_{ac} is set to ~ 3 Oe by varying

'*f*' between 0.17 Hz and 510 Hz under zero H_{dc}. It is clearly evident from both the graphs figure 5.5(a), (b), that the peak position T_P in $\chi'(T)$ and $\chi''(T)$ shifts towards higher temperature side. A convenient gauge to understand the nature of the spin-glass freezing processes lies in the determination of relative shift (Φ) of the peak temperature per decade frequency using the expression $\Phi = [\Delta T_p/(T_p\, \Delta \log f)]$, where ΔT_P is the change in T_P with change in $\Delta \log f$. Consequently, we have calculated the values of $\Phi = 0.00115$ and 0.000815 using χ' versus T and χ'' versus T, respectively. From the available literature data corresponding to the number of conventional spin-glass systems and magnetic ultrafine-particles, it is known that $\Phi \geq 0.13$ is observed in non-interacting nanometre size particles, whereas, for interacting particles Φ lies in the range 0.05- 0.13. Thus, 'Φ' decreases with increase in the strength of the interaction. For typical spin-glasses, the parameter Φ should lie between 0.005 and 0.05 [193]. Therefore, in the present case Φ values estimated from both χ' versus T and χ'' versus T are consistent with the spin-glass ordering. To examine this issue further the change in T_P with '*f*' is analysed using the following dynamic scaling equation [42, 194].

$$f = f_0\left(\frac{T_P - T_F}{T_F}\right)^{z\nu} \quad \ldots \quad (5.1)$$

In the above equation 'f_o' is the value of attempt frequency, 'T_F' is the spin-glass transition temperature, '*z*' is the dynamical critical exponent and 'ν' is the critical exponent of correlation length. The insets (*ii*) in both the figures 5.5(a), (b) shows the frequency variation of the peak position estimated from both $\chi'(T)$ and $\chi''(T)$. In these plots, the solid lines connecting the scattered symbols for both cases, represents the best fit to the above equation which is in good agreement with the experimental data. Further, using the values of $T_P(\chi')$ and $T_P(\chi'')$, we executed the least square fitting of the data by plotting logarithmic variation i.e. ln[*f*] against $\ln[(T_P\text{-}T_F)/T_F]$ by varying T_F until a straight line is obtained. Such analysis yields the following important parameters for $Co_2Ti_{0.6}Sn_{0.4}O_4$: $f_o = 7.76 \times 10^{16}$ Hz, $T_F = 45.66$ K and '$z\nu$' = 6.009 ± 0.007 for $T_P(\chi')$ and $f_o = 6.007 \times 10^{16}$ Hz, $T_F = 45.56$ K and '$z\nu$' = 6.004 ± 0.003 for T_P (χ''). These magnitudes of 'f_o' and '$z\nu$' are consistent with the previously reported prototype spin-glasses; in particular, the magnitude of $f_o \simeq 10^{20}$ Hz corresponds to spin-flip frequency of magnetic moments of ions or atoms [192 – 194]. The insets (*i*) of figures 5.5 (a), (b) show the best fit representation of the data that was obtained using the Vogel-Fulcher law which is usually expressed as

$$f = f_0 \exp\left(\frac{-E_a}{k_B(T - T_0)}\right) \ldots\ldots (5.2)$$

where f_o is the characteristic frequency of the clusters, T_o is a measure of the interaction between magnetic clusters, k_B is the Boltzmann constant and E_a is the activation energy or the potential barrier separating two adjacent clusters. This exercise yields $T_o = 44.98$ K (44.90 K) and $f_o = 3.15 \times 10^{14}$ Hz (7.5×10^{14} Hz) for $\chi'(\chi'')$. Such large values of f_o has been seen in other systems as well, for example AgMn,[192] CuMn,[120] and AuFe [195] which indicates the presence of interacting magnetic spin clusters of significant sizes in the system. The competition between ferrimagnetism and magnetic frustration in the system is the main source of existence of spin clusters

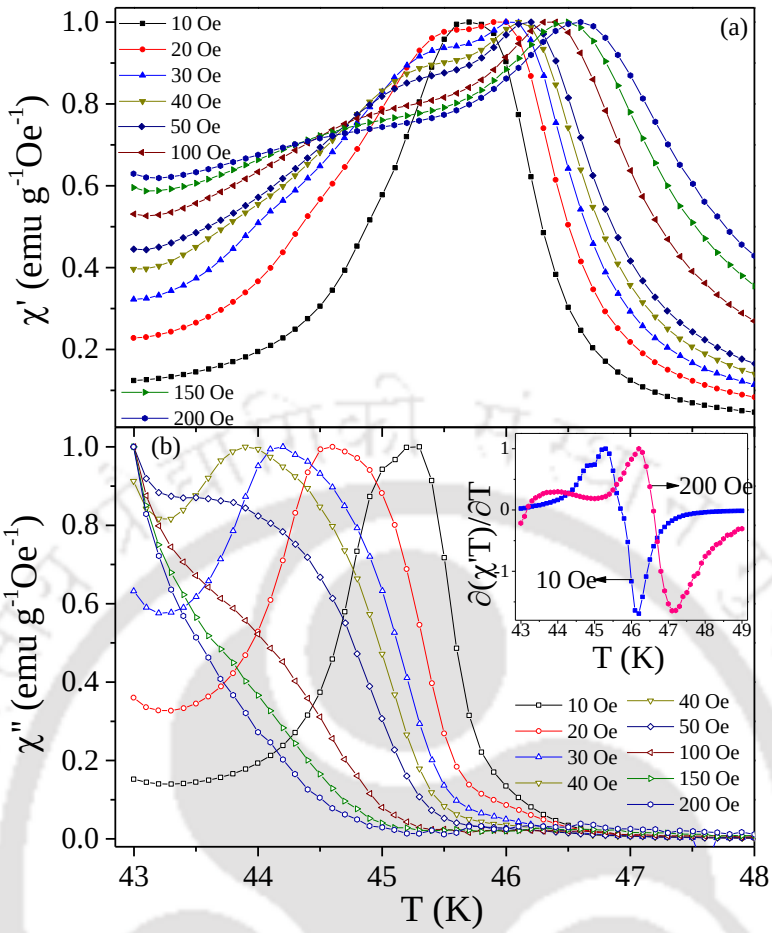

Figure 5.6: Temperature dependence of ac-magnetic susceptibility (a) real part $\chi'(T)$, and (b) imaginary $\chi''(T)$ components of bulk $Co_2Ti_{0.6}Sn_{0.4}O_4$ recorded at various bias fields H_{dc} ($10\ Oe \leq H_{dc} \leq 200\ Oe$) with constant frequency 2 Hz and amplitude of 3 Oe. The insets of figure b depict the temperature variation of $\partial(\chi'_{ac}T)/\partial T$ plots at different bias fields H_{dc} = 10 and 200 Oe.

which leads to a short range order occurring below T_N. Earlier studies related to the magnetic properties of $Y_{0.7}Ca_{0.3}MnO_3$ and $La_{0.96-y}Nd_yK_{0.04}MnO_3$ ($0 \leq y \leq 0.4$) reported the formation of such spin-clusters with short-range order [121, 196].

Previous studies on un-doped Co_2TiO_4 and Co_2SnO_4 by Srivastava *et al*. reported four transitions in the $\chi_{ac}(T)$ data recorded in the presence of (f = 21 Hz, V_{p-p} ~ 0.5 Oe) with dc-magnetic field in the range 285 Oe - 460 Oe [79, 108]. The location of first two transitions and their field dependence is consistent with the $T_N(T_{P1})$ and $T_F(T_{P2})$ observed in the $\chi_{ZFC}(T)$ data as discussed above. Accordingly, for $Co_2Ti_{0.6}Sn_{0.4}O_4$ system we have performed a detailed temperature dependence of the ac-magnetic susceptibilities superimposed with various dc-bias fields H_{dc} ($10\ Oe \leq H_{dc} \leq 200\ Oe$) similar to that discussed in chapter 3. During the measurement frequency and ac-peak-peak amplitude h_{ac} was kept constant at f = 2 Hz with h_{ac} = 3 Oe, respectively. The data were recorded in close temperature intervals of ~ 0.1 K between 43 K and 48 K to probe the small features present if any and avoid any error in the location of transition. Figure 5.6 shows the $\chi'(T)$ and $\chi''(T)$ measured at various H_{dc}. The amplitude of

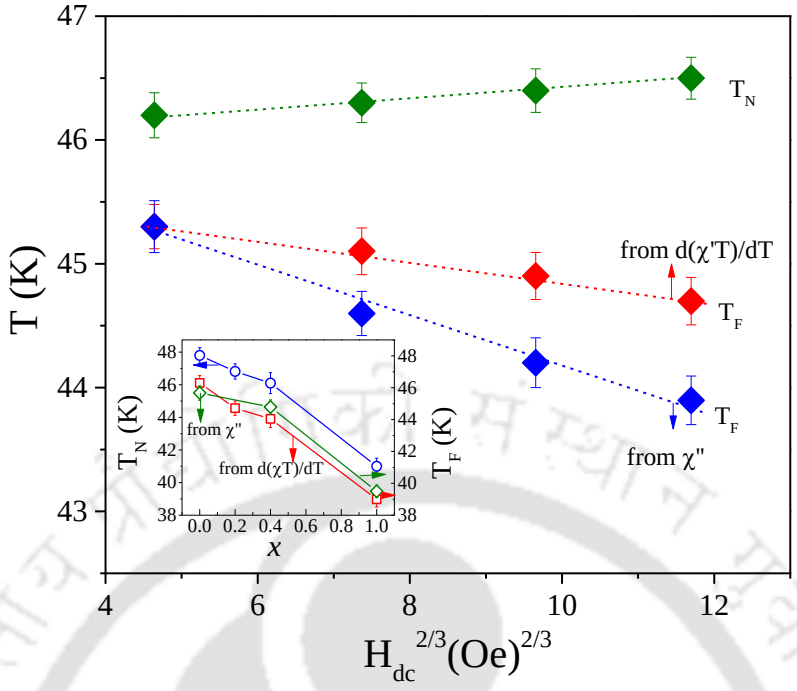

Figure 5.7: $H_{dc}^{2/3}$ dependence of ferrimagnetic Néel temperature T_N and freezing temperature T_F. The solid lines show the linear fit to the data (often called the de Almeida-Thouless AT line). The inset shows compositional variation of T_N and T_F.

both $\chi'(T)$ and $\chi''(T)$ decreases significantly with increasing the H_{dc}, however, two peaks are clearly evident in $\chi'(T)$ curves with the extent of splitting increases with increase of H_{dc}. This behavior is consistent with the two-peak scenario in dc-susceptibility data ($\chi_{ZFC}(T)$) discussed above.

The out-of-phase susceptibility χ'' exhibits only a broad cusp with a weak shoulder. The amplitude of this cusp decreases and shifts to lower temperatures with increase in H_{dc}. As H_{dc} approaches to zero, the cusp in χ'' is centered across 45.30 K which is lower than the T_N = 46.10 K. Since $\chi''(T)$ is the out-of-phase component of the $\chi_{ac}(T)$, it is related with the transverse spin components. These observations depict the coexistence of ferrimagnetism in the longitudinal spin component at T_N and spin-glass ordering of the transverse spin component at a slightly lower temperature T_F. Such phenomenon of semi-spin-glass state was predicted in the papers by Gabay and Toulouse [122], and Villian [40] in insulators with non-magnetic impurities. Subsequently, the temperature dependence of χ'' and $\partial(\chi'T)/\partial T$ are found to be comparable in many systems which have a strong theoretical basis **[**6, 77, 78]. The inset of figure 5.6(b) clearly shows two-peaks corresponding to T_F and T_N. These observed peaks in χ'' and $\partial(\chi'T)/\partial T$ are almost analogous near the magnetic phase transitions similar to Co_2SnO_4 data (discussed in the chapter 3) and the nanoparticles of quasi-two-dimensional ferromagnet α-$Ni(OH)_2$ [124]. The dc-magnetic field variations (T_P versus $H_{dc}^{2/3}$) of the two peaks in χ'', and positive and negative points in $\partial(\chi'T)/\partial T$ are plotted together in figure 5.7. The peak associated with T_N has been justified, since, its shift towards higher temperature with increase in the field is characteristic of ferromagnets because of the direct coupling of the order parameter

with applied magnetic field [117, 118]. Also χ' being the in-phase component represents the longitudinal spin constituent. The straight line behavior in figure 5.7 also shows that the position of the second peak in $\partial(\chi'T)/\partial T$ and the single peak in χ'', and their shifts with magnetic field are identical. Such characteristic $H^{2/3}$ variation of this peak position, shown in the figure 5.7, is consistent with the A-T line like behavior [192]. The A-T line analysis is a well-established model often used to examine the presence of spin-glass-like characteristics in a variety of disordered systems [124, 127 - 130]. The inset of figure 5.7 shows the variation of T_N and T_F as a function of 'Sn' doping concentration: since the unit-cell volume increases progressively with increasing composition, which in turn, affects the exchange interaction between the magnetic ions and finally leading to the alteration of T_N and T_F.

5.3.3 Observation of Giant-Coercivity and Exchange Bias:

The coercive field H_C is often considered as a measure of canting of the spin configuration, because, Néel theory predicts that the mean-square value of the disordered transverse spin component significantly increases the coercive field [77]. Therefore, for a detailed understanding of the nature of magnetic ordering below T_N, we performed a series of hysteresis loop measurements at different temperatures. Such magnetization versus field (M-H) measurements were executed under both ZFC and 20 kOe field-cooled (FC) conditions for x = 0.4 ($Co_2Ti_{0.6}Sn_{0.4}O_4$). During the measurement of each M-H loop the system was brought to the perfect paramagnetic state by increasing the temperature above T_N. In the course of FC mode, the sample was first cooled down to 5 K in the presence of 20 kOe magnetic field from the paramagnetic state, and the M-H loops was ramped in the range -70 kOe $\leq H_{dc} \leq$ 70 kOe. This whole process was repeated for different temperatures. Figures 5.8 and 5.9 depict the complete M-H hysteresis loops at selected temperatures recorded under both ZFC and FC conditions. The coercive field (H_C), remanence magnetization (M_R), and the loops asymmetry (H_{EB}) (EB = exchange-bias) were measured from the above loop asymmetry, and their temperature dependence are plotted separately in the figures 5.10 and 5.11. All these hysteresis loops are unsaturated even up to 68 kOe and exhibits anomalous temperature dependence with giant H_C values (~ 15.52 kOe) for T < 20 K under both ZFC and FC conditions. A clear anomaly across the compensation temperature is evident from H_C-T, H_{EB}-T and M_R-T curves (as indicated by arrow marks in figure 5.10 and 5.11). At very low temperatures T $\leq$ 5 K, these M-H loops exhibit linear behavior with lesser H_C values, and shift towards left from the origin. However, as the temperature approaches 10 K, M-H loop opens-up widely, and exhibits maximum H_C value, thereafter, starts decreasing continuously with increasing the temperature, as shown in the figures 5.10 and 5.11. Finally, the M_R and H_C approach to zero as T$\longrightarrow T_N$.

The most striking feature of these M-H loops (measured under the ZFC condition) is that a substantial shift towards left side from the origin. This feature becomes more significant under FC condition (with H @ 20 kOe), as depicted in the figure 5.9. Using this key result we quantified the loop asymmetry by defining the exchange-bias field H_{EB}, i.e., the amount of shift in the center of M-H loop with respect to the origin as $H_{EB} = (H_+ + H_-)/2$, and the resultant coercive field, i.e., $H_C = (H_+ - H_-)/2$, where H_+ and H_- characterizes the magnitude of field at

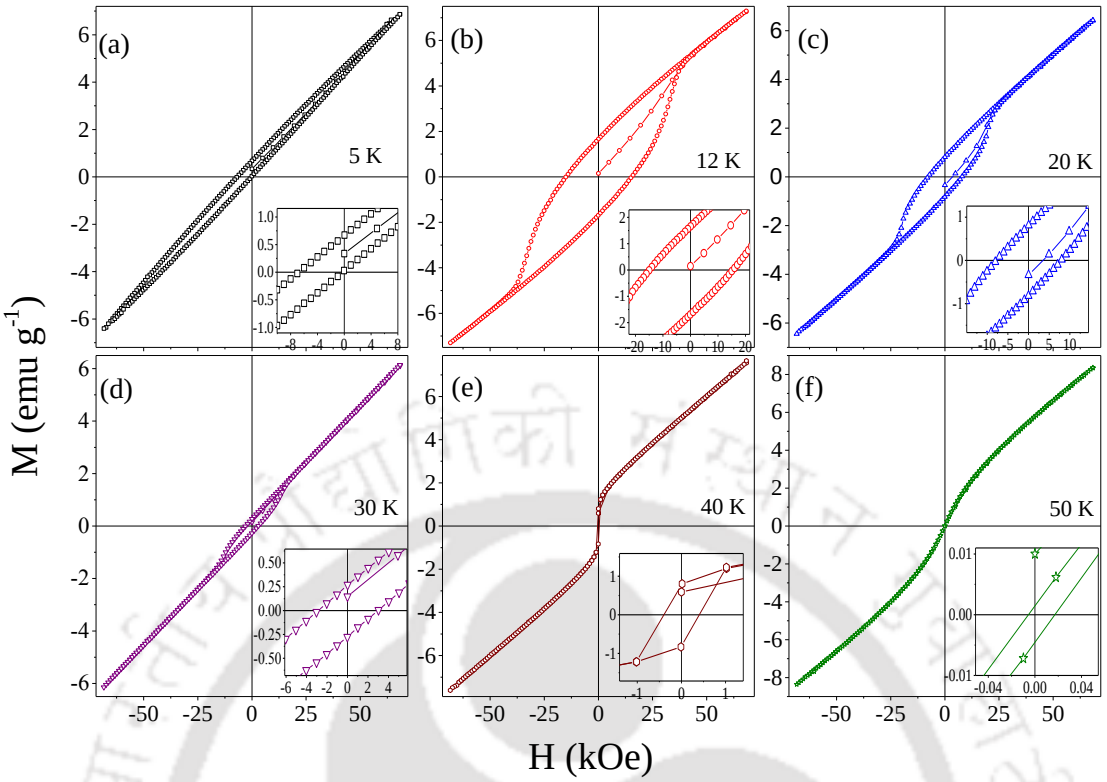

Figure 5.8: The magnetization (M) versus field (H) hysteresis loops of $Co_2Ti_{0.6}Sn_{0.4}O_4$ samples recorded at select temperatures (a) 5 K, (b) 12 K, (c) 20 K (d) 30 K (e) 40 K and (f) 50 K under zero-field-cooled ZFC condition. The insets show the zoomed view of M-H loops near origin showing the asymmetry in the loops.

right-hand-side and left-hand side of the origin of M-H graph. Figure 5.10 shows the temperature variation of such exchange-bias $H_{EB}(T)$ and coercive field $H_C(T)$ under both ZFC and FC conditions. Both $H_C(T)$ and $H_{EB}(T)$ takes peak shape across T = 8 K and drops suddenly. Also, for $T < T_{COMP}$, the $M_R(T)_{ZFC}$ and $M_{MAX}(T)_{ZFC}$ show a cusp like shape with the maximum value of $M_R^{Max} = 1.36$ emu g^{-1}. For $T > T_{COMP}$, both the curves $M_{MAX}(T)$ and $M_R(T)$ again start to increase up to T_N and fall off gradually beyond T_N (identical scenario was observed in FC condition as well). Both $H_{EB\text{-}FC}(T)$ and $H_{EB\text{-}ZFC}(T)$ gradually decrease with increasing temperature, and approaches zero across T_N. The increase of the coercive field below T_F may be due to the growing up of the spin-glass component. The $H_C(T)$ curve takes a peak shape with maximum value $H_C^{Max} = 17.02$ kOe at 8 K under ZFC and ~ 15.52 kOe at 12 K under FC. It is interesting to note that an unusual crossover of sign from positive to negative values of H_{EB} (= - 3.71 kOe and - 3.53 kOe under ZFC and FC conditions, respectively) was observed below 7 K (clearly shown in the inset of figure 5.10b). Such giant bipolar switching of H_{EB} clearly signifies the role of field induced negative magnetization due to the underlying magnetic compensation effect. On the other hand, the M_R versus T and the temperature dependence of maximum magnetization values M_{Max} measured at H = 68.3 kOe drops to zero at T_{COMP} where the two-sublattice magnetizations (M_A and M_B) balances with each other (figure 5.11). Also, the M_R versus T curve exhibits a second maximum centered at T_{SG} and finally drops to zero. Generally, H_{EB} has been experimentally witnessed only in the systems cooled under the presence of external magnetic field well above the

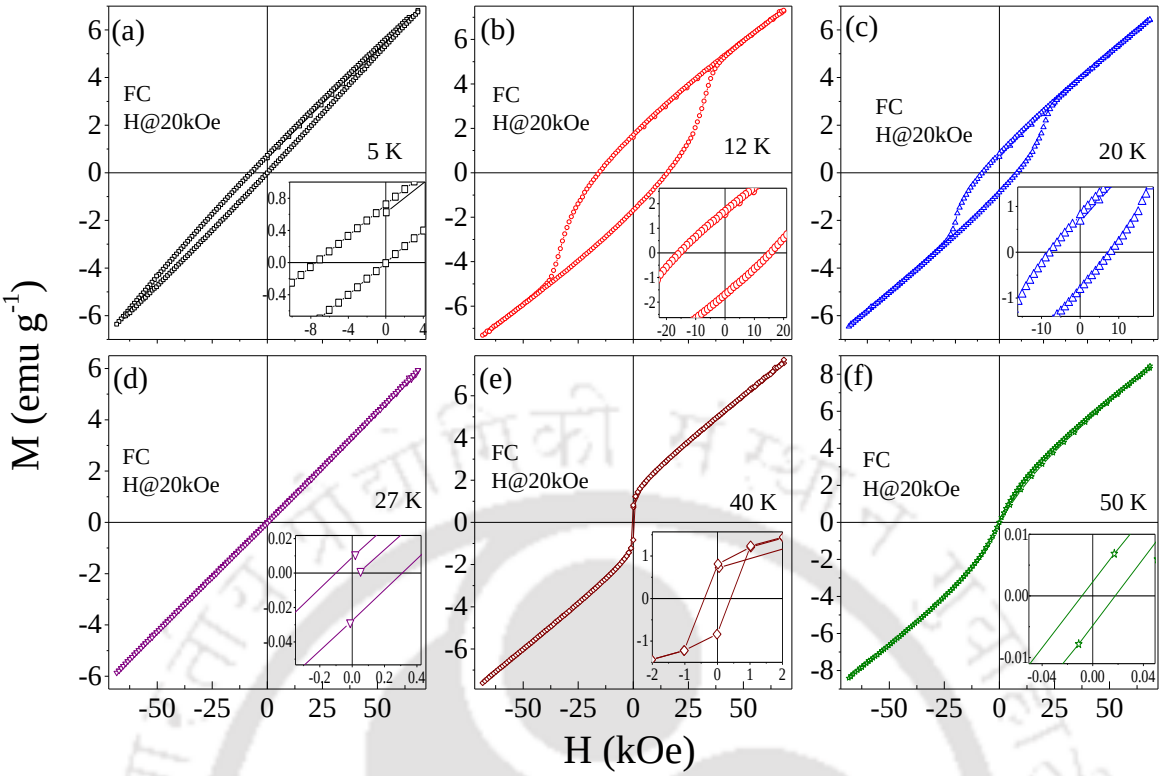

Figure 5.9: The magnetization (M) versus field (H) hysteresis loops of $Co_2Ti_{0.6}Sn_{0.4}O_4$ samples recorded at select temperatures (a) 5 K, (b) 12 K, (c) 20 K (d) 27 K (e) 40 K and (f) 50 K under @ 20 kOe field-cooled (FC) condition. The insets show the zoomed view of M-H loops near origin showing the asymmetry in the loops.

Néel temperature or spin-glass freezing point. Such systems usually comprises of variety of interfaces like ferromagnetic (FM) - antiferromagnetic (AFM) [130], FM-SG [131], FM-ferrimagnetic [132], AFM-ferrimagnetic [133] and AFM-SG [134, 135]. However, few recent papers have reported significant H_{EB} even under the zero-field cooled samples of bulk Ni-Mn-In alloys [136] and in bulk Mn_2PtGa [137]. The source of such unusual H_{EB}, under zero-field-cooled sample, was attributed to the presence of complex magnetic interfaces such as ferrimagnetic/spin-glass or AFM/spin-glass phases [135, 136]. Few recent reports suggested that large exchange anisotropy originating from the exchange interaction between the compensated host and ferromagnetic clusters that arise from intrinsic anti-site-disorder (ASD) [179, 197]. It is believed that the origin of H_{EB} in the present context is likely resulting from similar phenomenon since the Co_2TiO_4/Co_2SnO_4 intrinsically possess disorder due to the dilution effect (by Ti/Sn atoms). Such disorder is expected to enhance even more by disturbing the spinel lattice with the incorporation of slightly different ionic size of Sn. The double perovskite like systems usually possesses high degree of ASD due to which mixed exchange interactions become prominent, and finally leading to the spin-glass like phase at low-temperatures. Such process in-turn cause loop-asymmetry (or exchange-bias) through the microscopic interfaces of spin-glass phase and ferrimagnetic phase [198]. Since the current system $Co_2Ti_{0.06}Sn_{0.04}O_4$ exhibits coexistence of spin-glass ordering and ferrimagnetic behavior, we expect the ASD is likely source of giant H_{EB} noticed at low-temperatures. The sign-reversal behavior of the exchange-bias

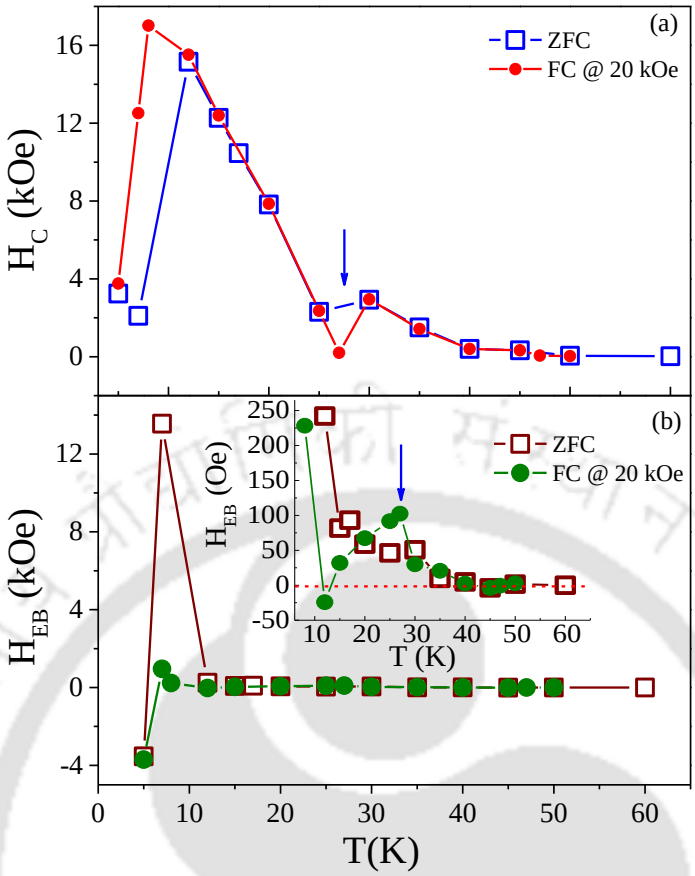

Figure 5.10: The temperature variation of (a) coercive field $H_C(T)$ and (b) exchange bias $H_{EB}(T)$ of $Co_2Ti_{0.6}Sn_{0.4}O_4$ recorded from the M-H curves measured under both ZFC and FC conditions. The inset of Figure (b) clearly shows the anomalous behaviour of H_{EB} across the T_{COMP}.

effect is clearly evident in both the pristine compounds Co_2TiO_4 and Co_2SnO_4 together with intermediate system $Co_2Ti_{0.6}Sn_{0.4}O_4$. Nevertheless, the magnitude of H_{EB} measured under FC protocol (below 10 K) is much lower than H_{EB} obtained in ZFC case for all the investigated systems. For T > 10 K, the magnitude of H_{EB} is quite small as compared to the H_{EB} values measured at lower temperatures, yet the anomalous behavior of $H_{EB}(T)$ is prominent across the ordering temperatures T_{COMP}, T_{SG} and T_N (Figure 5.10). Moreover, the sign reversal of H_{EB} closely related with large increase in the magnetic entropy dS/dT (not shown) and ground state spin configuration of Co^{2+} ions in the field of tetrahedral crystal field symmetry [152]. The inability of the spins in the frozen clusters to follow the magnetic field below 10 K, is one main possible source of obtaining very large H_C and H_{EB} values.

Following the Néel's theory, the collapse of M_R and H_C near the T_{COMP} is frequently related to the corresponding collapse of the mean-square value of the disordered transverse spin component considered over a macroscopic scale [199, 200]. Yet, we believe that the reversal of the magnetic moments on either side of the T_{COMP} leads to the sign reversal of H_{EB}. Therefore, in the presence of magnetic field the transition at T_{COMP}, M_R suddenly collapses, and anomalies observed in $H_{EB\text{-}FC}(T)$ have a common origin of the local spin-reversal of the Co^{2+} magnetic moments occupied in the A- and B-sites of the spinel configuration. The concept of magnetization

reversal can be clearly seen in the figure 5.11, where, a sudden decrease of the M_{MAX} values to 6 emu g^{-1} occurs exactly at T_{COMP} = 27 K for $Co_2Ti_{0.6}Sn_{0.4}O_4$. Since the ground state ($^4T_1$) spin configuration of Co^{2+} ions in the octahedral symmetry, is significantly split by the spin-orbit coupling into six Kramers doublets. Thus, one can expect a distinctly different spin arrangement of all the ions occupied in the tetrahedral crystal field. Therefore, the interaction of externally applied magnetic field with such diverse spin configuration, significantly alters the net alignment of magnetization with unequal amounts, and finally resulting in the sign reversal of total magnetization on either side of T_{COMP}. Such features may appear more significant at very high fields, for example, $H_{dc} \geq 50$ kOe, because, at low fields (10 - 20 kOe) the transition in $C_P(T)$ for the x = 0 system (chapter 4, section 4.3.7) shows a feeble anomaly at 31.74 K, but, this anomaly becomes more prominent at $H_{dc} \geq 50$ kOe. Similarly, we expect even larger values of $H_{EB\text{-}FC}(T)$ than - 3.71 kOe at 5 K, if we cool the system in the presence of higher magnetic fields greater than 50 kOe.

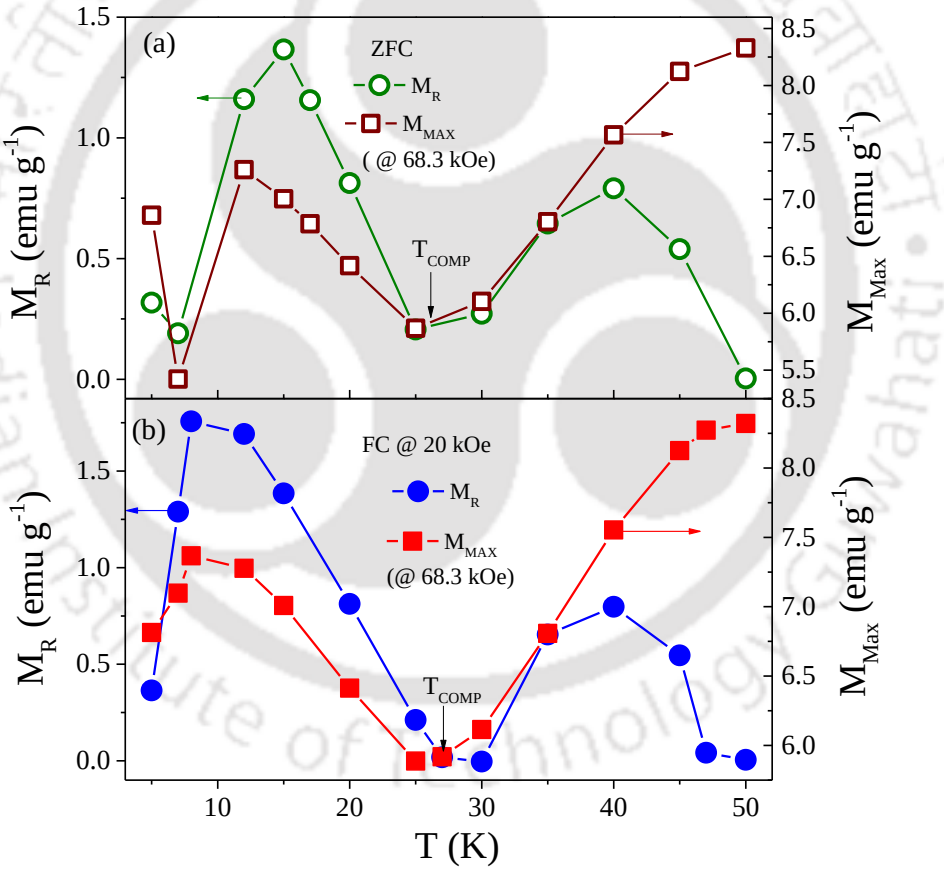

Figure 5.11: Left-hand-side scale shows the remanence magnetization versus temperature (M_R versus T) of $Co_2Ti_{0.6}Sn_{0.4}O_4$ system measured under (a) zero-field-cooled (ZFC), and (b) field-cooled (FC) conditions. The right-hand-side scale shows the variation of the high field (H~ 68.3 kOe) magnetization versus temperature measured under both (a) ZFC and (b) FC conditions. All these cures clearly show the sudden drop of magnetization value across the T_{COMP} (~ 27 K).

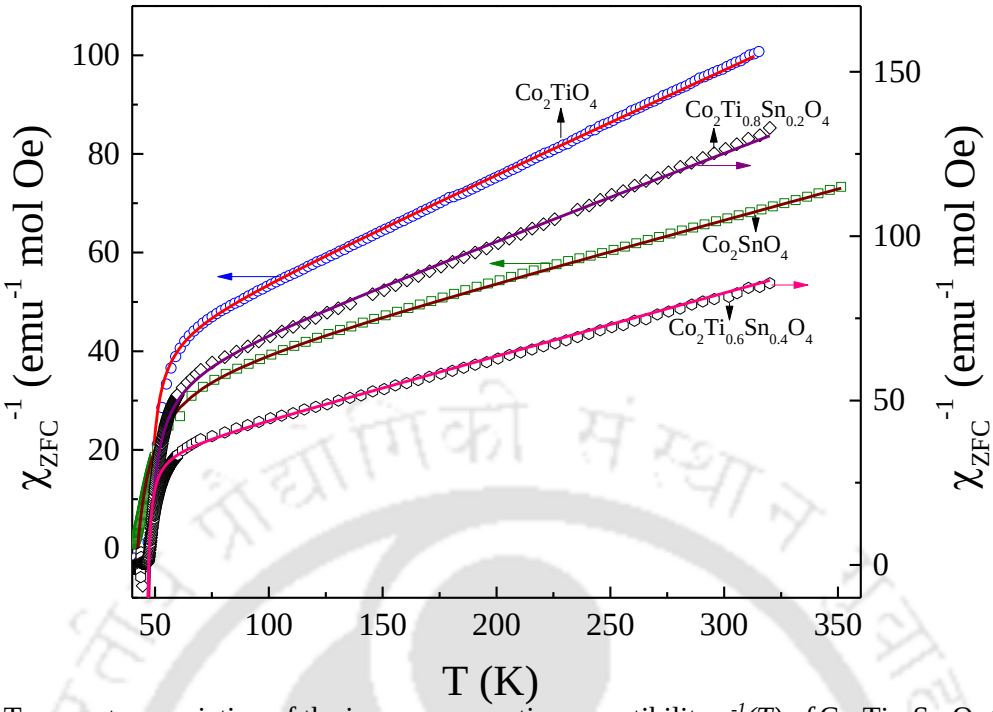

Figure 5.12: Temperature variation of the inverse-magnetic susceptibility $\chi^{-1}(T)$ *of* $Co_2Ti_{1-x}Sn_xO_4$ ($0 \leq x \leq 1$). The solid lines are best-fits to the Néel's expression for ferrimagnets as discussed in the text.

5.3.4 Temperature Dependence of the Paramagnetic Susceptibility:

The temperature dependence of inverse dc-magnetic susceptibility curves $\chi^{-1}(T)$, for various compositions of $Co_2Ti_{1-x}Sn_xO_4$ samples, recorded under zero-field cooled condition is fitted to the Néel's expression $(1/\chi) = (T/C) + (1/\chi_0) - [\sigma_0/(T- \theta)]$ for ferrimagnets, as shown figure 5.12. The scattered symbols are representing the experimental data points and the solid curve is theoretical fit to the above expression. The fitting parameters obtain from the Néel's expression are shown in table 5.2. The strength of the antiferromagnetic exchange coupling, between the two Co^{2+} spins on the tetrahedral 'A' and octahedral 'B' sites, are often termed as asymptotic Curie temperature $T_a = C/\chi_0$. The corresponding values of T_a being 162.11 K, 177.55 K, 121.67 K, 112.133 K for the compositions $x = 0, 0.2, 0.4, 1.0$ respectively. The effective magnetic moment $\mu_{eff} = 6.16\ \mu_B$ per formula unit (f.u.) of parent compound Co_2TiO_4 is determined using $C = N\mu_{eff}^2/3k_B$. Since the tetrahedral co-ordination does not allow orbital contribution, the magnetic moment at A-site of Co^{2+} ions is fixed as $\mu(A) = 3.87\ \mu_B$ with spin S = 3/2 and g = 2 and $\mu(B) = 4.79\ \mu_B$ is estimated using the formula $\mu_{eff}^2 = [\mu(A)]^2 + [\mu(B)]^2$ for Co_2TiO_4. Table 5.2 summarizes the magnetic moments at tetrahedral A- and octahedral B- sites for various compositions of 'Sn' substituted Co_2TiO_4. The important feature of Co_2TiO_4, is that the observation of compensation temperature at 32 K below which the system retains its ferrimagnetic character. On the contrary, similar compensation point was not exhibited by Co_2SnO_4 even though for T < 7 K, there was no coercive force or remanence magnetization in this system which is typical characteristics of a compensated state. The large magnitudes of the coercivity, observed in tin substitute cobalt-orthotitanate, in the uncompensated state is most likely results from the growth

Table 5.2: The list of various parameters obtained from the Néel's fits of χ^{-1} versus T curve with the experimental data points of various compositions of $Co_2Ti_{1-x}Sn_xO_4$ ($0 \leq x \leq 1$) recorded under zero-field-cooled condition. [*Co_2TiO_4 sample sintered at 1100°C, results of previous chapter].

System	C (emu K $mol^{-1}Oe^{-1}$)	χ_o (emu $mol^{-1}Oe^{-1}$)	σ_o ($emu^{-1}Oe$ mol K)	θ (K)	μ_{eff} (μ_B)	μ (A) (μ_B)	μ (B) (μ_B)
Co_2TiO_4	4.75±0.02	0.029±0.013	98.04±0.01	45.48±0.01	6.16±0.01	3.87	4.79±0.01
$Co_2Ti_{0.8}Sn_{0.2}O_4$	3.79±0.01	0.021±0.012	201.97±0.01	44.19±0.01	5.50±0.0	3.87	3.91±0.01
$Co_2Ti_{0.6}Sn_{0.4}O_4$	5.09±0.01	0.042±0.011	32.83±0.01	46.50±0.01	6.38±0.01	3.87	5.07±0.01
Co_2SnO_4	4.89±0.01	0.044±0.012	102.37±0.01	39.5±0.01	6.25±0.01	3.87	4.91±0.01
*Co_2TiO_4	5.25±0.02	0.042±0.012	31.55±0.01	49.85±0.01	6.5±0.01	3.87	5.19±0.01

of frozen-spin clusters formed as a result of the different magnetic moments of the cations residing in the octahedral B-sites. Also, the field dependent magnetization reversal, and lack of saturation of the magnetization noticed in these systems, below the ferrimagnetic ordering in magnetic fields up to as high as 150 kOe, suggests the complex canting of the magnetic moments, which can be best determined by neutron diffraction measurements.

5.3.5 Compositional Dependence of Exchange-Interaction:

Usually, the superexchange interaction in magnetically ordered insulators with spinel-crystal structure was adequately described by three nearest neighbour exchange constants (J_{AA}, J_{AB} and J_{BB} where A and B refer to the ions on the tetrahedral and octahedral sites, respectively). Among various theoretical and experimental techniques established to evaluate the magnitude of such exchange-parameters, the temperature dependence of paramagnetic susceptibility is one constructive experimental method through which one can estimate the precise values of *J*. Using the parameters obtained from the Néel's fits we have determined the molecular field constants (N_{AA}, N_{BB} and N_{AB}) and the corresponding exchange constants (J_{AA}, J_{BB} and J_{AB}) for all the compositions (figure 5.13a and 5.13b) [131]. The magnitudes of antiferromagnetic exchange constants evaluated from the Néel's expression are J_{AA} = 3.92 k_B (5.77 k_B), J_{BB} = 6.62 k_B (7.85 k_B) and J_{AB} = 5.24 k_B (7.07 k_B) for $Co_2Ti_{0.6}Sn_{0.4}O_4$ (un-doped), respectively. Below 'T_N' the net small moment of 0.92 μ_B per f.u (μ(B) - μ(A)) was noticed from the M-T data. With increasing the 'Sn' content, the μ_{eff} decreases first to 5.50 μ_B for 20 at% of 'Sn', and then increases to 6.38 μ_B for x = 0.4. This effect is consistent with the variation of the exchange integral (J) with respect to the Sn-composition (x), as shown in the figure 5.13b. It is interesting to note that for the composition x = 0.2, both the 'A' and 'B' sites magnetic moments becomes almost equal ($\Delta\mu$ = μ(B) - μ(A) ~ 0.04 μ_B), signifying the lacking

of spin-orbit coupling on the B-sites of $Co_2T_{0.8}Sn_{0.2}O_4$. Whereas, the difference in the magnetic moments at A and B sites $\Delta\mu \sim 1.20\ \mu_B$ and $1.03\ \mu_B$ for $Co_2T_{0.6}Sn_{0.4}O_4$ and Co_2SnO_4 systems, respectively suggesting the signature of spin-orbit coupling on the B-sites. The molecular field constants and exchange constants of various compositions of $Co_2Ti_{1-x}Sn_xO_4$ ($0 \leq x \leq 1$) are listed in table-5.3. Generally, for antiferromagnetic interaction between two spins, the estimated molecular field constants should satisfy the general requirements of $N_{BB} > N_{AA}$ (for spinels), however, in the present case, we noticed that N_{AB} is dominant over N_{BB} and N_{AA} for all the compositions [18]. It is clear from the figure 5.13a that all the molecular field constants show maximum value for 20 at% Sn substituted Co_2TiO_4 sample. Also, the exchange constant J_{AA} shows maximum value for $Co_2Ti_{0.8}Sn_{0.2}O_4$. On the other hand, for 100% Sn substitution (i.e. Co_2SnO_4) the exchange constants follows the trend $J_{AB} > J_{BB} > J_{AA}$, whereas J_{BB} is dominating over other two exchange constants in the Co_2TiO_4 and $Co_2Ti_{0.6}Sn_{0.4}O_4$ samples (figure 5.13b). As discussed in the above section that possibility of ASD could result mixed exchange interactions, which may cause the collapse of long-range order, and lead to the spin-glass like phase at low-temperatures [137]. Dionne *et al*. reported that two entirely different set of exchange constants are needed to fit the inverse-magnetic- susceptibility data [201]. Moreover, the substitution of non-magnetic ions inside the magnetic-spinel sublattice alters the exchange-constants drastically, as, noticed in the current study for the intermediate composition $x = 0.2$ $J_{AA} > J_{AB} > J_{BB}$. Nevertheless, a complicated three-sublattice (A, B′, B″)

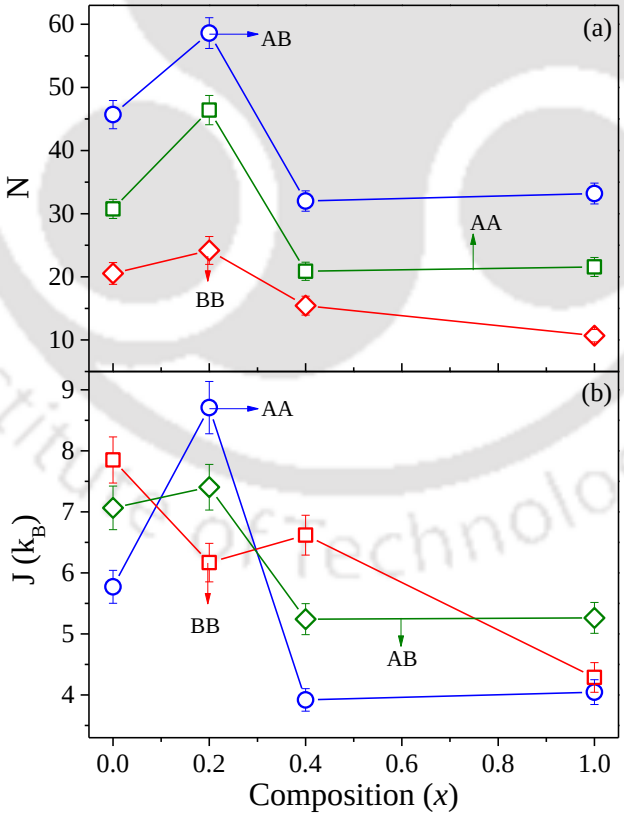

Figure 5.13: The compositional variation of the (a) molecular field constants, and (b) exchange constants of $Co_2Ti_{1-x}Sn_xO_4$.

Table 5.3: The list of molecular -field constants, exchange constants and Landé g-splitting factors (g_A =2 and g_B) obtained from the Néel's fits of paramagnetic susceptibility χ^{-1} versus T for various compositions of $Co_2Ti_{1-x}Sn_xO_4$ ($0 \leq x \leq 1$) recorded under zero-field-cooled condition. *Co_2TiO_4 sample sintered at 1100°C.

System	N_{AA}	N_{BB}	N_{AB}	J_{AA} (k_B)	J_{BB} (k_B)	J_{AB} (k_B)	g_B
Co_2TiO_4	30.76±1.51	20.54±1.72	45.69±2.23	5.77±0.27	7.85±0.38	7.07±0.36	2.47±0.02
$Co_2Ti_{0.8}Sn_{0.2}O_4$	46.41±2.32	24.18±2.21	58.62±2.43	8.71±0.43	6.17±0.32	7.40±0.37	2.02±0.02
$Co_2Ti_{0.6}Sn_{0.4}O_4$	20.88±1.44	15.44±1.50	32.01±1.61	3.92±0.18	6.62±0.33	5.24±0.25	2.61±0.03
Co_2SnO_4	21.56±1.51	10.68±0.98	33.20±1.65	4.05±0.20	4.28±0.24	5.26±0.25	2.53±0.03
*Co_2TiO_4	17.32±1.54	35.70±1.71	12.72±1.12	3.25±0.16	3.18±1.51	4.47±0.24	2.47±0.02

molecular-field approximation model with different routes of superexchange interaction via the ligands was suggested by Srivastava *et al*. [165]. This approach is more appropriate for the inverse-spinel ferrite like compounds such as $M^{2+}Fe^{3+}O_4$ (M = Cu^{2+}, $Li_{0.5}^{+}$, $Fe_{0.5}^{3+}$, Mn^{2+}, Co^{2+}, Ni^{2+}, Fe^{2+}, $Fe_{0.5}^{3+}$) than the two-sublattice model proposed by Néel [165]. The molecular-field (H_i) experienced by each ion located on the i^{th} sublattice, is related with the corresponding magnetization (M_j) and molecular-field constant (N_j) located at j^{th} sublattice through the following equations; $H_A = N_{AA}M_A - N_{AB'}M_{B'} - N_{AB''}M_{B''}$, $H_B = -N_{AB'}M_A + N_{B'B''}M_{B'} + N_{B'B''}M_{B''}$, and $H_C = -N_{AB''}M_A + N_{B'B''}M_{B'} + N_{B'B''}M_{B''}$. In these equations, the quantity N_{ij} is equivalent to $2Z_{ij}J_{ij}/\lambda_j g_i g_j \mu_B^2$, where, Z_{ij} is the number of nearest neighbour atoms on the j^{th} sublattice to an atom on the i^{th} sublattice, λ_j is the number of atoms per unit volume on the j^{th} sublattice, g_i and g_j are the Landé factors for the ions on the i^{th} and j^{th} sublattice respectively, and μ_B is the Bohr magneton. On the basis of the above procedure Srivastava *et al*. reported six superexchange constants for various types of inverse spinels [165]. For example, $CoFe_2O_4$ with lattice constant a_o ~ 8.38 Å and the number of *d*-electrons (n) = 7, the three-sublattice model yields $-J_{AA}$ ~ 15 K, $-J_{AB'}$ ~ 22.7 K, $-J_{AB''}$ ~ 26 K, $-J_{B'B''}$ ~ 18.5 K, and $-J_{B''B''}$ ~ 7.5 K for the configurations $d^{n=5}$– $d^{n=5}$,$d^{n=5}$– $d^{n=6}$, $d^{n=5}$– $d^{n=5,}$ $d^{n=6}$– $d^{n=6}$, $d^{n=5}$– $d^{n=6}$, and $d^{n=5}$– $d^{n=5}$, respectively. Similar analysis for the current systems may provide additional information, which will be helpful to completely understand the nature of the re-entrant magnetic ordering of the current system.

5.3.6 Summary:

To sum-up, the nature of magnetism in 'Sn' doped Co_2TiO_4 was studied using detailed temperature dependence of dc-magnetization and ac-susceptibility. Our experimental results demonstrates the co-existence of ferrimagnetic ordering, and reentrant spin-glass state together with a magnetic compensation effect, similar to

Co_2TiO_4 but with different ordering temperatures e.g. T_N ~ 46.1 K and T_F ~ 44.05 K, and T_{COMP} = 27.1 K for $Co_2Ti_{0.6}Sn_{0.4}O_4$. The interesting finding is polarity-reversal giant exchange-bias effect below T_{COMP} under both ZFC and FC conditions (i.e. coexistence of positive and negative H_{EB}), and the collapse of M_R and H_C in the proximity of T_{COMP}. The ferrimagnetic transition at T_N is associated with ordering of the longitudinal-spin-component, whereas, spin-glass transition T_F is due to the freezing of the transverse spin component. These observations confirm the theoretical predictions proposed by Villian [40] in insulating magnetic systems containing the nonmagnetic impurities. The molecular field constants (N_{AA} = 20.88, N_{BB} = 15.44, and N_{AB} = 32.01) determined from the fitting of experimentally obtained temperature dependence of inverse paramagnetic susceptibility to the Néel's expression for ferrimagnetism were found to be antiferromagnetic in nature. Subsequently, the effective magnetic moments evaluated from the above method at A- and B-sites are $\mu(A) = 3.87\ \mu_B$ and $\mu(B) = 5.07\ \mu_B$ respectively.

Chapter 6

Crystal Structure, Vibrational Excitations, Dielectric and Magnetic Properties of Co_3O_4 and Co_2TiO_4 Two-Phase Composites

6.1 Background:

The physical and chemical properties of binary transition-metal oxides (e.g: CoO, NiO, MnO, CuO etc.) and their alloys are well studied in the literatures because of their potential applications in Li-ion batteries, catalysis, transformer cores, sensors and ultra-high density magnetic recording media [3, 153, 202]. Such oxides with spinel crystal structure (Co_3O_4, Mn_2O_3 and Mn_3O_4) are unique compounds because of their interesting physics resulting from a variety of distribution of magnetic cations between the tetrahedral A-sites and octahedral B-sites [103, 174, 203, 204]. Among such spinels tricobalt tetraoxide (Co_3O_4) and its solid-solutions under reduced-dimension, and bulk grain size have received much attention recently due to their unique photocatalytic properties, heterogeneous catalytic activity for NO_x reduction, carbon monoxide oxidation, and removal volatile organic compounds (VOC) [10, 134, 205]. Co_3O_4 ($Co^{2+}[Co^{3+}]_2O_4$) belongs to a normal spinel family with occupation of tetrahedral sites by Co^{2+} ions and octahedral sites by Co^{3+} ions respectively. The net magnetic moment arises due to Co^{2+} ions largely because of spins, with a small contribution from spin–orbit coupling. On the other hand, the ground state configuration of the free Co^{3+} ion is $3d^6$. In the strong crystal field limit, the 3d electrons are paired in the t_{2g} levels and the Co^{3+} is in the low spin state. Thus, Co^{3+} ions have no permanent magnetic moment as a consequence of the splitting of 3d levels by the octahedral crystal field and complete filling of t_{2g} levels. Co_3O_4 shows an antiferromagnetic to paramagnetic transition with Néel temperature $T_N \approx 40$ K with each Co^{2+} ion in the A-site having four neighboring Co^{2+} ions of opposite spins [134, 174]. Recently, many studies have been initiated due to its prospective application in various field [206 - 208]. In particular, Jeong *et al*. reported that Cr-doped Co_3O_4 nanorods can act as chemi-resistor for ultra-selective monitoring of methyl benzene [209]. Wu *et al*. reported that Li-doped Co_3O_4 nanopowders with particle size 30 nm can act as promising oxygen evolution reaction (OER) catalysts [210]. Investigations on Ce-doped Co_3O_4 nanostructures divulge the existence of multi-emission centers and ferromagnetic ordering at room-temperature caused by the surface effects and oxygen vacancies [211]. Origin of such long-range magnetic ordering is debatable due to the fact that Co_3O_4 exhibits antiferromagnetic behavior with Néel temperature ($T_N = 30$ K) far below the room-temperature [10, 205, 206]. Recent studies by Durand *et al*. affirmed that the anomalous magnetic and structural properties exhibited by the $LaCoO_3$ are due to the presence of crystalline impurity phases, predominately that of Co_3O_4 [212]. Wang *et al*. suggested that nanocomposites made-up of N-doped porous carbon and Co_3O_4 can assist as potential anode material for lithium-ion batteries [213].

Excellent battery-cycling stability was noticed in the composites comprising of Co_3O_4 and mesoporous carbon with large surface area as compared with the reference system synthesized in pure ethanol [214]. The Co_3O_4

nanowires decorated with functionalized carbon-nanotubes have been explored recently for the high-performance super-capacitive properties (559 F g^{-1}) as compared with the pristine compound. Such 3D nanostructures exhibit exceptional cycling-stability i.e. little increase in the capacitance value instead of degradation after 10^3 cycles of charge-discharge process performed at the rate of 2 A g^{-1}[215]. Furthermore, Lin *et al*. exploited the gas-sensing characteristics of 1D Co_3O_4/polyethyleneimine-carbon-nanotube composite [216]. Development of such complexes may open a constructive approach to create low-cost and large-scale production of carbon monoxide and NH_3 gas sensors. Majority of the reports in the literature are focused on the catalytic properties, gas sensing features, and enhanced electrode performance in Li-ion batteries by either substituting different elements within the Co_3O_4 matrix or making nanocomposites consisting of Co_3O_4 [214 - 218]. Previous studies by Inagaki *et al.* reported that Co_2TiO_4 decomposes to Co_3O_4 and $CoTiO_3$ at 727°C [219]. The submicron particles of TiO_2 and Co_3O_4 react at about 700°C to form the $CoTiO_3$, which crystallizes into ilmenite crystal structure. However, this phase is not stable at very high temperatures T > 1200°C, instead Co_2TiO_4 forms as a stable phase. Despite of various reports available, a systematic study of 'Ti' doped Co_3O_4 or the solid solutions of Co_3O_4 and Co_2TiO_4 were not reported in the literature when we started to work on this problem. Therefore, a detailed study related to the diffusion of TiO_2 within the Co_3O_4 matrix was initiated in this chapter. Eventually, the solid-solution system forms a stable two-phase composite system comprising of both Co_2TiO_4 and Co_3O_4. We synthesized various compositions (x) of the solid solutions of (1-x) Co_3O_4 + x Co_2TiO_4 ($0 \leq x \leq 1$) and investigated the changes occurring in their (*i*) crystal structure, (*ii*) elemental analysis and local environment, (*iii*) vibrational excitation spectroscopy, (*iv*) magnetic, and (*v*) dielectric properties.

6.2. Experimental Details:

Various compositions of two-phase composites (1-x) Co_3O_4 + x Co_2TiO_4 ($0 \leq x \leq 1$) were synthesized by solid state reaction method starting with the stoichiometric amount of Co_3O_4 (Alfa Aesar, purity 99.99%) and TiO_2 (Alfa Aesar, purity 99.99%) as precursors. These mixed powders were first ground in an agate mortar and then pressed into cylindrical pellets of 13 mm diameter using a hydraulic press, followed by sintering at 1200ºC for 8 h in air to yield final compound. To examine the structural properties of these samples an X-ray diffractometer from Rigaku (model: TTRAX III) with Cu-K_α radiation of wavelength $\lambda = 1.5406$ Å was employed. Microstructure of the samples were examined using a Scanning Electron Microscope (SEM, LEO 1430 VP) equipped with energy dispersive X-ray analyzer. Raman spectra were recorded on the powder samples at room temperature using a micro-Raman spectrometer from Horiba Jobin Vyon (LabRam HR) operating at 514 nm wavelength excitation laser. For the low-temperature Raman measurements (down to 25 K) a different (Jobin Yvon T64000) spectrometer was employed, which is equipped with a dedicated heating/cooling sample stage (Linkam, THMS600). All the spectra of sintered samples were recorded in back-scattered geometry equipped with a 50x objective, appropriate edge filter, and a Peltier cooled charge-coupled device detector. An Ar^+ ion excitation laser

source under high-resolution dispersive geometry was used for these low-temperature micro-Raman measurements with wavelength λ = 514 nm and an 1800 lines/mm grating. The spectral resolution of the system is approximately 1 cm^{-1}. For high degree of positional accuracy the grating was fixed at unmoved condition during the entire temperature scan. The FTIR spectra of the compounds were recorded using a Perkin-Elmer 180 Spectrometer in the range of 4000–400 cm^{-1} with the spectral resolution of ± 2 cm^{-1}. A small amount of sample was first diluted with 150 milligrams of vacuum-dried IR-grade potassium bromide powder and subjected to a pressure of 39.2 bar. For the elemental analysis of the elements present in the samples, a dual source X-ray photoelectron spectroscope (Al-K_α @ 1486.8 eV, Mg-K_α @ 1253.6 eV) from VG Microtech, equipped with ultra-high vacuum (8×10^{-10} Torr) chamber with pass energy of 100 eV, was employed. The XPS spectra were recorded using mono-chromatized Al-K_α radiation, and the binding energies were calibrated against the C-1s peak 284.5 eV. Both dc-magnetization and frequency dependence (0.17 Hz - 1.2 kHz) of ac-magnetic susceptibility measurements were performed using a superconducting quantum interference device (SQUID) based magnetometer from Quantum Design with temperature capabilities of 5 K – 320 K and magnetic field (H) up to ± 70 kOe. High frequency (100 Hz ≤ f ≤ 30MHz) ac-electrical resistivity and dielectric permittivity studies of all the composites were performed between the temperatures -120 K and 570 K using the impedance and gain-phase analyzer from from Novocontrol Alpha AN impedance analyzer with Quatro cryosystem. A pour-fill liquid nitrogen cryostat was assembled with the impedance analyzer to achieve the low-temperatures below 300 K, where as a home-made heater was designed to realize high temperature measurements.

6.3. Characterizations:

6.3.1. Structural Analysis:

Figure 6.1 shows the X-ray diffraction pattern and the corresponding Rietveld refinement data of (1 - x) Co_3O_4 + x Co_2TiO_4 samples for different values of x wt% including pure Co_3O_4 (x = 0 wt%) and Co_2TiO_4 (x = 100 wt%). The Rietveld refinement was performed using FullProf suite. For the un-doped case (i.e. Co_3O_4) and lower values of 'x' i.e. dilute substitution of Co_2TiO_4. The X-ray diffraction patterns were analogous to the normal spinel structure similar to that of pure Co_3O_4 without any secondary phase. All these diffraction pattern were corresponding to the space group $Fd\bar{3}m$ (227) [JCPDS 43-1003]. However, slight difference in the lattice parameter ('a' = 8.074 Å) was noticed as compared with the standard values of Co_3O_4 ('a' = 8.077 Å). As the composition increases, the diffraction peaks corresponding to the inverse spinel cobalt-orthotitanate (Co_2TiO_4) becomes more prominent (lattice parameter a = 8.45 Å). This secondary phase formation increases progressively with increasing the x. The Miller indices of planes are shown in blue color in figure 6.1 and the obtained lattice constant is in close agreement with the standard value 8.434 Å [JCPDS 39-1410]. The weight % of both these phases were quantitatively analyzed using the following equation [110].

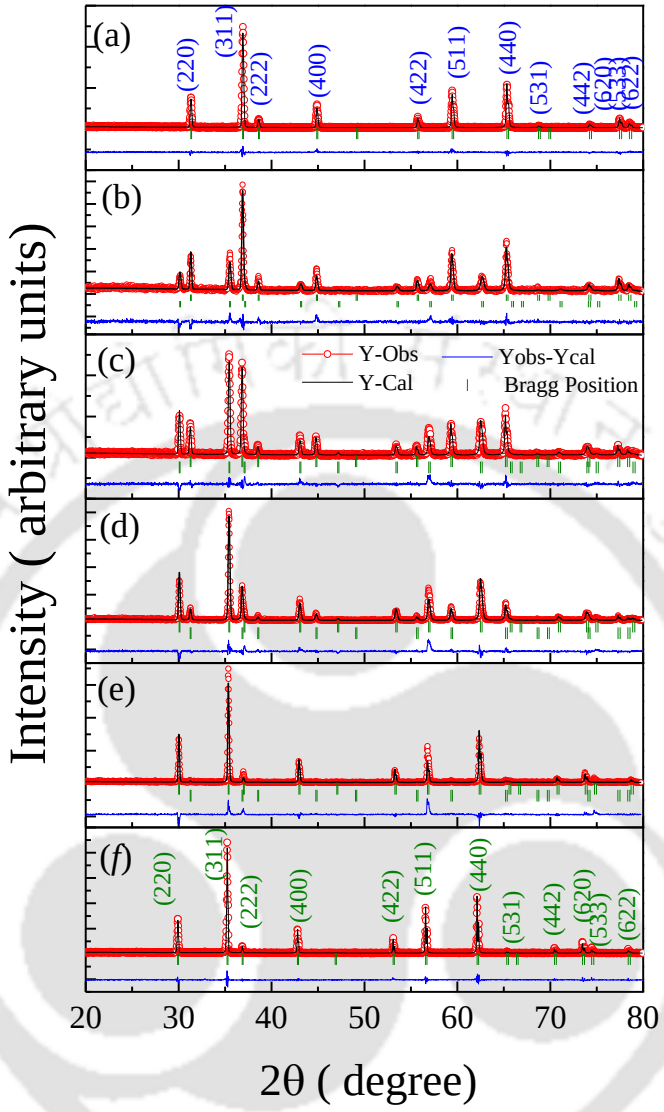

Figure 6.1: The X-ray diffraction pattern together with the Rietveld refined data of composite system (1-*x*) Co_3O_4 + *x* Co_2TiO_4 for (a) *x* = 0, (b) *x* = 0.23, (c) *x* = 0.463, (d) *x* = 0.706, (e) *x* = 0.882, and (f) *x* = 1.

$$W_{CTO} = [1/\{1 + 1.265\ (I_{CO}/I_{CTO})\}] \times 100 \quad \ldots (6.1)$$

where W_{CTO} indicates the weight fraction of the Co_2TiO_4 phase, I_{CTO} and I_{CO} represents the strongest X-ray diffraction line intensities of the Co_2TiO_4 and Co_3O_4, respectively. In the present case, diffraction intensity of (311) peak of both the phases were considered as highest intensity peak. Using the above equation the evaluated weight % (*x*) of Co_2TiO_4 are *x* = 0, 23.05, 46.3, 70.6, 88.8 and 100% consistent with the theoretically estimated weighed quantities 0, 23, 45, 70, 88 and 100% respectively. The intensity ratio of the XRD peak intensities of two phases Co_2TiO_4 and Co_3O_4 are shown as a function of wt% (figure 6.2(a)).

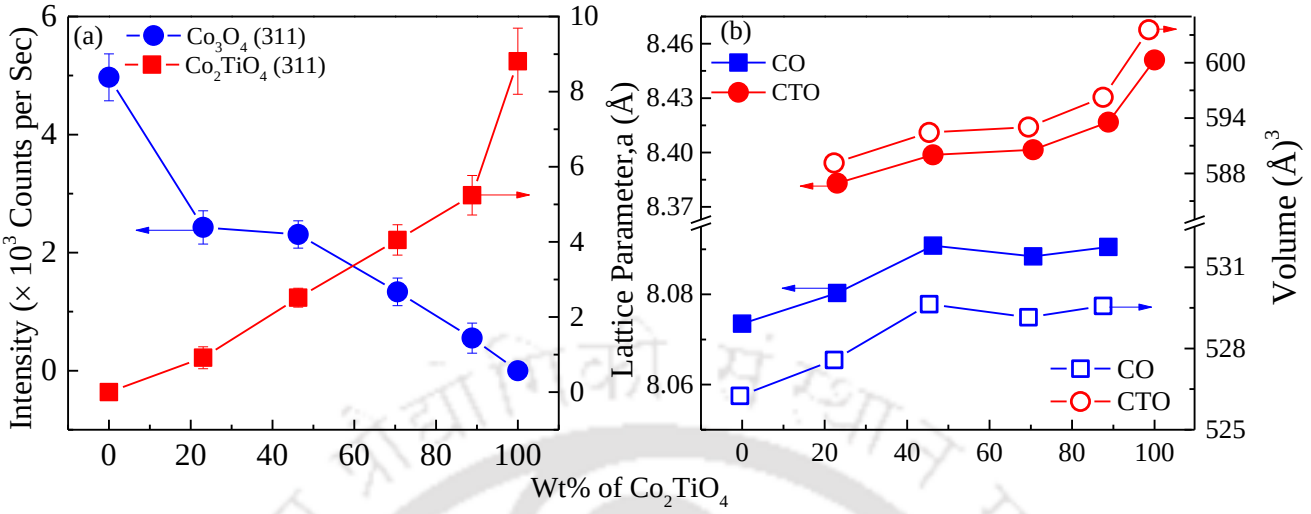

Figure 6.2: (a) Intensity of the (311) reflection of both Co_3O_4 and Co_2TiO_4 phases of the composites ((1-*x*) Co_3O_4+ *x* Co_2TiO_4 [$0 \leq x \leq 1$ (100 wt%)]) (b) The composition variation of lattice parameter 'a' and unit-cell volume 'V' of Co_3O_4 /Co_2TiO_4 two phase composite. Note: The contribution of both the phases (Co_3O_4 and Co_2TiO_4) is plotted separately.

Figure 6.2(b) shows the variation of lattice parameters 'a' and the volume of the unit-cell 'V' as a function of Co_2TiO_4 wt% (*x*). Up to $x = 0.463$ both 'a' and 'V' increases (for Co_3O_4) and attains a maximum value of 8.09 Å, beyond which no significant variation was noticed. On the contrary, for Co_2TiO_4 both 'a' and 'V' were found to increase progressively with increasing the '*x*'. Since the ionic radius of either Ti^{4+} (= 0.605 Å) or Ti^{3+} (= 0.67 Å) is larger than the ionic radius of Co^{3+} (0.545 Å) at the octahedral location (i.e. B-sites), one can expect a significant expansion of the unit-cell volume due to the substitution of 'Ti' ions at the Co^{3+} locations in the Co_3O_4 matrix. Nevertheless, for $x = 0.463$ the formation of Co_2TiO_4 grains disturbs the 'A' and 'B' sites of Co_3O_4 system which may cause some alteration in the average unit cell volume. Beyond $x = 0.463$, the secondary phase Co_2TiO_4 dominates over Co_3O_4 phase and no significant change in the 'a' and 'V' values was noticed for both the systems. For a clear understanding of such fine variations in 'a' and 'V' we have estimated the bond-angles (A-O-B and B-O-B) and bond-lengths (A-O and B-O) of major phase for various compositions as shown in figure 6.3. These bond-angles and bond-lengths are corresponding to the major phase (*i.e.* normal spinel Co_3O_4) up to $x = 0.463$ (46.3 wt%), beyond which, the bond-angles and bond-lengths parameters corresponding to the inverse spinel Co_2TiO_4 phase, which is the dominant phase in the composite system. For lower compositions the bond angle A-O-B (122.72º) at first decreases and then suddenly increases reaching a maximum value of 130.35º for $x = 0.706$ (70.6 wt%), and again starts decreasing as the formation of inverse-spinel structure dominates. However, exactly opposite trend was noticed in the case of B-O-B angle. As the system transforms from normal to inverse spinel the bond length A-O = 1.854 Å for $x = 0$ (i.e. for Co_3O_4) and 1.984 Å for $x = 1$ (100 wt% or Co_2TiO_4 as a whole) and B-O = 1.958 Å for $x = 0$ (i.e. for Co_3O_4) and 2.025 Å (i.e. for Co_2TiO_4). Nonetheless, these values are slightly higher as compared to the standard bond angles ($121^{\circ}_{\text{A-O-B}}$, $95.7^{\circ}_{\text{B-O-B}}$) of Co_3O_4. No significant lattice strain was

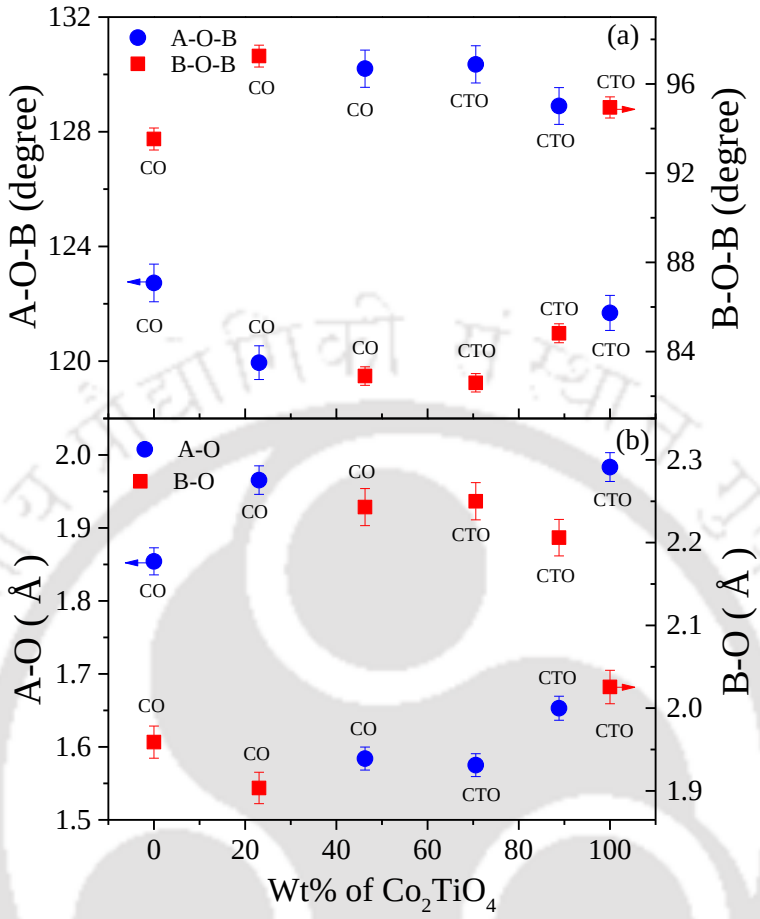

Figure 6.3: The composition variation of (a) bond-angles [(B-O-B) and (A-O-B)] (b) and bond-lengths [(A-O) and (B-O)].

detected from the X-ray line-broadening (with very less micro-strain $\eta \leq 2.5\times10^{-3}$) as estimated from the Williamson-Hall analysis when the Co_2TiO_4 content increases inside the parent Co_3O_4 matrix. The average grain sizes lies in the micrometer range and is consistent with the values obtained from SEM-micrographs recorded under secondary electron mode.

6.3.2 Morphology and Microstructure Analysis:

Figure 6.4a shows the SEM images of pure Co_3O_4 bulk sample sintered at 1200°C for 8 h in air without any Co_2TiO_4. For this sample the grain sizes are lying in the range 0.8 to 0.95 μm. Figures 6.4(b), 6.4(c) and 6.4(d) show the 0.463 (46.3 wt %), 0.706 (70.6 wt %) and 1 (100 wt %) of Co_2TiO_4 grains inside the Co_3O_4 matrix having the grain sizes in the range 1.5 – 1.65 μm, 1.7 – 1.8 μm and 2.2 – 2.35 μm, respectively. From these figures we noticed a progressive increase of grain sizes with increase of quantity of secondary phase Co_2TiO_4.

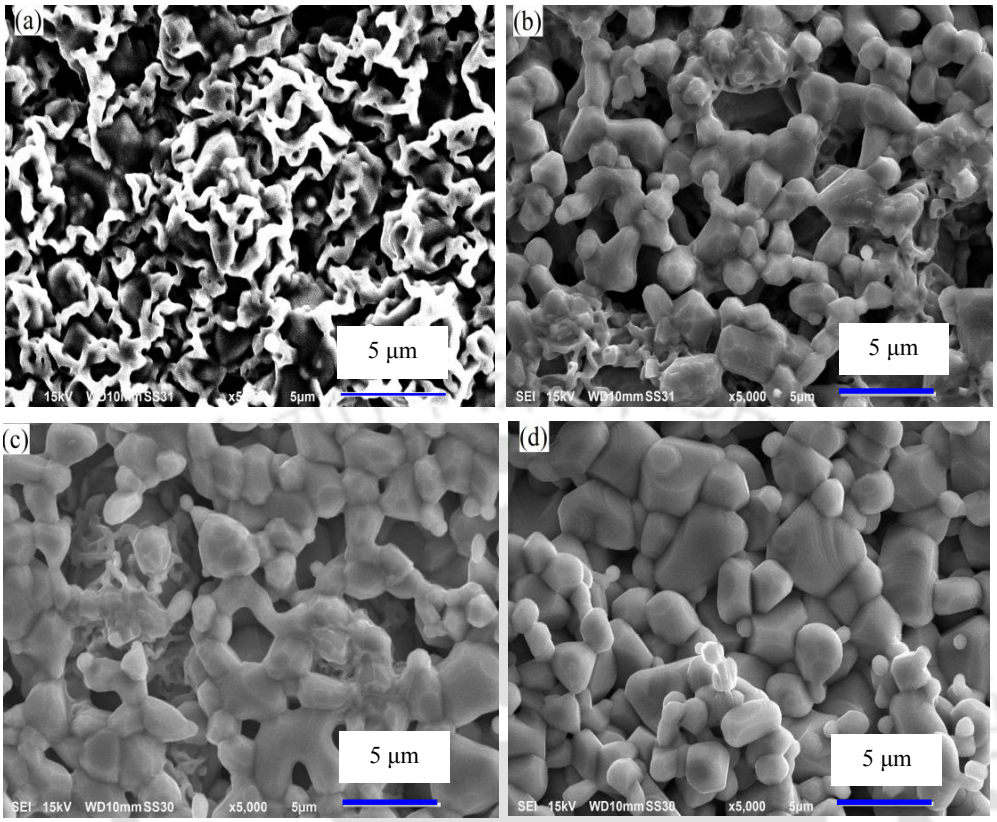

Figure 6.4: Scanning electron micrographs of two-phase composites recorded under secondary-electron (SE) mode for different compositions (a) $x = 0$, (b) $x = 0.463$, (c) $x = 0.706$, and (d) $x = 1$.

6.3.3 Vibrational Excitations and Micro-Raman Spectroscopy:

In order to probe the phonon dynamics (vibrational excitations) of investigated oxides we have performed the Raman spectroscopy measurements both at room temperature and low-temperatures down to 25 K using liquid helium. In the literature till now there have been no Raman spectroscopic studies of either Co_2TiO_4 or its solid-solutions. Figure 6.5 shows the room temperature Raman spectra of the investigated system. We observed five Raman active modes centered at 194.6, 480, 517.8, 617.7 and 688.1 cm^{-1} for pure Co_3O_4 (i.e. for $x = 0$ wt %). The strongest modes appeared across 688.1 cm^{-1} correspond to symmetric stretching of oxygen (O_2^-) in tetrahedral groups (AO_4), and according to accepted convention, can be considered as A_{1g} symmetry. The vibrational modes E_g ~ 480 cm^{-1} corresponds to symmetric bending of oxygen with respect to cations in tetrahedral surrounding. The two vibrational F_{2g} modes, $F_{2g}(2)$ ~ 517.8 cm^{-1} and $F_{2g}(3)$ ~ 617.7 cm^{-1} are due to the asymmetric stretching and bending of the oxygen anion in the octahedral group (BO_6). The mode at 194.6 cm^{-1} ($F_{2g}(1)$) is due to translational movement of the whole tetrahedron. These results are consistent with the previous findings of Hadjiev *et al*. who identified five Raman-active modes (A_{1g}, E_g and $3F_{2g}$) in the single-crystals of Co_3O_4 samples measured at 312 K except slight shift of about 2 cm^{-1} towards the lower wavenumber side [220].

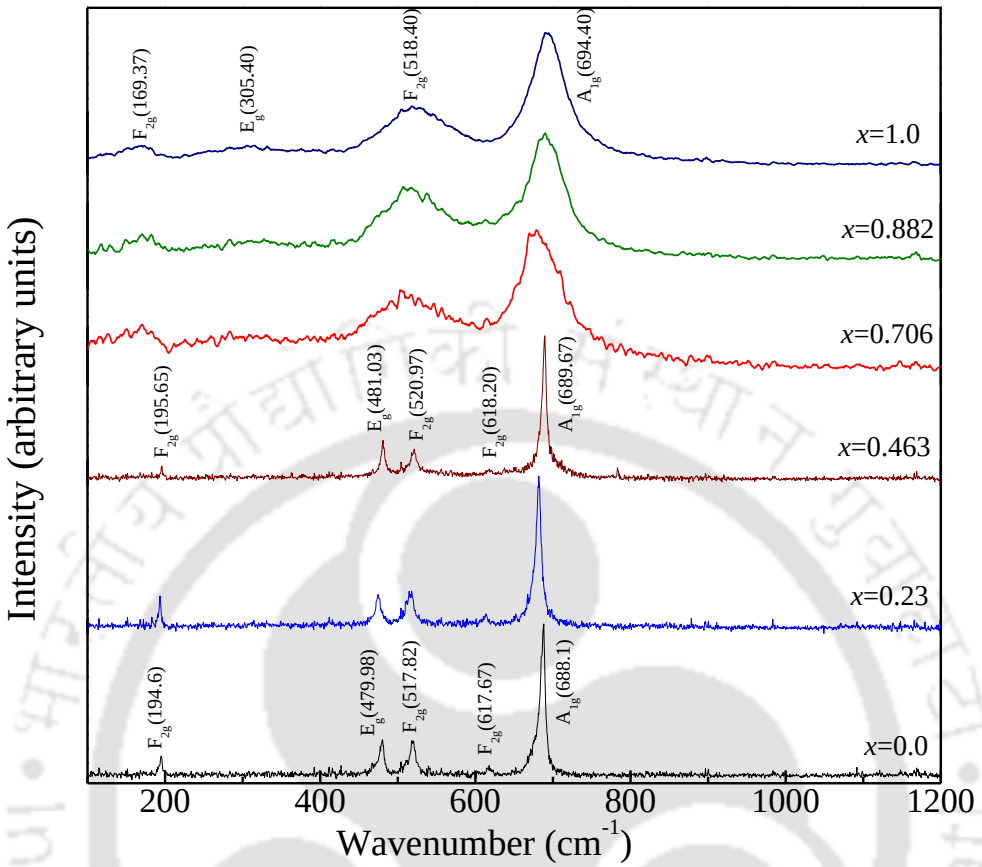

Figure 6.5: Room temperature Raman spectra (intensity versus wavenumber) of the two-phase composites (1-*x*) Co_3O_4 + *x* Co_2TiO_4 ($0 \leq x \leq 1$). The peaks represent various vibrational modes of the spectra.

The vibrational modes of normal cubic-spinel Co_3O_4 (space group F_{d3m}-O^7_h) with fourteen atoms in the primitive unit cell can be represented as-

$$\Gamma\ (k = 0) = A_{1g} + E_g + 3F_{2g} + 5F_{1u} + 2A_{2u} + 2E_u + 2F_{2u} \ldots (6.2)$$

Following the extensive investigations of the vibrational modes, of Rousseau *et al*. [221], the 42-dimensional representation 'Γ' at k = 0 can be reduced into 16 irreducible representations of the factor group O_h (listed above) [220 - 223]. Among the five F_{1u} modes, four are infrared active and one is acoustic mode. The remaining modes F_{1g}, $2A_{2u}$, $2E_u$ and $2F_{2u}$ are inactive. The A_{1g}, E_g, and the three F_{2g} modes are Raman active. For moderate substitution of Co_2TiO_4 inside the Co_3O_4 matrix, the intensity of F_{2g} mode located at 617.7 cm^{-1} starts decreases and disappears altogether when the system transforms to complete inverse spinel Co_2TiO_4. Also, it is interesting to observe that the A_{1g} mode shifts by ~ 6.3 cm^{-1} towards the higher wavenumber side with giant peak broadening for pure Co_2TiO_4 sample. Also, the $F_{2g}(3)$ and $F_{2g}(2)$ modes are unable to distinguish in Co_2TiO_4, instead a highly broadened peak centered at 517.82 cm^{-1} was noticed. Nevertheless, a giant bathochromic red shift ~ 25.23 cm^{-1} of F_{2g} mode is noticed in the case of Co_2TiO_4. Such shift occurs due to the substitution of 'Ti' ions in the octahedral

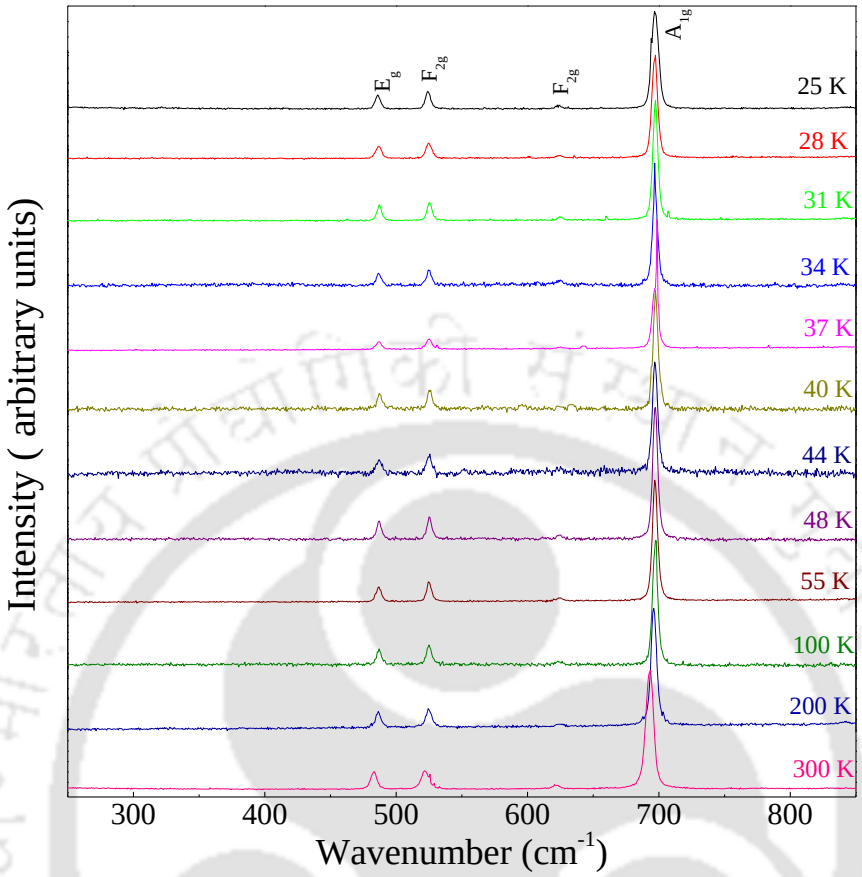

Figure 6.6: Raman spectra of Co_3O_4 recorded at various temperatures in the range 300 K – 25 K.

sites, which enhanced the bond length between the octahedral cations and oxygen (B-O) [224]. The list of positions and the full-width-of-half-maxima (FWHM) of the Raman active phonon modes of both Co_3O_4 and Co_2TiO_4 together with $x = 0.463$ samples measured at 300 K are listed in the table 6.1. The unusual behavior of the intensity and the shape of the peak can be related to the distribution of cations in the solid-solutions of the series (1-x) Co_3O_4 + x Co_2TiO_4. The electron hopping between the Co^{2+} and Co^{3+} ions in pure Co_3O_4 causes polaronic conduction at room temperature. But, when we incorporate Ti ions, it disturbs the polaronic conduction as a result peak broadening occurs. The reason for anisotropic Raman line shape may be due to random cationic distribution in the octahedral site and little amorphous nature present in the system [225, 226].

For a detailed understanding of the temperature induced changes in the vibrational modes we have performed the low-temperature Raman measurements (up to 25 K) on both the systems Co_3O_4 and Co_2TiO_4. Figures 6.6 and 6.7 show the Raman spectra measured at different temperatures between 300 K and 25 K. The temperature variation of peak positions of A_{1g} and F_{2g} modes up to 25 K is separately shown in the figure 6.8. It is clear from the figure that both the phonon modes show clear anomalies across 25 K to 55 K which is associated with their change in the paramagnetic to antiferromagnetic ordering. For Co_3O_4 case we observed a sharp rise in the shift of

Table 6.1: Line positions and widths (FWHM) of the Raman-active modes of (1-*x*) Co_3O_4 + *x* Co_2TiO_4 (*x* = 0, 0.46(46.3) and 1(100 wt%) sintered at 1200ºC in air recorded at Room temperature.

Phonon mode	Co_3O_4 (*x* = 0 wt%)				*x* = 0.463(46.3 wt%)		Co_2TiO_4 (*x* = 1(100 wt%)	
	Present data		Ref. [40]					
	Peak Position (cm^{-1})	FWHM (cm^{-1})	Peak Position (cm^{-1})	FWHM (cm^{-1})	Peak Position (cm^{-1})	FWHM (cm^{-1})	Peak Position (cm^{-1})	FWHM (cm^{-1})
F_{2g}	194.6	10.7	194.4	4.9	195.6	4.2	169.4	47.7
E_g	480	9.9	482.4	6.0	481.0	6.3	305.4	16.1
F_{2g}	517.8	11.0	521.6	9.5	520.9	8.4	518.4	93.3
F_{2g}	617.7	10.1	618.4	6.7	618.2	10.5	--	--
A_{1g}	688.1	10.8	691.0	6.2	689.7	7.0	694.4	51.4

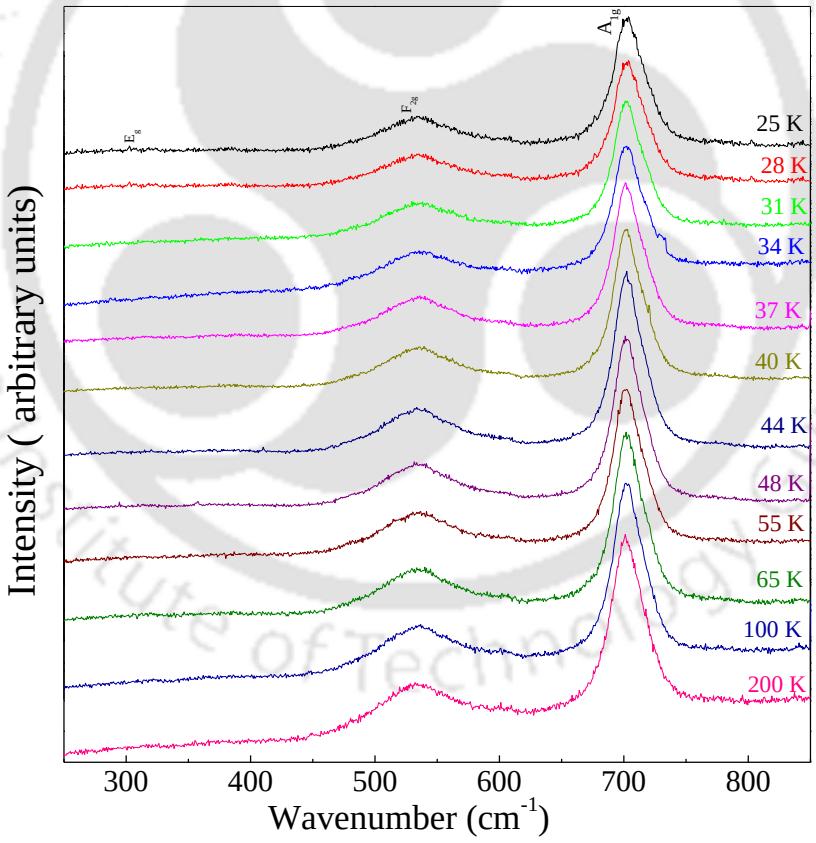

Figure 6.7: Raman spectra of the inverted spinel Co_2TiO_4 at various temperatures between 300 K and 25 K.

both phonon modes A_{1g} and F_{2g} across 40 K. Such sharp change is associated with the change in the magnetic ordering of Co_3O_4 across the Néel temperature $T_N \sim 30 \pm 10$ K [174]. On the other hand, the A_{1g} and F_{2g} peak of

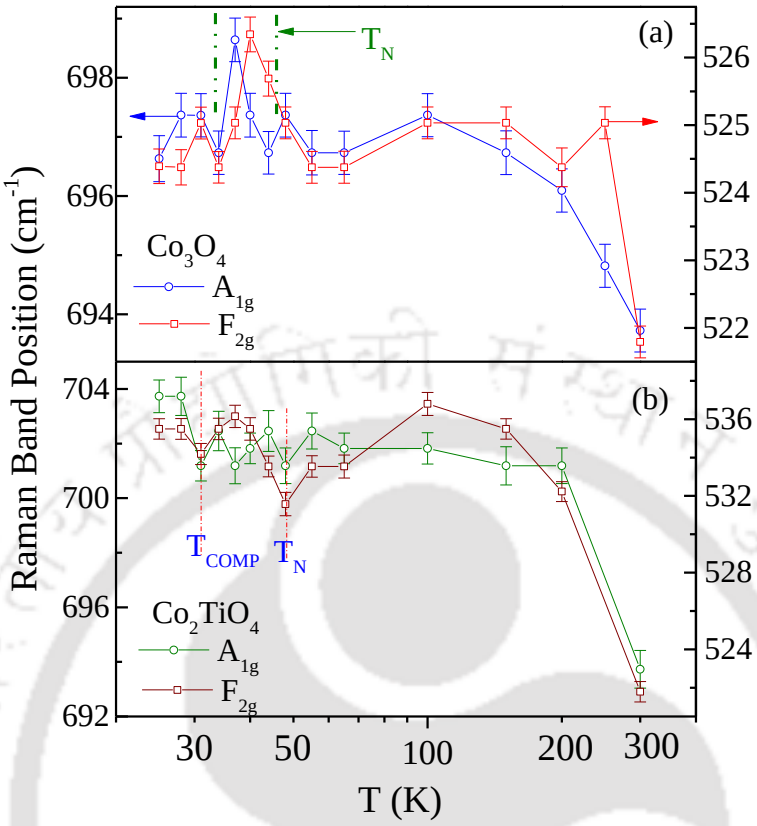

Figure 6.8: Temperature variation of the location of Raman active phonon modes A_{1g} and F_{2g} of (a) normal spinel Co_3O_4, and (b) inverse spinel Co_2TiO_4.

Co_2TiO_4 shifts to high frequency side with anomalies across 31 K and 48 K associated with the magnetic compensation temperature and ferrimagnetic Néel temperature, respectively (figure 6.8b) [77, 80].

It is well known that Co_2TiO_4 exhibits clear change in the temperature dependent dc-magnetic susceptibility across 31 K and 48 K. The change across 48 K was due to the ferrimagnetic ordering which is resulting from different magnetic moments of Co^{2+} on the A-sites (3.87 μ_B) and B-sites (5.19 μ_B). On the other hand, the transition at 31 K is associated with the magnetic compensation temperature effect, where the bulk-magnetization of two-sublattices balances each other. The impact of such magnetic ordering is on the A_{1g} and F_{2g} modes are significant as seen from the anomalies noticed in figure 6.8.

6.3.4. Fourier Transform Infrared (FTIR) Spectroscopy:

Figure 6.9 shows the FTIR spectra (Transmittance T (%) versus wavenumber (cm^{-1})) of various compositions of the two-phase composites. All the spectra were recorded between the wavenumbers 400 and 4000 cm^{-1}. For all the samples except the higher compositions, IR spectra exhibits two distinct bands across 576 cm^{-1} and 665 cm^{-1} indicated by B_1 and B_2, respectively. These bands originate from the vibrational stretching of the metal-

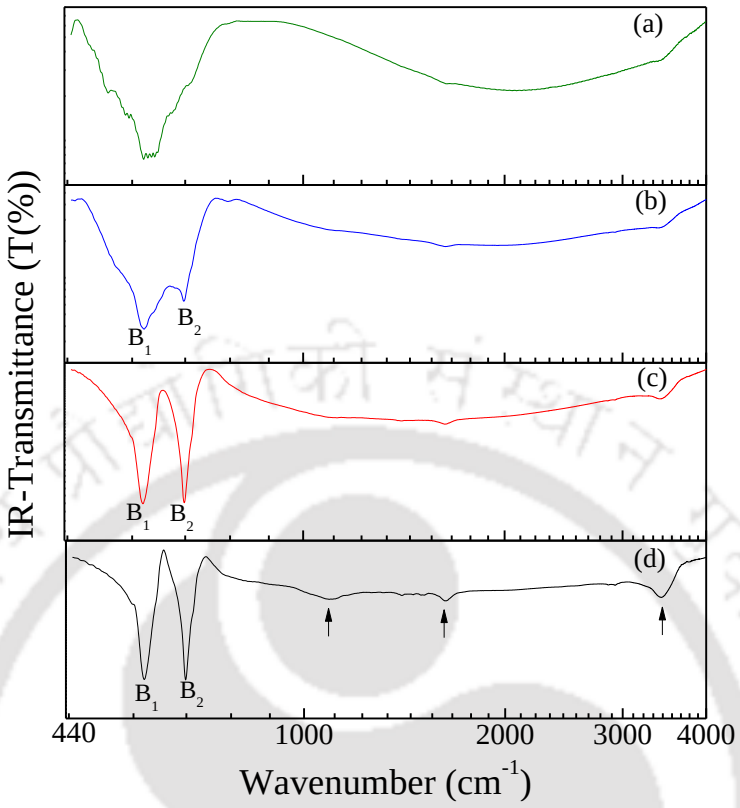

Figure 6.9: Transmittance (T(%)) versus wavenumber (cm^{-1}) of Fourier-transform infrared spectroscopy (FTIR) spectra of (1 - x) Co_3O_4 + x Co_2TiO_4 two-phase composites recorded at room temperature for different compositions (a) x = 1, (b) x = 0.706, (c) x = 0.23, (d) x = 0.

oxygen bonds of length ~195.8 pm and ~185.4 pm. The intensity of sharp bands located at B_1 and B_2 gradually smeared-off as the system changes from normal to inverse spinel structure. For x = 0 (Co_3O_4 case) the B_1 band is associated with the vibrational stretching of bonds between the cations located at octahedral sites *i.e.* B-O-B_3 ⇒ Co^{3+}-O-$[Co^{3+}]_3$ of normal spinel-lattice [227- 229]. The second band B_2 was attributed to the vibrational stretching of bonds between cations located at tetrahedral and octahedral sites i.e. A-B-O_3 ⇒ [Co^{2+}-Co^{3+}-O_3] [229 - 231]. For dilute compositions the IR spectrum shows similar kind of stretching vibrations as that of pure Co_3O_4 with slight changes in the intensity of 'B_1' and 'B_2'. In general, for spinel systems, the bond vibrational between the oxygen ion and highest-valence cation, exhibits highest intensity IR-absorption at higher wavenumber side (*i.e.* in the high-frequency range) regardless of the co-ordination of the cation [227, 232].

The absorption bands appeared in the mid- and higher-wavenumber regimes often exhibits complex vibrational spectrum. Nevertheless, the IR spectrum of inverse spinel compound Co_2TiO_4 is completely different. Figure 6.10 shows the zoomed-view of the transitions appeared in figure 6.9(a) in the wavenumber range 500 cm^{-1} - 700 cm^{-1}. Two more transitions are viewed across 578 cm^{-1} and ~ 511 cm^{-1}, which are associated with the CoO_6 octahedra in which cobalt possess trivalent oxidation state in the octahedral vacancy. These findings are in-line

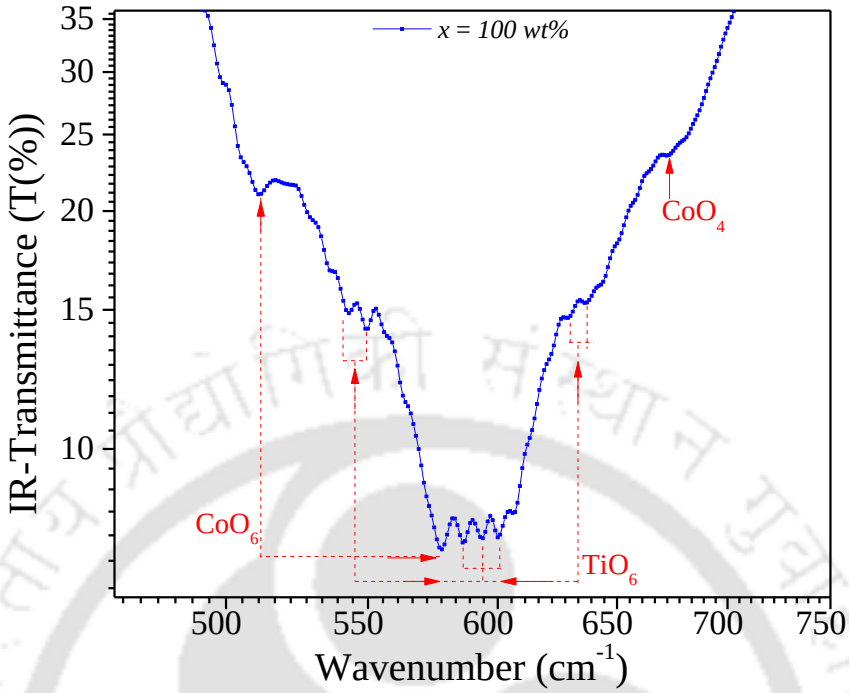

Figure 6.10: The enlarge view of the Fourier-transform infrared spectroscopy (FTIR) spectra of Co_2TiO_4 sample between 450 to 750 cm^{-1}.

with the previously reported data by Tang *et al*. [229]. The absorption bands noticed in the range 550 - 650 cm^{-1} are associated with the vibrational stretching frequency of Ti-O bond of the condensed [TiO_6] octahedral groups, which is consistent with the earlier reports [227, 233 - 237]. The final isolated vibrational mode observed at 673 cm^{-1} is the characteristic to the vibrational stretching frequency of Co^{2+}-Co^{3+}-O_3, in which Co^{2+} ions occupies the tetrahedral sites of inverse spinel lattice [229, 238]. Moreover, the absorption bands observed around 3427 cm^{-1}, 1632 cm^{-1} and 1084 cm^{-1} (shown by the arrow marks in figure 6.9(d) are assigned to the stretching and bending vibrations of the water molecules absorbed by the potassium bromide sample [239, 240].

6.3.5 Elemental Analysis using X-ray Photoelectron Spectroscopy:

For a detailed understanding of the valance state of the cations we have performed the X-ray photoelectron spectroscopy (XPS) measurements for both the systems Co_3O_4 (x = 0) and Co_2TiO_4 (x = 1) in the form of sintered pellets. Figure 6.11 and 6.12 show the XPS spectra of Co-2p orbitals for Co_3O_4 and Co_2TiO_4 samples respectively. Both these spectra exhibits two characteristic peaks at 780 eV and 796 eV corresponds to Co-2$p_{3/2}$ and Co-2$p_{1/2}$, respectively along with two satellite peaks at 789.7 eV and 803.1 eV. It is well known that both Co(II) and Co(III) exhibit similar binding energy peaks but the energy splitting ΔE between the two levels is different due to different spin-orbit coupling of Co^{2+} and Co^{3+} states with ΔE = 15.7 eV and 15.0 eV, respectively [112 - 114]. Figures 6.11b and 6.11c show the zoomed view of transitions Co-2$p_{3/2}$ and Co-2$p_{1/2}$, which clearly depicts the

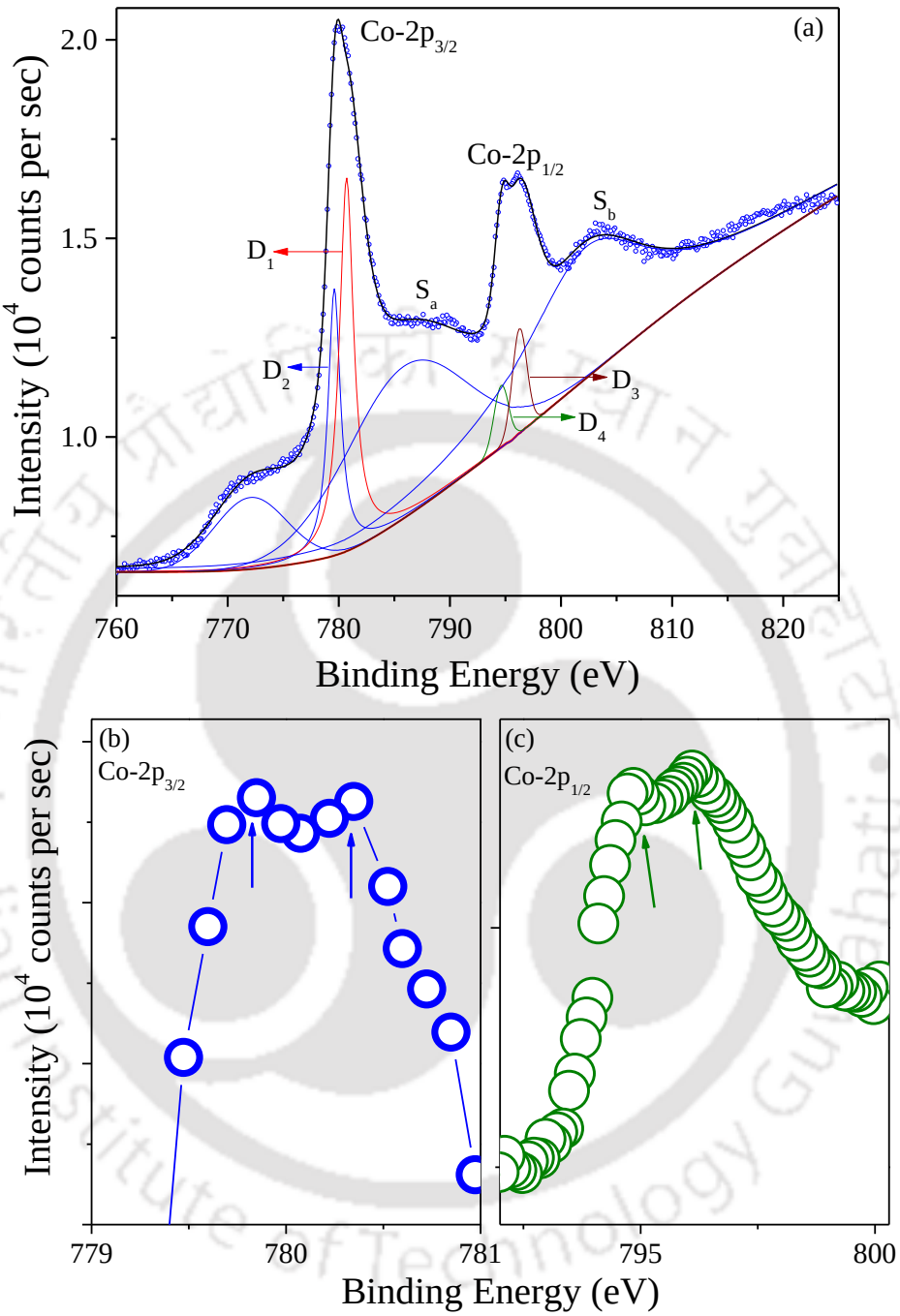

Figure 6.11: The core-level X-ray photoelectron spectra of (a) Co-2*p* peak of un-doped Co_3O_4 sample, (b) and (c) shows the enlarged views of Co-2$p_{3/2}$ and Co-2$p_{1/2}$ peaks, respectively.

splitting of these levels at D_1 = 779.8 eV, D_2 = 780.3 eV and D_3 = 794.8 eV, D_4 = 796.1 eV, respectively. These values are in good agreement with the previously reported data by Chuang *et al*. [158]. The energy separation obtained between the doublet peaks $\Delta E_{D1\text{-}D3}$ = 15.1 eV and $\Delta E_{D2\text{-}D4}$ = 15.7 eV are very close to the standard values

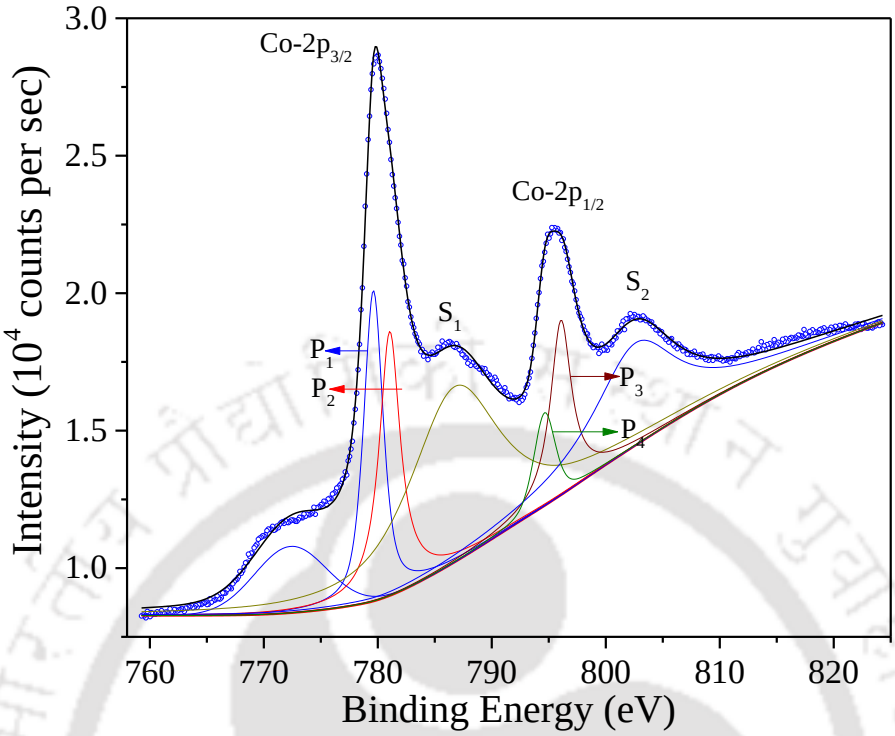

Figure 6.12: The core-level X-ray photoelectron spectra of Co-2*p* peak of Co_2TiO_4 sample.

15 eV and 15.7 eV for the Co^{3+} and Co^{2+}, respectively in Co_3O_4 bulk system, which signify the presence of trivalent and divalent cobalt cations in the Co_3O_4 system. Moreover, the XPS spectra of Co-2$p_{3/2}$ and Co-2$p_{1/2}$ for Co_2TiO_4 sample are slightly different (Figure 6.12). This figure consists of the raw-data as well as the Gaussian-Lorentzian fitting of Co-2*p* which depicts two different intensity doublets labeled by P_1 and P_2 for Co-2$p_{3/2}$ and P_3 and P_4 for Co-2$p_{1/2}$. The difference between those two doublets turns out to be $\Delta E_{P1\text{-}P3}$ = 15 eV and $\Delta E_{P2\text{-}P4}$ = 15.4 eV respectively, which confirms the signature of both Co^{2+} and Co^{3+} [112 - 115]. In general, trivalent configuration of cobalt cation is not possible in the inverted spinel Co_2TiO_4 = [Co^{2+}($Co^{2+}Ti^{4+}$) O_4]. However, in the present case, we observed the signatures of Co^{3+} contribution at the octahedral sites of Co_2TiO_4, which may play a vital role on the magnetic properties [section 4.3.3]. This trivalent configuration also decides most of the properties including the internal d-d transitions.

In most cases, the standard binding energy of Ti-2$p_{3/2}$ state in titanium-dioxide TiO_2 locates at 459.5 eV which corresponds to the '4^{+}' oxidation state of titanium ion [159]. But, the maximum intensity peak for Ti-2$p_{3/2}$ appears at 457.6 eV in Co_2TiO_4 as shown in the figure 6.13a. Also, a second highest intensity peak was noticed at 463.5 eV which is associated with Ti-2$p_{1/2}$. This result confirms the existence of '3^{+}' oxidation state of 'Ti' instead of 'Ti^{4+}' in Co_2TiO_4 [section 4.3.2]. The Ti^{3+} peak positions are consistent with the previously reported data of Ti^{3+} surface defects at 457.7 eV in TiO_2 system [241]. These results also rule out the presence of any metallic 'Ti' ions

in Co_2TiO_4 matrix, which usually shows their signatures in the XPS spectra ~ 454 eV. The line separation between Ti-2$p_{3/2}$ and Ti-2$p_{1/2}$ was δE = 5.87 eV, which is greater than the standard binding energy difference (5.7 eV) between the Ti-2$p_{3/2}$ and Ti-2$p_{1/2}$ states of Ti^{4+} configuration [241 - 244]. In case of Anatase TiO_2 powders both the tetravalent Ti-2$p_{3/2}$ and Ti-2$p_{1/2}$ locates at 458.8 eV and 464.6 eV respectively, although slight decrease of these binding energies was noticed in Co-doped Anatase TiO_2 powders [242].

Often the binding energy (BE) difference between the O-1*s* and Ti-2$p_{3/2}$ (Δ[O1s - Ti2$p_{3/2}$] = BE(O-1*s*) - BE(Ti-2$p_{3/2}$)) is used to characterize the standard valence state of the 'Ti' ions and also be used to avoid the contributions

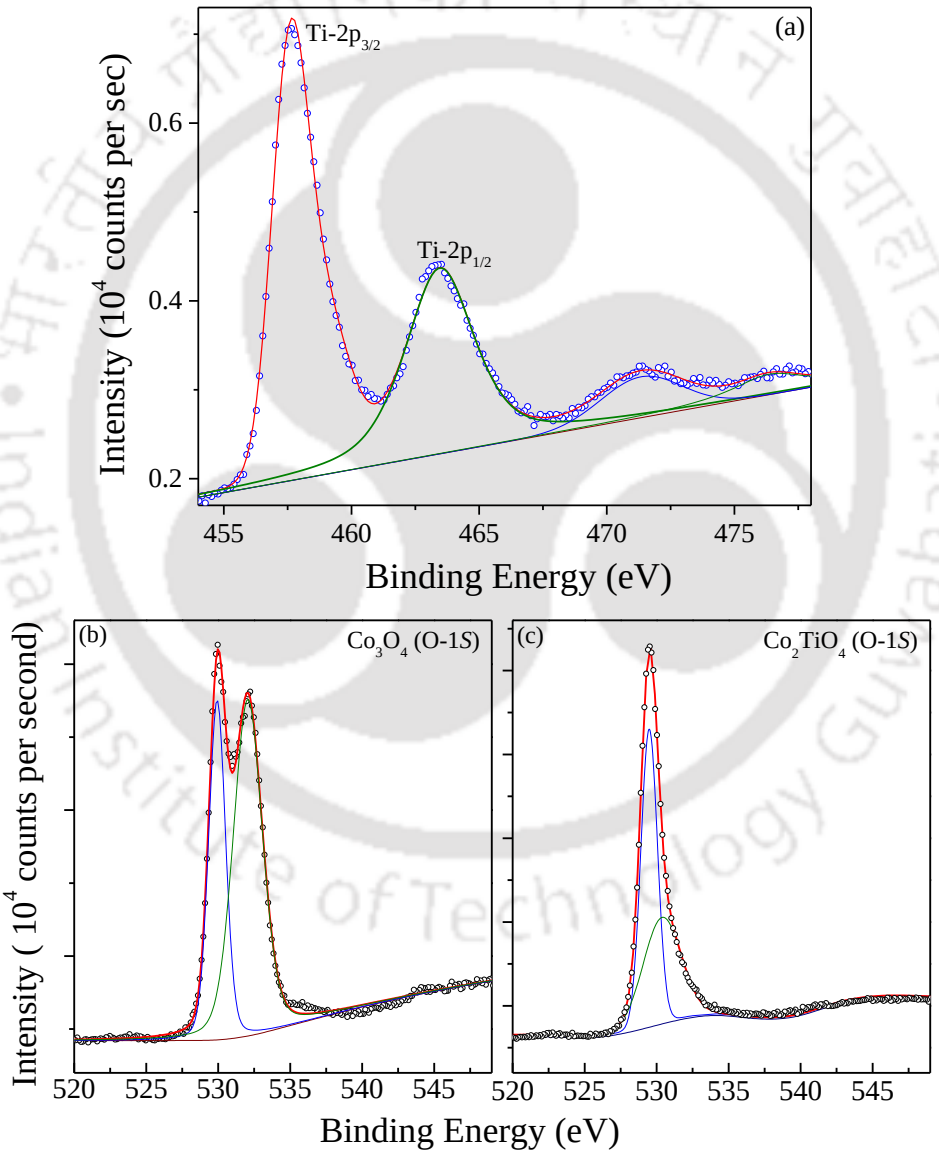

Figure 6.13: The core-level X-ray photoelectron spectra of (a) Ti-2*p* peak of Co_2TiO_4 sample, (b) and (c) are O-1s peak of Co_3O_4 and Co_2TiO_4 respectively.

Table-6.2: Atomic quantification of the normal-spinel Co_3O_4 and the inverse-spinel Co_2TiO_4 using the XPS data.

System	Atoms	I/F	Atomic concentration (%)		Theoretically calculated atomic concentration (%)
Co_2TiO_4	O-1s	49671.21	59.48		57.14
	Ti-2p	9739.47	11.66		14.28
	Co-2p	24092.20	28.85	Co^{3+} = 9.37 Co^{2+} = 19.48	28.57
Co_3O_4	O-1s	27688.39	64.58		57.14
	Co-2p	15180.20	35.41	Co^{3+} = 21.99 Co^{2+} = 13.41	42.85

from different energy scale calibration and charging effects [244]. The transfer of valance electrons from 'Ti' to 'O' plays a vital role in deciding the Ti-O chemical bond formation which in-turn cause in the shift of binding energy positions of Ti- $2p_{3/2}$ to higher level and O-1*s* to lower level. To avoid such sensitive discrepancies it is often convenient and advantageous to use the binding energy difference criterion Δ[O1*s*-Ti2$p_{3/2}$] for characterizing the exact electronic state of the 'Ti' cations. In the present case, the characterizing parameter Δ[O1*s*-Ti2$p_{3/2}$] turnout to be 71.8 eV for trivalent state, which was slightly higher as compared to the 71.4 eV for tetravalence 'Ti' ions [245- 247]. For Ti^{2+} case the BE difference Δ[O1s-Ti2$p_{3/2}$] is quite high ~ 75-76.7 eV [248, 249]. It has been reported that relatively higher BE difference (72.9 - 73.4 eV) of Ti^{3+} containing compounds such as Ti_2O_3, $Sn_{0.5}NbTiP_3O_{12}$ and $Fe_{0.33}NbTiP_3O_{12}$ [248, 250, 251].

The XPS peak of O-1s spectra deconvoluted into two different Gaussian sub-peaks centered at 529.9 eV and 532.2 eV, reflecting two different oxygen environment existing in the Co_3O_4 system (shown in figure 6.13b) [126, 248, 249, 252, 253]. The peak centered at 529.9 eV arises from the oxygen atoms bonded with nearest neighbor metal ions in the lattice. The peak located at 532.2 eV is attributed to the oxygen atoms in the vicinity of an oxygen vacancy and also the surface oxygen presence in the system [254]. On the other hand, for the case of Co_2TiO_4 the O-1*s* peak appears at ~ 529.52 eV (Figure 6.13c) with some weak signature of surface oxygen (530.5 eV), in Co_2TiO_4 bulk system [248, 249, 253]. Since the difference of the electronegativity's of 'Ti' (1.54) and 'O' (3.44) is higher than the difference between the 'Co' (1.88) and 'O', titanium tends to combine more strongly with oxygen anion. Thus 'Ti' dopant behaves as an oxygen vacancy suppressor, which also reduces the amount of surface oxygen in cobalt-orthotitanate [255, 256].

The XPS data are also fitted using a relative area ratio of 1:2 for the 2*p* component peaks keeping the constant FWHM of all core level peaks. Generally, the atomic percentage in A-B-O type system was evaluated using the

correlation between the atomic concentration, photoelectron intensity 'I' and atomic sensitivity factor 'F', using the following equation [257].

$$Atomic\ \%\ of\ A = \frac{\frac{I_A}{F_A}}{\frac{I_A}{F_A}+\frac{I_B}{F_B}+\frac{I_C}{F_C}} \times 100 \ldots (6.3)$$

The magnitude of the atomic sensitivity factor '*F*' can be obtained from the relation $F = \sigma\ \xi\ T\ \lambda$, where 'σ' is the ionization constant, 'ξ' is the spectrometer angular acceptance, 'T' is the spectrometer transmittance and 'λ' is the inelastic mean free path [257]. The experimentally obtained values of atomic % together with the theoretically obtained values are compared in the Table 6.2 in which the theoretical results are consistent with the experimental data. We also determined the content of Co^{2+} and Co^{3+} present for both the cases $x = 0$ and 1 (Table-6.2). For $x = 1$, the ratio of Co^{3+} and Co^{2+} turns out to be 1 : 2 but the content of Co^{3+} present in Co_2TiO_4 is almost matches with that of Ti^{3+} (Co^{3+} : Ti^{3+} = 1:1.1).

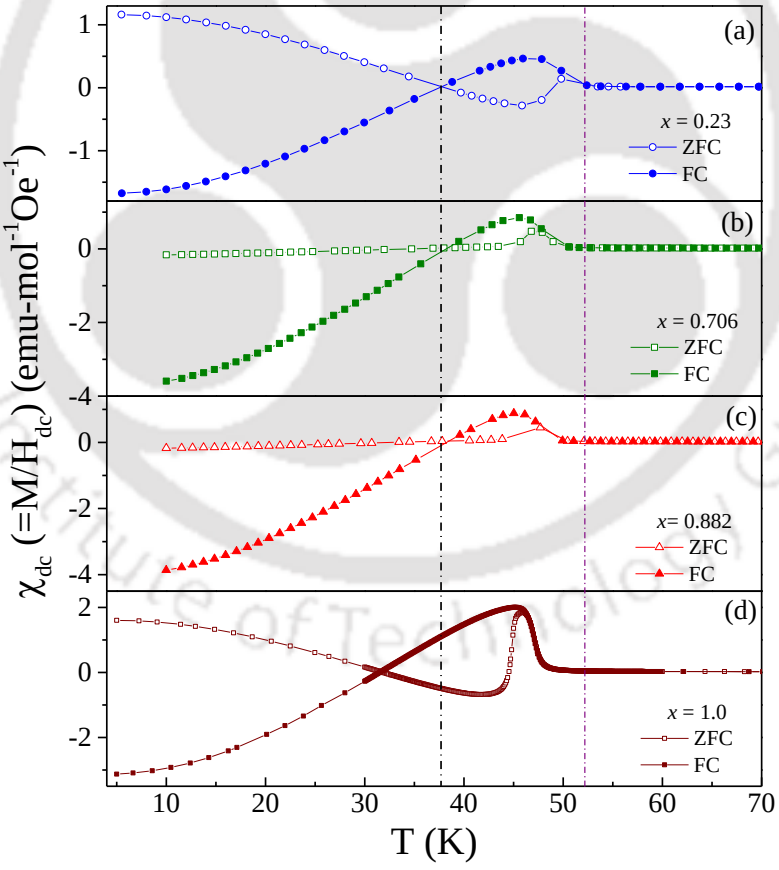

Figure 6.14: Temperature dependence of dc-magnetic susceptibility $\chi_{dc}(T) = M/H_{dc}(T)$ for (a) $x = 0.23$, (b) $x = 0.706$ (c) $x = 0.882$ (d) $x = 1.0$ measured under both zero-field-cooled (ZFC) and field-cooled (FC)conditions recorded at magnetic field $H_{dc} = 50$ Oe.

6.3.6 Tailoring the Compensation Point (T_{COMP}) and Néel Temperature (T_N):

Figure 6.14 depicts the temperature dependence dc-magnetic susceptibility χ_{dc} (=M/H_{dc}) for various compositions of (1-*x*) Co_3O_4 + *x* Co_2TiO_4 ($0.23 \leq x \leq 1$) recorded under both zero-field-cooled (ZFC) and field-cooled (FC, H @ 50 Oe) conditions. For all the compositions both the curves $\chi_{ZFC}(T)$ and $\chi_{FC}(T)$ exhibits a characteristic peak T_P (~ 49 K(ZFC) and ~ 46 K(FC) for $x = 0$) corresponding to the ferrimagnetic Néel temperature T_N; while a slight variation in the peak position was noticed with increasing the Co_2TiO_4 content. Below the characteristic peak, both the $\chi_{ZFC}(T)$ and $\chi_{FC}(T)$ curves exhibits magnetic-compensation (T_{COMP}) effect, where, $\chi(T)$ approaches to zero due to the complete balance of two sublattices magnetizations. Needless to say that he magnetic behavior of the two phase composites is dominated by negative magnetization character of Co_2TiO_4 (as discussed in chapter 4 section 4.3.3). Figure 6.15 shows the variation of the T_N (obtained from $\partial(\chi_{dc}T)/\partial T$ plots shown in figure 6.16) and T_{COMP} as a function of Co_2TiO_4 wt% (i.e., *x*). One can clearly see from the figure that T_N attains a maximum value ~ 53.3 K for $x = 0.882$ (88.2 wt%) whereas T_{COMP} decreases from ~ 38 K to ~ 32 K as the system transform to complete inverse spinel structure. These results are consistent with the magnetization data of Co_2TiO_4 reported by Hubsch *et al.* [77]. In order to probe the glassy behavior, in these composites we have further investigated the temperature variation of the dynamic magnetic susceptibility.

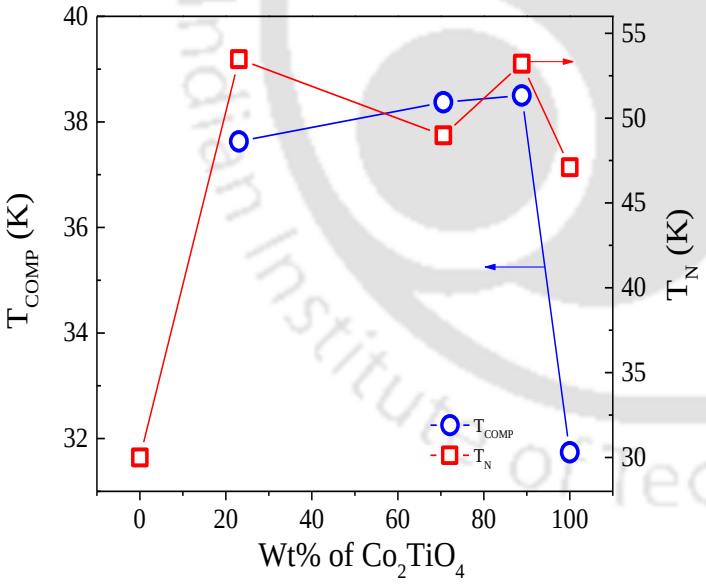

Figure 6.15: The compositional variation of compensation temperature (T_{COMP}) and ferrimagnetic Néel temperature (T_N).

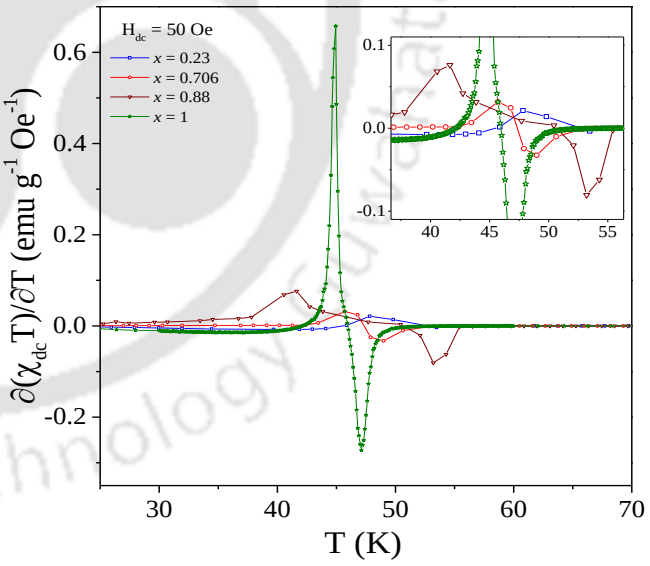

Figure 6.16: The plots of $\partial(\chi_{dc}T)/\partial T$ versus T of (1 - *x*) Co_3O_4 + *x* Co_2TiO_4 (*x* = 0.23, 0.706, 0.882 and 1.0) sample at external fields H_{dc} = 50 Oe. The inset shows the zoomed view of peak variation of various composites.

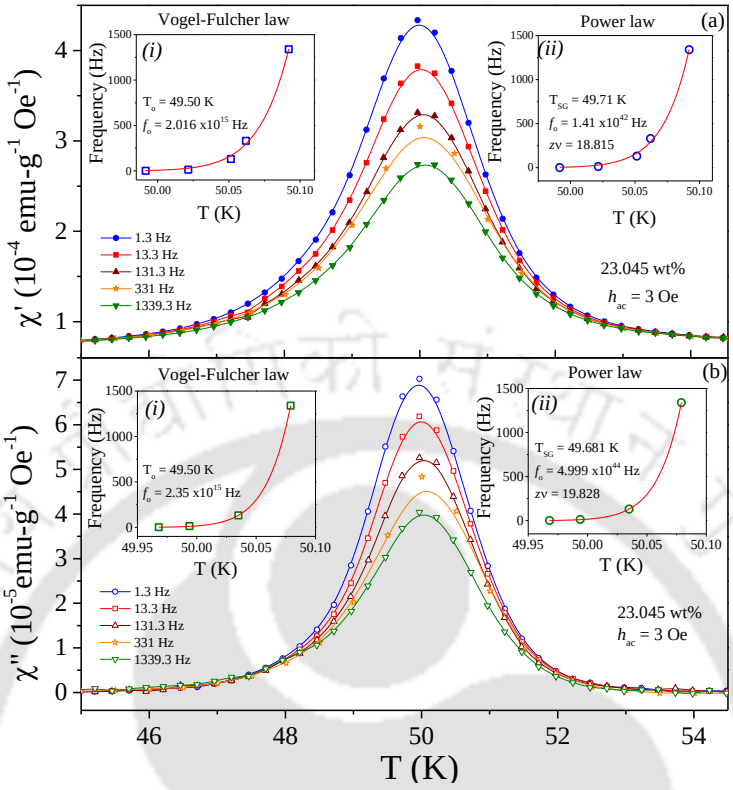

Figure 6.17: Temperature dependence of the ac-magnetic susceptibility of the composite system (1 - x) Co_3O_4 + x Co_2TiO_4 for x = 0.23 with (a) the real component $\chi'(T)$, and (b) the imaginary component $\chi''(T)$ recorded at various frequencies (1.3 Hz $\leq f \leq$ 1339.3 Hz) under warming condition using h_{ac}= 3 Oe and zero static magnetic field. The scattered symbols shown in the inset (*i*) of figure (a), and inset (*i*) of figure (b) represents the frequency dependence of peak position whereas the solid line shows the Vogel-Fulcher law fit of experimental data. The inset (*ii*) of figure (a) and inset (*ii*) of figure (b) shows the frequency dependence of peak positions in $\chi'(T)$ and $\chi''(T)$, respectively. The solid line shows the theoretical fit to the experimental data.

Figures 6.17 - 6.19 show the temperature dependence of in-phase (real component $\chi'(T)$) and out-of-phase (imaginary component $\chi''(T)$) of the ac-magnetic susceptibilities $\chi_{ac}(T)$ for three different compositions (x = 0.23, 0.706 and 0.882) measured at various frequencies (f) between the temperatures 45 K and 55 K. For all the frequencies, a broad cusp was noticed with very feeble shift of the peak position towards higher temperature side with increasing 'f' from 1.3 Hz to 1339.3 Hz. Nevertheless, the peak shift in $\chi'(T)$ and $\chi''(T)$ does not follow neither Vogel-Fulcher law nor Power law of critical slowing down for interacting particle system (insets of these figures). The parameters obtained from the fitting analysis are listed in table 6.3. The large values of 'f_0' indicates the absence of spin-glass phase transition below T_N [67]. It is interesting to note that the M-H loops (Figure 6.20) measured under field cooled (@20 kOe) mode for all the three compositions at 10 K exhibits large coercivity (H_C) and exchange-bias (H_{EB}). Figures 6.21(a) shows the magnitude of H_C and H_{EB} plotted as a function of 'x'. One can clearly observe from the figure that H_C^{Max} ~ 19 kOe at 10 K for x = 1, whereas, $H_{EB}(x)$ shows a maximum 887 Oe at x = 0.23 due to the dominant role of Co_2TiO_4 over Co_3O_4, and these results were consistent with the composition

Table-6.3: The fitting parameters obtained from Vogel-Fulcher law and Power law of (1-*x*) Co_3O_4 + *x* Co_2TiO_4 (*x* = 0, 0.706(70.6) and 0.882(88.2 wt%) sintered at 1200°C.

x		Vogel-Fulcher law		Power-Law		
		f_o (Hz)	T_o (K)	f_o (Hz)	T_{SG} (K)	zν
0.23	From χ′	2.01×10^{15}	49.5	1.41×10^{42}	49.71	18.81
	From χ″	2.35×10^{15}	49.5	4.99×10^{44}	49.68	19.82
0.706	From χ′	5.93×10^{26}	47.43	1.21×10^{45}	47.76	16.64
	From χ″	7.43×10^{46}	47.43	5.14×10^{59}	47.70	20.53
0.882	From χ′	1.44×10^{11}	47.42	1.16×10^{19}	47.62	6.009
	From χ″	5.19×10^{29}	47.03	2.30×10^{42}	47.49	16.68

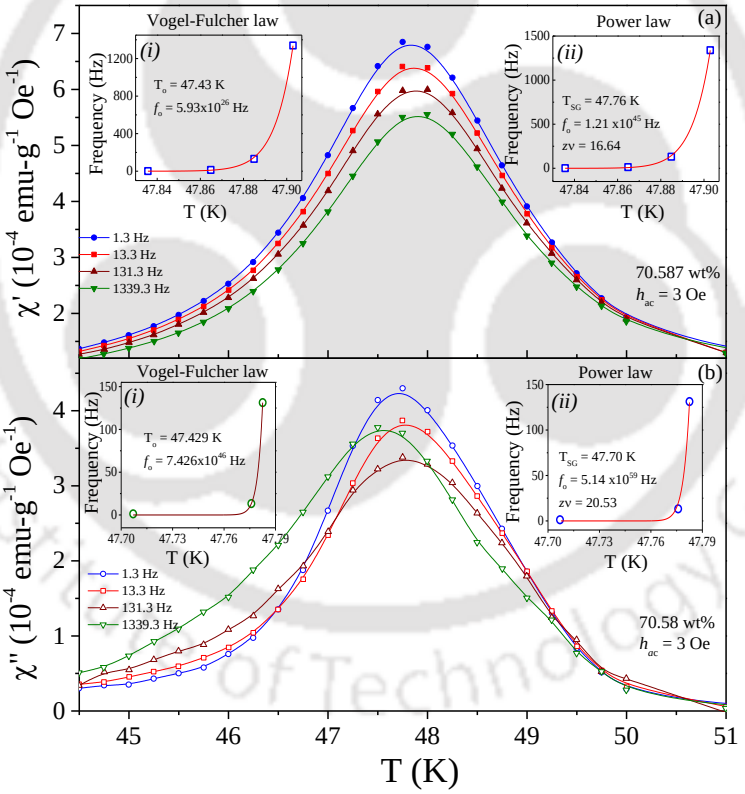

Figure 6.18: Temperature dependence of the ac-magnetic susceptibility of the composite system (1 - *x*) Co_3O_4 + *x* Co_2TiO_4 for *x* = 0.706 with (a) the real component χ′(T), and (b) the imaginary component χ″(T) recorded at various frequencies (1.3 Hz ≤ *f* ≤ 1339.3 Hz) under warming condition using h_{ac}= 3 Oe and zero static magnetic field. The scattered symbols shown in the inset (*i*) of figure (a), and inset (*i*) of figure (b) represents the frequency dependence of peak position whereas the solid line shows the Vogel-Fulcher law fit of experimental data. The inset (*ii*) of figure (a) and inset (*ii*) of figure (b) shows the frequency dependence of peak positions in χ′(T) and χ″(T), respectively. The solid line shows the theoretical fit to the experimental data.

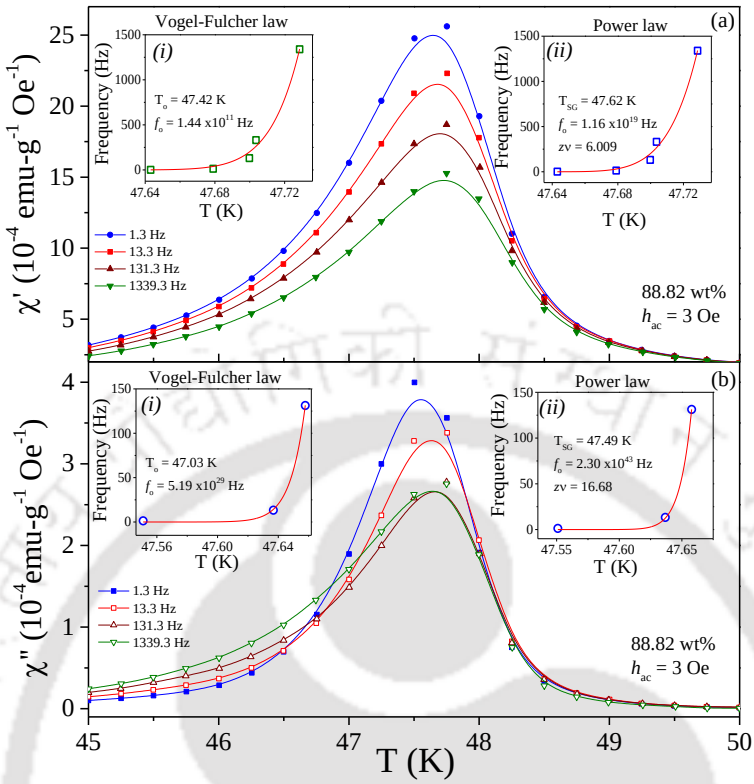

Figure 6.19: Temperature dependence of the ac-magnetic susceptibility of the composite system (1 - x) Co_3O_4 + x Co_2TiO_4 for x = 0.882 with (a) the real component $\chi'(T)$, and (b) the imaginary component $\chi''(T)$ recorded at various frequencies (1.3 Hz $\leq f \leq$ 1339.3 Hz) under warming condition using h_{ac}= 3 Oe and zero static magnetic field. The scattered symbols shown in the inset (*i*) of figure (a), and inset (*i*) of figure (b) represents the frequency dependence of peak position whereas the solid line shows the Vogel-Fulcher law fit of experimental data. The inset (*ii*) of figure (a) and inset (*ii*) of figure (b) shows the frequency dependence of peak positions in $\chi'(T)$ and $\chi''(T)$, respectively. The solid line shows the theoretical fit to the experimental data.

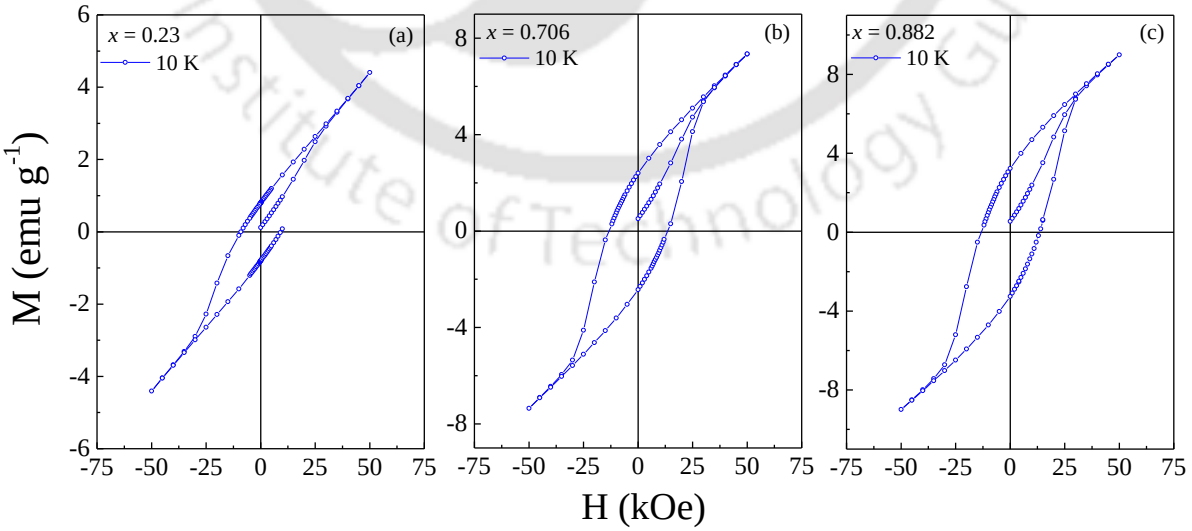

Figure 6.20: Magnetization versus field (M vs. H) hysteresis loops recorded under field-cooled (FC) conditions at constant temperature T = 10 K for (1 - x) Co_3O_4 + x Co_2TiO_4 (a) x = 0.23 (b) x = 0.706 (c) x = 0.882.

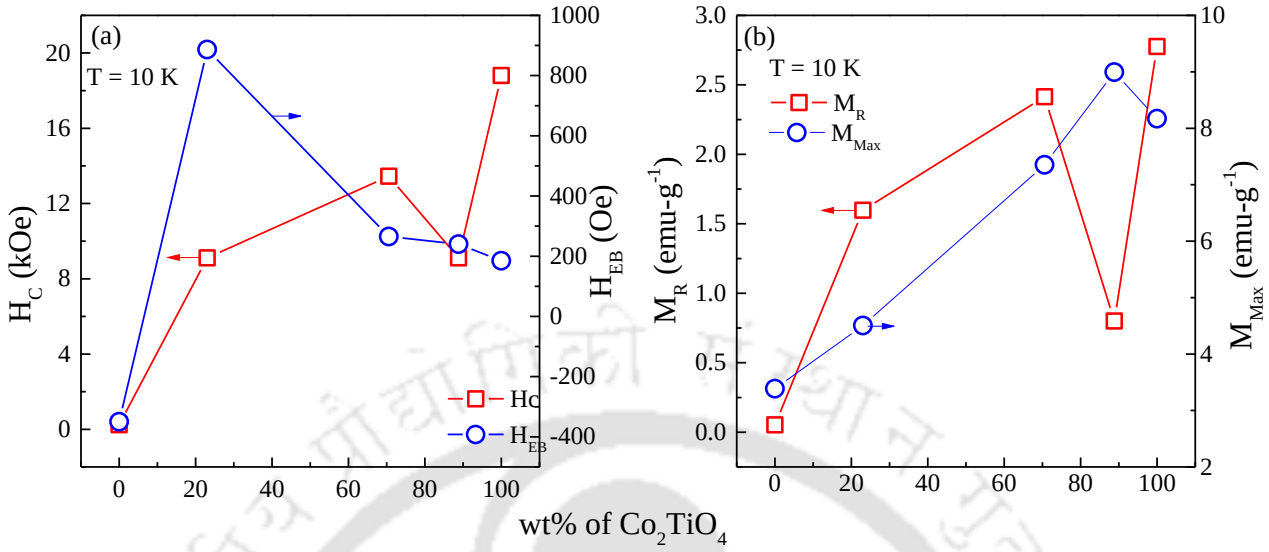

Figure 6.21: (a) The composition variation of the coercive field $H_C(x)$ [LHS]and exchange bias $H_{EB}(x)$ [RHS] estimated from the M-H curves measured at 10 K under 20 kOe field cooled (FC) condition (b) The composition variation of the remanence magnetization $M_R(x)$ [LHS] and maximum magnetic moment @ 50 kOe ($M_{MAX}(x)$ [RHS] obtained from the M-H curves measured at 10 K under 20 kOe field cooled (FC) condition.

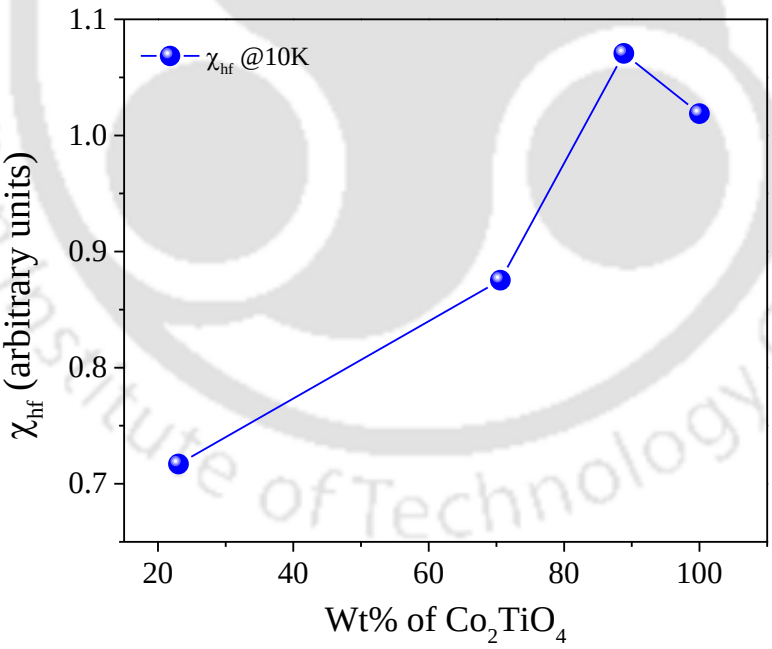

Figure 6.22: Composition variation of high field susceptibility $\chi_{hf}(x)$ calculated from the 50 kOe M-H loops measured at 10 K under field-cooled (FC) condition.

variation of remanence magnetization $M_R(x)$, maximum magnetization at 50 kOe $M_{MAX}(x)$, and high field ac-magnetic susceptibility $\chi_{hf}(x)$ (Figure 6.21(b) and 6.22).

6.3.7 Dielectric Permittivity and AC-Conductivity:

Figures 6.23 show the frequency variation of real component of dielectric permittivity ($\varepsilon'(f)$) for $x = 0.23$, 0.46 and 1.0 (insets show imaginary component ($\varepsilon''(f)$). These measurements are performed systematically below the room temperature (125 K ≤ T ≤ 290 K) and above room temperature (303 K ≤ T ≤ 573 K). From the figure we observed that the value of dielectric constant decreases as we increase frequency due to effect of interfacial and dipolar polarization at low frequency. The decrease of dielectric constant with increase of frequency is quite common in any insulating spinel system. Lazarevic *et al.* observed similar kind of frequency variation in $\varepsilon'(f)$ for the case of nickel ferrites in which a robust interaction is expected among the free charge carriers (either electrons or holes) with potential barrier at grain boundaries [258]. Such process may result to enhancement of conductivity across the grain boundaries which will be discussed later [258, 259]. Moreover, decrease in the value of ε' with increasing frequencies is more prominent at high temperature as compared to lower temperature. We observe anomalous change in $\varepsilon'(f)$ between the frequencies 10^4 and 10^5 Hz due the electronic and ionic polarization. From the figures we also noticed that, as the temperature rises, ε' slowly increases with increase in temperature for whole frequency range. The sharp rise in both ε' and ε'' at low frequencies can be attributed to LC-resonance like features arising from the electrode and sample [260, 261]. Figures 6.24 and 6.25 represents the Cole-Cole plots (Nyquist plot ε'' versus ε') of (1-*x*) Co_3O_4 + *x* Co_2TiO_4 ($0 \leq x \leq 1$) for high temperature and low-temperature regimes. For dilute compositions $x < 0.3$, Nyquist plot does not takes semi-circular shape, rather it present straight line with large slope suggesting the domination of grain boundary effect [262]. As *x* increases, depressed semi-circular behavior of the Cole-Cole plots was noticed (figures 6.24 (*iii*) and (*iv*)). Such depressed semi-circle behavior signifies the contribution of grain interior (bulk) as well as grain boundary contribution. For higher *x* values (> 0.8), perfect semi-circle arcs are observed (figures 6.24 (*v*) and (*vi*)). Such type of Cole-Cole plots suggest a single relaxation process dominates over the conduction mechanism, which can be identified as grain-effect. Small grain boundary effect was also noticed from these plots, as, they exhibited a straight line behavior after the termination of the semi-circle. Therefore, from the Cole-Cole analysis we conclude that, for lower '*x*' values, the conduction mechanism is dominated by the grain-boundary effect, whereas with increasing '*x*' the grain effect starts dominating and the plots are perfect semi-circular in shape.

In order to understand the ac-electrical transport in these two phase composites, we calculate the ac-electrical conductivity (σ_{ac}) using the following relation: $\sigma_{ac}(\omega) = \omega\varepsilon''\varepsilon_o$ [263]. In this equation ε_o is free space permittivity (8.854×10^{-12} F/m). Figures 6.26 and 6.27 shows the frequency variation of ac-conductivity $\sigma_{ac}(\omega)$ over a wide temperature range, 120 K ≤ T ≤ 293 K and 303 K ≤ T ≤ 573 K. As one can see from the figures that conductivity curve for a particular temperature is characterized by a frequency independent plateau region (lower frequency side) and a frequency dispersive region at higher frequency. The frequency independent plateau region (dc conductivity) at low frequency can be attributed to long range translation motion of charge carriers due to the

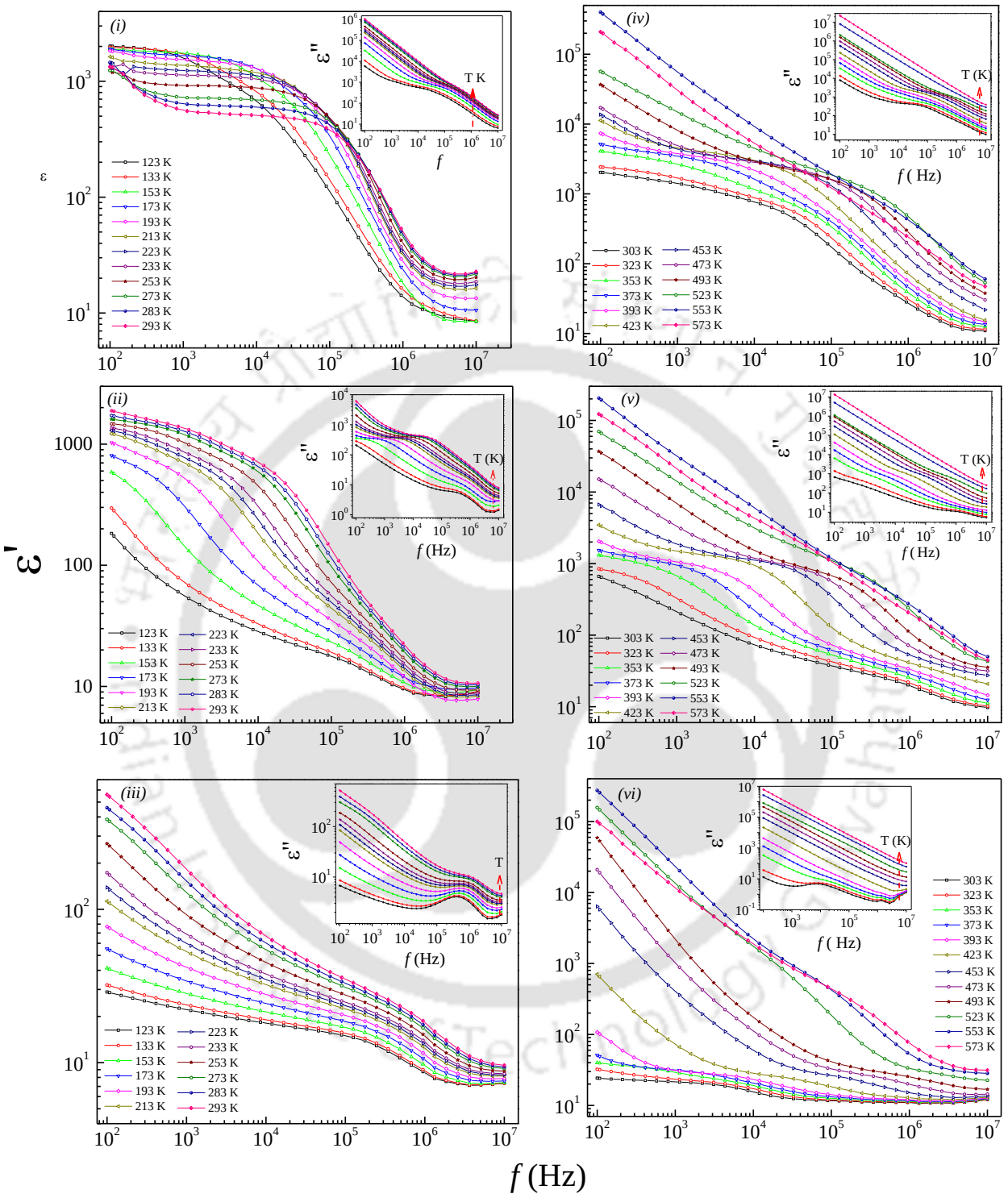

Figure 6.23: The frequency dependence of real component of complex permittivity (ε') for different compositions (*i*) x = 0 (*ii*) x = 0.23 (*iii*) x = 0.46 of two-phase composites ((1-x) Co_3O_4 + x Co_2TiO_4) measured between the temperatures 123 K and 293 K; and (*iv*) x = 0 (*v*) x = 0.23 (*vi*) x = 0.46 of two-phase composites ((1-x) Co_3O_4 + x Co_2TiO_4) measured between the temperatures 303 K and 573 K. Insets shows the corresponding frequency dependence of imaginary component of complex permittivity (ε″).

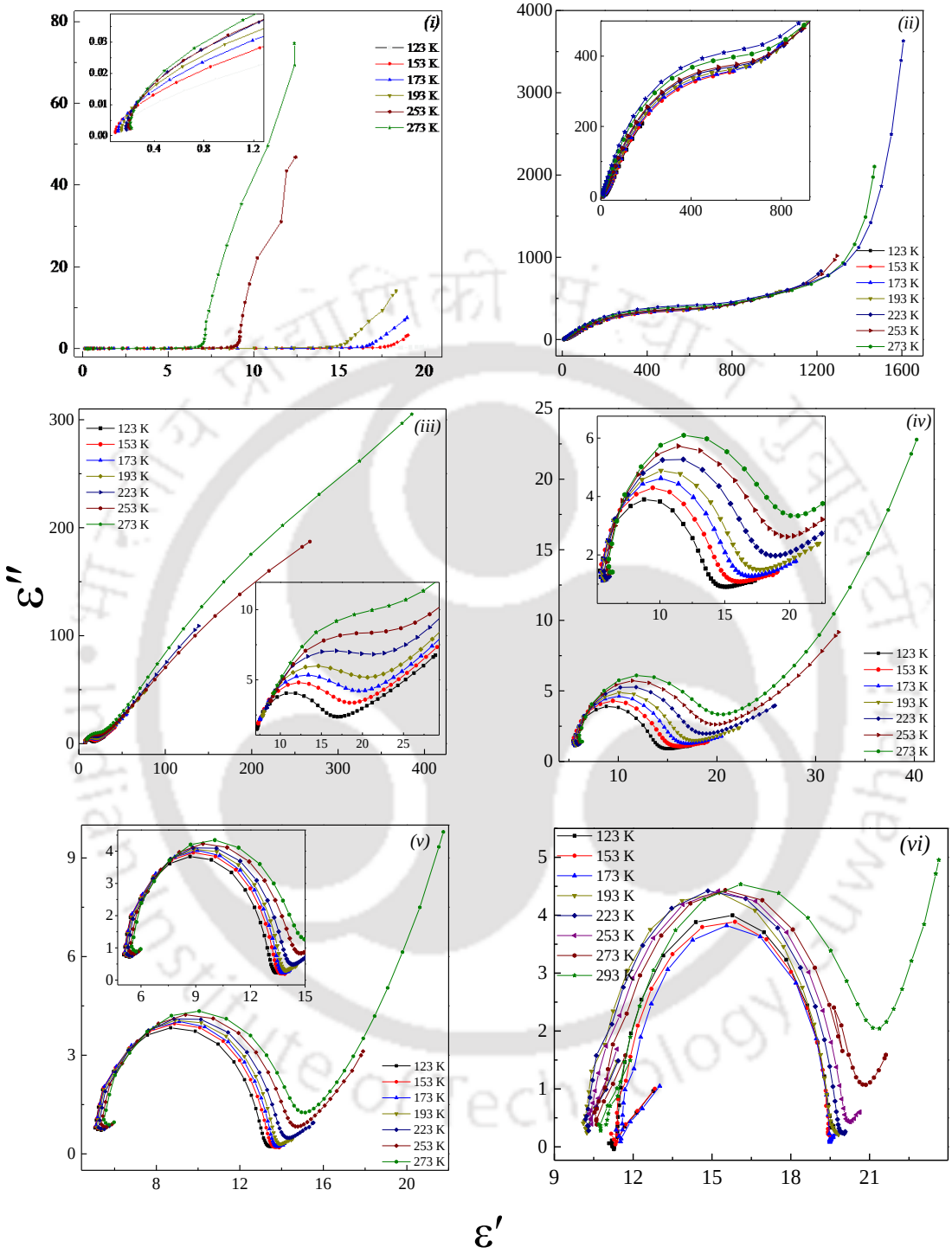

Figure 6.24: Cole-Cole plots (ε″ vs. ε′) recorded at different temperatures between 123 K and 273 K for different compositions (*i*) $x = 0$, (*ii*) $x = 0.23$, (*iii*) $x = 0.46$, (*iv*) $x = 0.706$, (*v*) $x = 0.882$, and (*vi*) $x = 1.0$. Insets show the zoomed view of the selected region.

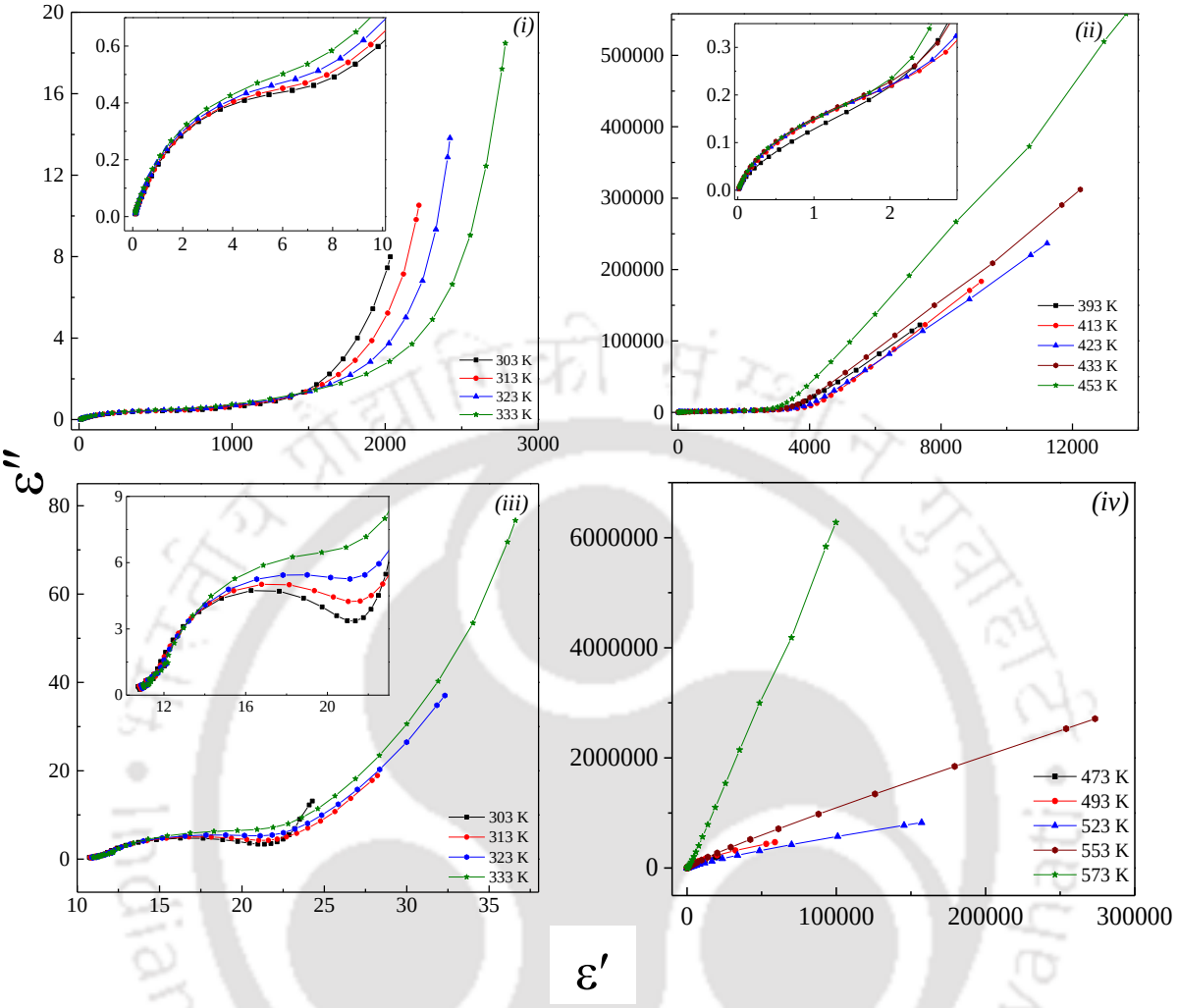

Figure 6.25: Cole-Cole plots (ε″ vs. ε′) recorded at different temperatures between 303 K and 573 K for different compositions (*i*) x = 0, (*ii*) x = 0.23, (*iii*) x = 0.46, (*iv*) x = 0.706, (*v*) x = 0.882, and (*vi*) x = 1.0). Insets show the zoomed view of the selected region.

successful hopping to neighborhood vacant sites. In 1993, Funke *et al*., successfully explained such kind of hopping mechanism using Jump-Relaxation model [264]. According to this model, there could be two process at high frequency region: *(i)* successful hopping and *(ii)* unsuccessful hopping. In the case of unsuccessful hopping, the jumping ion may come back to its initial position, whereas, for successful hopping the neighborhood ions become relaxed with respect to the jumping ions position and the jumping ion occupies a new site. With increase in frequency the ratio of the successful to unsuccessful hopping increases, as a result the dispersive conductivity increases at higher frequencies. Such frequency dependent conductivity can be explained mathematically by Jonscher's Power Law (JPL) [265]:

$$\sigma_{ac} = \sigma_{dc} + A\omega^{s} \quad (6.4)$$

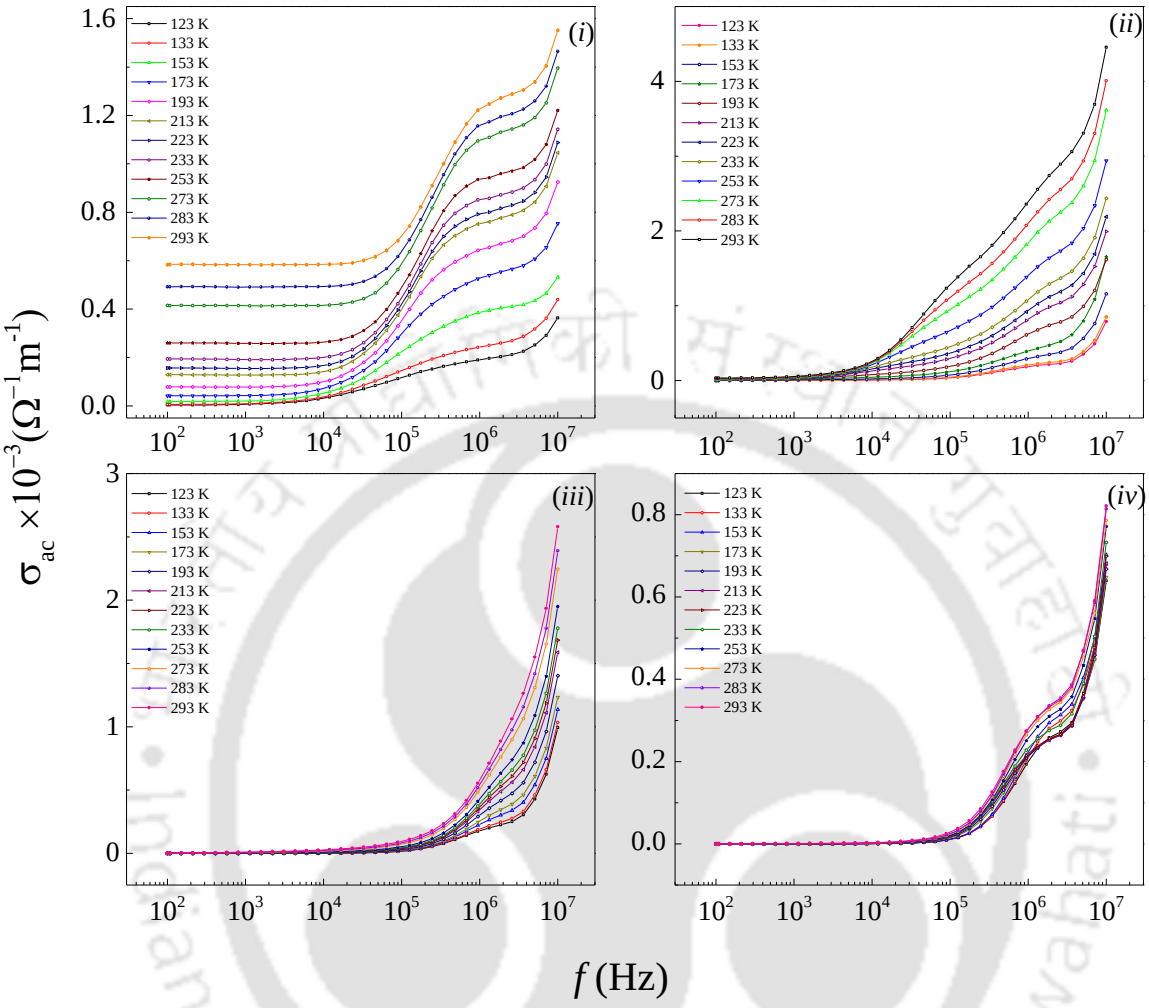

Figure 6.26: Frequency dependence of ac-electrical conductivity of (1-*x*) Co_3O_4 + *x* Co_2TiO_4 for different compositions (*i*) *x* = 0, (*ii*) *x* = 0.23, (*iii*) *x* = 0.46, and (*iv*) *x* = 0.706 measured at various temperatures between 123 K and 293 K.

where σ_{dc} is the frequency independent conductivity of the material, 'A' is the dispersion parameter and 's' is the dimensionless frequency exponent factor, which represents the measure of the degree of interaction. Using the above equation, we evaluated the magnitude of '*s*' (0.2 - 2.9) for different compositions of the two phase composites and plotted as a function of '*x*' (Figure 6.28). Within the JPL framework, the 's' values usually lie between 0 and 1 ($0 \leq s \leq 1$) for semiconductors, polymers, ceramics, ion conducting glasses and heavily doped ionic crystals [265]. Nonetheless, $s > 1$ is also reported for few ion-conducting glasses [266, 267], single crystals of K_2SO_4 [268], $K_3H(SeO_4)$ [269], perovskite compound such as $Pr_{0.6}Sr_{0.4}Mn_{0.6}Ti_{0.4}O_{3\pm\delta}$ [270], $Ca_{1-x}Sr_xTiO_3$ [271], $BaZr_{0.05}Ti_{0.95}O_3$ [272], and in multiferroic layer thin films of $PbZr_xTi_{1-x}O_3/CoFe_2O_4$ [272]. In the present case 's' values lie in both less than and greater than unity. The less than unity value of 's' can be attributed to the hopping conduction of mobile charge carriers through the energy barrier between two sites [273]. Whereas the 's' value

greater than 1 can be attributed to the motion of charge carriers or oxygen vacancies from site to site with quantum mechanical tunneling between asymmetric double-well potential [274].

The Arrhenius ac-conductivity plots of $\ln\sigma_{ac}$ versus 1000/T at different frequencies are shown in figure 6.29 and 6.30 for low temperature region (123 K ≤ T ≤ 293 K) and high temperature region (303 K ≤ T ≤ 573 K), respectively. A change in the slope of the curve clearly reflects from the figures. It is believed that slight change in the slope corresponds to a specific transition in the compound. But in the present case, there is no phase transitions in the temperature range shown in the figures. The change in the slope can be due to the contribution of different regions in the polycrystalline samples, such as grains, grain boundaries etc. [275] Therefore, the change in the slope is a reflection of different conduction mechanism. From this variation it is clear that the

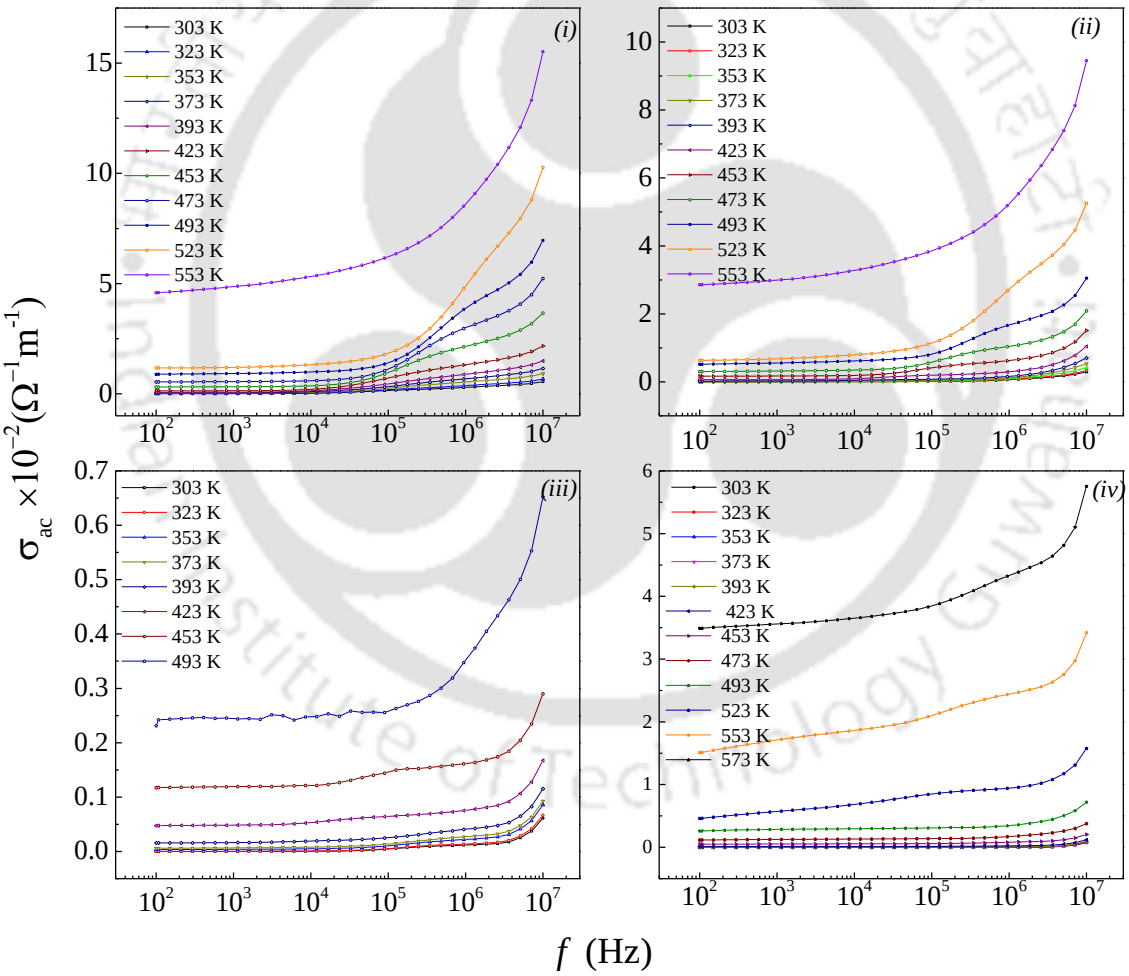

Figure 6.27: Frequency dependence of ac-conductivity of (1-*x*) Co_3O_4 + *x* Co_2TiO_4 (*i*) *x* = 0.23, (*ii*) *x* = 0.46 (*iii*) *x* = 0.706, and (*iv*) *x* = 1.0 measured at various temperatures between 303 K and 573 K.

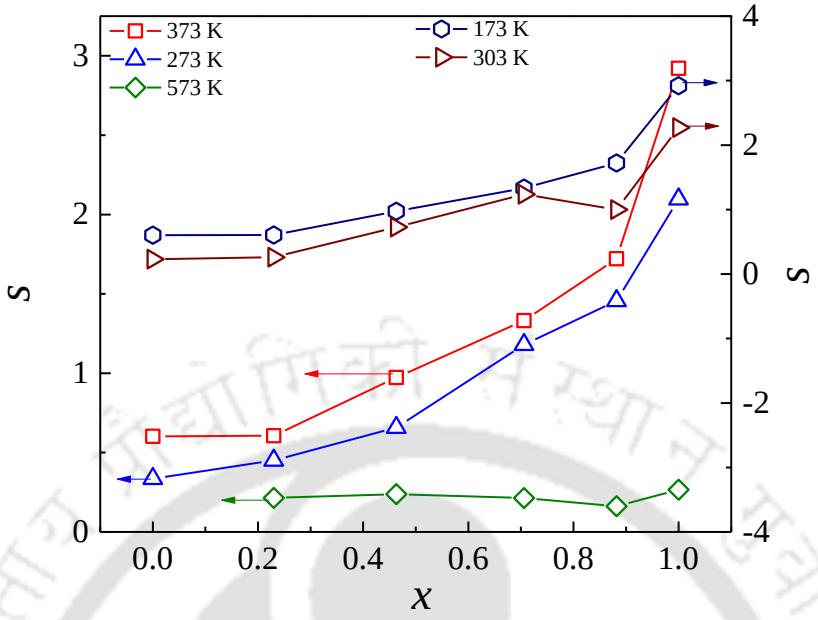

Figure 6.28: Frequency exponent (s) plotted as a function of composition (x) measured at selected temperatures.

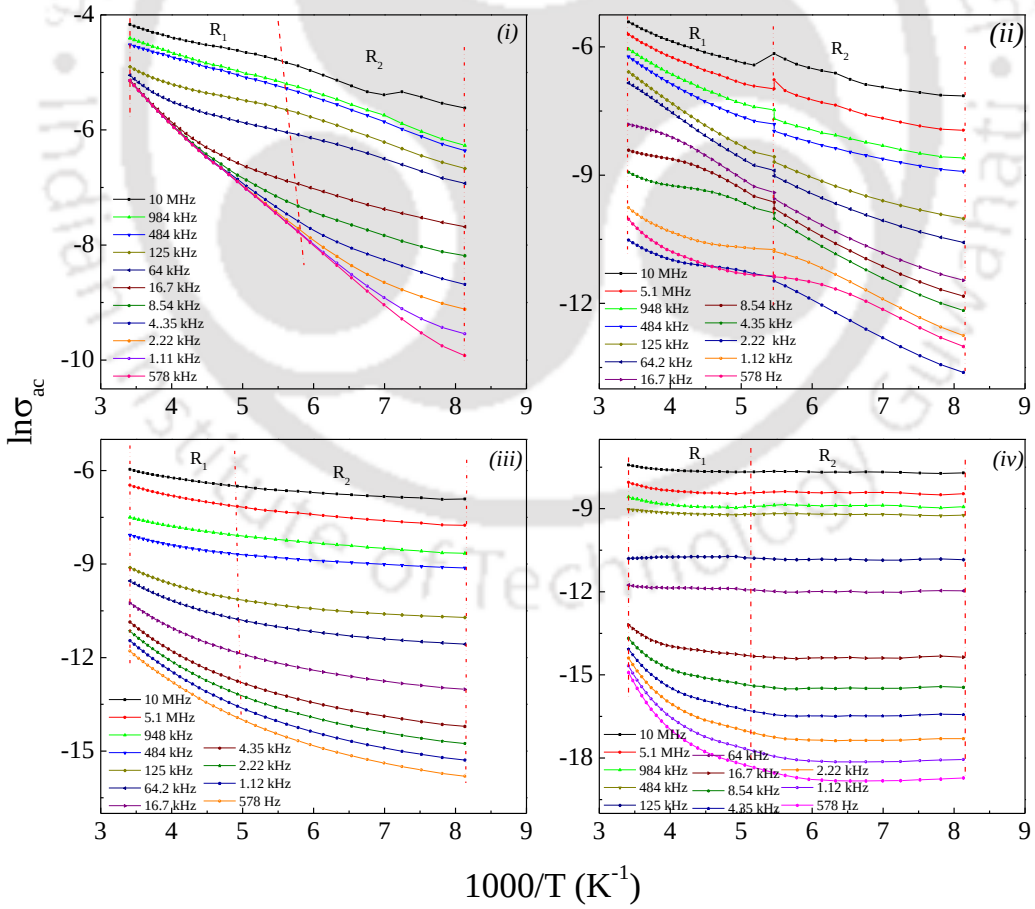

Figure 6.29: Logarithmic variation of σ_{ac} versus 1000/T for the compositions (*i*) x = 0.0, (*ii*) x = 0.23, (*iii*) x = 0.46, and (*iv*) x = 0.882 calculated at different frequencies.

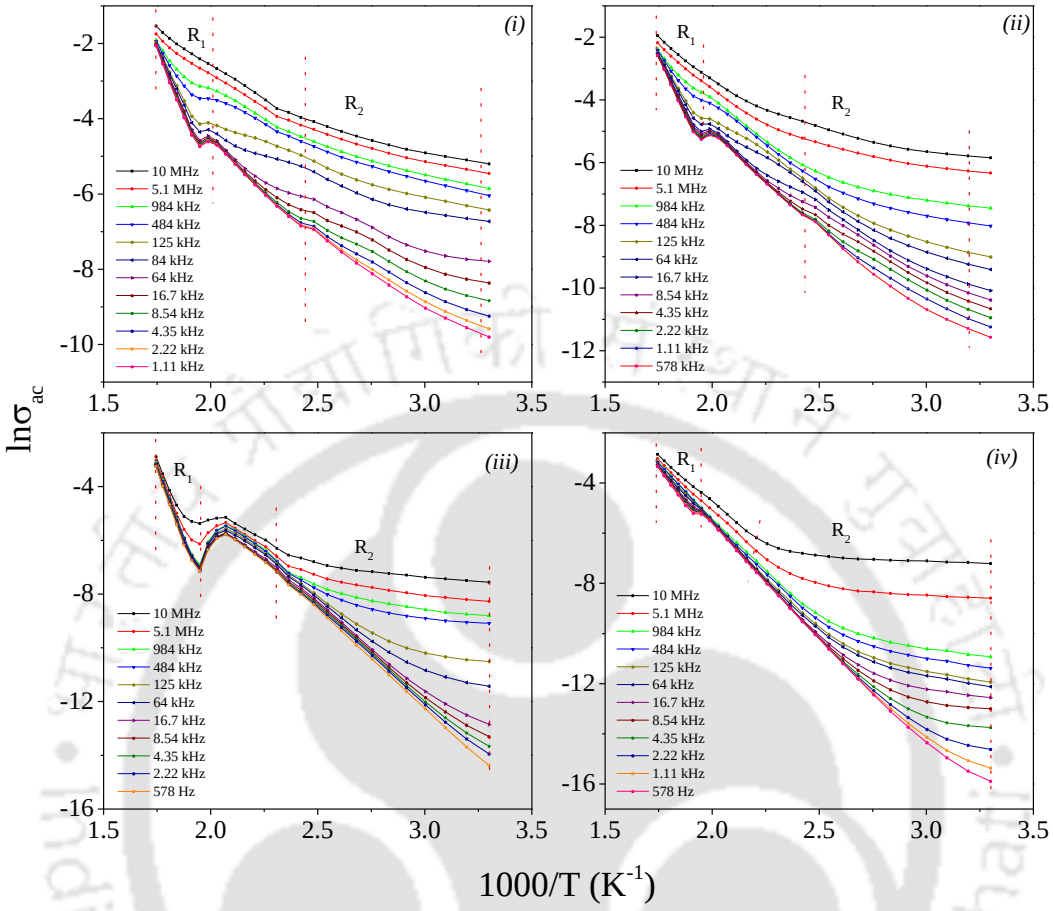

Figure 6.30: $\ln\sigma_{ac}$ versus 1000/T for (*i*) $x = 0.0$, (*ii*) $x = 0.23$, (*iii*) $x = 0.46$, and (*iv*) $x = 0.882$ composites; measured at different frequencies.

conductivity variation in the composites is a thermally activated process. The activation energy (E_a) of the thermally activated process can be calculated by the Arrhenius equation:

$$\sigma = \sigma_o \exp\left(-\frac{E_a}{k_B T}\right) \ldots (6.5)$$

Where σ_o is the pre-exponent factor, E_a is the activation energy, k_B is the Boltzman constant and 'T' is the measurement temperature.

Figure 6.31 shows the frequency variation of E_a [E_1; in region 1 (R_1) and E_2 in region 2 (R_2)] for (1-*x*) Co_3O_4 + *x* Co_2TiO_4 ($0 < x < 1$) two phase composites. From the figure we observed that the activation energy has a tendency to decrease with increase in frequency due to the enhancement of the electronic jumps between localized states as the frequency increases. We also study the variation of activation energy (E_a) as a function of '*x*' for two selected frequency 125 kHz and 16.7 kHz (figure 6.32). For all the samples we obtained lower values of activation

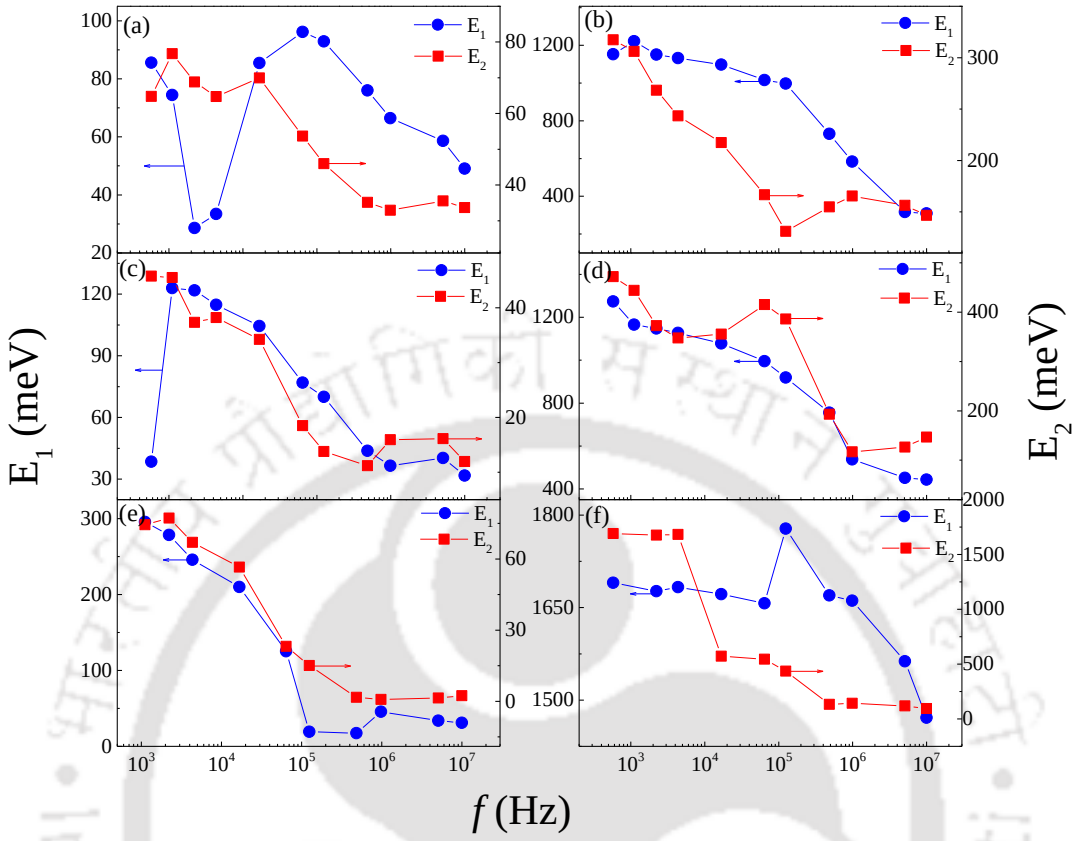

Figure 6.31: Frequency dependence activation energies (E_1 and E_2) of various compositions (*a*) x = 0.23, [for 123K ≤ T ≤ 293K] (*b*) x = 0.23 [for 303K ≤ T ≤ 573K], (*c*) x = 0.46 [for 123K ≤ T ≤ 293K], (*d*) x = 0.46 [for 303K ≤ T ≤ 573K], (*e*) x = 0.882 [for 123K ≤ T ≤ 293K], (*f*) x = 0.882 [for 303K ≤ T ≤ 573K].

energies. Such low value of activation energy can be attributed to the influence of electronic contribution to the overall conductivity [276].

6.3.8 Summary:

In summary, we studied the structural, vibrational, magnetization, dielectric behavior of (1-x) Co_3O_4 + x Co_2TiO_4 ($0 \leq x \leq 1$) two-phase composites. Major changes in the bond-angles and bond-lengths were noticed for various compositions of the solid-solutions (1-x) Co_3O_4 + x Co_2TiO_4. The bond angle A-O-B exhibits a maximum value of 130.35° for x = 0.706 as compared to 122.7° for dilute compositions. Conversely, the B-O-B bond angle shows its minimum value of 82.6° for x = 0.706. On the other hand, the bond lengths of A-O and B-O varies from 1.854 Å to 1.984 Å and 1.958 Å to 2.025 Å, respectively as the system transforms from normal spinel (x =0) to inverse spinel (x =1). Such changes are associated with the higher ionic sizes of 'Ti' ions (1.34 Å) as compared to the Co ions (1.09 Å).

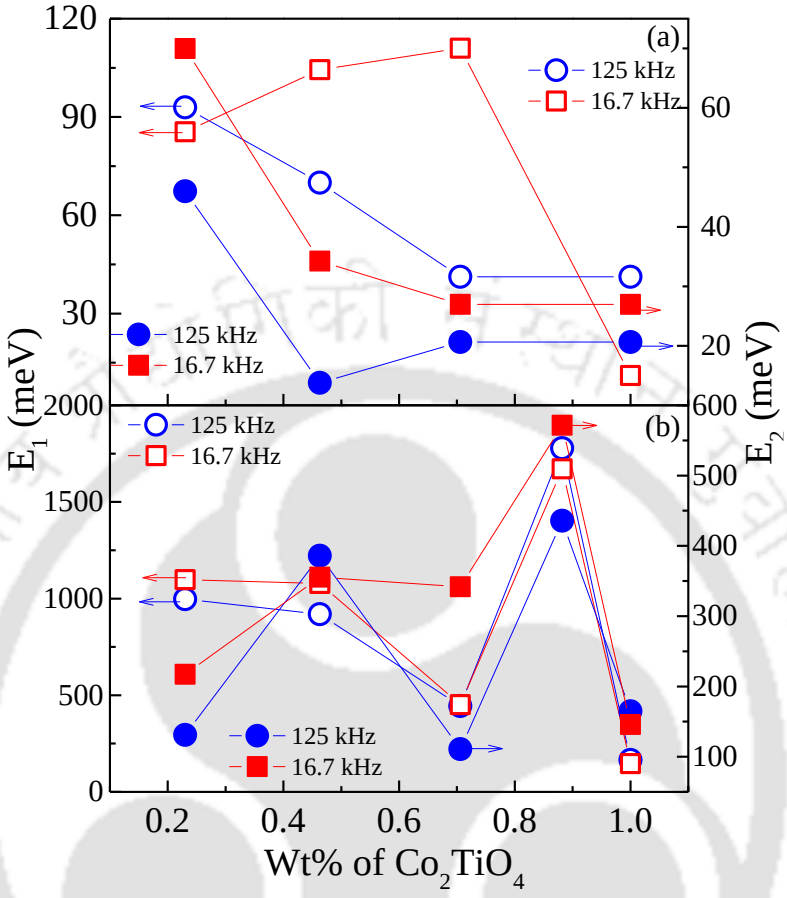

Figure 6.32: Activation energies (E_1 and E_2) plotted as a function of compositions measured at two different frequencies (16.7 kHz and 125 kHz).

Five Raman-active modes centered at 194.6 cm^{-1}, 480 cm^{-1}, 517.8 cm^{-1}, 617.7 cm^{-1}, 688.1 cm^{-1} were observed for all the compositions '*x*' which are associated to the $F_{2g}(3)$, $E_g(1)$, and $A_{1g}(1)$ vibrational modes. The substitution of Co_2TiO_4 grains within the Co_3O_4 matrix leads to hipsochromic-shift of 6.3 cm^{-1} of A_{1g} vibrational modes due to the smaller atomic mass and larger ionic radius (0.67 Å) of Ti^{3+} than Co^{3+} ions (0.545 Å). A giant bathochromic-redshift (~ 25.23 cm^{-1}) of F_{2g} mode was noticed when the system crossovers from normal-spinel (Co_3O_4) to inverted-spinel (Co_2TiO_4). The third Raman active mode F_{2g} located at 617.7 cm^{-1} vanishes totally in the Co_2TiO_4 system due to the complete occupation of octahedral sites by Ti^{3+} ions. The temperature variation of peak positions of A_{1g} and F_{2g} phonon modes show clear anomalies across 25 K to 55 K which are associated with the change in the paramagnetic to antiferromagnetic ordering. For lower 'Ti' compositions the characteristic binding energies of Co-$2p_{3/2}$, $2p_{1/2}$ reveals the trivalent and divalent oxidation states of Co at the octahedral and tetrahedral sites, respectively. However, for $x \geq 0.706$ typical signatures of trivalent character of 'Ti' ions at the octahedral sites of

inverse spinel structure was observed instead of tetravalent 'Ti' ions. Also, a weak 'Co^{3+}' character together with 'Co^{2+}' (major component) at the octahedral sites of Co_2TiO_4 was noticed.

Magnetic characterization reveals dominant ferrimagnetic interaction in all these composites below 50 K with different magnetic moments of 'Co' on the A sites (3.87 μ_B) and B sites (5.19 μ_B) for $x = 1$. For $T < T_N$, both the $\chi_{ZFC}(T)$ and $\chi_{FC}(T)$ curves exhibits magnetic-compensation (T_{COMP}) phenomena where $\chi(T)$ approaches to zero value due to the complete balance of two sublattices magnetizations. A gradual increase of T_{COMP} from 31.74 K to 37.72 K was noticed when 'x' changes from 1 to 0.23. Below T_N large magnitudes of H_C (~19 kOe for $x = 0.23$ at T = 10 K) and exchange bias H_{EB} (~ 887 Oe for $x = 1$ at T = 10 K) was observed. The frequency variation of ac-conductivity was found to increase with increase in frequency and follows a power-law relation ($\sigma_{ac} \sim A\omega^s$). These studies reveal the dominance of Arrhenius like conductivity with activation energy in the range 2 meV to 1800 meV. The Cole-Cole analysis revealed the dominance of grain-boundary and grain for dilute and heavily substitution of Co_2TiO_4, respectively.

Chapter 7

Lock-in Transition at 38 K in Tetragonally Distorted Frustrated Spinel Mn_3O_4

7.1 Literature Survey:

Strongly correlated systems are characterized by a competing magnetic interaction involving spin, charge, lattice, and orbital degrees of freedom, which often leads to a near degeneracy between competing phases [277]. Such degeneracy can also cause the coexistence of phases, giant magneto-dielectric and magneto-thermal properties in response to external perturbations such as magnetic field and temperature [89, 278 - 288]. Spinel oxides exhibit strong correlations between spin, charge, orbital, and lattice degrees of freedom due to a magnetically frustrating sublattice and anisotropy. Consequently, a wide variety of phenomena have been reported for spinels, including charge ordering [289, 290], heavy fermion behavior [291], and multiferroicity [292 - 296]. Magnetic frustration in spinel oxides with orbital degeneracy provides an exciting platform for some novel ordered as well as spin-disordered states often called as spin liquid-like states [297 - 299]. This chapter is dedicated to highly frustrated tetragonally distorted ferrimagnetic spinel Mn_3O_4 (hausmannite), which, exhibits novel phenomena in the magnetically ordered state; such as large magnetodielectric, magnetoelastic responses, field-induced structural changes in the low-frequency dielectric constant and giant atomic displacement [85, 89, 90]. All these changes in Mn_3O_4 have been attributed to the field-induced transitions between two distinct magnetostructural phases [85, 89, 90]. In Mn_3O_4, the di- and tri-valent Mn-ions (AB_2O_4; A = Mn^{2+}, B = Mn^{3+}) arrange in a tetragonally distorted array below 1433 K above which it shows perfect cubic spinel [21, 139, 300 - 308]. Its magnetic properties were investigated long ago but still the subject of active research because of new observations [85 – 91, 307, 309 - 313]. The most significant findings being: (a) magnetic field dependent tetragonal-to-monoclinic structural phase transformation below 33 K, [91] (b) new magnetic anomaly of lock-in transition at 38 K, [312] (c) Giant atomic displacement of 0.25 Å without breaking inversion symmetry and colossal magnetic anisotropy,[300](d)strong magneto-dielectric coupling,[89, 90] and (e) large magnetic entropy difference of ~11 J K^{-1} kg^{-1} for a field change of 20 kOe at 43 K [313]. Mn_3O_4 is a normal-spinel with Mn^{2+} and Mn^{3+} ions in $3d^5$ and $3d^4$ configuration, respectively, but exhibits very complex magnetic ordering (figure 7.1). Also, it undergoes several magnetic phase transitions below the ferri-magnetic Néel temperature T_N ~ 43 K [138, 140]. Another important characteristic is the prevalence of strong anti-ferromagnetic interaction between Mn^{3+} ions vis-a-vis Mn^{2+} - Mn^{3+}, which happens to be unfavorable to collinear structure leading to geometrical frustration [85, 140, 314]. However, some improvement in understanding the unique physical properties of Mn_3O_4 has been possible due to the novel characterization techniques like magnetic-field dependent Raman scattering, ^{55}Mn nuclear magnetic resonance (NMR), neutron diffraction, etc.[88, 93, 311, 314, 315].

The first-order phase transition, associated with tetragonal to monoclinic structural transformation, observed by Kim *et al*. at T_2 = 33 K using temperature and field dependent Raman scattering experiments motivated several

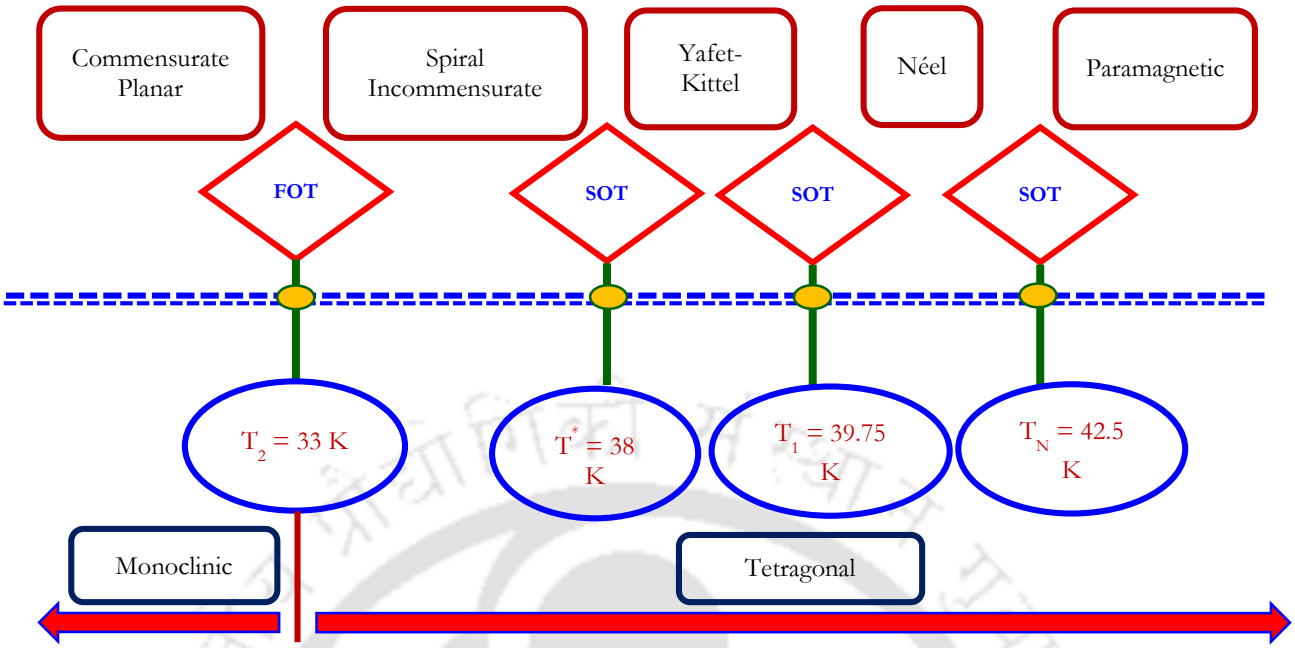

Figure 7.1: The schematic representation of magnetic and structural transitions observed in polycrystalline Mn_3O_4 below the Néel temperature T_N. The abbreviations FOT and SOT correspond to first- and second-order transitions, respectively [312, 313].

researchers to re-investigate the physical properties of Mn_3O_4 [86, 91]. Previous studies reported four magnetic transitions below T_N along with a well-defined magneto-dielectric coupling [89, 90, 93, 138, 140, 307, 312, 314, 315]. The magnetic ordering follows the sequence given in figure 7.1. On the other hand, magnetic field and temperature dependence of dielectric permittivity $\{\varepsilon_r(H,T)\}$ and strain $\{\Delta L/L(H,T)\}$ data of Mn_3O_4 single crystals revealed three distinctly different characteristics below T_N with large anisotropic magneto-capacitance [103]. Also, the evidence of magneto-dielectric coupling associated with the spin-phonon interaction has been reported in polycrystalline Mn_3O_4 [103].

Although numerous studies exist on Mn_3O_4, its dynamic behavior of magnetism at small ac-magnetic fields of varying frequencies were lacking in the literature when we initiated this problem. Therefore, the present chapter is devoted to the ac-magnetic response of all the phase transitions occurring below T_N under the superimposition of various dc-bias fields. In addition, the nature of these transitions has been studied under both cooling and heating cycles of magnetic-field dependent dielectric permittivity with special emphasis on the lock-in transition at 38 K [312, 313].

7.2 Experimental Details and Growth of Hausmannite:

Oxalate based sol-gel process has been chosen to synthesize Mn_3O_4 polycrystalline sample. Thermal decomposition of the oven-dried product ($MnC_2O_4.2H_2O$) (Alfa Aesar, purity 99.99%) at 500°C for 2 h duration

yields Mn_2O_3 as a major product; further annealing of this sample at 1100°C for 4 h in air leads to the formation of Mn_3O_4 powder. This powder is grounded in an agate mortar, pressed into bars and finally sintered at 1100°C for 12 h. During the sintering process abrupt quenching was done from 1473 K to 77 K using liquid nitrogen. Since the melting temperature of Mn_2O_3 is 1213 K one can expect the formation of Mn_3O_4 at any temperature T > 1213 K depending on the availability of oxygen content. Thus, abrupt quenching from 1473 K to 77 K will avoid the formation of Mn_2O_3 (i.e. preventing the memory retrace) and pure Mn_3O_4 will remains intact as primary product. The crystallinity of the sample and the structure has been studied using a Panalytical X'pert Pro diffractometer using Cu-K_α radiation, which indicate monophasic nature of this compound consistent with the hausmannite Mn_3O_4 reported in the literature [313]. A superconducting quantum interference device (SQUID) based magnetometer (Quantum design MPMS-XL5) has been used for the temperature dependent magnetization measurements $M_H(T)$ in low-field, while magnetic isotherms $M_T(H)$ up to 90 kOe were recorded by means of an extraction technique in a "physical property measurement system" (PPMS, Quantum design). The heat capacity curves $C_P(T)$ (for H = 0 and 20 kOe) were recorded from 2 K to 100 K by using a semi-adiabatic relaxation technique in the PPMS.

7.3 Experimental Results and Analysis:

7.3.1 Structural and Morphological Characterization:

The X-ray diffraction pattern recorded at room temperature using the Cu-K_α X-ray source of wavelength λ = 1.5406 Å along with the Rietveld refinement data (performed by FullProf program) of Mn_3O_4 sample (without quenching) is shown in figure 7.2 (a). The diffractogram contains mainly Mn_3O_4 phase. However, a detailed analysis of the X-ray diffraction pattern reveals a tiny peak near the Bragg angle $2\theta = 32.027^\circ$ corresponding to the 100% intensity peak of (222) reflection from Mn_2O_3 (inset of the figure 7.2(a)). This analysis indicates that the synthesized sample contains a tiny amount of unreacted Mn_2O_3 as secondary phase. From this result we can conclude, that Mn_3O_4 retraces its memory by forming Mn_2O_3 phase while cooled naturally. The weight % of secondary phase i.e. Mn_2O_3 present in the sample can be quantitatively estimated using the following formula [110].

$$W_{Mn_2O_3} = [1/\{1 + 1.265\,(I_{Mn_3O_4}/\,I_{Mn_2O_3})\}] \times 100 \quad \ldots (7.1)$$

where W_{Mn2O3} indicates the weight fraction of the Mn_2O_3 phase, and I_{Mn2O3} and I_{Mn3O4} represents the strongest X-ray diffraction line intensities of the Mn_2O_3 and Mn_3O_4, respectively. In the present case, intensities of (211) peak for Mn_3O_4 phase and (222) peak for Mn_2O_3 were considered as maximum intense Miller Indices of reflections. Using the above equation we found that ~ 2.35 wt% of Mn_2O_3 present in the sample as a secondary phase.

In order to avoid the formation of Mn_2O_3 phase we quenched the temperature of sintered sample from 1100°C to liquid-nitrogen temperature 77 K. The X-ray diffraction pattern of the sintered Mn_3O_4 pellet after quenching indicates monophasic nature of this compound (figure 7.2(b)). The lattice parameters obtained from the Rietveld

Table 7.1: List of various crystal structure parameters (*i*) lattice parameter, (*ii*) bond Length and (*iii*) bond angles of both quenched and without quenched Mn_3O_4 samples obtained from the refinement process.

System	Lattice Parameter		Interaxial angles	Bond Length		Bond Angle	
	$a = b$	c	$\alpha = \beta = \gamma$	A-O	B-O	A-O-B	B-O-B
Mn_3O_4 (without uenching)	5.76 ± 0.01 Å	9.47 ± 0.01 Å	90°	2.03 ± 0.01Å	1.92 ± 0.02Å	120.68°± 0.61°	94.16°± 0.48°
Mn_3O_4 (with quenching)	5.76 ± 0.01 Å	9.47 ± 0.01 Å	90°	2.03 ± 0.02Å	1.93 ± 0.02Å	119.79°± 0.62°	94.86°± 0.47°

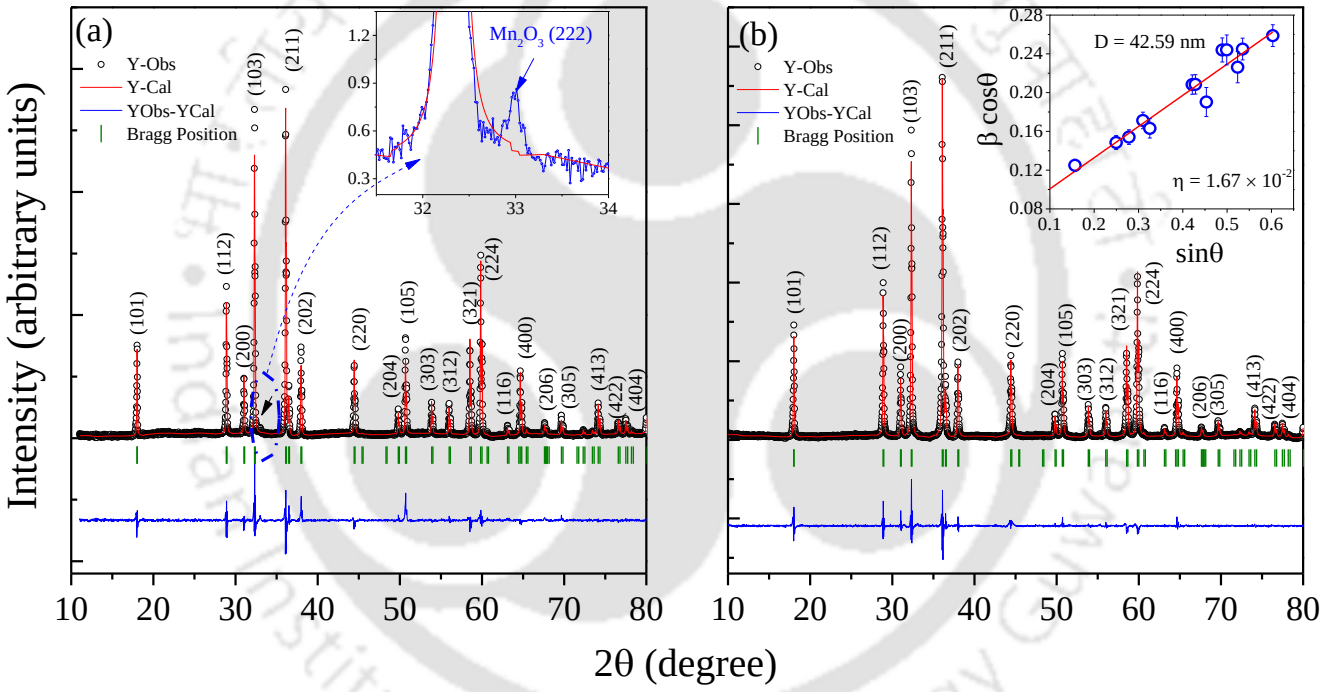

Figure 7.2: XRD pattern and the corresponding Rietveld refined data of Mn_3O_4 polycrystals prepared from the thermal decompositions of the oven dried precursors followed by (a) sintering at 1100°C without quenching and (b) after quenching from 1100°C to liquid nitrogen temperature (77 K). The inset of (a) shows zoomed view of the reflection pattern between 2θ = 31.5° and 34° depicting the reflection of (222) peak of Mn_2O_3 which is presented as minor phase and inset of (b) shows the Williamson hall plot.

refinement process using FullProf suit are a = b = 5.76 Å and c = 9.46 Å with space group $I4_1/amd$. Table-7.1 summarizes the parameters of both quenched and without quenched samples obtained from the refinement process. Using these lattice parameters we have estimated the unit-cell density ρ = 4.83 g/cm^3 for polycrystalline Mn_3O_4 sample, which is consistent with the standard reported value (4.86 g/cm^3) in the literature. Using

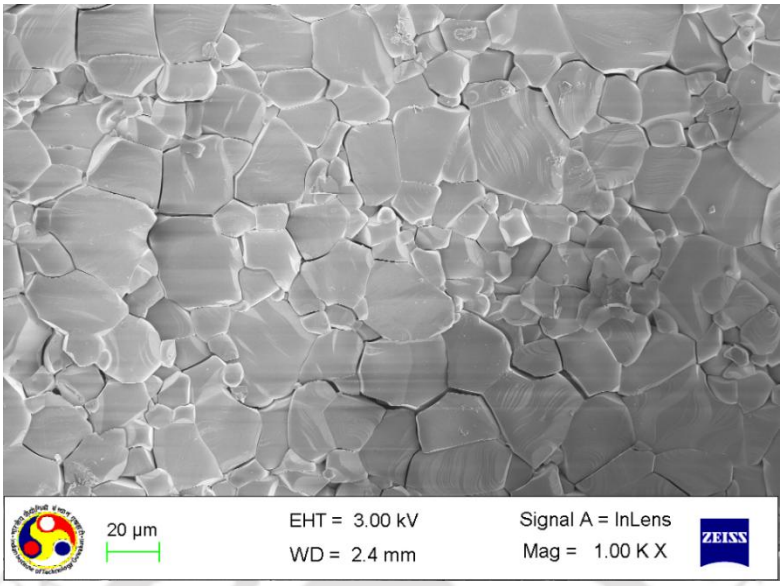

Figure 7.3: Field Emission Scanning Electron Microscope image of Mn_3O_4

Williamson-Hall analysis we have also estimated the average grain size (D) and micro-strain (η) present in the sample. The Williamson-Hall equation can be written as:

$$\beta\cos\theta = \frac{K\lambda}{D} + 4\eta\sin\theta \quad \ldots (7.2)$$

where, β is the full-width-at-half-maximum of diffraction peak and the constant 'K' is shape factor (= 0.89). From the β cosθ versus sinθ plot shown in the inset of figure 7.2(b) we have estimated the values of D and η are 42.59 nm and 1.67×10^{-2}, respectively. This analysis indicates that the contribution from lattice strain is significant (cannot be neglected) due to abrupt quenching of the sample from 1100°C to 77 K. Morphology of Mn_3O_4 sample sintered at 1100ºC has been studied using FESEM. Figure 7.3 represents the FESEM micrograph recorded under secondary electron mode depicting grain sizes in the range 8-20 µm.

7.3.2 Magnetic Properties and Evidence for the Lock-in transition:

Figure 7.4 depicted the temperature dependence of the magnetization M(T) of Mn_3O_4 sample measured under zero-field cooled (ZFC) and field-cooled (FC) conditions at an external magnetic field H_{dc} of 200 Oe for T < 60 K. The magnetization data was recorded at a very close temperature interval (ΔT) of 0.1 K from 20 to 60 K and ΔT = 1 K for T ≤ 20 K (marked by arrows in figure 7.4). Note that both M_{ZFC} and M_{FC} show a sharp transition across T_P ~ 39.5 K below the ferrimagnetic Néel temperature T_N ~ 43 K with strong irreversibility below T_N arising due to the local anisotropy effect.

Since the average grain sizes of the Mn_3O_4 samples after quenching to 77 K are in the range of 8 - 20 µm (figure 7.3), the irreversibilities cannot be due to blocking/spin-glass effects. It is well known that such irreversibilities indicated by the difference between the magnetization under ZFC and FC conditions arise from

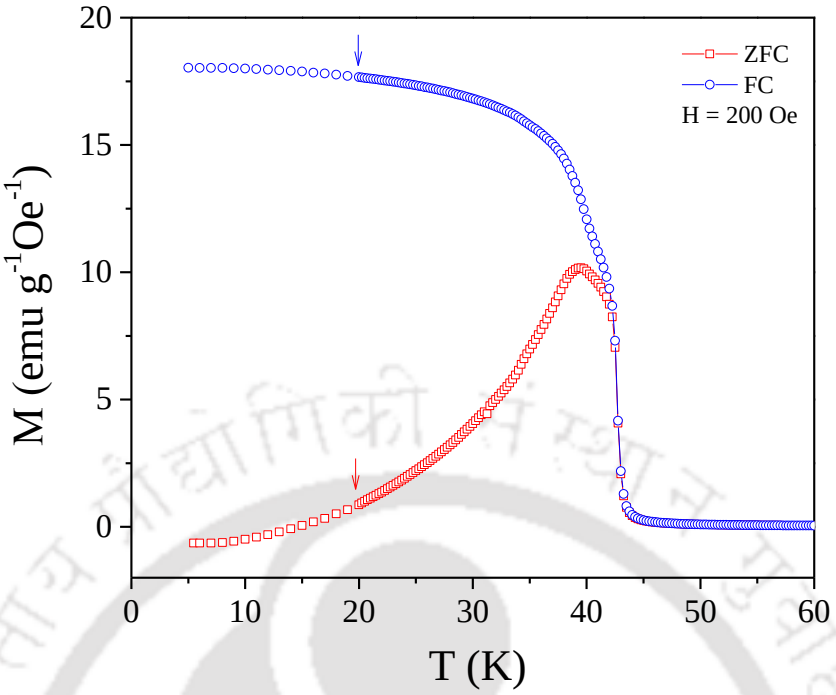

Figure 7.4: Temperature dependence of dc magnetization M(T) recorded under zero-field cooled ZFC and field cooled FC conditions at an external magnetic field 200 Oe.

the macroscopic magnetic anisotropy. Both M_{ZFC} and M_{FC} are related to each other through the coercivity which is a measure of the anisotropy. For non-interacting magnetic particles, the blocking temperature T_B is equivalent to $K_aV/k_B \ln(f_0/f_m)$ where 'K_a' is the average anisotropy constant of K_{Mn2+} and K_{Mn3+} , 'V' is the volume of the particles, k_B is the Boltzmann constant, f_0 is the attempt frequency typically equal to 10^{11} Hz for antiferromagnets and f_m is the measuring frequency. For f_m = 1 Hz, T_B approximately equal to $K_aV/25k_B$. Therefore, T_B is proportional to not only the anisotropy 'K_a', but, also to the volume of the particles which is equally important. Although there is some particle size dependence of 'K_a' due to contribution from surface anisotropy, it is in fact the volume 'V' of the particles that control the 'T_B' for a given system. If $T_B = T_P \simeq 39.5$ K observed in Mn_3O_4 where due to blocking effect then using the relation $T_B \simeq K_aV/25k_B$, one can determine the volume of the particles if an estimate of 'K_a' is known. From the coercivity $H_c \simeq 1.5$ kOe, $K_a = M_sH_c/2$, one can roughly estimate the magnitude of K_a (= 1.66×10^5 ergs/cm^3 for M_s = 45.6 emu/g at 90 kOe). Since 'M_s' is far from saturated state, this 'K_a' is likely underestimated. Using this magnitude and the value of $T_B \simeq 39.5$ K, we obtained the crystallite size D ≃ 3.4 nm for spherical particles. Since our measured crystallite size using transmission electron microscopic measurements were about 8-20 µm in range, therefore, T_P couldn't be attributed due to the blocking effects, as, the estimated particle size in such case should be of the order ~ 3.4 nm. The directional dependent magnetization studies reported on the single crystalline Mn_3O_4 reveals that *c*-axis is the magnetically hard axis and [110] direction is the easy axis direction, even though, a negligibly small difference in the magnitude of magnetization value of

M-H curves was observed along [100] and [110] crystallographic directions [103]. The giant magneto-crystalline anisotropy fields of approximately 65 kOe has been reported recently in the Mn_3O_4 system by means of nuclear magnetic resonance NMR measurements [86]. Contrary to the previous reports, Kim *et al*. reported that Yafet-Kittel structure under zero-field condition should entail one Mn^{2+} moment and two Mn^{3+} moments lie in the *ab*-plane [86]. However, in the presence of magnetic field along c-axis, a 25˚ tilt of Mn^{2+} ions from the *ab*-plane has been noticed. The extent of the direction of tilt is decided by the anisotropy constants (K_{Mn2+} and K_{Mn3+}) and the strength of exchange interaction (J_{Mn2+} and J_{Mn3+}).

Usually, the peak in the magnetic susceptibility in antiferro or ferrimagnetic system usually occurs at a few percent higher than the corresponding ordering temperature [117, 118, 134]. Hence the ordering temperature is considered at the peak of the $\partial(\chi_{dc}T)/\partial T$ versus T plot rather than χ_{dc}(=M/H) versus T plot. In fact, the singular behavior of a magnetically ordered system in the transition region should resemble closely to the function $\partial(\chi_{dc}T)/\partial T$ and magnetic specific-heat $C_p(T)$ variation of a typical antiferromagnet [117]. This inference is supported experimentally and its implication on the susceptibility curve near the transition has been studied thoroughly [118]. In order to deduce the exact transition temperature, $\partial(\chi_{dc}T)/\partial T$ versus T plots were drawn using magnetization data under both ZFC and FC protocols at low magnetic fields of 50 Oe, 100 Oe and 200 Oe (figure 7.5). While the minimum occurs at T_N = 42.8 ± 0.2 K, three peaks T_1, T^*, T_2 observed at 39.75 K, 38 K, and 34 K

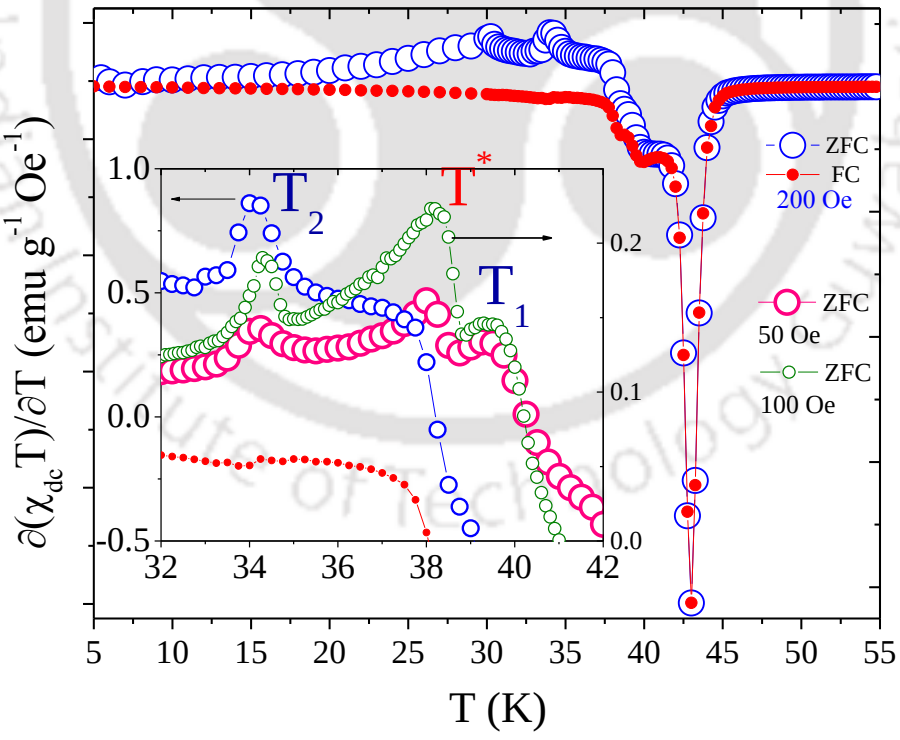

Figure 7.5: The temperature variation of the first derivative plots of dc-magnetic susceptibility $\partial(\chi_{dc}T)/\partial T$ for the magnetic fields H = 50 Oe, 100 Oe and 200 Oe. Inset shows the zoomed view of magnetically ordered regime which clearly depicts all the magnetic transitions.

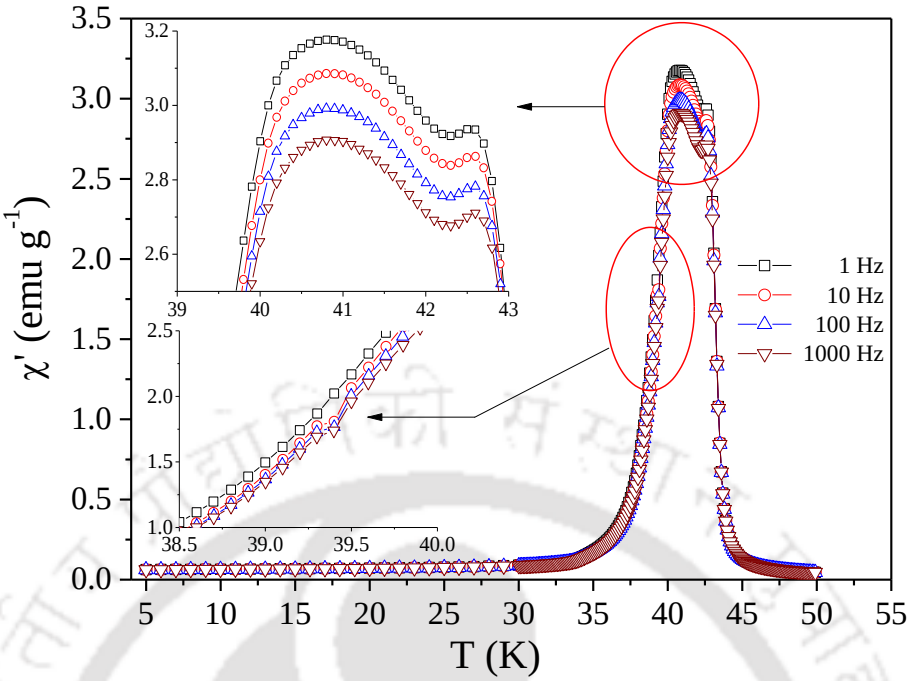

Figure 7.6: Temperature dependence of real component ac-magnetic susceptibility $\chi'(T)$ recorded at various frequencies under warming condition. The inset shows the zoomed view of the susceptibility cusps within the regime 39 K to 43 K and 38.5K to 40 K.

correspond to the triangular Yafet-Kittle to spiral incommensurate transition, lock-in transition, and spiral-incommensurate to cell-doubled commensurate state associated with the field dependent tetragonal to monoclinic structural transition, respectively [91]. The shift in T_N and T_2 towards higher temperatures results due to saturation of the magnetic moments of a typical ferrimagnet. However, no perceptible changes are noticed in the position of transitions at T_1 and T^*.

The frequency (f) of the ac-magnetic field has significant effect on all the four transitions. Such dynamic variation of the magnetization in Mn_3O_4 is studied for the first time. The in-phase $\chi'(T)$ and out-of-phase $\chi''(T)$ components were derived from the temperature variation of ac-susceptibility $\chi_{ac}(T)$ data recorded at various frequencies in the range 1-10^3 Hz. The peak to peak amplitude h_{ac} of the ac-magnetic field has been maintained constant at 2 Oe throughout the measurement. The $\chi'(T)$ curves exhibit two sharp peaks at 40.8 K and 42.6 K with a small kink at 39.4 K (figure 7.6). Figure 7.7 shows the temperature dependence of the imaginary part of the ac-susceptibility $\chi''(T)$ at different frequencies. At the onset of spiral in-commensurate phase, all these curves exhibits broad maximum. Particularly, the curve $\chi''(T)$ recorded at 1 Hz shows a sharp peak at 39.8 K, however, with increasing the frequency from 1 Hz to 10 Hz this sharp maximum quickly shifts to 41 K with significant decrease in the magnitude. No major changes were observed on further increasing the frequency from 10 Hz to 10^3 Hz. Such a sharp shift of the peak position of the imaginary-component of the ac-susceptibility with respect to the frequency increasing from 1 Hz to 10^3 Hz, across the onset of incommensurate phase (33 K < T < 39 K), may be

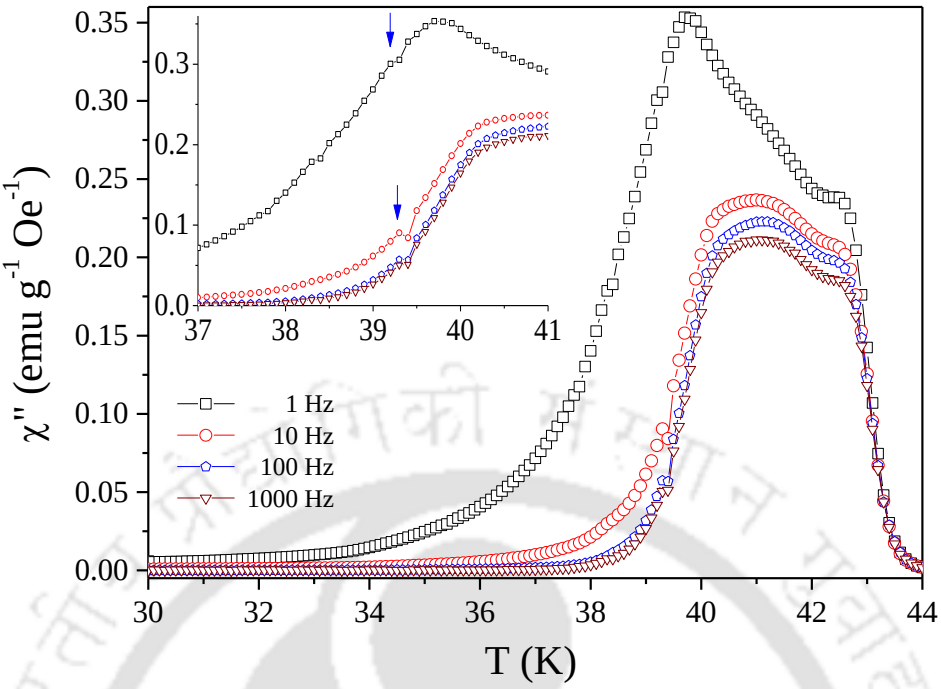

Figure 7.7: Temperature dependence of imaginary component ac-magnetic susceptibility $\chi''(T)$ recorded at various frequencies under warming condition. The inset shows the zoomed view of the susceptibility cusps within the regime 37 K to 41 K.

ascribed to the disturbance of the conical spin structure of the Mn^{3+} ions. Generally, the Mn^{2+} spins, which are in the *ab* plane, try to orient along the applied field direction. Even though the direction of orientation of the Mn^{2+} moments ([110]) is determined by the equilibrium condition among the torques due to the competing interactions of anisotropy energy, exchange interactions, and external field. On the contrary, the cone axis (resultant or sum vector of two Mn^{3+} spins) will try to precesses along the negative applied field direction either it is ac or dc- field i.e, in between the [0 0 1] or [0 0 − 1] but canted from [−1 – 1 0] direction. While the low frequency (f < 1 Hz) sinusoidal variation of the h_{ac} will still keep the Mn^{3+} conical spin undisturbed in its state intact. But once the ac-magnetic signal frequency increases from 1 Hz to 10 Hz or even higher frequencies Mn^{3+} spins cannot be able to follow the dynamic variation of h_{ac} and deviates from the precession along the negative cone axis, rather Mn^{3+} spins modulate sinusoidally but keep the coplanar structure undisturbed. This may be the reason why all the $\chi''(T)$ curves for frequencies greater than 1 Hz almost collapse into one trace and peaks almost at the same temperature. This effect is expected to be even more prominent in the case of single crystalline sample. There is another transition occurring at the ferrimagnetic ordering temperature (42.4 K) itself. A close examination of all the $\chi''(T)$ curves, the lock-in transition (T^*) at 38 K can be distinguished which shifts towards higher temperature side with increasing frequency (marked by arrows in the inset of figure 7.7). Also, the minimum value of $\chi''(T)$ and the peak in the $\chi'(T)$ occur nearly at the same temperature and correspond to T_N extracted above using $\partial(\chi_{dc}T)/\partial T$ versus T curves. No significant changes were observed in the peak positions (though the heights decrease) of the

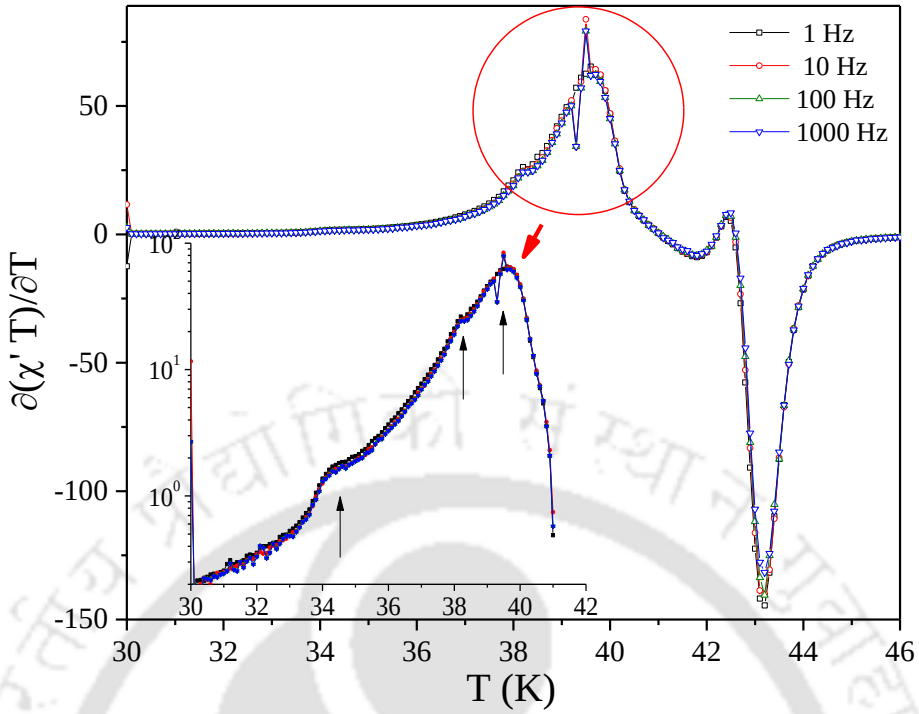

Figure 7.8: Derivative plots of χ′T (i.e. ∂(χ′T)/∂T) plotted as a function of temperature for various frequencies. Inset represent the zoomed view of the derivative plots where all the transitions are clearly able to trace (vertical arrows indicates the magnetic transitions).

transitions T_1 and T_N with increase in the ac-driving frequency. An opposite trend was noticed for T^*, whose existence can be clearly noticed only at slightly higher frequencies $f \geq 10$ Hz in the $\chi''(T)$ curves. Nevertheless, the existence of transition at T_2 is very weak in both $\chi''(T)$ and $\chi'(T)$ curves. This result is consistent with the temperature dependent field induced structural data reported by Kim *et al.* [86, 91]. Such crystallographic transitions are prominent only at the moderate applied field (typically ~ 10 kOe). Therefore, the applied ac-signal (magnitude and its frequency) is not sufficient here to probe the commensurate cell-doubling transition and observe intensity variation in the ac-susceptibility at T_2. The temperature variation of χ'' and $\partial(\chi' T)/\partial T$ resembles closely with each other and reported in various systems earlier with theoretical justification [117, 118]. In fact, identical peaks should be observed in χ'' and $\partial(\chi' T)/\partial T$ versus (T) curves near the magnetic-phase transition [117, 118]. In the present case, such an analysis yields all the complex magnetic phase transitions including the features not observed in the χ''(T) data in ferrimagnetic Mn_3O_4. Figure 7.8 shows $\partial(\chi' T)/\partial T$ versus T plots with a sharp minimum at T_N (43.2 K) coinciding with the temperature at which χ'' (T) drops to zero. The inset depicts positive values of $\partial(\chi' T)/\partial T$ on a logarithmic scale. From this graph one can clearly demonstrates the transitions at 34 K, 38 K and 39.7 K associated with the field induced structural transition (T_2), lock-in transition (T^*), and crossover from Néel type ferrimagnetic arrangement to triangular Yafet-kittle type spin ordering, respectively. While the transition at T_2 is first-order and associated with the tetragonal to monoclinic structural phase change, the other two are second-order in nature [91, 312, 313].

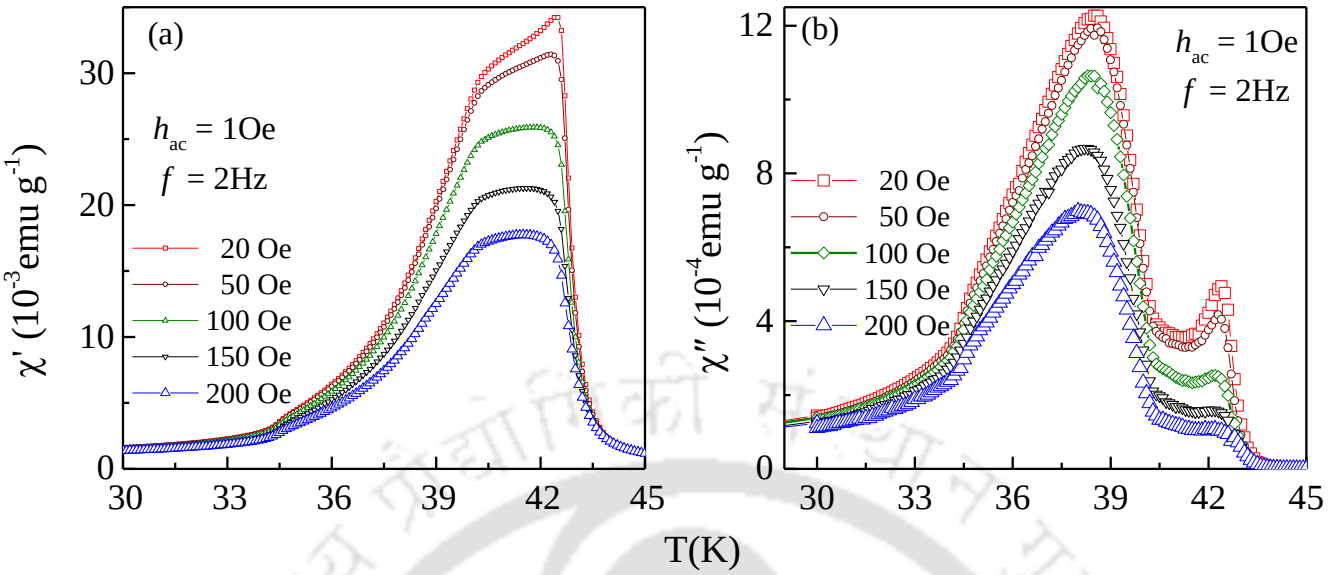

Figure 7.9: The temperature dependence of the (a) real component χ′(T) (b) imaginary component χ″(T) of the ac-magnetic susceptibility recorded under the superposition of different weak static bias magnetic fields for constant frequency 2 Hz and constant ac-field amplitude h_{ac} = 1Oe

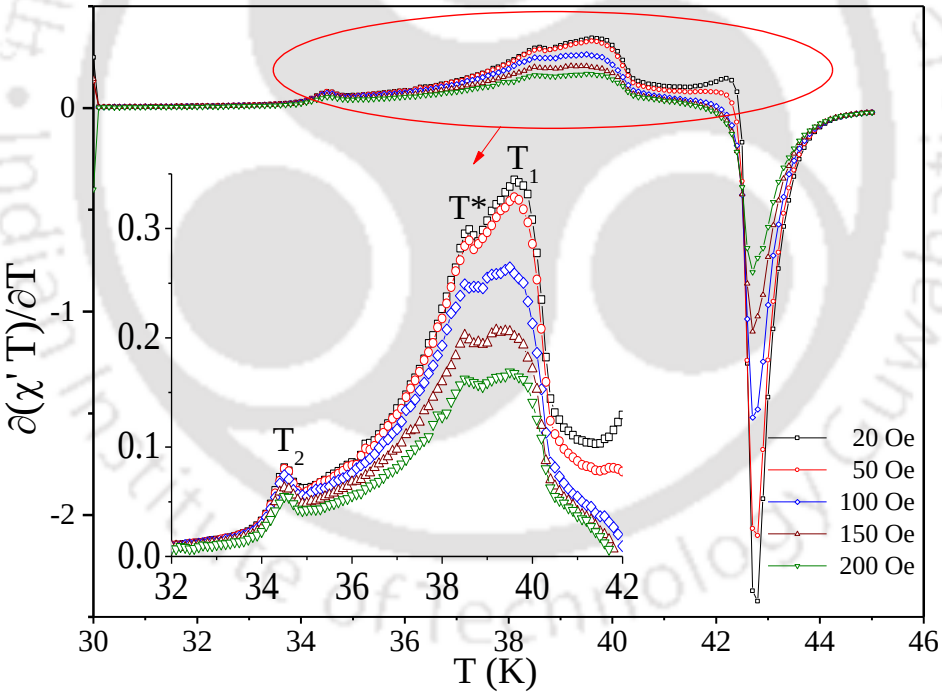

Figure 7.10: The temperature dependence of the ∂(χ′T)/∂T plots for various static magnetic fields (H_{dc}). The in inset shows zoomed view of the graph depicting the magnetic transitions at T_2, T_1 and T^*.

In order to probe the above discussed sequential transitions, we have carried out the dc-bias field dependent χ_{ac} (T) studies. Figure 7.9(a) and (b) shows the real-part χ′(T) and imaginary parts χ″(T) of the ac-magnetic susceptibilities for f = 2 Hz with amplitude h_{ac} = 2 Oe superimposed with various dc-bias fields (20 Oe ≤ H_{dc} ≤

200 Oe). This analysis is very useful to examine the effect of dc-magnetic field on all the sequence of transitions below the onset of long-range ordering. Two major peaks at 42.4 K and 40.4 K along with a small hump at 34 K are evident in the $\chi'(T)$. Also, the extent of splitting between 42.4 K and 40.4 K increases progressively with increasing applied dc-field (H_{dc}). While these two peaks are well resolved in case of out-of-phase component, but, sharp decrease in intensity with almost no shift in peak position was noticed in the transition occurring at 40 K. Also, the peak at 42.4 K associated with T_N shifts towards higher temperatures with increase in H_{dc}**.** Nonetheless, the analysis of $\partial(\chi'T)/\partial T$ versus T plots (figure 7.10) clearly demonstrates the existence of magnetic transitions corresponding to T_2, T^*, T_1, and T_N, but with a shift of + 0.6 K. Obviously, the temperature variation of $\partial(\chi'T)/\partial T$ provides more insight about the complex magnetic transitions than the direct measurements of $\chi'(T)$.

7.3.3 Dielectric and Magneto-dielectric Properties:

The dielectric anomalies associated with the spin-ordering transitions in Mn_3O_4 both in the form of single crystal and polycrystalline samples were observed earlier [89, 90]. However, a detail investigation of all the magnetic transitions (mentioned above at T_2, T^*, T_1 and T_N) at a very small temperature interval (0.1 K) is still remains open. To address this issue, magneto-dielectric effects in Mn_3O_4 are studied in detail. Figure 7.11 shows the temperature dependence of the relative of dielectric permittivity $\varepsilon_r(T)$ of polycrystalline Mn_3O_4 under different

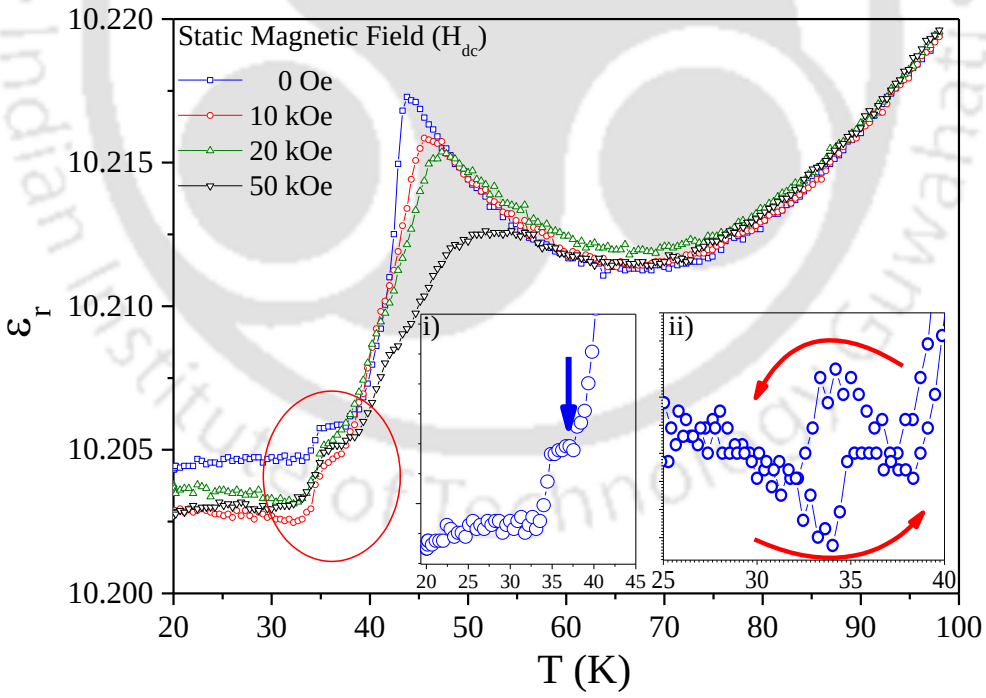

Figure 7.11: The temperature dependence of the relative dielectric permittivity $\varepsilon_r(T)$ measured under zero-magnetic field. The inset (*i*) shows the dielectric anomaly corresponding to the transition T^*. The inset (*ii*) shows the hysteresis lag in $\varepsilon_r(T)$ measured during cooling and heating cycles as represented by the red color arrow marks.

magnetic fields (0 - 5 T) at a constant ac-electric field having frequency 1 kHz. The data is recorded during warming after cooling the system down to 7 K. Under zero field condition, a sharp peak was observed in $\varepsilon_r(T)$ across the T_N as reported previously [89, 90]. Besides this, a step like transition occurs at 37.7 K, i.e., close to the second order lock-in transition at T^* as discussed in the above section. The inset of figure 7.11(*i*) clearly shows the dielectric anomaly around the lock-in transition at T^*. For further clarification, the zero field dielectric measurements were repeated under both cooling and heating cycles at different frequencies (1 kHz- 100 kHz) of the ac-electric filed. A significant shift of the step like behavior is noticed with a broad hysteresis of about ~ 5.15 K across T_2, confirming the first order nature of the transition (inset of figure 7.11(*ii*)). Such hysteresis shift is 8 time large as compared to the ~ 0.6 K lag observed in heat capacity measurements recorded under cooling and heating cycles [17]. The dielectric permittivity remains almost constant up to 35 K and drops suddenly at 34 K, i.e., near the onset of first order transition at T_2. This step like feature is more clearly able to trace in $\varepsilon_r(T)$ under zero-field condition. Beyond the saddle point (~ 65 - 70 K), the dielectric permittivity increases monotonically. All the anomalies together with the sharp peak around T_N shifts towards the high temperature as the magnetic field strength increases to very high values H → 14 kOe. Although the change in relative dielectric permittivity values is very small at all the temperatures but all the anomalies can be resolved clearly and these results are highly reproducible. The magnitude and trend of the $\varepsilon_r(T)$ obtained in the polycrystalline samples are nearly equal to the values obtained with the out-of-plane (E ∥ [100]) dielectric constant versus temperature of single crystalline Mn_3O_4 [90]. Since the global dielectric response is closely resembles with the data recorded with the ac-electric-field applied under out-of-plane configuration, on can expect that majority of the crystals aligned along [100] direction even though the current sample is in the polycrystalline from.

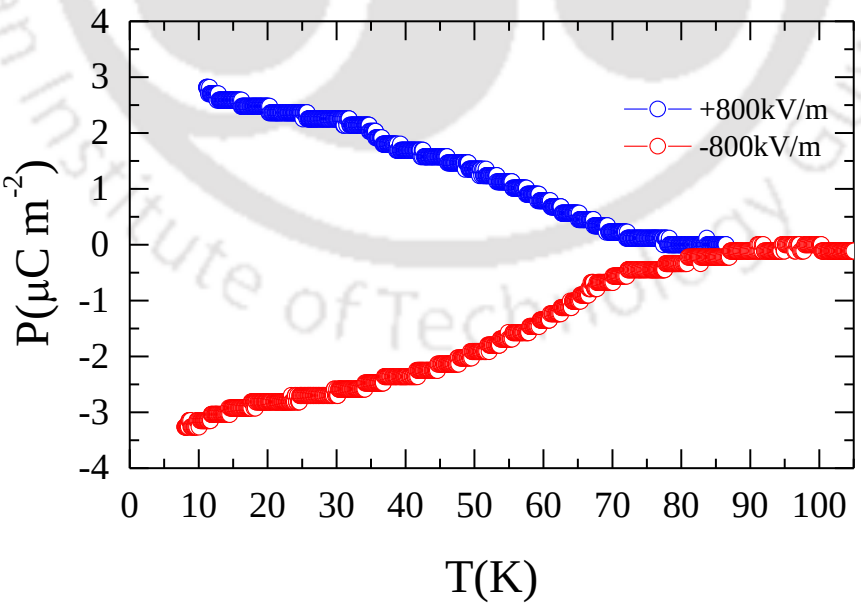

Figure 7.12: The positive and negative branches of the Polarization (P) versus temperature (T) curves measured in the temperature range 7 K - 100 K after poling with the static-electric field of strength ± 800 kV/m.

In order to see the presence of electric polarization in magnetically order state we have measured the remnant polarization '**P**' as a function of temperature. Figure 7.12 shows the **P** versus T measurements after poling the sample by means of a static poling-electric field as mentioned in the experimental section. This is the first report dealing with the temperature dependence of the polarization measurements in Mn_3O_4 polycrystals. The remnant polarization value decreases continuously with raising the temperature and becomes zero above 70 K. This shows a clear paraelectric to ferroelectric transition. Very small values of remnant polarization was noticed ($P_r \sim 3\times10^{-6}$ C/m^2 at 10 K) in Mn_3O_4 system even though a giant atomic displacement (0.25 Å) was observed below T_N [311]. Small values of remnant polarization could be due to the possible formation of opposite polarization clusters in a different direction than the adjacent domains, and in a polycrystalline sample the resultant polarization will be the average of polarization from different directions. Nonetheless, the observed resultant polarization is very small and the anomalies as observed in dielectric results are very difficult to trace in the electric polarization measurements. Figure 7.13 shows the five cycle hysteresis mode of $\Delta\varepsilon_r/\varepsilon_r(\%)$ versus H recorded at various temperatures below T_N. All the magnetic transitions occurring between the Yafet-Kittel and the incommensurate phase display significant variation in the magnetic field dependence (-14 kOe ≤ H ≤ 14 kOe) of the relative change of permittivity $\Delta\varepsilon_r/\varepsilon_r(\%)$. For low magnetic fields (H < ± 5 kOe), the magnitude of $\Delta\varepsilon_r/\varepsilon_r(\%)$ (~ 3×10^{-3}) are in close agreement with the relative shift of the permittivity measured in Mn_3O_4 single crystals

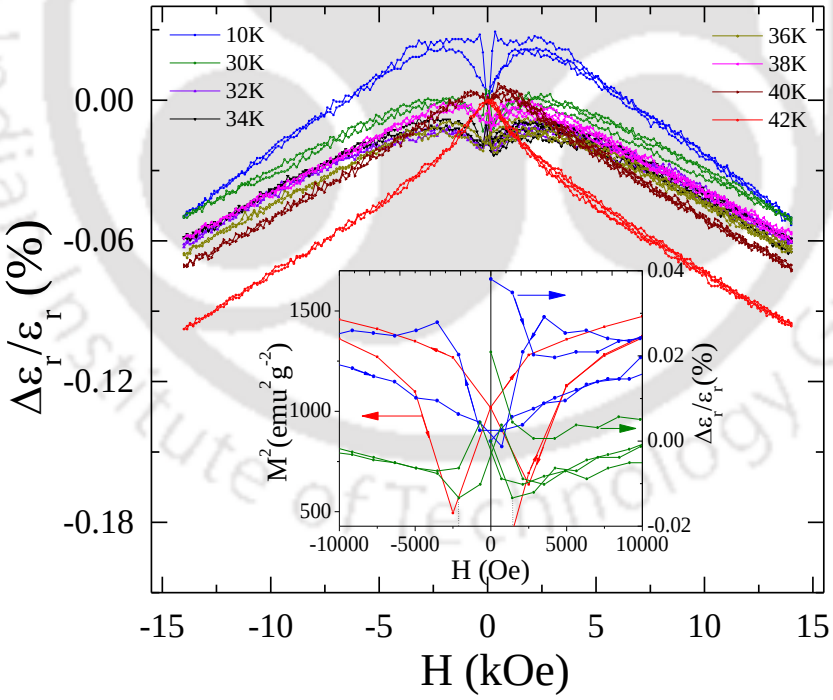

Figure 7.13: The relative dielectric permittivity $\Delta\varepsilon_r/\varepsilon_r$ (%) scanned as a function of static magnetic field H_{dc} under decreasing and increasing cycles (±15 kOe) of magnetic field at various temperatures. Here $\Delta\varepsilon_r/\varepsilon_r = ([\varepsilon_r (H=0)-\varepsilon_r(H)]/\varepsilon_r(H=0))$. The inset shows the square of the magnetization value M^2 in red colored data points plotted on the left hand side scale as a function of magnetic field and a zoomed view of the low field hysteresis response of $\Delta\varepsilon'/\varepsilon'_{H=0}$ (%) versus magnetic field H_{dc}.

under out-of-plane configuration, that is both H, E are parallel to crystallographic direction [001]. The hysteresis is significant at very low temperatures (< 10 K) where $\Delta\varepsilon_r/\varepsilon_r$(%) reaches a maximum value at H ~ 5.2 kOe and decreases thereafter. However, as the temperature approaches to the commensurate planar temperature regime, hysteresis decreases gradually and $\Delta\varepsilon_r/\varepsilon_r$ varies linearly with the ramping field. This effect becomes more significant in the paramagnetic regime for $T > T_N$ (inset of figure 7.13). Except for the case of T = 10 K, all $\Delta\varepsilon_r/\varepsilon_r$ versus H plots exhibit negative values but with a positive curvature up to a critical field of H_T ~ 5.2 kOe and changes to negative curvature thereafter (as shown by the dotted lines in the inset of figure 7.13). Inset of figure 7.13 shows the comparative behavior of the relative shift obtained in dielectric permittivity at T = 10 and 30 K and the square of the magnetization (M^2) at T = 30 K (plotted on the left-hand-side scale) for five hysteresis cycles protocol shown by the arrows. It is expected that the relative dielectric permittivity at moderate electric field frequencies (~ 1 kHz) is dominated by the optical phonons [90]. The force constant between the ions Mn^{2+}-O^{2-} significantly influenced by the external magnetic field direction which will cause variation of the phonon frequency and finally leading to the magnetic field dependence of capacitance [90]. Thus, the magneto-capacitance is driven by the effective change of the optical-phonon frequency controlled by the externally applied magnetic field direction.

For temperatures below T_N and magnetic fields below H_T, one-to-one correspondence is observed between the M^2 versus H and $\Delta\varepsilon_r/\varepsilon_r$ versus H in Mn_3O_4. The dotted line shows identical minimum in both curves in the final cycle, where, all the magnetic domains reach the same state at the coercive field. Such a relationship of low temperature hysteresis behavior between the dielectric permittivity and magnetization is prominent in magnetically ordered regime only. For all the temperatures the magnetodielectric curves $\Delta\varepsilon_r/\varepsilon_r$ (H) are symmetric about the H=0 axis contrary to the asymmetric magnetodielectric behavior observed in Ref [89]. Except this difference all the present observations are in-line with those of Tackett *et al.* and Suzuki *et al.* who explained the origin of magneto-dielectric effects using the spin-phonon coupling [89, 316].

7.3.4 Isothermal Magnetization:

In this section we explored the correlation between the isothermal magnetic field dependent magnetization and dielectric behavior. Figure 7.14 shows the ratio of magnetic field (H) to the value of magnetization (M) versus square of the magnetization (H/M versus M^2) curves (i.e., Arrott plots) extracted from the isothermal magnetization ($M\text{-}H_{1st\text{-}quadrant}$) curves recorded at various temperatures in the range 5-40 K (figure 7.15). In both figures 7.14 and 7.15 we have shown only few curves at characteristic temperatures in order to avoid the overcrowding. The temperature was brought to 300 K each time to ensure that the measurement should begin from a virgin magnetic state (without any magneto-thermal history) followed by a zero-field cooling.

Also, the temperature difference (ΔT) between the two successive isotherms was set low in the region of the transitions (i.e., 27 - 46 K) whereas ΔT was maintained high at other transitions (5 - 25 K and 48 - 65 K). The

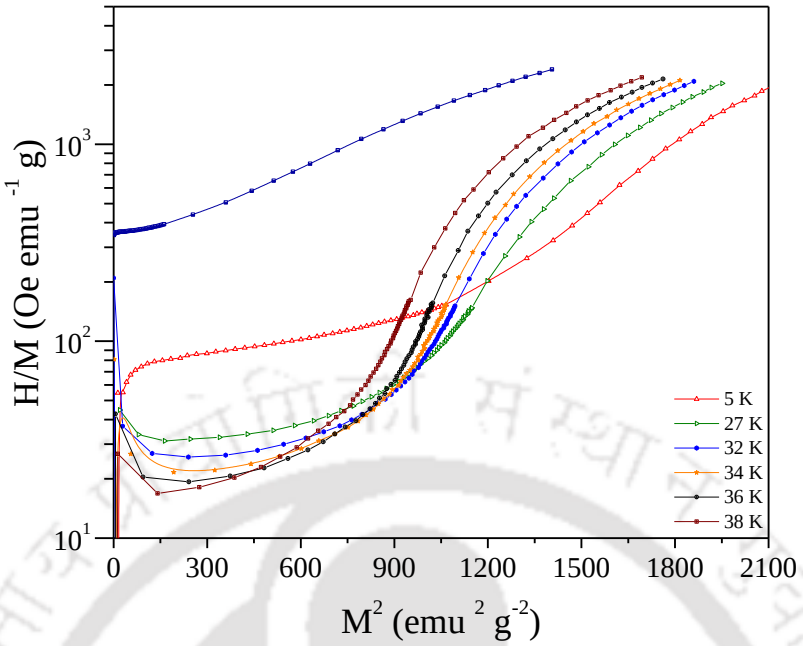

Figure 7.14: The ratio of magnetic field 'H' and its corresponding magnetization 'M' values (H/M) plotted as a function of the square of magnetization (M^2) for different temperature $T<T_N$ (Arrott plots). Note: Only selected M-H curves and H/M-M^2 plots are shown at characteristic temperature intervals.

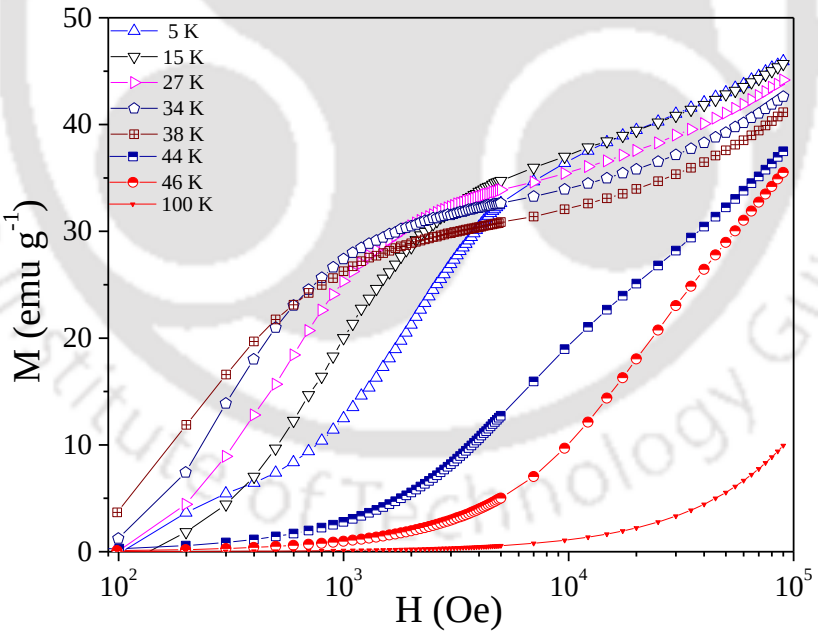

Figure 7.15: The magnetization versus field (M-H) isotherms recorded at various temperatures $T<T_N$. Note: Only selected M-H curves are shown at characteristic temperature intervals.

magnetization data was recorded by increasing the magnetic field from zero to 90 kOe. The deviation from positive slopes can be clearly noticed in the Arrott plots within the magnetically ordered regime. The isotherms recorded between 10 and 38 K show decreased negative slope in the H/M versus M^2 plots confirming the magnetic field

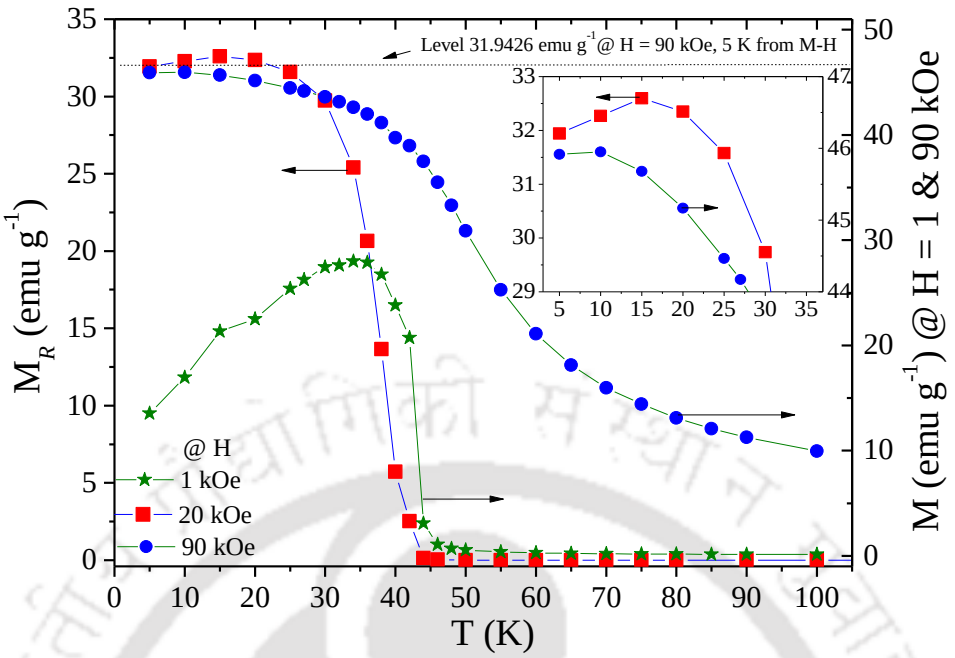

Figure 7.16: Temperature dependence of remanence magnetization M_r(T) shown on the left-hand-side scale and the right-hand-side scale depicts the magnetization values recorded at H=1 kOe and 90 kOe during the hysteresis loop measurements at various temperatures. The inset shows zoomed view of the low-temperature regime of M_r(T) depicting the down turn of the M_r values below 15 K.

induced first-order discontinuous transition across T_2 in the polycrystalline Mn_3O_4 [168, 169, 317, 318]. This observation is further confirmed by the existence of weak meta-magnetic-like character of the isotherms represented in the logarithmic scale as shown in figure 7.14 [317, 318]. Since the Arrott plots in other temperature regimes exhibit no negative slope, indicating that the transitions are of second-order continuous nature [168, 169]. This type of transition occurring at T_N is supported by ac- susceptibility $\chi_{ac}(H,T)$ versus T plots at various fixed dc-magnetic fields under warming condition[167, 318 - 320]. It has been demonstrated in the literature that Arrott plot criterion can be capable of establishing the order of both sequential transitions as well as isolated phase transitions [167]. The applicability of Arrott criterion for both first- and second-order transitions possibly replicates the fact that magnetization at low fields drops across the temperatures below the structurally coupled transition (i.e. incommensurate-to-commensurate transition at T_2). Such transitions are well described on the basis of 'interaction component mechanism' [312]. According to this mechanism the incommensurate-to-commensurate transition must be first-order in nature. Such predictions were experimentally proved in the case of $CoCr_2O_4$, $Ni_3V_2O_8$, and CuO [312].

Figure 7.16 shows the temperature dependence of remanence magnetization M_r(T) obtained from the M-H isotherms for a ramping field of 1 kOe and 90 kOe. The value of M_r(T) drops abruptly across the T_N as expected. It assumes a maximum value of 32.6 emu g^{-1} and decreases below 15 K to 31 emu g^{-1} at 5 K as shown in the inset figure 7.16. Such a low value of remanence magnetization is connected with the low temperature first order meta-

magnetic behavior of the Mn_3O_4 system. As the magnetic field increases beyond 1 kOe the significant diffusiveness in the $M_r(T)$ behavior is noticed owing to the saturation effects. The nature of magnetic transitions in Mn_3O_4 described above are consistent with the heat capacity measurements reported earlier [312, 313]. Across 90 kOe, $M_r(T)$ shows a tail above T_N which persist up to 70 K and matches with the onset of polarization (Figure 7.12). Such consistency between the temperature variation of polarization and remanence magnetization indicates that the existence of weak magnetic ordering even above 42 K; this inference is further supported by the $\varepsilon_r(T)$ which gradual increasing for $T > 42$ K.

7.3.5 Summary:

The complex magnetic ordering in polycrystalline Mn_3O_4 was investigated by means of ac-magnetic susceptibility $\chi_{ac}(f_{ac\text{-}Mag}, H_{dc}, T)$ and relative dielectric permittivity ε_r ($f_{ac\text{-}Elec}$, H_{dc} ,T). All the transitions occurring below the ferrimagnetic Néel temperature including the fine lock-in transition at 38 K was successfully probed by means of $\chi_{ac}(f_{ac\text{-}Mag}, T)$ superimposed with a small static-bias magnetic field in the range 20 - 200 Oe. Mn_3O_4 exhibits isokaps in the field dependent ac susceptibility curves $\chi_{ac}(H_{dc},T)$, which displays a succession of peaks corresponding to each transition except T_2 that decrease in amplitude with increase in temperature as the magnitude of the static magnetic-field increases. Such humps are unequivocal signature of a continuous second-order transition. While the M-H isotherms near to T_2 display the *S*-shaped feature associated with meta-magnetic like first-order transition. The zero-field temperature dependence of the dielectric permittivity curves exhibits a large hysteresis of about ~ 5.15 K in consonance with the first order nature of spiral incommensurate to commensurate planar transition occurs at 34 K. The magnetic and dielectric properties show clear evidence of magneto-electric coupling in Mn_3O_4 and finite electric polarization in magnetically order state.

Chapter 8

Conclusions and Scope for Future Research

8.1 Conclusions:

A summary of important findings of the present thesis is presented in this concluding chapter. This thesis is mainly focused on the similarities and differences of the magnetic structure of three different inverse spinel oxides. The structural, magnetic, dielectric, specific-heat, and other physical properties of: *(i)* Cobalt-Orthostannate (Co_2SnO_4) *(ii)* Cobalt-Orthotitanate (Co_2TiO_4) *(iii)* Hausmannite (Mn_3O_4), and *(iv)* the two phase composites comprising of Co_3O_4 – Co_2TiO_4 are recapitulated here. Magnetic measurements in these polycrystalline samples have shown several interesting features including semi-spin-glass behavior, bipolar exchange bias, and spin-liquid type structure at low-temperatures. Following a brief summary of the key results, we concluded this chapter by identifying a few possible frontiers of future research work related to the tailoring of the exchange interactions.

The nature of magnetic ordering and electronic structure of $Co_2SnO_4 = [Co^{2+}][Co^{2+}Sn^{4+}]O_4$ was investigated by measuring the temperature dependence of its dc, ac-susceptibilities and X-ray photo electron spectroscopy, respectively. We have shown that the ferrimagnetic (FiM) ordering was originated from different magnetic moments of Co^{2+} on A sites (3.87 μ_B) and B-sites (4.91 μ_B) with the antiferromagnetic molecular constants N_{AA} = 21.56, N_{AB} = 33.02 and N_{BB} = 10.68. The analysis of the frequency dependence ac-magnetic susceptibility data using Vogel-Fulcher Law and the Power-Law of the critical slowing down suggests the existence of spin-glass (SG) phase T_{SG} ~ 39 K. The FiM is associated with the longitudinal spin component, whereas, the SG is arising due to the freezing of the transverse spin component. These observations confirm the prediction of Villain [40] in magnetic insulators with non-magnetic substituents such as Sn, Ti, and Al. Random distribution of the Sn^{4+} ions on the B-sites are the main source of weakening of the A-B exchange coupling, thereby producing random canting of the Co^{2+} moments below FiM ordering. Application of magnetic field reduces the random canting, thereby shifting T_{SG} to lower temperatures and dwindles the SG phase.

Next we have studied the role of 'Ti' dilution at the octahedral sites of Co_2TiO_4 by analyzing the temperature and magnetic field dependence of its magnetization, specific heat (C_P), ac susceptibilities χ' and χ'' measured at different frequencies, and the hysteresis loop parameters. X-ray diffraction of the sample synthesized by the solid-state reaction route confirmed the cubic spinel structure without any secondary phases. However, we observed trivalent nature of 'Ti' instead of tetravalent state from the X-ray photo electron spectroscopy; unveiling the electronic structure of Co_2TiO_4 equivalent to $[Co^{2+}][Co^{3+}Ti^{3+}]O_4$. Analysis of the dc magnetic susceptibilities combined with the weak anomalies in the C_P versus T data shown the existence of quasi-long range ferrimagnetic state below 47.8 K and a compensation effect across 32 K. From the analysis of Néel fitting of the inverse-paramagnetic susceptibility we obtained the magnetic moments $\mu(A)$ = 3.87 μ_B and $\mu(B)$ = 5.19 μ_B on the A and B sites in Co_2TiO_4. These magnitudes are different from Co_2SnO_4 which are resulting from the different electronic

structure. Additional noteworthy features in Co_2TiO_4 are (*a*) lack of perfect spin-glass phase transition below 48 K, (*b*) negative slopes of Arrott plots below 32 K, (*b*) zero-crossover of isothermal magnetic-entropy-changes (ΔS) signifying the presence of pseudo first order discontinuous magnetic phase transition in the low temperature regime ($5\ K \leq T \leq 32\ K$), (*c*) large coercivity $H_C \sim 20$ kOe and sign-reversal exchange bias H_{EB} (= - 20 kOe for $T < 15$ K).

We have studied the effect of 'Sn' doping (at octahedral 'Ti' sites) on the global magnetic properties of Co_2TiO_4 polycrystalline system. We found the co-existence of longitudinal FiM behavior with Néel temperature T_N = 46.1 K and re-entrant transverse spin-glass state at 44.05 K in $Co_2Ti_{0.6}Sn_{0.4}O_4$ system. The magnetic compensation temperature T_{COMP} shifts from 31.74 K to 27.1 K when 40 at% 'Sn' substitutes 'Ti' at B-sites. For $T > T_N$, χ_{dc} (= M/H_{dc}) fits well with the Néel's expression for the two-sublattice model with antiferromagnetic molecular field constants $N_{BB} \sim 15.44$, $N_{AB} \sim 32.01$, and $N_{AA} \sim 20.88$. The frequency dependence of ac-magnetic susceptibility (χ_{ac}) data follows the Vogel-Fulcher law and the power-law of critical slowing-down with 'zv' = 6.01 suggests the existence of spin-clusters. This system exhibits unusual hysteresis loops with large $H_{EB} \sim 13.6$ kOe (at 7 K) after zero-field cooling process from an un-magnetized state, and a dramatic collapse of remanence (M_R) and coercive field (H_C) across T_{COMP}. Such anomalous H_{EB} under zero-field cooled condition originates from the ferrimagnetic/spin-glass interface. We have also studied the temperature dependence of micro-Raman spectroscopy of (1- x) Co_3O_4 + x Co_2TiO_4 ($0 \leq x \leq 1$) two-phase composites. Five Raman active modes are observed at 689, 618, 518, 480, and 195 cm^{-1} for all the lower and intermediate compositions, these modes are associated with A_{1g}, E_g and $3F_{2g}$ phonon symmetries. Conversely, pure Co_2TiO_4 exhibits a broad spectrum of width ~ 93.3 cm^{-1} without any signatures of the $F_{2g}(3)$ mode. At 25 K the A_{1g} and F_{2g} modes shift towards high frequency side with anomalies across the FiM and antiferromagnetic ordering temperatures of Co_2TiO_4 and Co_3O_4. All the compositions exhibit two distinct bands at 576 cm^{-1} (B_1) and 665 cm^{-1}(B_2) in the Fourier transform infrared spectra recorded at 310 K which are associated with the vibrational stretching of the metal-oxygen bonds of length ~ 195.8 pm (B-O) and ~185.4 pm (A-O) respectively. The intensity of these sharp bands gradually smeared-off as the crystal structure transforms from normal-spinel (a = 8.07 Å) to inverse-spinel structure (a = 8.45 Å). The $\chi_{dc}(T)$ data of these composites shows increase of T_N from 47.4 K to 53.5 K, and T_{COMP} from 31.74 K to 37.72 K with increasing x from 1 to 0.23. We also observed lack of spin-glass transition in these two-phase composites. For $T < T_N$ we observed large magnitude of H_C (~ 19 kOe for x = 0.23 at T = 10 K) and H_{EB} (~ 887 Oe for x = 1 at T = 10 K) which were tailored with respect to the composition 'x'. The temperature and frequency dependence of ac-conductivity $\sigma(T,\omega)$ studies confirms the possibility of Arrhenius like behaviour in $\sigma(T)$ and Jonscher's power law ($\sigma_{ac} \sim A\omega^s$) behaviour which signifies the fact that the motion of charge carriers from site to site with quantum mechanical tunneling between asymmetric double-well potential dominated at T > 300K. These studies yield activation energy (E_A) in the range 2-1800 meV. The Cole-Cole analysis revealed the dominance of grain-

boundary effects for dilute compositions whereas conductivity within grains play a major role in heavily substituted Co_2TiO_4.

In chapter 7, we have studied the magnetic, dielectric and magneto-dielectric properties of tetragonally distorted normal spinel Mn_3O_4. Various complex magnetic transitions occur below the ferrimagnetic ordering of Mn_3O_4 are successfully probed by the ac-magnetization dynamics ($\chi_{ac}(T)$), relative dielectric permittivity $\varepsilon_r(T)$ and magneto-dielectric ($\Delta\varepsilon_r/\varepsilon_r(H)$) measurements. Besides the known sequence of transitions (T_N at 42.75 K and field-induced structural transition at 32 K), a new lock-in transition at 38 K (T^*) has been successfully probed by both $\chi_{ac}(T)$ and $\varepsilon_r(T)$. We also observed a clear hysteresis of about 5.15 K in the zero-field $\varepsilon_r(T)$ across 34 K which provides evidence to the first-order nature of this transition. Our $\Delta\varepsilon_r/\varepsilon_r(H)$ results demonstrates the evidence of magneto-electric coupling in Mn_3O_4 system. The temperature dependence of electric polarization takes maximum value ($P \sim 3 \times 10^{-6}$ C/m^2) below the spiral-incommensurate to commensurate planar transition at 33 K.

8.2 Future Scope:

In the current thesis we explored only structural, magnetic and electrical properties of spinel oxides Co_2SnO_4, Co_2TiO_4 and Mn_3O_4. Below we enumerate some possible extensions of the current work.

- One can study the temperature dependence of Neutron diffraction below the ferrimagnetic ordering temperatures which can provide additional information about the magnetic structure. Such studies also verify the conclusions drawn from the magnetic measurements.
- To perform the electronic band-structure calculations using density function theory and make a comparative study with the experimental results obtained from the optical measurements (in UV-Vis-NIR regime) by means of diffusive reflectance spectroscopy.
- To synthesize the low-dimensional nanostructures of Co_2SnO_4, Co_2TiO_4 and Mn_3O_4 and make a systematic comparative study of their structural, optical and magnetic properties with their bulk counterpart. Such nanostructures play a major role in the fuel-cells, Li-ion batteries and catalysts.
- This study can be extended with various other doping elements either non-magnetic or magnetic (e.g. Al, Mn, Ru, V, and Cr at 'Ti' and 'Sn' sites) and probe the differences occurring in the structural, optical and magnetic properties as compared the pristine compounds.

[1] A. Goldman, "*Magnetic Components for Power Electronics*", Springer (Nov. 2001).

[2] D. W. Bruce, "*Functional Oxides*", Wiley (2010).

[3] V. G. Harris, A. Geiler, Y. Chen, S. D. Yoon, M. Wu, A. Yang, Z. Chen, P. He, P. V. Parimi, Zuo, C. E. Patton, and C. Vittoria, J. Magn. Magn. Mater. **321**, 2035 (2009).

[4] P. Saha, M. K. Datta, O. I. Velikokhatnyi, A. Manivannan, D. Alman, and P. N. Kumta, Materials Science **66**, 1 (2014).

[5] F. S. Galasso, "*Structure and Properties of Inorganic Solids: International Series of Monographs in Solid State Physics*" Elsevier, January 26, 2016.

[6] P. W. Anderson, Phys. Rev. **102**, 1008 (1956).

[7] M. Robbins, G. K. Wertheim, R. C. Siterwood and D. N. E. Buchanan, J. Phys. Chem. Solids **32**, 717 (1971).

[8] W. Schiessl, W. Potzel, H. Karzel, M. Steiner, G. M. Kalvius, A. Martin, M. K. Krause, I. Halevy, J. Gal, W. Schäfer, G. Will, M. Hillberg, and R. Wäppling, Phys. Rev. B **53**, 9143 (1996).

[9] D. C. Kim, S. K. Ihm, Environ. Sci. **35(1)**, 222 (2001).

[10] S. Thota, B. Prasad and J. Kumar, Mat. Sci. Eng. B **167**,153 (2010).

[11] L. Zhou, H. B. Wu, T. Zhu and X.W. Lou, J. Mater. Chem. **52**, 7986 (2012).

[12] F. Basiri and M. Taei, Microchim Acta **184**, 155 (2017).

[13] B. Antic, G. F. Goya, H. R. Rechenberg, V. Kusigerski, N. Jovic and M. Mitric, J. Phys.: Condens. Matter **16**, 651 (2004).

[14] R. E. Newnhan, "*Properties of Materials: Anisotropy, Symmetry, Structure"* (Oxford University Press, New York, 2005).

[15] L. Zhou, H. B. Wu, T. Zhu and X.W. Lou, J. Mater. Chem. **52**, 7986 (2012).

[16] J. Zhang, J. Liang, Y. Zhu, D. Wei, L. Fan, and Y. Qian, J. Mater. Chem. A **2**, 2728 (2014).

[17] R. E. Newnhan, "*Properties of Materials: Anisotropy, Symmetry, Structure"* (Oxford University Press, New York, 2005).

[18] A. H. Morrish, "*The Physical Principles of Magnetism"*, by Allan H. Morrish, pp. 696. ISBN 0-7803-6029-X. WileyVCH, January 2001. 1 (2001).

[19] E. Prince, Acta. Cryst. **10**, 554 (1957).

[20] J. S. Kasper, Bull. Am. Soc. **4**, 178 (1959).

[21] I. S. Jacobs, J. Phys. Chem. Chem. Solids **11**, 1 (1959).

[22] I. S. Jacobs, J. Phys. Chem. Solids **15**, 54 (1960).

[23] R. Nathans, S. J. Pickart, S. E. Harrison and C. J. Kerrisman, Proc. IEEE (London), Suppl. **5 104-B**, 217 (1957).

[24] L. M. Corliss, J.M. Hastings and F. G. Brockman, Phys. Rev. **90**, 1013 (1953).

[25] S. J. Pickart and R. Nathans, Phys. Rev. **116**, 317 (1959).

[26] W. C. Hamilton, Phys. Rev. **110**, 1050 (1958).

[27] L. Néel, Ann. Phys. (Paris) **18**, 5 (1932).

[28] L. Néel, Ann. Phys. (Paris) **5**, 232 (1936).

[29] F. Bitter, Phys. Rev. **54**, 79 (1938).

[30] J. H. Van Vleck, J. Chem. Phys. **9**, 85 (1941).

[31] M. Reehuis, M. Tovar, D. M. Többens, P. Pattison, A. Hoser, and B. Lake, Phys. Rev. B **91,** 024407 (2015).

[32] K. Tomiyasu, J. Fukunaga, and H. Suzuki, Phys. Rev. B **70**, 214434, (2004).

[33] S. H. Lee, C. Broholm, W. Ratcliff, G. Gaasparovic, G. Huang, T. H. Kim, and S. W. Cheong, Nature (London) **418**, 856 (2002).

[34] K. Manna, A. K. Bera, M. Jain, S. Elizabeth, S. M. Yusuf, and P. S. Anil Kumar, Phys. Rev. B **91**, 224420, (2015).

[35] M. Viswanathan and P. S. Anil Kumar, Phys. Rev. B **80**, 012410 (2009).

[36] P. Anil Kumar, R. Mathieu, P. Nordblad, S. Ray, O. Karis, G. Andersson, and D. D. Sarma, Phys. Rev. X **4**, 011037 (2014).

[37] J. Hubsch, G. Gavoille and J. Bolfa, J. Appl. Phys. **49**, 1363 (1978).

[38] K. Sato, T. Naka, T. Nakane, D. Rangappa, S. Takami, S. Ohara, and T. Adschiri, J. Magn. Magn. Mater. **350**, 161 (2014).

[39] F. Bodénan, V. B. Cajipe, M. Danot, and G. Ouvrard J. Solid State Chem. **137**, 249 (1998).

[40] J. Villian, Z. Phys. B **33**, 31 (1979).

[41] K. Kamala Bharathi, R. J. Tackett, C. E. Botez, and C. V. Ramana, J. Appl. Phys. **109**, 07A510 (2011).

[42] T. Sarkar, V. Duffort, V. Pralong, V. Caignaert, and B. Raveau Phy. Rev. B **83**, 094409 (2011).

[43] R. A. Brand, H. Georges-Gibert, J. Hubsch and J. A. Heller, J. Phys. F: Met. Phys. **15**, 1987 (1985).

[44] A.V. Mahajan, D.C. Johnston, D.R. Torgeson, F. Borsa, Phys. Rev. B **46,** 10966 (1992).

[45] H.C. Nguyen, J.B. Goodenough, Phys. Rev. B **52,** 324 (1995).

[46] Y. Ren, A. A. Nugroho, A.A. Menovsky, J. Strempfer, U. Rütt, F. Iga, T. Takabatake, and C.W. Kimball, Phys. Rev. B **67**, 014107 (2003).

[47] N. Shirakawa and M. Ishikawa, Jpn. J. Appl. Phys. **30**, L755 (1991).

[48] M. M. Ibrahim, M. S. Seehra, and G. Srinivasan, J. Appl. Phys. **75**, 6822 (1994).

[49] V.K. Lakhani, B. Zhao, L. Wang, U.N. Trivedi, and K.B. Modi, J. Alloy. Compd. **509**, 4861 (2011).

[50] G. Lawes, B. Melot, K. Page, C. Ederer, M.A. Hayward, T. Proffen, and R. Seshadri, Phys. Rev. B **74**, 024413 (2006).

[51] D. P. Dutta, J. Manjanna, and A.K. Tyagi, J. Appl. Phys. **106**, 043915 (2009).

[52] L. Néel, Ann. Phys. (Paris) **3,** 137 (1948).

[53] S. Chikazumi, "*Physics of Ferromagnetism"*, Oxford University Press, London, 1997.

[54] J. S. Smart, Am. J. Phys. **23,** 356 (1955).

[55] T. Nagata, "*Rock Magnetism, second ed."*, Maruzen, Tokyo, 1961.

[56] E. W. Gorter, Philips Res. Rept. **9**, 103 (1954).

[57] M. Abe, M. Kawachi, S. Nomura, J. Phys. Soc. Jpn. **31,** 940 (1971).

[58] H.-g. Zhang, W.-h. Wang, E.-k. Liu, X.-d. Tang, G.-j. Li, H.-w. Zhang, G.-h. Wu, Phys. Status Solidi B **250**, 1287 (2013).

[59] R. Padam, S. Pandya, S. Ravi, A.K. Grover, and D. Pal, AIP Conf. Proc. **1512**, 1112 (2013).

[60] J.A. Schulkes and G. Blasse, J. Phys. Chem. Solids **24**, 1651 (1963).

[61] K. P. Belov, Phys. Usp. **39,** 623 (1996).

[62] A. Kumar and S. M. Yusuf, Physics Reports **556**, 1 (2015).

[63] S. M. Yunus, H. S. Shim, C.H. Lee, M.A. Asgar, F.U. Ahmed, and A.K.M. Zakaria, J. Magn. Magn. Mater. **232,** 121 (2001).

[64] S. M. Yunus, H. S. Shim, C. H. Lee, M. A. Asgar, F. U. Ahmed, and A. K. M. Zakaria, J. Magn. Magn. Mater. **241,** 40 (2002).

[65] A. K. M. Zakaria, M.A. Asgar, S.G. Eriksson, F.U. Ahmed, S.M. Yunus, and H. Rundlöf, J. Magn. Magn. Mater. **265**, 311 (2003).

[66] A. K. M. Zakaria, and M.A. Asgar, J. Alloy. Compd. **396,** 44 (2005).

[67] J. A. Mydosh, *Spin glasses: An Experimental Introduction.* Taylor and Francis: 1993.

[68] R. M. Pickup, R. Cywinski, C. Pappas, B. Farago, P. Fouquet, Phys Rev Lett, **102**, 097202 (2009).

[69] K. A. Weron, J. Phys.: Condens. Matter **3**, 9151 (1991).

[70] J. Krok-Kowalski, J. Warczewski, P. Gusin, T. Śliwińska, T. Groń, G. Urban, H. Duda, E.Malicka, A. Pacyna, L.I. Koroleva, J. Phys.: Condens. Matter **21**, 035402 (2009).

[71] G. Parisi, "*Mean field theory of spin glasses: statistic and dynamics"*, [arXiv: 0706.0094]

[72] D. Sherrington, S. Kirkpatrick, Phys. Rev. Lett. **26**, 1792 (1975)

[73] K. Binder, A. P. Young, Rev. Mod. Phys. **58,** 801, (1986).

[74] B. M. Wang, Y. Liu, P. Ren, B. Xia, K. B. Ruan, J. B. Yi, J. Ding, X. G. Li, and L. Wang, Phys. Rev. Lett. **106**, 077203 (2011).

[75] Z. D. Han, B. Qian, D. H. Wang, P. Zhang, X. F. Jiang, C. L. Zhang, and Y. W. Du, Appl. Phys. Lett. **103**, 172403 (2013).

[76] J. Krishna Murthy and A. Venimadhav, Appl. Phys. Lett. **103**, 252410 (2013).

[77] J. Hubsch and G. Gavoille, Phys. Rev. B **26**, 3815 (1982).

[78] G. Gavoille, J. Hubsch, and S. Koutani, J. Magn. Magn. Mater. **102**, 283 (1991).

[79] J. K. Srivastava, J. A. Kulkarni, S. Ramakrishnan, S. Sing, V. R. Marathe, G. Chandra, V. S. Darshane, and R. Vijayaraghavan, J. Phys. C: Solid State **20**, 2139 (1987).

[80] S. Ogawa and S. Waki, J. Phys. Soc. Jpn. **20**, 540 (1965).

[81] E. Harmon, D. J. Simkin, R. J. Haddad, and W. B. Muir, J. Phys. Colloq. **38**, CI-131 (1977). AIP Conf. Proc. **29**, 576 (1976).

[82] K. de Strooper, Phys. Status Solidi A **39**, 431 (1977).

[83] V. Sagredo, B. Watts, and B. Wanklyn, J. Phys. IV France **7,** C1-279 (1997).

[84] S. Hiari, A. M. dos Santos, M. C. Shapiro, J. J. Molaison, N. Pradhan, M. Guthrie, C. A. Tulk, I. R. Fisher and W. L. Mao, Phys. Rev. B **87**, 014417 (2013).

[85] Y. Nii, H. Sagayama, H. Umestu, N. Abe, K. Taniguchi and T. Arima, Phys. Rev. B **87**, 195115 (2013)

[86] C. Kim, E. Jo, B. Kang, S. Kwon, S. Lee, J. H. Shim, T. Suzuki and T. Katsufuji, Phys. Rev. B **86**, 224420 (2012).

[87] M. Kim, X. M. Chen, X. Wang, C. S. Nelson, R. Budakian, P.Abbamonte and S. L. Cooper, Phys. Rev. B **84**, 174424 (2011).

[88] E. Jo, K. An, J. H. Shim, C. Kim and S. Lee, Phys. Rev. B **84**, 174423 (2011).

[89] R. Tackett, G. Lawes, B. C. Melot, M. Grossman, E. S. Toberer and R. Seshadri, Phys. Rev. B **76**, 024409 (2007).

[90] T. Suzuki and T. Katsufuji, Phys. Rev. B **77**, 220402(R) (2008).

[91] M. Kim, X. M. Chen, Y. I. Joe, E. Frankdin, P. Abbamonte and S. L. Cooper, Phys. Rev. Lett. **104**, 136402 (2010).

[92] L. L. Hench and J. K. West, Chem. Rev. **90**, 33 (1990).

[93] S. Thota, T. Dutta, and J. Kumar, J. Phys. Cond. Matt. **18**, 2473 (2013).

[94] S. Hofman, "*Auger and X-ray Photoelectron Spectroscopy in Materials Science*", Springer-Verlag, Berlin Heidelberg (2013) pp- 47.

[95] S. Huffner, "*Photoelectron Spectroscopy Principles and Applications*", Second Edition, Springer-Verlag, Berlin Heidelberg, (1996) pp 112.

[96] J. Clarke, "*The New Superconducting Electronics"* (eds H. Weinstock, and R. W. Ralston), Kluwer, Dordrecht, 1993, pp. 123.

[97] B. Batlogg, "*Physical Properties of High-Tc Superconductors"*, June 1991, p44.

[98] B. D. Josephson, Phys. Lett. **1** (7), 251 (1962).

[99] B. D. Josephson, Rev. Mod. Phys. **46** (7), 251 (1974).

[100] J. S. Hwang, K. J. Lin, and C. Tien, Review of Scientific Instruments 68 (1997).

[101] E. Dachs and A. Benisek, Cryogenics **51**, 460 (2011).

[102] T. Panmatarith, N. Hayeemayang, and N. Baka-Lee, J. Sci. Technol. **27**, 1113 (2005);

[103] T. Suzuki and T. Katsufuji, Phys. Rev. B **77**, 054412 (2008).

[104] D. A. Skoog, F. J. Holler, S. R. Crouch *"Principles of instrumental analysis"*. 6th ed. Cengage Learning; (2006).

[105] H. H. Willard, Jr. L. L. Meritt, J. J. Dean, Jr. F. A. Settler *"Instrumental methods of analysis.* 7th ed. New Delhi: CBS Publisher & Distributors; (1988).

[106] F. A. Settle *"Handbook of instrumental techniques for analytical chemistry"*. New Jersey: Prentice, Inc.; (1997).

[107] E. Smith, G. Dent, *"Modern Raman spectroscopy: a practical approach"* England, Chichester: John Wiley & Sons; (2005).

[108] J. K. Srivastava, S. Ramakrishnan, V. R. Marathe, G. Chandra, R. Vijayaraghavan, J. A. Kulkarni and V. S. Darshane and S. Singh, J. Appl. Phys. **61**, 3622 (1987).

[109] Y. Chen, J. E. Snyder, C. R. Schwichtenberg, K. W. Dennis, R. W. McCallum, and D. C. Jiles, IEEE Trans. Magn. **35**, 3652 (1999).

[110] T. Asanuma, T. Matsutani, C. Lui, T. Mihara and M. Kiuchi, J. Appl. Phys. **95**, 6011 (2004).

[111] J. M. Themlin, M. Chtaib, L. Henrard, P. Lambin, J. Darville and J. M. Gilles, Phys. Rev. B **46**, 2460 (1992).

[112] J. K. Kwak, K. H. Park, D. Y. Yun, D. U. Lee, T. W. Kim, D. I. Son, J. H. Han and J. Y. Lee J. Korean Phys. Soc. **57**, 1803 (2010).

[113] J. G. Kim, D. L. Pugmire, D. Battaglia and M. A. Langell, Appl. Surf. Sci. **165**, 70 (2000).

[114] S. C. Petitto, E. M. Marsh, G. A. Carson and M. A. Langell, J. Mol. Catal. A **281**, 49 (2008).

[115] J. Xu J, P. Gao and T. S. Zhao, Energy Environ. Sci. **5**, 5333 (2012).

[116] P. N. Shelke, Y. B. Khollam, K. R. Patil, S. D. Gunjal, S. R. Jadkar, M. G. Takwale and K. C. Mohite, J. Nano Electron. Phys. **3**, 486 (2011).

[117] M. E. Fisher, Philos. Mag. **7**, 1731 (1962).

[118] E. E. Bragg and M. S. Seehra, Phys. Rev. B **7**, 4197 (1973).

[119] B. Raveau, V. Caignaert, V. Pralong, D. Pelloquin, and A. Maignan, Chem. Mater. 20, 6295 (2008).

[120] J. Souletie and J. L. Tholence Phys. Rev. B **32**, 516 (1985).

[121] R. Mathieu, P. Nordblad, D. N. H. Nam, N. X. Phuc and N. V. Khiem Phys. Rev. B **63**, 174405 (2001).

[122] M. Gabay and G. thoulouse, Phys. Rev. Lett. **47**, 201 (1981).

[123] V. Singh, M. S. Seehra, and J. Bonevich, J. Appl. Phys. **105**, 07B518 (2009).

[124] J. D. Rall and M. S. Seehra, J. Phys.: Condens. Matter **24**, 076002 (2012).

[125] J. L. Dormann, L. Bessais, and D. Fiorani, J. Phys. C **21**, 2015 (1988).

[126] J. O. Andersson, C. Djurberg, T. Jonsson, P. Svedlindh, and P. Nordblad, Phys. Rev. B **56**, 13983 (1997).

[127] B. Martinez, X. Obradors, Ll. Balcells, A. Rouanot, and C. Monty, Phys. Rev. Lett. **80**, 181 (1998).

[128] S. D. Tiwari and K. P. Rajeev, Phys. Rev. B **72**, 104433 (2005).

[129] M. K. Singh, R. S. Katiyar, W. Prellier, and J. F. Scott, J. Phys.:Condens.Matter **21**, 042202 (2009).

[130] W. H. Meiklejohn and C. P. Bean, Phys. Rev. **102**, 1413 (1956).

[131] M. Ali, P. Adie, C. H. Marrows, D. Greig, B. J. Hickey and R. L. Stamps, Nature Mater. **6,** 70 (2007).

[132] W. C. Cain and M. H. Kryder, J. Appl. Phys. **67**, 5722 (1990).

[133] G. Salazar-Alvarez, J. Sort, S. Surinach, M. Dolors Baro and J. Nogues, J. Am. Chem. Soc. **129**, 9102 (2007).

[134] P. Dutta, M S. Seehra, S. Thota and J. Kumar, J. Phys.:Condens. Matter **20**, 015218 (2008).

[135] A. Punnoose, M. S. Seehra, J. van Tol and L. C. Brunel, J. Magn. Magn. Mater. **288**, 168 (2005).

[136] B. M. Wang, Y. Liu, P. Ren, B. Xia, K. B. Ruan, J. B. Yi, J. Ding, X. J. Li and L. Wang, Phys. Rev. Lett. **106**, 077203 (2011).

[137] A. K. Nayak, M. Nicklas, S. Chadov, C. Shekhar, Y. Skourski, J. Winterlik and C. Felser, Phys. Rev. Lett. **110**, 127204 (2013).

[138] G. Srinivasan and M. S. Seehra, Phys. Rev. B **28**, 1 (1983).

[139] I. S. Jacobs, J. Appl. Phys. **30**, 301S (1959).

[140] K. Dwight and N. Menyuk, Phys. Rev. **119**, 1470 (1960).

[141] M. Imada, A. Fujimori, and Y. Tokura, Rev. Mod. Phys. **70**, 1039 (1998).

[142] R. N. Bhowmik and R. Ranganathan, J. Magn. Magn. Mater. **248**, 101 (2002).

[143] R. N. Bhowmik, R. Ranganathan, and R. Nagarajan, J. Magn. Magn. Mater. **299**, 327 (2006).

[144] M. S. Seehra, J. C. Dean, and R. Kannan, Phys. Rev. B **37**, 5864 (1988).

[145] F.-J. Borgermann, H. Maletta, and W. Zinn, Phys. Rev. B **35**, 8454 (1987).

[146] M. S. Seehra, Z. Feng and R. Gopalakrishnan, J. Phys. C: Solid State Phys. **21**, L1051 (1988).

[147] M. S. Seehra, R. Kannan and M. M. Ibrahim, J. Appl. Phys. **73**, 5466 (1993).

[148] P. A. Kumar, R. Mathieu, R. Vijayaraghavan, S. Majumdar, O. Karis, P. Nordblad, B. Sanyal, O. Eriksson, and D. D. Sarma, Phys. Rev. B **86**, 094421 (2012).

[149] T. Sarkar, V. Pralong, V. Caignaert and B. Raveau Chem. Mater. **22**, 2885 (2010).

[150] R. Mathieu, J. P. He, Y. Kaneko, H. Yoshino, A. Asamitsu and Y. Tokura Phys. Rev. B **76**, 014436 (2007).

[151] N. Menyuk, K. Dwight, D.G. Wickham, Phys. Rev. Lett. **4**, 119 (1960).

[152] N. Sakamoto, J. Phys. Soc. Jpn. **17**, 99 (1962).

[153] E.W. Gorter, Philips Res. Rept. **9,** 295 (1954).

[154] G. Blasse, Philips Res. Rept. **3**, 96 (1964).

[155] T.V. Chandrasekhar Rao, P. Raj, S.M. Yusuf, L.M. Rao, A. Sathyamoorthy, V.C. Sahni, Philos. Mag. B **74**, 275 (1996).

[156] N. Kumar, A. Sundaresan, Solid State Commun. **150**, 1162 (2010).

[157] P. K. Manna and S. M. Yusuf, Phys. Rep. **535**, 61 (2014).

[158] T. J. Chuang, C. R. Brundle, D. W. Rice, Surf. Sci. **59**, 413 (1976).

[159] Y. Fu, H. Du, S. Zhang, and W. Huang, Mater. Sci. Eng., A **403**, 25 (2005).

[160] E. McCafferty and J. P. Wightman, Surf. Interface Anal. **26**, 549 (1998).

[161] S. Ivanov, R. Tellgren, F. Porcher, G. Andre, T. Ericsson, P. Nordblad, N. Sadovskaya, G. Kaleva, E. Politova, M. Baldini, et al., Mater. Chem. Phys. **158**, 127 (2015).

[162] J. Souletie and J. Tholence, J. Chem. Phys. **21**, 168 (1953).

[163] J. Rall, M. S. Seehra, and E. S. Choi, Phys. Rev. B **82**, 184403 (2010).

[164] M. S. Seehra and V. Singh, J. Phys.: Condens, Matter **25**, 356001 (2013).

[165] C. Srivastava, G. Srinivasan, and N. Nanadikar, Phys. Rev. B **19**, 499 (1979).

[166] S. Thota, Q. Zhang, F. Guillou, U. L¨uders, N. Barrier, W. Prellier, A. Wahl, and P. Padhan, Appl. Phys. Lett. **97**, 112506 (2010).

[167] X. Zhou, W. Li, H. Kunkel, and G. Williams, Phys. Rev. B **73**,012412 (2006).

[168] A. Arrott, Phys. Rev. **108**, 1394 (1957).

[169] A. Arrott and J. E. Noakes, Phys. Rev. Lett. **19**, 786 (1967).

[170] B. Banerjee, Phys. Lett. **12**, 16 (1964).

[171] X. Zhou, W. Li, H. P. Kunkel, and G. Williams, J. Phys.: Condens. Matter **16**, L39 (2004).

[172] E. Gopal, "*Specific heats at low temperatures*" (New York: Plenum Press) **1** (1996).

[173] M. Bouvier, P. Lethuillier, and D. Schmitt, Phys. Rev. B **43**, 13137 (1991).

[174] W. Roth, J. Phys. Chem. Solids **25**, 1 (1964).

[175] N. Tsujii and H. Kitazawa, J. Phys.: Condens. Matter **19**, 145245 (2007).

[176] A. Ramirez, G. Espinosa, and A. Cooper, Phys. Rev. B **45**, 2505 (1992).

[177] A. Ramirez, G. Espinosa, and A. Cooper, Phys. Rev. Lett. **64**, 2070 (1990).

[178] W. De Sorbo, J. Chem. Phys. **21**, 168 (1953).

[179] A. K. Nayak, M. Nicklas, S. Chadov, P. Khuntia, C. Shekhar, A. Kalache, M. Baenitz, Y. Skourski, V. K. Guduru, A. Puri, U. Zeitler, J. M. D. Coey, C. Felser, Nat. Mater. **14**, 679 (2015).

[180] X. Yuanhua, W. Rui, Z. Yinfeng, L. Shunquan, D. Honglin, H. Jingzhi, W. Changsheng, C. Xiping, X. Lei, Y. Yingchang, Y. Jinbo, Phys. Rev. B. **96**, 064440 (2017).

[181] "*Magnetic Spinels- Synthesis, Properties and Applications*" Edited by M. S. Seehra, ISBN 978-953-51-2974-5 (2017).

[182] C. P. Sandhya, B. John, and C. Gouri, Ionics **20,** 601 (2014).

[183] A. K. Mondal, D. Su, S. Chen, A. Ung, H. S. Kim and G. Wang, Chem. Eur. J. **21**, 1526 (2015).

[185] J. Zhu and Q. Gao, Micropor. Mesopor. Mat. **124**, 144 (2009).

[186] J. Guo, H. Lou, H. Zhao, D. Chai and X. Zheng, Appl. Catal. A **273**, 75 (2004).

[187] A. Feltz and W. Pölzl, J. Eur. Ceram. Soc. **20**, 2353 (2000).

[188] S. Patoux, L. Daniel, C. Bourbon, H. Lignier, C. Pagano, F. L. Cras, S. Jouanneau, S. Martinet, J. Power Sources **189**, 344 (2009).

[189] A. K. Padhi, K. S. Nanjundaswamy, and J. B. Goodenough, J. Electrochem. Soc. **139**, 363 (1992).

[190] K. M. Begam, M. S. Michael, and S. R. S. Prabaharan, J. Solid State Electrochem. **12**, 971 (2007).

[191] K. de Strooper, A. Govaert, C. Dauwe, and G. Robbrecht, Phys. Stat. Sol. (a) **37**, 127 (1976).

[192] J. R. L. de Almeida and D. J. Thouless, J. Phys. A **11**, 983 (1978).

[193] S. Shtrikman and E. P. Wohlfarth, Phys. Lett. A **85**, 467 (1981).

[194] J. L. Tholence, Solid State Commun. **88**, 917 (1993).

[195] A. B. Harris and R. Fisch Phys. Rev. Lett. **38**, 796 (1977).

[196] R. Mathieu, P. Svedlindh and P. Nordblad, Europhys. Lett. **52**, 441 (2000).

[197] H. S. Nair, T. Chatterji and A. M. Strydom, Appl. Phys. Lett. **106**, 022407 (2015).

[198] R. Pradheesh, H. S. Nair, V. Sankaranarayanan, and K. Sethupathi, Appl. Phys. Lett. **101**, 142401 (2012).

[199] A. Kirilyuk, A. V. Kimel, and T. Rasing, Rep. Prog. Phys. **76,** 026501 (2013).

[200] P. D. Kulkarni, U. V. Vaidya, S. K. Dhar, P. Manfrinetti, and A. K. Grover, J. Phys. D: Appl. Phys. **42,** 082001 (2009).

[201] G. F. Dionne, J. Appl. Phys. **41**, 4878 (1970).

[202] J. Bhattacharya and C. Wolverton, Phys. Chem. Chem. Phys. **15**, 6486 (2013).

[203] P. Cossee, J. Inorg. Nucl. Chem. **8**, 483 (1958).

[204] J. Tejada, J. Fontcuberta, and R. Rodriguez, J. Solid State Chem. **27**, 329 (1979).

[205] X. Xie, Y. Li, Z.Q. Liu, M. Haruta, and W. Shen, Nature **458**, 746 (2009).

[206] C. Y. Ma, Z. Mu, J. J. Li, Y. G. Jin, J. Cheng, G. Q. Lu, Z. P. Hao, and S. Z. Qiao, J. Am. Chem. Soc. **132**, 2608 (2010).

[207] M. Roy, S. Ghosh, and M.K. Naskar, Phys. Chem. Chem. Phys. **17**, 10160 (2015).

[208] T. Warang, N. Patel, A. Santini, N. Bazzanella, A. Kale, and A. Miotello, Appl. Catal. A **423**, 21 (2012).

[209] H. M. Jeong, H. J. Kim, P. Rai, J.W. Yoon, and J.H. Lee, Sensors and Actuators B: Chem. **201**, 482 (2014).

[210] X. Wu and K. Scott, Int. J. Hydrogen. Energ. **38**, 3123 (2013).

[211] G. Anandha babu, G. Ravi, T. Mahalingam, M. Navaneethan, M. Arivanandhan, and Y. Hayakawa, J. Phys. Chem. C **118**, 23335 (2014).

[212] A. Durand, T. Hamil, D. Belanger, S. Chi, F. Ye, J. Fernandez-Baca, Y. Abdollahian, and C. Booth, J. Phys.:Condens. Matter **27**, 126001 (2015).

[213] L. Wang, Y. Zheng, X. Wang, S. Chen, F. Xu, L. Zuo, J. Wu, L. Sun, Z. Li, H. Hou et al., Appl. Mater. Interfaces **6**, 7117 (2014).

[214] F. Wang, L. Liang, L. Shi, M. Liu, and J. Sun, J. Alloys Compd. **633**, 65 (2015).

[215] Q. Ke, C. Tang, Z.C. Yang, M. Zheng, L. Mao, H. Liu, and J. Wang, Electrochim. Acta **163**, 9 (2015).

[216] Y. Lin, K. Kan, W. Song, G. Zhang, L. Dang, Y. Xie, P. Shen, L. Li, and K. Shi, J. Alloys Compd. **639**, 187 (2015).

[217] S. K. Ujjain, G. Singh, and R.K. Sharma, Electrochim. Acta **169**, 276 (2015).

[218] K. Khun, Z. Ibupoto, X. Liu, V. Beni, and M. Willander, Mater. Sci. Eng., B **194**, 94 (2015).

[219] M. Inagaki and S. Naka, J. Solid State Chem. **13**, 365 (1975).

[220] V. Hadjiev, M. Iliev, and I. Vergilov, J. Phys. C: Solid State Phys. **21**, L199 (1988).

[221] D. Rousseau, R.P. Bauman, and S. Porto, J. Raman Spectrosc. **10**, 253 (1981).

[222] J. M. Malezieux and B. Piriou, Bull. Mineral. **111**, 649 (1988).

[223] A. Chopelas, High-Pressure Res. **5**, 711 (1990).

[224] M. Laguna-Bercero, M. Sanjuan, and R. Merino, J. Phys.:Condens. Matter **19**, 186217 (2007).

[225] N. V. Minh and I. Yang, Vib. Spectrosc. **35**, 93 (2004).

[226] A. M. Thorndike, A. J. Wells and E. Bright Wilson Jr., J. Chem. Phys. **15**, 157 (1947).

[227] I. Mihailova, L. Radev, and D. Mehandjiev, Oxidation Communications **35**, 58 (2012).

[228] B. Abu-Zied and S. Soliman, Catal. Lett. **132**, 299 (2009).

[229] C. W. Tang, C. B. Wang, and S. H. Chien, Thermochim. Acta. **473**, 68 (2008).

[230] G. Kustova, E. Burgina, G. Volkova, T. Yurieva, and L. Plyasova, J. Mol. Catal. A **158**, 293 (2000).

[231] Y. Z. Wang, Y. X. Zhao, C. G. Gao, and D. S. Liu, Catal Lett. **116**, 136 (2007).

[232] J. Preudhomme and P. Tarte, Spectrochim Acta A Mol. Spectrosc. **28**, 69 (1972).

[233] J. Preudhomme and P. Tarte, Spectrochim Acta A Mol. Spectrosc. **27**, 1817 (1971).

[234] P. Tarte, A. Rulmont, M. Liegeois-Duyckaerts, R. Cahay, and J. Winand, Sol. St. Ionics. **42**, 177 (1990).

[235] L. Chen, X. Pang, G. Yu, and J. Zhang, Adv. Mater. Lett. **1**, 75 (2010).

[236] C. Nasr, K. Vinodgopal, L. Fisher, S. Hotchandani, A. Chattopadhyay, and P. V. Kamat, J. Phys. Chem. **100**, 8436 (1996).

[237] S. Music, M. Gotic, M. Ivanda, S. Popovic, A. Turkovic, R. Trojko, A. Sekulic, and K. Furic, Mater. Sci. Eng. B **47**, 33 (1997).

[238] M. S. St Christoskova, M. Georgieva, and D. Mehandjiev, Mater. Chem. Phys. **60**, 39 (1999).

[239] S. Farhadi, J. Safabakhsh, and P. Zaringhadam, Journal of Nanostructure in Chemistry **3**, 1 (2013).

[240] M. Hema, A. Y. Arasi, P. Tamilselvi, and R. Anbarasan, Chem. Sci. Trans. **2**, 239 (2013).

[241] C. Huang, X. Liu, L. Kong, W. Lan, Q. Su, and Y. Wang, Appl. Phys. A **87**, 781 (2007).

[242] A. Manivannan, M. Seehra, S. Majumder, and R. Katiyar, Appl. Phys. Lett. **83**, 111 (2003).

[243] M. Yoon, M. Seo, C. Jeong, J. H. Jang, and K.S. Jeon, Chem. Mater. **17**, 6069 (2005).

[244] V. V. Atuchin, V. G. Kesler, N.V. Pervukhina, and Z. Zhang, J. Electron. Spectrosc. **152**, 18 (2006).

[245] L. T. Hudson, R. L. Kurtz, S. W. Robey, D. Temple, and R. L. Stockbauer, Phys. Rev. B **47**, 1174 (1993).

[246] J. Marco, J. R. Gancedo, and F. J. Berry, Polyhedron **16**, 2957 (1997).

[247] C. N. Sayers and N. R. Armstrong, Surf. Sci. **77**, 301 (1978).

[248] D. Watanabe, J. Castles, A. Jostsons, and A. Malin, Acta Crystallogr. **23**, 307 (1967).

[249] J. Gautier, E. Trollund, E. R´ıos, P. Nkeng, and G. Poillerat, J. Electroanal. Chem. **428**, 47 (1997).

[250] F. J. Berry, C. Greaves, and J. F. Marco, J. Solid State Chem. **96**, 408 (1992).

[251] C. E. Rice and W. R. Robinson, Mater. Sci. Bull. **11**, 1355 (1976).

[252] B. Marsan, N. Fradette, and G. Beaudoin, J. Electrochem. Soc. **139**, 1889 (1992).

[253] G. Tyuliev, D. Panayotov, I. Avramova, D. Stoichev, and T. Marinova, Mater. Sci. Eng., C **23**, 117 (2003).

[254] Y. Jeong, C. Bae, D. Kim, K. Song, K. Woo, H. Shin, G. Cao, and J. Moon, Appl. Mater. Interfaces **2**, 611 (2010).

[255] J. C. Fan and J. B. Goodenough, J. Appl. Phys. **48**(8), 3524 (1977).

[256] E. M. C. Fortunato, L. M. N. Pereira, P. M. C. Barquinha, A. M. Botelho do Rego, G. Gonçalves, A. Vilà, J. R. Morante and R. F. P. Martins, Appl. Phys. Lett. **92**(22), 222103 (2008).

[257] J. Modular, W. Stickle, P. Sobol, and K. Bomben, "*Handbook of X-ray Photoelectron Spectroscopy*", Published by : Physical Electronics Division. 1992 **1** (1992).

[258] Z. Z. Lazarevic, C. Jovalekic, D. L. Sekulic, A. Milutinovic, S. Balos, M. Slankamenac, and N. Z. Romcevic, Mater. Res. Bull. **48**, 4368 (2013).

[259] J. Maier, S. Prill, and B. Reichert, Solid State Ion. **1465**, 28 (1988).

[260] R. Thomas, V. K. Varadan, S. Komarneni, D. C. Dube, J. Appl. Phys. **90**, 1480 (2001).

[261] Y. H. Gao, J. Yang, H. Shen, J. L. Sun, X. J. Meng, J. H. Chu, Appl. Phys. Lett. **104**, 122902 (2014).

[262] K. S. Cole and R. H. Cole, J. Chem. Phys. **9**, 341 (1941).

[263] R. Gerson and H. Jaffe, J. Phys. Chem. Solids **24**, 979 (1963).

[264] K. Funke, Prog. Solid State Chem. **22**, 111 (1993).

[265] A. K. Jonscher, Nature **267**, 673 (1977).

[266] D. P. Singh, K. Shahi, K. K. Kar, Solid State Ion. **287**, 89 (2016).

[267] C. Cramer, S. Brunklaus, E. Ratai, Y. Gao, Phys. Rev. Lett. **91**, 266601 (2003).

[268] R. H. Chen, R. J. Wang, T. M. Chen, C. S. Shern, J. Phys. Chem. C **61**, 519 (2000).

[269] R. H. Chen, R. Y. Yang, S. C. Shern, J. Phys. Chem. C **63**, 2069 (2002).

[270] S. Khadhraoui, A. Triki, S. Heini, S. Zemini, M. Qurmezzine, J. Magn. Magn. Mater. **371**, 69 (2014).

[271] H. M. El-Mallah, N. A. Hegab, J. Mater. Sci. **42**, 332 (2006).

[272] S. Mahajan, D. Haridas, S. T. Ali, N. R. Munirathnam, K. Sreenivas, O. P. Thakur, C. Prakash **451**, 114 (2014).

[273] N. Ortega, A. Kumar, P. Bhattacharya, S. B. Majumder, R. S. Katiyar, Phys. Rev. B 77, 014111 (2008).

[274] S. R. Elliot, Solid State Ion. **70**, 27 (1994).

[275] S. Sumi, P. Prabhakar Rao. M. Deepa, and P. Koshy, J. Appl. Phys. **108**, 063718 (2010).

[276] R. Rai, I. Coondoo, R. Rani, I. Bdikin, S. Sharma, and A. L. Kholkin, Curr. Appl. Phys. **13,** 430 (2013).

[277] E. Dagotto, Science **309**, 257 (2005).

[278] E. Dagotto, S. Yunoki, C. S¸ en, G. Alvarez, and A. Moreo, J. Phys.: Condens. Matter **20**, 434224 (2008).

[279] K. H. Ahn, T. F. Seman, T. Lookman, and A. R. Bishop, Phys. Rev. B **88**, 144415 (2013).

[280] J. Wu and C. Leighton, Phys. Rev. B **67**, 174408 (2003).

[281] C. S. Snow, S. L. Cooper, D. P. Young, Z. Fisk, A. Comment, and J.-P. Ansermet, Phys. Rev. B **64**, 174412 (2001).

[282] S. A. Kivelson, E. Fradkin, and V. J. Emery, Nature (London) **393**, 550 (1998).

[283] T. Kimura, T. Goto, H. Shintani, K. Ishizaka, T. Arima, and Y. Tokura, Nature **426**, 55 (2003).

[284] A. P. Ramirez, J. Phys.: Condens. Matter **9**, 8171 (1997).

[285] A. N. Lavrov, S. Komiya, and Y. Ando, Nature **418**, 385 (2002).

[286] M. Kim, X. M. Chen, Y. I. Joe, E. Fradkin, P. Abbamonte, and S. L. Cooper, Phys. Rev. Lett. **104**, 136402 (2010).

[287] G. Lawes, A. P. Ramirez, C. M. Varma, and M. A. Subramanian, Phys. Rev. Lett. **91**, 257208 (2003).

[288] K. A. Gschneidner, Jr., V. K. Pecharsky, and A. O. Tsokol, Rep. Prog. Phys. **68**, 1479 (2005).

[289] R. W. McCallum, D. C. Johnston, C. A. Luengo, and M. B. Maple, J. Low Temp. Phys. **25**, 177 (1976).

[290] A. Irizawa, S. Suga, G. Isoyama, K. Shimai, K. Sato, K. Iizuka, T. Nanba, A. Higashiya, S. Niitaka, and H. Takagi, Phys. Rev. B **84**, 235116 (2011).

[291] M. Kopec, J. R. Dygas, F. Krok, A. Mauger, F. Gendron, B. Jaszczak-Figiel, A. Gagor, K. Zaghib, and C. M. Julien, Chem. Mater. **21**, 2525 (2009).

[292] Y. Yamasaki, S. Miyasaka, Y. Kaneko, J.-P. He, T. Arima, and Y. Tokura, Phys. Rev. Lett. **96**, 207204 (2006).

[293] K. Dey, S. Majumdar, and S. Giri, Phys. Rev. B 90, 184424 (2014).

[294] G. Giovannetti, A. Stroppa, S. Picozzi, D. Baldomir, V. Pardo, S. Blanco-Canosa, F. Rivadulla, S. Jodlauk, D. Niermann, J. Rohrkamp, T. Lorenz, S. Streltsov, D. I. Khomskii, and J.Hemberger, Phys. Rev. B **83**, 060402 (2011).

[295] A. Maignan, C. Martin, K. Singh, Ch. Simon, O. I. Lebedev, and S. Turner, J. Solid State Chem. **195**, 41 (2012).

[296] K. Singh, A. Maignan, C. Simon, and C. Martin, Appl. Phys. Lett. **99**, 172903 (2011).

[297] L. Balents, Nature (London) **464**, 199 (2010).

[298] Y. Zhou, K. Kanoda, and T. K. Ng, Rev. Mod. Phys. **89**, 025003 (2017).

[299] M. Fu, T. Imai, T. H. Han, and Y. S. Lee, Science **350**, 655 (2015).

[300] I. S. Jacobs and J. S. Kouvel, Phys. Rev. **122**, 412 (1961).

[301] M. S. Jagadeesh and M**.** S. Seehra, Phys. Rev. **23**, 1185 (1981).

[302] D. G. Wickham, W. J. Croft, J. Phys. Chem. Solids, **7,** 351 (1958).

[303] G. B. Jensen, O. V. Nielsen, J. Phys. C: Solid State Phys, **7**,409 (1974).

[304] C. Franchini, J. Zabloudil, R. Podloucky, F. Allegretti, F. Li, S. Surnev, F. P. Netzer, J. Chem. Phys. **130**, 124707 (2009).

[305] R. A. Robie, B.S. Hemingway, J. Chem. Thermodynam, **17**, 165 (1985).

[306] K. Chhor, J.F. Bocquet, C. Pommier, J. Chem. Thermodynam **18**, 89 (1986).

[307] J. H. Chung, K. H. Lee, Y.S. Song, T. Suzuki, and T. Katsufuji, J. Phys. Soc. Jpn. **82**, 034707, (2013).

[308] B. Chardon and F. Vigneron, J. Magn. Magn. Mater. **58**, 128 (1986).

[309] S. Pal and S. Lal, Phys. Rev. B **96**, 075139 (2017).

[310] T. Byrum, S. L. Gleason, A. Thaler, G. J. MacDougall, and S. L. Cooper, Phys. Rev. B **93**, 184418 (2016).

[311] S. Hirai, A. M. dos Santos, M. C. Shapiro, J. J. Molaison, N. Pradhan, M. Guthrie, C. A. Tulk, I. R. Fisher, and W. L. Mao, Phys. Rev. B **87**, 014417 (2013).

[312] F. Guillou, S. Thota, W. Prellier, J. Kumar, and V. Hardy, Phys. Rev. B **83**, 094423 (2011).

[313] S. Thota, F. Guillou, V. Hardy, A. Wahl, W. Prellier, and J. Kumar, J. Appl. Phys. **109**, 053902 (2011).

[314] A. Kuriki, Y. Moritomo, S. Xu, K. Ohoyama, K. Kato, A. Nakamura, J. Phys. Soc. Jpn, **72**, 458 (2003).

[315] B. Boucher, R. Buhl, and M. Perrin, J. Phys. Chem. Solids **32**, 2429 (1971).

[316] T. Suzuki and T. Katsufuji, J. Phys.: Conf. Ser. **150**, 042195 (2009)

[317] S. Thota, Q. Zhang, F. Guillou, U. Luders, N. Barrier, W. Preellier, A. Wahl and P. Padhan, Appl. Phys. Lett. **97**, 112506, (2010).

[318] S. K. Banerjee, Phys. Lett. **12**, 16 (1964).

[319] X. Zhou, W. Li, H. P. Kunkel, G. Williams, J. Phys.: Condens. Matter **16**, L39 (2004).

[320] X. Zhou, W. Li, H. P. Kunkel, G. Williams, and S. Zhang, J. Appl. Phys. **97**, 10M515 (2005).